ORNL-5218

Liquid Metal Fast Breeder Reactor Materials Deveiopment Program Quarteriy Progress Report for Period Endlng June 30, 1976

OAK RIDGE NATIONAL LABORATORY

OPERATED BY UNION CARBIDE CORPORATION FOR THE ENERGY RESEARCH AND DEVELOPMENT ADMINISTRATION

DISCLAIMER

Printed in the United States of America. Available from
the Energy Research and Development Administration,
Technical Information Center
P.O. Box 62, Oak Ridge, Tennessee 37830
Price: Printed Copy $8.00 ; Microfiche $3.00

ORNL-5218
Distribution Category
UC-79b, -h, -k

Contract No. W-7405-eng-26

METALS AND CERAMICS DIVISION

LIQUID METAL FAST BREEDER REACTOR MATERIALS DEVELOPMENT PROGRAM QUARTERLY PROGRESS REPORT FOR PERIOD ENDING JUNE 30, 1976

P. Patriarca, Person in Charge

Principal Investigators

R. G. Donnelly (ORNL)

J. M. Duke (Westinghouse-Tampa)

S. D. Harkness (Combustion Engineering)

R. T. King (ORNL)

E. Shuster (Midvale-Heppenstall)

G. M. Slaughter (ORNL)

Compiled and edited by Sigfred Peterson

Date Published: November 1976

OAK RIDGE NATIONAL LABORATORY
Oak Ridge, Tennessee 37830
operated by
UNION CARBIDE CORPORATION
for the
ENERGY RESEARCH AND DEVELOPMENT ADMINISTRATION

FOREWORD

This report continues a new series of quarterly reports on LMFBR materials programs conducted or overseen by the ORNL Metals and Ceramics Division. In essence it combines two previously issued series of reports, on the Fuels and Materials Development Program and the Steam Generator Materials Technology Program. Five chapters make up the contents:

1. Steam Generator Materials Development for Clinch River Breeder Reactor Plant (189a No. OH028).
2. Alternate LMFBR Structural Materials (189a No. OH038).
3. Mechanical and Metallurgical Behavior of Weldments for LMFBR (189a No. OH024).
4. Large Diameter Pipe and Fitting Development (189a No. OH103).
5. Advanced Absorber Materials (189a No. OH029).

The first two chapters cover programs previously reported in the *Steam Generator Materials Technology Program Quarterly Progress Report* series, and the third and fifth in the *Fuels and Materials Development Program Quarterly Progress Report* series. The fourth reports a new program. Recent previous reports in these series are listed below.

LMFBR Materials

ORNL-5117	Period Ending September 30, 1975
ORNL-5131	Period Ending December 31, 1975
ORNL-5157	Period Ending March 31, 1976

Steam Generator Reports

ORNL-TM-4969	Period Ending March 31, 1975
ORNL-TM-5027	Period Ending June 30, 1975

Fuels and Materials Reports

ORNL-TM-4250	Period Ending March 31, 1973
ORNL-TM-4355	Period Ending June 30, 1973
ORNL-TM-4405	Period Ending September 30, 1973
ORNL-TM-4524	Period Ending December 31, 1973
ORNL-TM-4620	Period Ending March 31, 1974
ORNL-TM-4688	Period Ending June 30, 1974
ORNL-TM-4726	Period Ending September 30, 1974
ORNL-TM-4878	Period Ending December 31, 1974
ORNL-TM-4940	Period Ending March 31, 1975
ORNL-TM-5029	Period Ending June 30, 1975

Progress on the program Mechanical Properties and Behavior for Structural Materials (189a No. OH050) is reported in a separate series for reports, the most recent of which is *Mechanical Properties Test Data for Structural Materials Quart. Progr. Rep. July 31, 1976,* ORNL-5200. Similarly, progress on Advanced NDT Development (189a No. OH061) is reported in *Nondestructive Testing Development Quart. Progr. Rep. June 30, 1976,* ORNL-5204.

Copies of these reports are available from the Energy Research and Development Administration, Technical Information Center, P.O. Box 62, Oak Ridge, Tennessee 37830.

CONTENTS

SUMMARY

1. STEAM GENERATOR MATERIALS DEVELOPMENT FOR CLINCH RIVER BREEDER REACTOR PLANT

The second heat-flux corrosion test with VAR 2 1/4 Cr-1 Mo steel, which lasted for 2977 hr, was completed, and the specimen was examined. The oxide was porous and cracked over the entire length, and a small amount of oxide had spalled from the surface on the hotter end of the specimen. The average corrosion penetration was 21.3 μm (0.84 mil), and 93% of the corrosion product was on the surface at the end of the test. In tests at a slightly higher temperature on air-melted 2 1/4 Cr-1 Mo steel, the extent of attack was slightly higher, and a greater percentage of oxide spalled from the surface during the same exposure period.

A postweld heat treatment study was conducted on internal-bore weldments in three heats of 2 1/4 Cr-1 Mo steel tubing. The different materials differed significantly in hardness (in both the as-welded and heat-treated conditions). A series of tubular tensile specimens containing bore weldments were tested at room temperature and 510°C (950°F). The specimens (which included both as-welded and postweld-heat-treated joints) all failed in the base metal well outside the weldment.

The tertiary creep behavior of annealed 2 1/4 Cr-1 Mo steel was studied at 545, 510, and 566°C (850, 950, and 1050°F). Many of the creep-rupture tests showed nonclassical creep curves with two steady-state stages. Using the values to the end of the second steady-state stage to determine the time to the onset of tertiary creep led to a consistent relationship with the rupture life.

Results are summarized for a report issued on the studies showing the effect of heat treatment on annealed 2 1/4 Cr-1 Mo steel.

We began tensile studies on a 2 1/4 Cr-1 Mo steel tubesheet forging manufactured by current industrial practices. We tested the material as received and laboratory annealed. Tensile tests and metallography on the as-received material indicate nonuniformity in strength and microstructure through the thickness of the forging.

Exposure of 2 1/4 Cr-1 Mo steel to sodium in an LMFBR steam generator can decarburize it and degrade its strength. We have obtained from MSA Corporation some tensile specimens that had been exposed to sodium in a stainless steel retort for 26,500 hr at 566°C (1050°F). This material, along with similar material that had been thermally aged for the same time, is being creep-ruture tested. This quarter we conducted tensile tests on the sodium-exposed specimens. The results verified the MSA results, which indicate a large drop in tensile properties after decarburization and aging.

Estimated cyclic stress-strain and relaxation behavior for fatigue involving long hold periods at peak strain for 2 1/4 Cr-1 Mo steel have been used to estimate possible damaging effects of creep-fatigue interaction. In addition, the strain range partitioning technique has been used to estimate possible "worst effects" creep-fatigue curves.

Available creep fatigue data for 2 1/4 Cr-1 Mo steel were analyzed by the methods of strain range partitioning and linear summation of damage. Even if modified to reflect the increased damage due to compression rather than tension hold periods, the linear summation approach does not fit the data well. On the other hand, the strain range partitioning approach yields very good results.

From comparisons with limited experimental data for a single heat of isothermally annealed, air-melted plate material of 2 1/4 Cr-1 Mo steel, it appears that isothermal, uniaxial relaxation behavior can be estimated from creep behavior using the hypothesis of strain hardening. Reasonable predictions were obtained by use of strain hardening in conjuntion with the creep equation for this material, although this approach tended to overestimate the amount of relaxation at lower temperatures ($\leqslant$ about 538°C) and higher stresses ($>$ yield strength).

The NDT program currently emphasizes the development of bore-side inspection techniques for the tube-to-tubesheet joints and tubing. Work on radiography with the microfocus rod-anode x-ray unit included modification of the x-ray target to expand the available x-ray beam width, studies and selection of improved cassette materials, examination of a large number of specimens with varying degrees of flaws, and drafting a paper on the radiographic studies and developments. The eddy-current work included studies and improvements to previously developed computer programs to allow simultaneous evaluation at three inspection frequencies for discrimination of flaws despite the presence of five other variables. The large number of parameters can be handled more accurately and rapidly in the inspection instrumentation, so digital microprocessors are being prepared for insertion into the modular equipment to allow real-time data processing. Improvements on the bore-side ultrasonic scanner now offer higher speed scanning and "C" scan (map) recording of flaws. Better ultrasonic probes have been fabricated and spin-off of fabricated technology to commercial suppliers is being successful. Several tube-to-tube joints were evaluated and, thus far, sensitivity to 10% (deep) flaws in the weld region has been demonstrated. Several lengths of stainless steel heat exchanger tubing were evaluated and shipped to Russia as part of a US/USSR technical exchange program. Ultrasonic properties in transition weld materials were measured and anisotropy was noted in weld metal when using shear waves. Preliminary examinations were performed with two crystal angle-beam longitudinal waves on sample weldments and flaws were detected through the weld metal. We are producing "C" scan maps of flaws during examination.

The hot-wire gas tungsten-arc welding equipment needed for development work on the CRBR transition joint program has been installed. Improvements

have been made to gain better control of the process. Most future welding work on this program will be performed with this equipment.

Our studies on the mechanical properties of transition joint materials continued. Creep-rupture curves and stress as a function of minimum creep rate curves are presented for tests at 454, 510, and 566°C (850, 950, and 1050°F). Creep-rupture tests were started at 621 and 677°C (1150 and 1250°F).

Continuous cycling and creep-fatigue tests on Inconel 82 weld metal have recently begun. Results of tests employing sound (defect-free) specimens indicated that the continuous cycling fatigue behavior of Inconel 82 at 538°C (1000°F) is similar to that of 2 1/4 Cr-1 Mo steel and type 316 stainless steel at the higher strain ranges (>0.5%); however, the cyclic life for Inconel 82 was superior to that for either of the other two transition weld joint materials at the lower strain ranges (<0.5%). Tests using specimens with flaws showed an 80 to 90% decrease in fatigue life at 538°C (1000°F). Several tests conducted with 0.1-hr strain hold periods each cycle at peak tensile or compressive strain amplitudes indicated an increasing reduction in fatigue life with decreasing strain range.

2. ALTERNATE LMFBR STURUCTURAL MATERIALS

Tensile results from room temperature to 704°C (1300°F) have been obtained during this period on two CE-developed alloys. These materials exhibit higher strengths than that reported for other 9 Cr steels; e.g., Sumitoma's HCM9M alloy.

Charpy V-notch impact testing on a series of low-nickel 9 Cr-1 Mo alloys showed excellent stability after aging for 2000 hr at 510°C (950°F). Only a minimum shift [3—6°C (5—10°F)] was observed in the 68-J (50-ft-lb) temperatures. Similar aging treatment applied to samples of the first 2300 kg (5000-lb) ingot material (heat 91887) revealed a decrease in upper-shelf energy and a shift in the 68-J (50-ft-lb) temperature.

Early stress-rupture tests for heat 91887 indicate better performance than both the Timken and HCM9M alloys. Stress-rupture testing in argon promotes a high minimum creep rate when compared with rates observed for testing in air.

The exceptional "hammer stopper" results previously reported on gas tungsten-arc weld samples are still under study. Transmission electron microscopy will be employed to characterize this material. Modification is now complete on the shielded metal-arc power supply, and evaluation of test plates has been initiated.

Mechanical property results obtained on 0.13-m (5-in.) ESR pilot heats have been found to be representative of 0.43-m-diam (17-in.) ingots.

Development work is in progress to make alloy 800 acceptable for elevated-temperature nuclear service under ASME Code Case 1592. Creep testing on several heats of alloy 800 in the 538 to 649°C (1000–1200°F) temperature range at lower stress is in progress. Transmission electron microscopy performed on creep specimens tested by a commercial vendor has demonstrated that γ' hardening occurs for some compositions within the specification range. Tubular burst specimens are under consideration to investigate the effects of triaxial stress. Presentation of data for alloy 800 to ASME code bodies has reopened consideration of the need for the present tertiary creep criterion for alloy 800.

3. MECHANICAL AND METALLURGICAL BEHAVIOR OF WELDMENTS FOR LMFBR

We are continuing to investigate and characterize austenitic stainless steel weld materials for high-temperature sodium applications. We are creep-rupture testing gas tungsten-arc (GTA) and submerged-arc (SA) welds made with commercial heats of filler wire that have controlled additions of B, P, and Ti. Preliminary results indicate that the SA welds are significantly weaker than GTA welds made with the same filler wires. Also, the GTA welds have creep strength and ductility values comparable to those of earlier experimental heats produced at ORNL.

The creep behavior of a submerged-arc type 308 stainless steel weld in three conditions has been determined at 649°C for rupture times from about 100 to 1000 hr, for both longitudinal and transverse specimen orientations. Weld metal annealed at 982°C (1800°F) for 4 hr has greater ductility than weld metal annealed 4 hr at 607°C (1125°F) or in the as-deposited condition. Prestraining less than 1% in creep for 500 hr at a lower stress severely reduces the ductility of specimens in subsequent testing to failure at a stress producing rupture in about 100 hr. Data from creep testing of a type 16-8-2 stainless steel submerged-arc weld are updated.

Previously obtained anisotropic elastic constants of a type 308 stainless steel electroslag weld have been used in a finite element program to demonstrate the mechanical response of a pipe with a circumferential weld. The limited results show that the anisotropic properties and the orientation of the anisotropy significantly affect the distribution of strain and stress in the vicinity of the weld.

A method for determining the velocity of sound as a function of direction in metal has been developed. The probe is moved by an immersed goniometric device about three cylindrical specimens. A cube is used for standardization. Measurements made on an electroslag type 308 stainless steel weld demonstrate anisotropic sound velocity that can be used to calculate elements of the dynamic elastic modulus matrix.

4. LARGE-DIAMETER PIPING AND FITTING DEVELOPMENT

Procurement of welded pipe is proceeding; two lots of pipe have been received, and three more are expected within a month. Only one supplier bid on a welded elbow. Preforms for the manufacture of spin-forged seamless pipe are also expected within a month.

A study of the effects of cold work and annealing on the structure and properties of welded pipe has shown that martensite is formed with as little as 10% cold work. Increasing amounts of cold work produce higher hardness and more martensite. Solution annealing returns the base metal to essentially the as-received condition, but the fusion zone grain size is refined significantly, increasing with increasing degree of cold work.

Initial characterization of centrifugally cast pipe shows highly variable ferrite levels within a given casting, generally in disagreement with accepted values based on bulk chemical composition. Calculated values range from 12.8 to 26.2 ferrite number, while measurements show a range of 0.3 to over 30. Metallographic observations confirm the high variability.

5. ADVANCED ABSORBER MATERIALS

Europium hexaboride (EuB_6) is a potential advanced neutron absorber for LMFBR application. A process for synthesizing EuB_6 powder and fabricating it into single-phase pellets of near theoretical density was demonstrated. The boride powder was synthesized by reacting europium oxide and boron carbide in vacuum at 1650°C, and the B/Eu molar ratio in the resulting heat-treated powders varied from 5.92 to 6.12 for corresponding values of 5.90 to 6.31 in the starting blend of oxide and carbide. Dense EuB_6 ceramic pellets were fabricated at 1850° and 1950°C by hot-pressing. The higher hot-pressing temperature produced pellets denser than 98% of theoretical for EuB_6 with Eu/B molar ratios varying from 5.83 to 5.99 depending on the ratio in the synthesis batch.

Microstructural data showed a bimodal grain size distribution in these hot-pressed ceramics with a matrix of grains of less than 10 μm in diameter surrounding larger grains up to 200 μm in diameter. Control of the grain size in these ceramics appears feasible by judicious control of the hot-pressing parameters during fabrication.

1. STEAM GENERATOR MATERIALS DEVELOPMENT FOR CLINCH RIVER BREEDER REACTOR PLANT*

G. M. Slaughter

1.1 INTRODUCTION

The LMFBR Steam Generator Materials Program has the broad responsibility for developing improved methods for fabricating and inspecting high-reliability components and for determining the properties and behavior of the various materials of interest under typical service conditions. The development and evaluation of methods for producing bore-side welds and transition welds are an important part of our program; simultaneously, nondestructive tests have to be developed to assure the required high quality of the as-fabricated component and assess the integrity of the component during service.

The service conditions include time, stress, and temperature for the base metals and weldments of interest. Because of the temperature requirements [>480°C (900°F)] for the steam generator, creep, stress rupture, fatigue, and stress relaxation are all important considerations. As part of this study, we will develop design data to meet the existing ASME Code requirements for components to operate in the creep regime.

Our environmental studies are concerned with the oxidation of 2 1/4 Cr-1 Mo steel in superheated steam under both heat transfer and isothermal conditions.

1.2 THE CORROSION OF VACUUM-ARC-REMELT 2 1/4 Cr-1 Mo STEEL BY SUPERHEATED STEAM — J. C. Griess, J. H. DeVan, and W. A. Maxwell†

The effect of heat flux on the corrosion of vacuum-arc-remelted (VAR) 2 1/4 Cr-1 Mo steel in superheated steam is being determined under conditions approaching those that will exist in the superheaters of the Clinch River Breeder Reactor Plant. The results from a similar series of tests with standard air-melted (AM) 2 1/4 Cr-1 Mo steel have been

---

*Progress on work performed under 189a, OH028.

†NUS Corp., Clearwater, Fla. 33515.

reported.[1] The tests with the VAR material use the same equipment, procedures, and specimen type as were used in the tests with the AM steel. Table 1.1 lists the conditions for both series of tests. The VAR specimens were exposed to a greater mass flow rate and velocity of steam and lower surface temperatures. Other test conditions were the same as for AM specimens. Eight individual specimens were used in the first series, but only four VAR specimens will be exposed.

In the last quarterly report[2] the oxidation results were presented for the first VAR 2 1/4 Cr-1 Mo steel specimen, which had been exposed for 1000 hr. During this quarter both VAR specimens in the heat-flux test loop were removed for visual examination, and the one that had been exposed for 2977 hr was replaced with a new one of the same material. The one that had been in test for 3977 hr was returned to the loop for additional exposure. Both specimens were covered with smooth black scales over most of their length, but a few small flecks of oxide were randomly

Table 1.1. Conditions for the Heat-Transfer Corrosion Tests with 2 1/4 Cr-1 Mo Steel

	AM Steel	VAR Steel
Bulk steam temperature, °C (°F)		
Inlet	468 (875)	486 (906)
Outlet	499 (930)	503 (938)
Specimen surface temperature, °C (°F)		
Inlet	510 (950)	502 (935)
Outlet	541 (1005)	522 (972)
Average heat flux, kW/m^2 (Btu hr^{-1} ft^{-2})	126 (40,000)	126 (40,000)
Steam pressure, MPa (psi)	10.5 (1525)	10.5 (1525)
Steam mass flow rate, kg/hr (lb/hr)	272 (600)	439 (966)
Steam velocity, m/sec (ft/sec)	13.1 (43)	36.6 (120)
Exposure times, hr	525, 584,[a] 951, 1026, 2007, 3026, 5989	1000, 2977 6000, 10,000

[a]Duplicate specimens.

missing from a 15 to 20 cm (6–8 in.) segment at the high-temperature end of each specimen. The temperature range over which the oxide had spalled was approximately 516 to 522°C (960–972°F). Visually the two specimens were about the same, although slightly more oxide may have been lost from the specimen with the longer exposure.

Two small transverse sections — one from the cooler and the other from the hotter end — were cut from the specimen and metallographically polished. The oxide on both sections contained cracks and pores, and except for being thicker looked like that on the 1000-hr specimen (see Fig. 1.1 in Ref. 2).

Following removal of the metallographic sections, the remainder of the specimen was descaled in Clarke's Solution. After appropriate corrections for the metal and oxide removed for the metallographic specimens, the weights of the metal oxidized and the oxide on the specimen were determined, and from the densities of the steel and the oxide the average penetration of the metal and the average oxide thickness were calculated. These values as well as the percent of oxide remaining on the specimen at the end of the test are shown in Table 1.2. The latter value was based on the assumption that all the metal oxidized was converted to stoichiometric Fe_3O_4. Also shown in Table 1.2 are the corresponding data obtained from the 1000-hr VAR specimen and for the AM specimens exposed for comparable times.

Table 1.2. Summary of Corrosion Data for Air-Melted and Vacuum-Arc-Remelted 2 1/4 Cr-1 Mo Steel Exposed to Superheated Steam

Nominal Test Time (hr)	Material	Average Penetration (μm)	Average Oxide Thickness (μm)	Oxide on Specimen (%)
1000	AM	15.5	29.2	90[a]
1000	VAR	11.2	22.9	97
3000	AM	25.9	44.7	83
3000	VAR	21.3	41.4	93

[a]Some oxide lost from specimen after removal from test.

The table shows that the VAR specimens have corroded less than the AM specimens at comparable times and that during the 3000-hr tests more oxide spalled from the AM than from the VAR specimens. Since the character of the oxides scales is very similar between the two grades of steel, the difference in corrosion behavior appears to be related to temperature rather than to any metallurgical differences.

The long-term corrosion behavior of the VAR steel cannot be determined from the two data points in hand since under the test conditions the corrosion rate is probably still decreasing with time. This possibility is suggested by the fact that there was no evidence of exfoliation after 1000 hr and only slight spalling of oxide after 2977 hr. With the AM steel at the higher temperature substantial spalling of the oxide had occurred over most of the length of the specimen after the same exposure. Even though there was less spalling at the lower temperature, the oxide on the specimen contained cracks and porosity, indicating that extensive spalling is likely to occur after longer test periods.

Tests of VAR specimens now in progress will provide corrosion rates for 6000- and 10,000-hr exposures. These tests are scheduled to be completed in February, 1977.

1.3 WELDING OF MATERIALS FOR STEAM GENERATORS — G. M. Slaughter

1.3.1 Tube-to-Tubesheet Welding Development — A. J. Moorhead

The purpose of this study is to conduct research and development activities that support the Clinch River Breeder Reactor (CRBR) steam generator program in the area of tube-to-tubesheet welding. These steam generators will be manufactured from annealed 2 1/4 Cr-1 Mo steel. The design of the tube-to-tubesheet weld joint is a tube-to-boss type as illustrated in the right hand portion of Fig. 1.1. This figure compares the geometries, advantages, and disadvantages for various types of tube-to-tubesheet connections. Note that the CRBR design (tube-to-boss) has the major advantage of eliminating the typical crevice between the tube and tubesheet, and is amenable to volumetric inspection techniques.

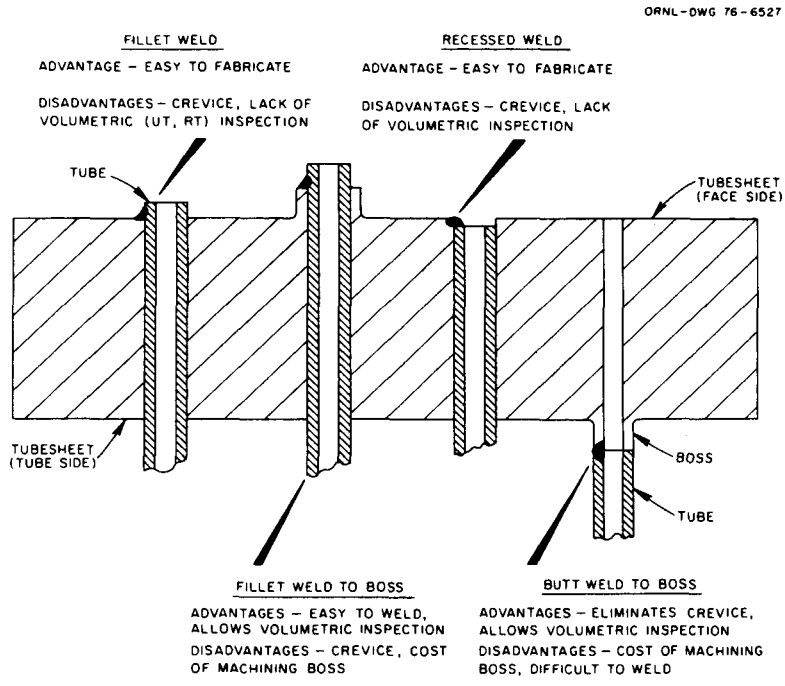

Fig. 1.1. Typical Configurations for Tube-to-Tubesheet Welds.

However, the close proximity of the tubes restricts access to the outside of the weld joint, so that the joint will be welded by an internal-bore-welding technique using a device shown schematically in a previous report[3] and illustrated in Fig. 1.2. Also, the weld joint will be inspected from the inside of the tube. The joining process used is gas tungsten-arc, using as an electrode a tungsten rod that is very short and pointed [because of the 10-mm (0.4-in.) inside diameter of the tubing] located by the arrow in the figure. The weld is produced autogenously because of the great difficulty expected if we tried to feed filler wire in such a confined space.

The specific objectives of our program at this time are:

1. Investigate the effects on weldability of heat-to-heat compositional variations; specifically determine the influence of silicon on weld metal fluidity, penetration, etc.

2. Determine the effect of procedure variables such as preheat temperature and postweld heat treatment conditions on weld quality and mechanical properties.

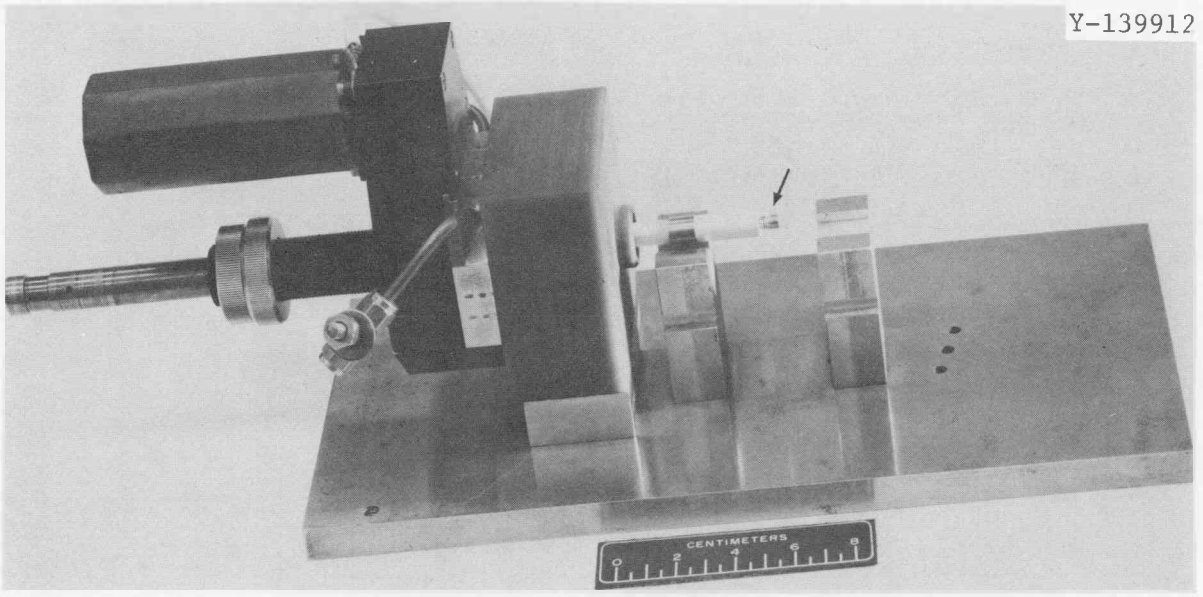

Fig. 1.2. Internal Bore Welding Head with Improved Alignment Fixture. The arrow indicates the location of the tungsten electrode.

3. Produce internal-bore-welded tube-to-tubesheet specimens for mechanical property and nondestructive tests, at least until the vendor is in a position to provide adequate numbers of specimens on a timely basis.

4. Maintain an in-house expertise on internal bore welding to supplement the efforts of vendors in case of manufacturing difficulties.

We previously reported on the commercially obtained internal welding head being adapted for this program,[4] on the development of welding procedures using this equipment,[5] on the welding of samples in air-melted (AM) and electroslag-remelted (ESR) materials,[5] on the reassessment of the need for this program,[6] and on radiographic inspection data for a number of internal bore welds in AM and ESR material.[6] Most recently[3] we observed significant differences in weld penetration in two heats of 2 1/4 Cr-1 Mo steel tubing drawn from tube hollows produced by vacuum arc remelting (VAR).

During this report period we (1) conducted an extensive study on the effect of postweld heat treatment time and temperature on the hardness of weldments in three heats of 2 1/4 Cr-1 Mo steel tubing, (2) made and tested a series of tensile specimens containing internal

bore welds, and (3) evaluated some changes in the welding head and fixturing. Each of these items will be discussed separately below.

The postweld heat treatment study was conducted on the three bead-on-tube weldments shown previously[3] to illustrate the difference in penetration between one AM and two VAR heats of tubing. The compositions of the tubing are given in Table 1.3. All welds were made according to identical welding procedures with no weld preheat. The welding speed was 1.7 mm/sec (4 in./min) with a constant arc current of 52 A dc. Each sample was cut into a number of 1.6-mm-thick (1/16-in.) transverse weld specimens, which were subsequently sealed in quartz capsules containing a partial pressure of argon. The samples were then heat-treated, each for one of the following 12 sets of conditions:

1 hr at 621°C (1150°F), 677°C (1250°F), 732°C (1350°F), 788°C (1450°F); 5, 10, 20, or 40 hr at 677 or at 732°C.

Duplicate specimens were run in some cases from different areas of a weldment to look for possible differences in microstructure and/or hardness as a function of circumferential position; for example, the "downslope" region vs the constant-current portion.

After heat treatment the sections were mounted and polished for metallographic examination, and a series of five microhardness (DPH) indentations was made across each weldment. The indentations were located so that the hardness of the fusion zone, three regions of the

Table 1.3. Chemical Composition of Three Heats of 2 1/4 Cr-1 Mo Steel Tubing Evaluated in the Postweld Heat Treatment Study

Tube	Heat	Composition,[a] wt %								
		Si	S	P	Mn	C	Cr	Ni	Mo	Al
VAR-02	56062	0.57	0.004	0.014	0.38	0.12	2.40	0.24	1.05	0.013
VAR-35	55262	0.15	0.012	0.013	0.58	0.087	2.33	0.16	1.07	0.001
AM-424[b]		0.22	0.011	0.011	0.45	0.062	2.15	0.14	1.02	0.019

[a] <0.01% Ti in all three materials.

[b] Tubing from an air-melted ingot. Saw service in the Atomics International Modular Steam Generator.

heat-affected zone, and the base metal could be determined. The results of these hardness traverses are summarized in Table 1.4. These data are still being analyzed, but as of this writing we can make the following observations and opinions:

1. Significant differences in hardness are found in the various weldments, either as welded or postweld heat-treated.

Table 1.4. Hardness of Internal-Bore Weldments in 2 1/4 Cr-1 Mo Steel Tubing as a Function of Postweld Heat Treatment Time and Temperature[a]

Section	Postweld Heat Treatment		Hardness, DPH (1 kg load)				
			Fusion Zone	Heat-Affected Zone			
	(hr)	(°C)		Just Outside Fusion Line	Central	Near Unaffected Base Metal	Base Metal
VAR-02-1	0		361	406	377	310	173
VAR-02-3	1	677	251	254	234	209	156
VAR-02-4	1	732	234	214	214	202	150
VAR-02-9	10	732	200	180	190	190	149
VAR-02-15[b]	10	732	194	182	194	184	146
VAR-02-11	20	732	180	182	190	182	142
VAR-02-13	40	732	180	177	186	180	142
VAR-35-1	0		283	298	323	273	135
VAR-35-3	1	677	204	218	214	200	148
VAR-35-4	1	732	196	200	202	188	146
VAR-35-9[b]	10	732	186	180	180	172	131
VAR-35-21	10	732	180	179	175	173	130
VAR-35-11	20	732	177	167	168	165	141
VAR-35-13	40	732	175	172	165	157	126
AM-424-1	0		266	287	287	231	149
AM-424-3	1	677	207	196	190	168	140
AM-424-4	1	732	188	190	188	168	132
AM-424-9	10	732	186	180	170	164	124
AM-424-23	10	732	177	180	170	167	125
AM-424-11	20	732	177	177	164	162	125
AM-424-13	40	732	173	168	157	154	119

[a]All samples sealed in quartz tubes containing a partial pressure of Ar.

[b]Section taken in current downslope area of weldment.

2. The behavior noted in (1) can likely be attributed to compositional differences (particularly carbon content) between the heats of tubing and the effect of certain elements on the hardenability of the steel.

3. The downslope and constant-current regions of the weldments have essentially the same hardness.

4. The hardness of the fusion zones remains significantly higher than that of the base metals, even after 40 hr postweld heat treatment at 732°C (1350°F).

5. The hardness of the weldments remains above the maximum hardness of DPH 170 (equivalent to Brinell 163) allowed by Sect. II of the ASME Code for this tubing, even after a postweld heat treatment of 10 hr at 732°C (1350°F).

A series of 12 tubular tensile specimens containing internal bore welds was tested at room temperature and 510°C (950°F). Two heats of VAR tubing were tested (tubes -02 and -35) in the as-welded condition as well as after postweld heat treatments of 1 hr at either 677 or 732°C (1250 or 1350°F). The welds were bead-on-tube made by the same welding procedure except that an extra revolution at welding current (53 A dc) was used for the VAR-02 material to achieve full penetration. After heat treatment (in air) the samples were machined both inside and out, leaving a final wall thickness of 1.57 mm (0.062 in.). The results of the testing of these specimens in air at a crosshead speed of 21 μm/sec (0.05 in./min) are given in Table 1.5. Note that every specimen failed in the base metal outside the weldment; an example can be seen in Fig. 1.3. This condition may be of significance, depending on how it affects the high-cycle fatigue behavior of the tube-to-tubesheet joints.

A new alignment fixture was designed and built during this report period. This device (shown in Fig. 1.2) has no adjustable parts and thus eliminates the alignment problems that have given us difficulty in the past.

We also evaluated a new material for potential use in making gas cups for the welding tip. This material (Macor machinable glass-ceramic) machined well and appears to resist cracking. However, the cup melted near the electrode, so Macor is unsuitable for our use, at least with the present tip design.

Table 1.5. Tensile Test Results[a] of Internal-Bore-Welded 2 1/4 Cr-1 Mo Steel Tubing

Specimen[b]	Test Temperature		0.2% Offset Yield Strength		Ultimate Strength	
	(°C)	(°F)	(MPa)	(psi)	(MPa)	(psi)
VAR-35-AW	Room		303	44,000	427	62,000
VAR-35-1250	Room		292	42,300	449	65,100
VAR-35-1350	Room		292	42,400	448	65,000
VAR-35-AW	510	950	228	33,000	400	58,000
VAR-35-1250	510	950	202	29,250	402	58,250
VAR-35-1350	510	950	203	29,500	424	61,500
VAR-02-AW	Room		300	43,500	532	77,200
VAR-02-1250	Room		312	45,250	521	75,500
VAR-02-1350	Room		312	45,250	514	74,500
VAR-02-AW	510	950	216	31,300	385	55,900
VAR-02-1250	510	950	203	29,500	399	57,900
VAR-02-1350	510	950	195	28,250	411	59,600

[a]Test conducted in air. All specimens failed oustide the 1-in. gage marks (i.e., in the base metal), crosshead speed of 21 μm/sec (0.05 in./min).

[b]Specimen code: AW ≡ as welded, 1250 ≡ PWHT 1 hr at 677°C in air before machining, and 1350 ≡ PWHT 1 hr at 732°C in air before machining.

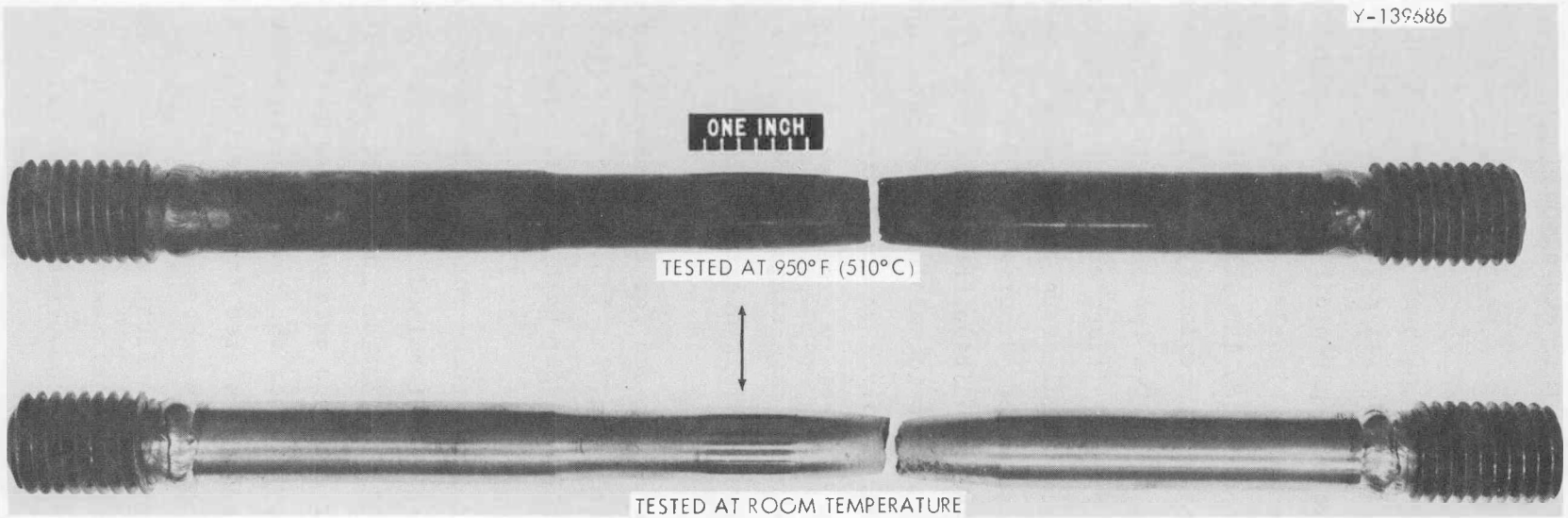

Fig. 1.3. Tensile Specimens Containing Internal Bore Welds in 2 1/4 Cr-1 Mo Steel (Tube VAR-35) Tested after Postweld Heat Treatment of 1 hr at 732°C (1350°F). The centerlines of the welds are indicated by an arrow.

1.4 MECHANICAL PROPERTIES OF STEAM GENERATOR MATERIALS — C. R. Brinkman

1.4.1 Creep and Rupture Behavior of 2 1/4 Cr-1 Mo Steel — R. L. Klueh

We are studying the effect of heat treatment on the creep and creep-rupture properties of annealed 2 1/4 Cr-1 Mo steel.[7,8] Pieces of a 25-mm-thick (1-in.) plate were given different annealing treatments: two pieces were fully annealed, labeled AN-1 and AN-2 (AN-2 was cooled faster than AN-1), and one piece, labeled IA, was isothermally annealed. The creep-rupture studies were previously reported and discussed.[7,8]

In those studies we noted two types of creep curves: a classical creep curve with single primary (transient), secondary (steady-state), and tertiary stages; nonclassical creep curves were also noted with two steady-state stages. A schematic diagram of these two types of curves is shown in Fig. 1.4. The transition from the first steady-state stage to the second involved an increasing creep rate, and since, by definition, tertiary creep involves an increasing creep rate, the question arises whether this is tertiary creep or whether the part of the curve after the second steady-state stage, where the creep rate again increases, is tertiary creep. This question will be addressed in this report.

All creep curves were examined for curve shape, and our observations are summarized schematically in Fig. 1.5. At 566°C (1050°F), tests at 103 and 124 MPa (15 and 18 ksi) for both heat treatments AN-1 and IA displayed classical creep curves. At 138 MPa (20 ksi) a nonclassical creep curve was observed. The creep rate for the second steady-state creep stage was quite easily determined for the tests up to and including 172 MPa (25 ksi). At 207 MPa (30 ksi), however, we could only determine one creep rate. Whether this was because a classical strain-time relationship again existed or whether the second steady-state stage was too short to be detected cannot be stated (the question mark after the C in Fig. 1.5 is meant to denote this uncertainty).

When the creep rate for the first steady-state stage for the nonclassical curves at 566°C (1050°F) was plotted against stress, a discontinuity was observed: the two low-stress tests fell on one curve, the

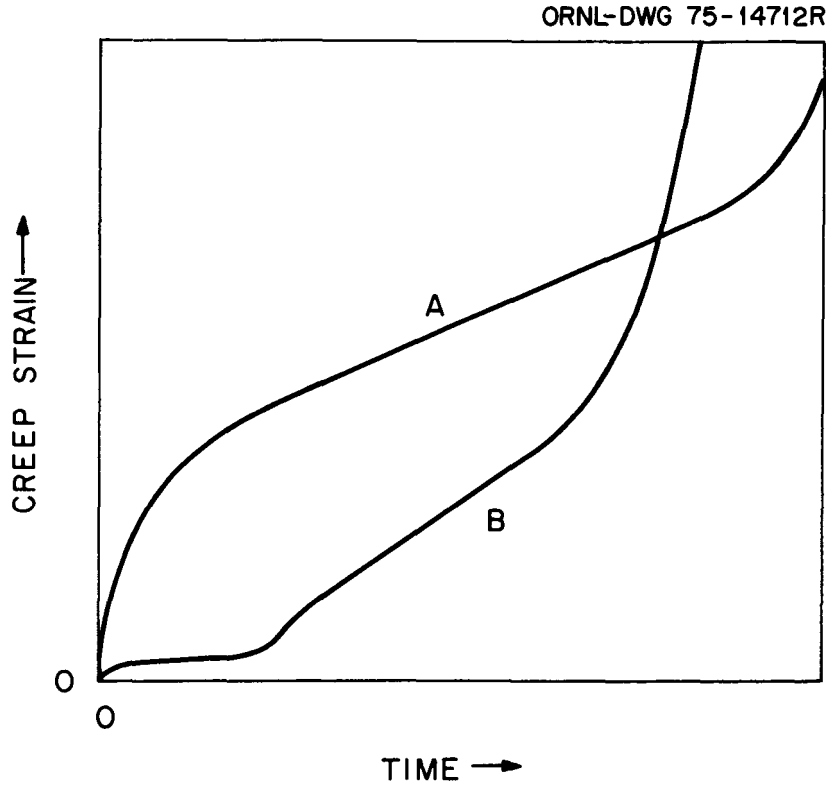

Fig. 1.4. Schematic Diagrams for Classical (A) and Nonclassical (B) Curves of the Type Observed for 2 1/4 Cr-1 Mo Steel.

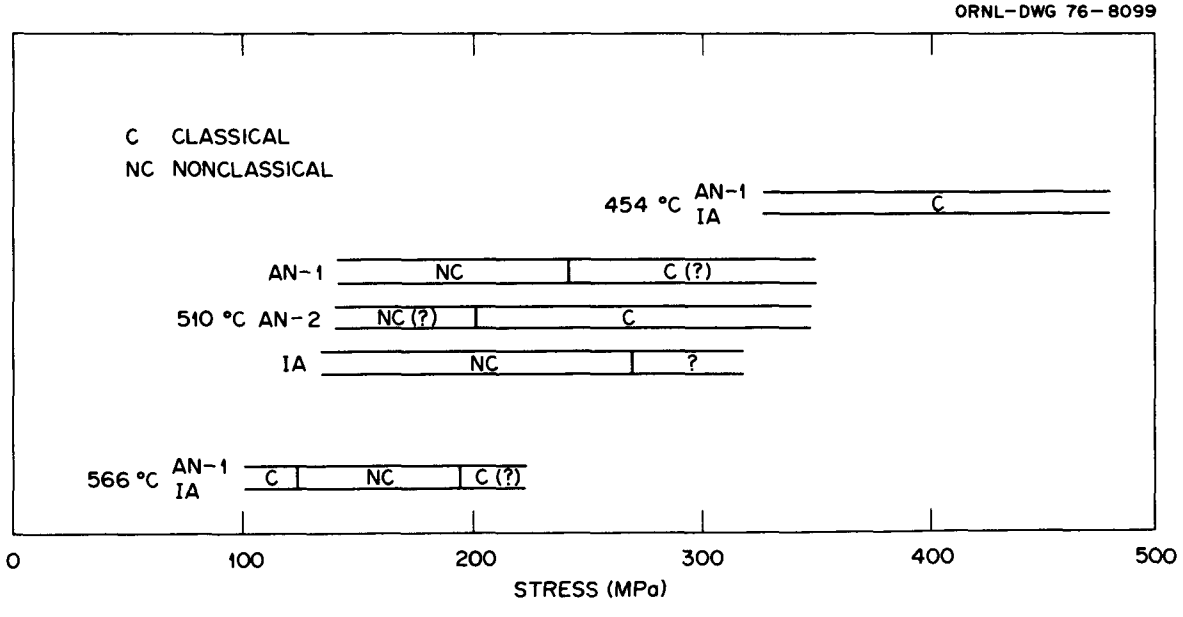

Fig. 1.5. Schematic Representation of Creep Curve Shape as a Function of Stress at 454, 510, and 566°C.

rest on a second curve.[7] However, when the creep rate for the second steady-state stage was used for the nonclassical curves, a continuous curve was obtained.[7]

Classical creep curves were observed for all the tests at 454°C (850°F) (Fig. 1.5). At 510°C (950°F), the type of behavior depended on stress and heat treatment. For the AN-2 specimens at 510°C, all the creep curves appeared classical, although there are indications that the curves at 207 MPa (30 ksi) may be nonclassical [the NC(?) region in Fig. 1.5].

For IA at 510°C, only nonclassical curves were observed. All curves for AN-1 were nonclassical below about 241 MPa (35 ksi). Above this stress only a single steady-state stage could be accurately determined [again, the reason for this is unknown and shown as C(?) in Fig. 1.5]. When the creep rate for the second steady-state stage was plotted against stress, a continuous curve resulted. This curve fell to the right of the one obtained[7] for the first steady-state stage.

In the present report, the tertiary creep behavior will be examined. Tertiary creep is easily defined for the classical curve (Curve A of Fig. 1.4): it is the point where the creep rate begins to increase after a period of constant creep rate (the minimum creep rate) during the secondary stage (steady-state creep). A 0.2% offset method is generally used to uniformly set the point of departure from steady state. Several investigators[9-12] have shown that a relationship exists between the start of tertiary creep and rupture life for various alloys, including 2 1/4 Cr-1 Mo steel. Usually, a relationship of the type

$$t_2 = A t_R^{\alpha} \tag{1}$$

is found, where t_2 is the time to the start of tertiary creep, t_R is the rupture life, and A and α are constants; α is often found to be unity. According to Eq. (1), a graph of log t_2 against log t_R should result in a straight line with a slope of α.

We have obtained t_2 values from all the creep curves, and in Fig. 1.6 these data are plotted according to Eq. (1). Where nonclassical creep

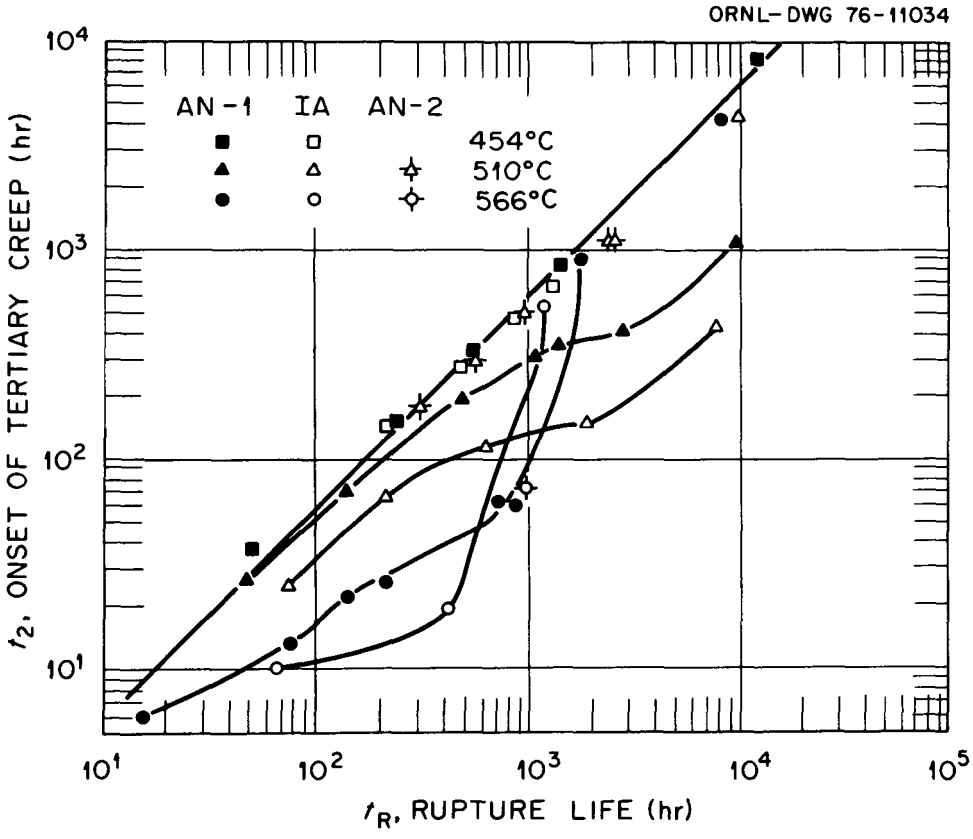

Fig. 1.6. Time to the Onset of Tertiary Creep Plotted Against Rupture Life. For tests where two steady-state stages were observed (i.e., at 510 and 566°C) the time to the end of the first steady-state stage is plotted.

curves were observed, the 0.2% offset from the first steady-state stage was used. The data used for Fig. 1.6 are given in Table 1.6.

It is obvious from Fig. 1.6 that the expected straight-line relationship does not apply for all the tests. The data are stratified, and four curves have been drawn. With the exception of the longest test at 454°C, the combined data for AN-1 and IA at 454°C and the AN-2 data at 510°C appear to fall on a straight line (a line with $\alpha = 1$ has been drawn through these data). The other curves in Fig. 1.6 are separate curves for AN-1 and IA at 510 and 566°C. At 510°C, data for IA and AN-1 are roughly parallel. Although the 566°C data parallel the 510°C data for short times, they deviate dramatically for longer rupture times:

Table 1.6. Time and Strain to Start of Tertiary Creep (0.2% Offset) for 2 1/4 Cr-1 Mo Steel

Heat Treatment	Temperature		Stress		Rupture Life (hr)	Transition to Tertiary Creep				$\varepsilon_2/\varepsilon_R$ (%)
						Time, hr		Strain, %		
	(°C)	(°F)	(MPa)	(ksi)		Stage 1	Stage 2	Stage 1	Stage 2	
AN-1	454	850	327	47.5	12,059.1	8,150	a	1.48	a	9
			358	52	1,435.3	820	a	2.28	a	13
			379	55	539.1	330	a	2.88	a	16
			413	60	233.4	150	a	2.86	a	15
			448	65	48.9	37	a	3.13	a	18
	510	950	152	22	9,650.3	1,100	5,300	0.38	6.63	20
			172	25	b	520	b	0.49	b	
			172	25	2,788.0	400	1,280	0.44	4.37	12
			189	27.5	1,396.4	350	780	0.52	4.77	13
			207	30	1,089.3	300	680	0.60	5.84	17
			241	35	476.0	200	326	1.23	4.06	15
			276	40	135.5	68	a	2.90	a	10
			310	45	47.5	26	a	2.75	a	10
	566	1050	103	15	8,194.8	4,200	a	3.75	a	20
			124	18	1,804.6	900	a	5.47	a	20
			138	20	707.3	63	380	0.32	5.38	17
			138	20	885.4	60	440	0.41	5.16	16
			152	22	222.9	26	113	0.20	7.13	15
			172	25	78.2	13	31	1.38	3.93	11
			172	25	136.5	22	78	0.85	6.75	17
			207	30	16.3	6		3.5		9
AN-2	510	950	207	30	2,372.8	1,110	c	0.46	c	1
			207	30	2,354.4	1,120	c	0.46	c	2
			276	40	952.9	500	a	0.70	a	3
			310	45	563.0	300	a	1.50	a	7
			345	50	308.4	175	a	2.41	a	12
	566	1050	138	20	982.2	83	540	0.34	4.89	15
IA	454	850	338	49	1,301.9	665	a	1.49	a	6
			358	52	854.9	475	a	2.59	a	15
			379	55	479.1	280	a	2.33	a	10
			413	60	214.6	144	a	2.55	a	16
	510	950	152	22	6,853.9	438	4,400	0.31	7.25	22
			172	25	1,879.5	150	850	0.34	3.71	9
			207	30	526.0	125	270	0.65	3.53	9
			241	35	204.5	69	138	1.15	6.15	14
			276	40	74.2	25	55	1.28	5.13	23
	566	1050	103	15	9,918.7	4,400	a	3.30	a	
			124	18	1,233.1	535	a	4.86	a	16
			138	20	400.4	19	175	0.48	6.15	13
			172	25	68.5	10	25	1.25	5.25	11

[a]Classical creep curve.

[b]Test discontinued after 1321 hr.

[c]There appeared to be a short second steady-state stage, but strains and times could not be accurately determined.

the 566°C curves cross the 510°C curves. It is interesting to observe in Fig. 1.6 that the data at 566°C that led to the deviation from the trends at 510°C (i.e., caused the curves to cross over) are from tests at 103 and 124 MPa (15 and 18 ksi). These were the tests that displayed classical creep curves at 566°C. Note also that at short times all these curves appear to approach the straight line for the 454°C data and the AN-2 data at 510°C. At these high stresses "classical" creep curves were observed (Fig. 1.5).

The above observations clearly indicate that the stratification of data evident from Fig. 1.6 is connected with the different creep curve shapes. To further examine the relationships between creep curve shape and tertiary creep, we determined the creep strain to the start of the two "tertiary creep stages." These values are given in Table 1.6; in Fig. 1.7 the strain values are plotted against stress.

The strain values fall into three distinct categories: (1) For the obviously nonclassical curves at 510 and 566°C (heat treatments AN-1 and IA), the strain to the end of the first steady-state stage is less than 1.5% (most are less than 0.7%); this also applies to the low-stress tests for AN-2 at 510°C, where no second steady-state stage could be clearly deliniated. (2) Strains for AN-1 and IA to the end of the second steady-state stage of the nonclassical curves at 510 and 566°C and the end of the steady-state stage of the classical curves at 103 and 124 MPa (the low-stress tests) at 566°C are from 4 to 7%. (3) The strains for AN-1 and IA at 454°C, for the higher stresses for AN-2 at 510°C, and for the higher stresses for AN-1 at 510 and 566°C — all of which show "classical" curves — are from 1.5 to 2.5%.

Table 1.6 also gives the ratio of $\varepsilon_2/\varepsilon_R$, where ε_R is the total elongation and ε_2 is the strain to the end of the steady-state stage; for nonclassical curves, it is the end of the second steady-state stage. For AN-1 and IA at 510 and 566°C, values between about 10 and 20% are observed. Similar results (with one exception) are observed at 454°C; the large $\varepsilon_2/\varepsilon_R$ values at 454°C occur, despite the low ε_2 values, because of the lower total elongation. Note also that this ratio is between 10

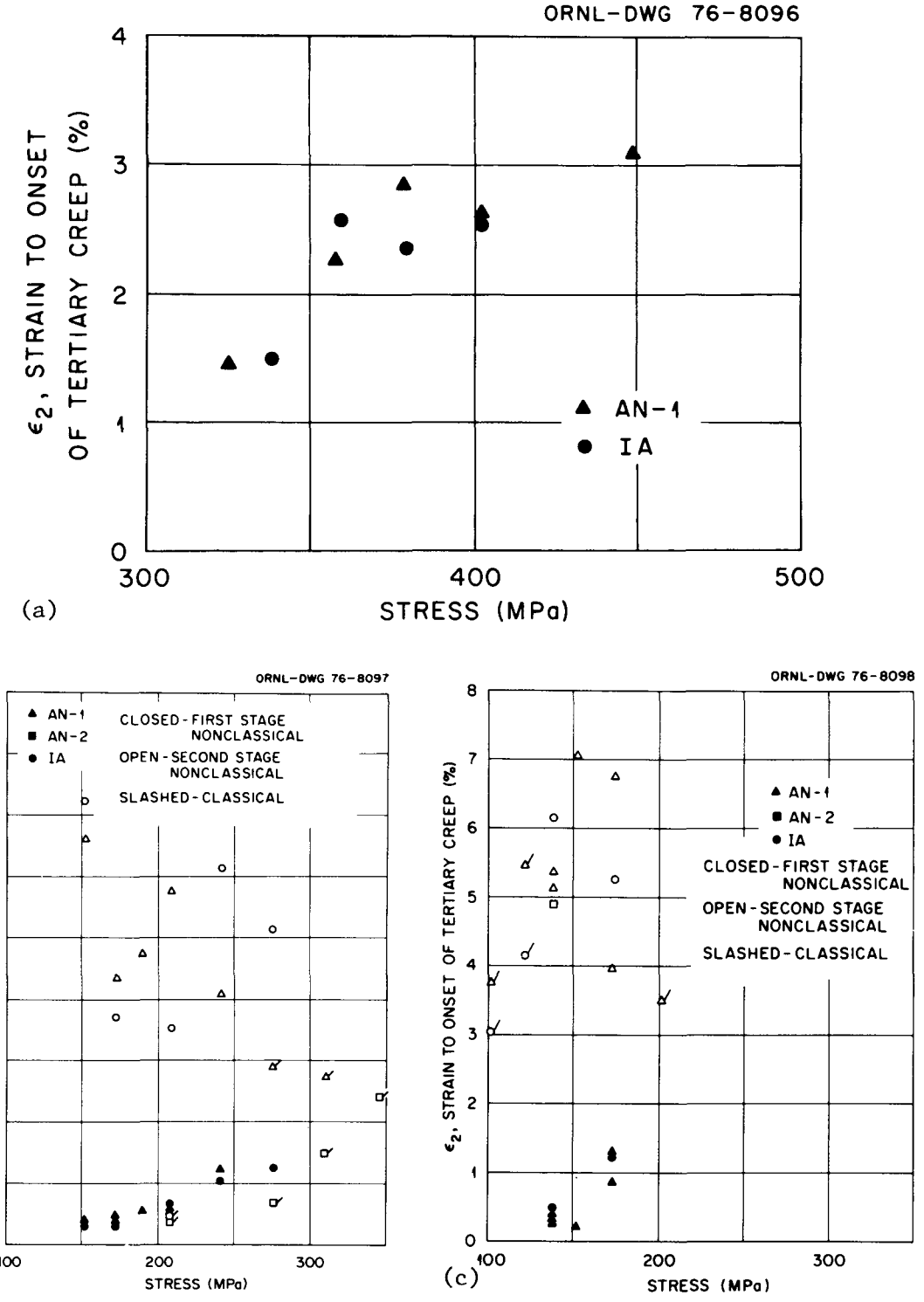

Fig. 1.7. Strain to the Onset of the Two "Tertiary Creep Stages" at (a) 454°C, (b) 510°C, and (c) 566°C.

and 20 for the high-stress tests on AN-1 at 510 and 566°C and the high-stress test on AN-2 at 510°C for a similar reason (i.e., although ε_2 decreases with increasing stress, the total elongation also decreases with increasing stress. Also, note how the $\varepsilon_2/\varepsilon_R$ ratio for the low-stress results for AN-2 at 510°C fall substantially below 10 (a similar low ratio would result if the time to the end of the first steady-state stage were used for ε_2).

As a result of these observations on the strains to the onset of tertiary creep and the previous observations[7] when the creep rates were plotted with the creep rate for the second steady-state stage used, the data of Table 3.14 were replotted according to Eq. (1). Figure 1.8 shows the data with strains that fall into the second category ($\varepsilon_2 \simeq 4$—7%), while Fig. 1.9 shows the data for strains that fall into category 3 ($\varepsilon_2 \simeq 1.5$—3%). For Fig. 1.8, the data for the nonclassical curves at 510 and 566°C are plotted with t_2 as the time to the end of the second steady-state stage. The data used in Fig. 1.9 include all the data at 454°C and the high-stress tests for AN-2 at 510°C and AN-1 at 510 and 566°C.

In both cases the data appear to fall on a straight line. The values for α and A for a least squares fit of the data are given in Table 1.7 (in all cases the correlation coefficient $R^2 \approx 0.99$). Since there was little difference in the values of α and A for the curves in Figs. 1.8 and 1.9, the data were combined and are shown in Fig. 1.10. The equation for the combined data is given by

$$t_2 = 0.489\ t_R^{1.016} \ . \qquad (2)$$

As seen in Table 1.7, combining the data did not significantly alter the standard error of estimate. Therefore, the combined representation would appear appropriate.

In the above discussion, the four low-stress tests on AN-2 were ignored (these data fall into category 1; they display "classical" curves, with $\varepsilon_2/\varepsilon_R < 10$). It will be pointed out in our next quarterly report that these curves are probably nonclassical, but because of the extended

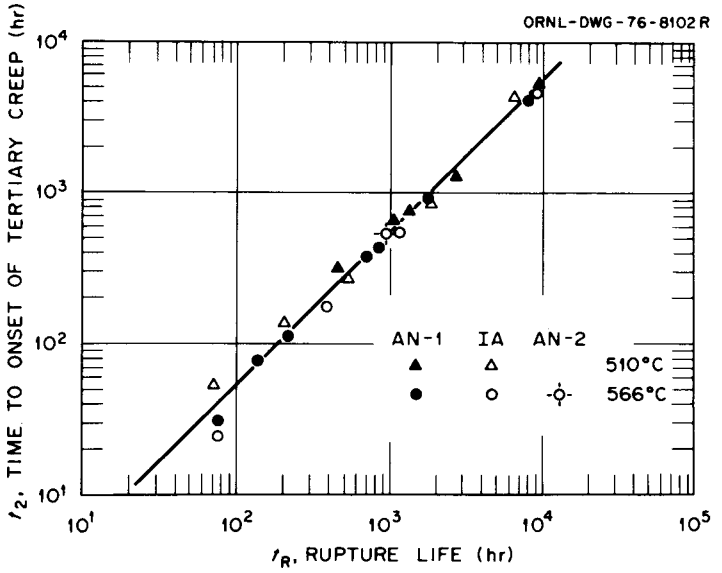

Fig. 1.8. Time to the Onset of Tertiary Creep Plotted Against Rupture Life at 510 and 566°C. For tests that had nonclassical creep curves, the end of the second steady-state stage was used.

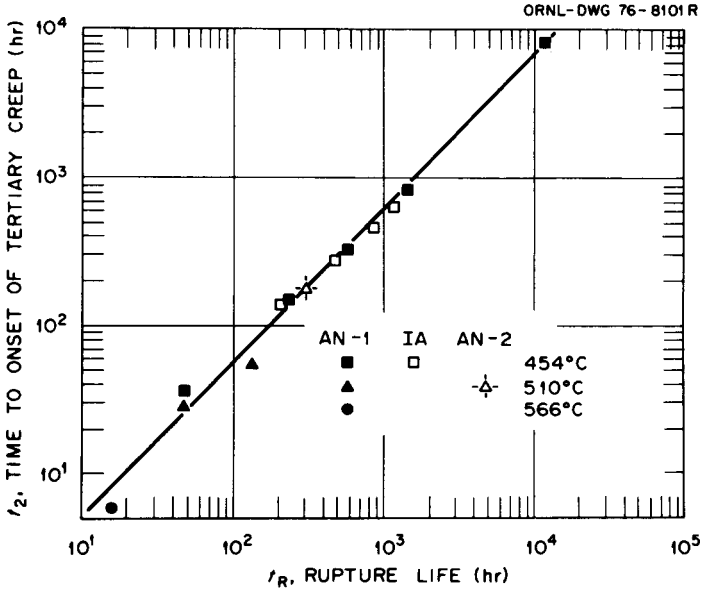

Fig. 1.9. Time to the Onset of Tertiary Creep Plotted Against Rupture Life for the Curves at 454 (AN-1 and IA) and 510°C (AN-2) that Displayed Classical Creep Curves.

Table 1.7. Coefficients for Empirical Relationship Between the Onset of Tertiary Creep and Rupture Life

Data	log A	A	α	Standard Error of Estimate
Category 2[a]	−0.307 ± 0.082	0.492	1.010 ± 0.028	0.0812
Category 3[b]	−0.353 ± 0.088	0.444	1.044 ± 0.034	0.0862
Categories 2 and 3[c]	−0.311 ± 0.059	0.489	1.016 ± 0.021	0.0838
Categories 1, 2, 3[d]	−0.300 ± 0.056	0.501	1.011 ± 0.020	0.0804

[a]Category 2: 21 datum points were used. These included: (1) all nonclassical curves at 510 and 566°C, where t_2 was taken as the time to the end of the second steady state stage, and (2) the low-stress classical curves at 566°C.

[b]Category 3: 12 datum points were used. These included all points at 454°C and the high-stress classical curves ($\varepsilon_2 \cong 1.5$–3%) at 510 and 566°C for AN-1 and AN-2.

[c]Categories 2 and 3: 33 datum points were used. These included all points used in a and b.

[d]Categories 1, 2, and 3: the 33 datum points used above were combined with the four low-stress tests on AN-2 at 510°C.

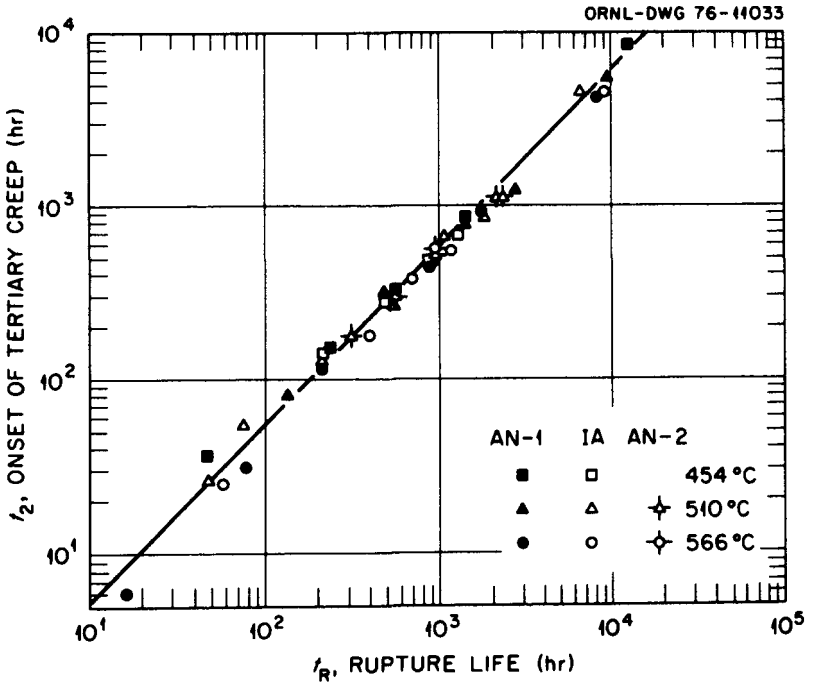

Fig. 1.10. Time to the Onset of Tertiary Creep Plotted Against Rupture Life for All Data. For nonclassical curves, the end of the second steady-state stage was taken as the onset of tertiary creep.

duration of the first steady-state stage, the second steady-state stage cannot be accurately deliniated. Presumably the second steady-state stage is of very short duration. Hence, the time to the end of this stage should not differ substantially from the time to the end of the first steady-state stage for these tests. These four tests are plotted on Fig. 1.10 (they were not used to establish the curve). It is seen that these points fall quite nicely on the curve established for all the data from categories 2 and 3. Finally, when an equation is determined for all the data, including these AN-2 tests, α and A are little changed from Eq. (2) (Table 1.7).

Since tertiary creep is often associated with gross structural instability (i.e., the formation of cracks, voids, or necking, which lower the specimen cross section and thus increase stress), one criterion used in the ASME code case 1592 to set allowable stresses in the creep regime is the time to the onset of tertiary creep. Tertiary creep is generally defined in terms of the classical creep curve as the point on the curve where the creep rate begins to increase (it decreases during the primary stage and is constant in the secondary stage of a classical creep curve). By such a definition, tertiary creep would begin at the end of the first steady-state stage (for nonclassical creep curves). We feel, however, that this is a point of metallurgical instability, not a structural instability (this will be discussed in more detail in the next quarterly report). Hence, for materials that display nonclassical creep curves, the proper start of tertiary creep — the one that precedes fracture and may be associated with structural instability — is that determined after the second steady-state stage is complete. Both the minimum creep rate studies[7] and the tertiary creep correlation in Fig. 1.10 lead to this conclusion.

The present studies have illustrated the difficulty involved in determining tertiary creep when two steady-state stages appear. This is especially true when the test has not gone to rupture. If a creep curve such as that shown in Fig. 1.11(a) is examined, as a first approximation, tertiary creep would be said to begin at about 1000 hr and about 0.07% strain (the 0.2% offset gives values of 0.28% strain and 2100 hr). The creep curve in Fig. 1.11(a) is the first part of a nonclassical curve.

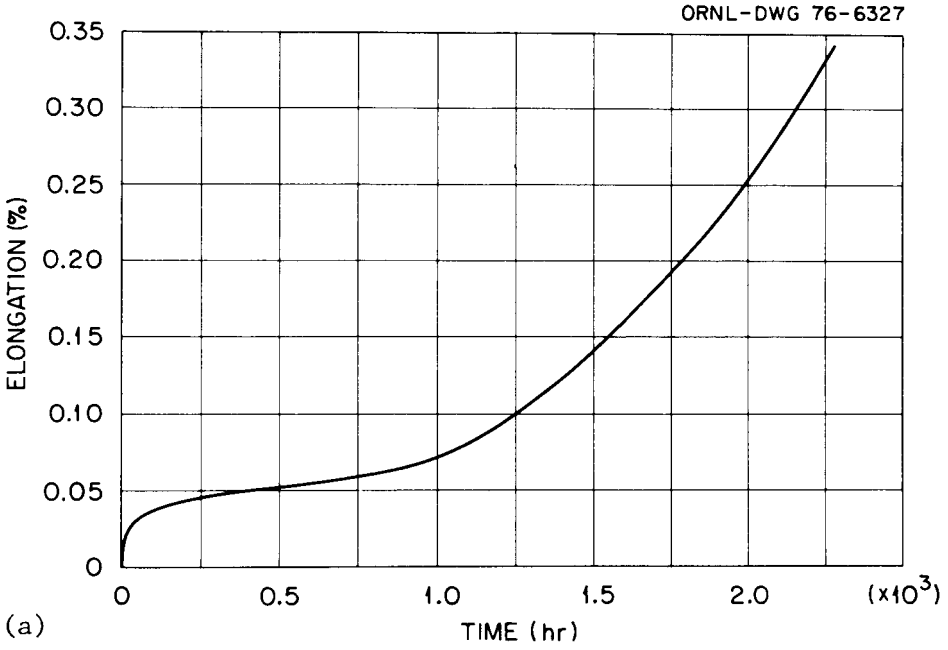

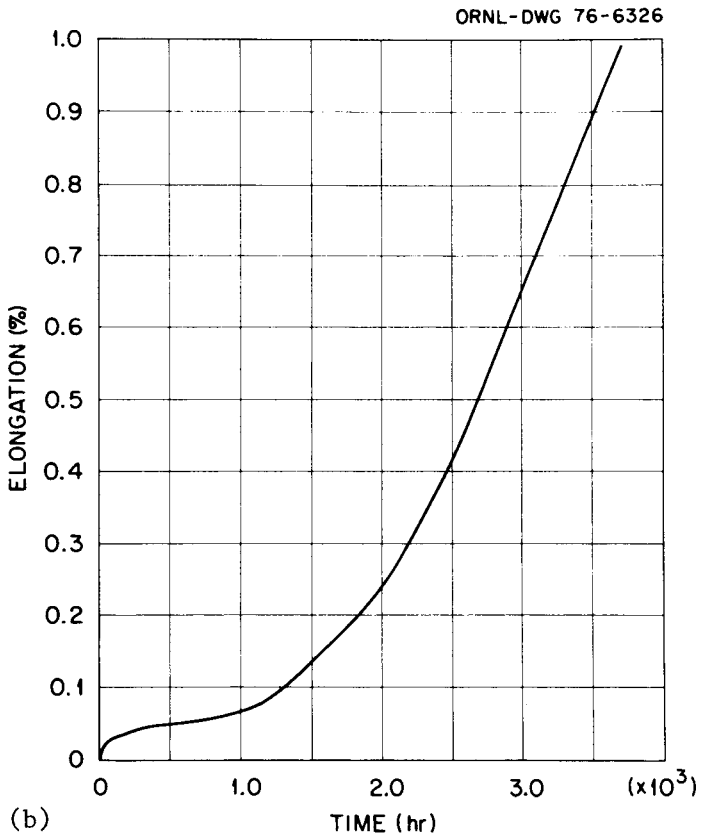

Fig. 1.11. Creep Curve for AN-2 Specimen Tested at 152 MPa (22 ksi) and 510°C. (a) After 2500 hr. (b) After 3700 hr, showing the second steady-state stage.

Only when the entire creep curve is examined and the second steady-state stage is taken into account can the real start of tertiary creep be determined. Figure 1.11(b) shows the curve after about 3800 hr and the second steady-state stage (the rupture life for this specimen is expected to approach 10,000 hr and tertiary creep has not yet begun). Note also the difference this will make in the determination of the strain to tertiary creep.

We showed that the tertiary creep data could be fit according to Eq. (1), although, interestingly enough, here the strains to the onset of tertiary creep did not seem to affect the fit of the data. For all three strain categories, one curve fit all the data.

Several investigators have found an α of unity[9-11] for a variety of alloys, including 2 1/4 Cr-1 Mo steel.[10,11] Leyda and Rowe[10] fit their data for annealed 2 1/4 Cr-1 Mo steel with

$$t_2 = F_s t_R \ , \tag{3}$$

where F_s is a constant. Their data were taken at 538, 593, and 649°C (1000, 1100, and 1200°F), and they found that F_s decreased slightly with temperature. Since our data showed no obvious stratification with temperature, we did not fit the data according to Eq. (3). Nevertheless, our $\alpha = 1.016$ cannot be assumed to be significantly different from unity, although our F_s is slightly greater than that obtained by Leyda and Rowe, who found an F_s of 0.459 at 538°C. Booker and Sikka,[12] on the other hand, fit tertiary data for 2 1/4 Cr-1 Mo steel from various sources, including some of the data obtained in the present investigation, and found $\alpha = 1.05$. Presently, we have no explanation for this discrepancy.

The results of the observations in this study have certain implications for design. By use of the creep rate for the second steady-state stage to determine the creep strength, the strength is lower, since the creep rate of the second steady-state stage is greater than that of the first. However, the time to the onset of tertiary creep is extended. As we shall show in our discussion next quarter, the first steady-state stage appears to have no relationship to structural instability, which is what the designer is interested in.

1.4.2 Heat-to-Heat Variation of 2 1/4 Cr-1 Mo Steel

1.4.2.1 Effect of Heat Treatment on Tensile Properties — R. L. Klueh

We have completed our studies on the effect of heat treatment on the tensile properties of 2 1/4 Cr-1 Mo steel,[13,14] and a report has been published.[15] The results of these studies are here summarized.

Room-temperature tensile properties were determined on six specimens that had been given different annealing treatments: three were furnace cooled from the austenitizing temperature (described as an anneal or full anneal) at three different controlled cooling rates, and three were isothermally annealed with three different controlled cooling rates from the austenitizing temperature to the isothermal anneal temperature [704°C (1300°F) for this study]. The rate at which the steel was cooled to room temperature during the full anneal had a large effect on both the microstructure and room-temperature tensile properties. With increased cooling rate, progressively more bainite was formed in the microstructure, and the strength increased. For the isothermally annealed steels, the rate at which the steel was cooled to the isothermal anneal temperature had a minor effect (much less than the cooling rate during the full anneal) on the microstructure and room-temperature tensile properties.

In the second part of the study, detailed tensile properties were determined over the temperature range 25 to 593°C (77 to 1065°F) and the strain rate range 2.67×10^{-6} to 6.67×10^{-3}/sec on specimens that had been taken from 25-mm-thick (1-in.) plates (from a single heat of steel) given the following heat treatments: annealed (full anneal), labeled AN-1, which was slow cooled from the austenitizing temperature; annealed, labeled AN-2, which was cooled faster; and isothermally annealed, labeled IA. The following observations and conclusions were made:

1. The microstructure and properties of AN-2 were considerably different than for the other two heat treatments. All three plates were primarily proeutectoid ferrite, but AN-2 contained more bainite, and its strength at all temperatures was significantly greater than that of the other two. The ductility of AN-2 was only slightly less than that of AN-1 and IA.

2. All three heat treatments displayed dynamic strain aging peaks between 200 and 400°C. The peak height for AN-2 was greatest and occurred at a higher temperature than for AN-1 and IA. The peak height for AN-1 was slightly greater than that of IA.

3. The dynamic strain aging was concluded to be the result of interaction solid solution hardening in the proeutectoid ferrite. This phenomenon involves interactions of molybdenum and carbon atoms or atom clusters with dislocations.

4. The larger dynamic strain aging effect in AN-2 was not the result of the greater amounts of bainite in this microstructure. Rather, the faster cooling rate for this plate had not allowed the precipitation of molybdenum and carbon in the proeutectoid ferrite to proceed as far as it had in the more slowly cooled plates. Precipitation removes these species from solid solution, and thus they are no longer available for interaction solid solution hardening.

5. When AN-2 was tempered for 1 hr at 704°C (1300°F), the dynamic strain aging peak was reduced, because tempering removes molybdenum and carbon from solid solution by precipitate formation.

1.4.2.2 Mechanical Properties of a 2 1/4 Cr-1 Mo Steel Forging for LMFBR Tubesheets — R. L. Klueh and J. L. Griffith

In an effort to obtain the mechanical properties of typical tubesheet forgings, three 2 1/4 Cr-1 Mo steel tubesheet forgings were purchased from National Forge Company.[16] These were produced from a single 0.69-m-diam (27-in.) big-end-up ingot taken from an electric-furnace air-melted, vacuum-degassed heat. This ingot was upset from a length of 1.9 m (76 in.) to 0.71 m (28 in.), an operation that increased the diameter to 1.1 m (45 in.). The resulting forging was then drawn to a diameter of 0.51 m (20 in.), the top and bottom were cropped, and the remainder was cut into two pieces. One 1.130-m-long (44 1/4-in.) piece was upset forged to 0.840 m diam by 0.483 m thick (33 3/4 × 19 in.). This piece of forging was used in the present study [the remainder was cut to make two 0.46-m-diam by 0.30-m-thick (18- by 12-in.) tubesheets].

The forging was isothermally annealed by holding it at 927°C (1700°F) for 20 hr, then furnace cooling to 732°C (1350°F) at 42°C/hr (75°F/hr);

after holding it for 3 hr at 732°C, it was air cooled. The heat-treated forging was machined to obtain a finished tubesheet 0.69 m diam by 0.30 m thick (27 by 12 in.).

National Forge reported composition, tensile properties, microstructure, and grain size. This information is summarized in Tables 1.8 and 1.9. The microstructure was reported as primarily proeutectoid ferrite with 1—2% pearlite. The ASTM Grain size number was given as 4—6. When the forging was examined ultrasonically with a 3.2-mm-diam (1/8-in.) calibration standard for inspection through the thickness and a 6.4-mm-diam (1/4-in.) calibration standard for inspection radially, no internal defects were detected. Examination of the surface with a magnetic particle technique revealed no surface flaws.

The object of the present study was twofold. First, we were interested in determining the properties of a typical tubesheet forging. Second, data from this product form is of interest for our heat-to-heat variation study, which is considering various product forms. It should be pointed out that the present plans for the CRBRP call for the use of vacuum-arc remelted (VAR) or electroslag-remelted (ESR) material to be used in the tubesheet forgings. Nevertheless, the results from this study should have meaning for forgings manufactured by any technique, since the properties are largely determined by the working procedure and the final heat treatment.

To obtain specimens from the forging, a wedge (pie-shaped cut) was removed from the cylinder. This wedge was sectioned so that specimens could be taken from three different orientations relative to the axis of the forging cylinder. Radial, axial, and tangential specimens were taken. In order that our results from this forging could be compared with other heats being tested in our heat-to-heat variation study, specimen blanks having these three orientations were isothermally annealed in the laboratory: they were heated for 1 hr at 927°C (1700°F), cooled at a rate of 83°C/hr (150°F/hr) to 704°C (1300°F), held at this temperature for 2 hr, then furnace cooled to room temperature. We will refer to the material given this latter heat treatment as laboratory annealed and the other material as as received. Keep in mind, however, that

Table 1.8. Vendor-Supplied Chemical Analyses for 2 1/4 Cr-1 Mo Tubesheet Forging

Sample	Content, %											
	C	Mn	P	S	Si	Ni	Cr	Mo	V	Cu	Co	Ti
Ladle	0.10	0.36	0.007	0.009	0.35	0.30	2.40	1.03		0.09	0.012	
Check 01	0.08	0.38	0.009	0.007	0.34		2.40	1.00	0.001			0.004
Check 02	0.09	0.39	0.009	0.009	0.35		2.40	1.01	0.001			0.004

Table 1.9. Vendor-Supplied Tensile Data for 2 1/4 Cr-1 Mo Tubesheet Forging

Position	Strength, MPa(psi)		Elongation (%)	Reduction of Area (%)
	Ultimate	0.2%		
12:00	470.5(68,250)	217(31,500)	31	75.9
6:00	429.2(62,250)	207(30,000)	33	75.9

both have received isothermal anneal heat treatments, although the times and temperatures were somewhat different (the size of the material heat-treated was also quite different).

Tensile tests were made over the range 25 to 566°C (75–1050°F) at nominal strain rates of 2.67×10^{-6} and 6.67×10^{-4}/sec. Specimens having a 6.35-mm-diam by 31.8-mm-long (0.250 × 1.25-in.) reduced section were tested on an Instron testing machine.

Our first tests were run to determine the effect of orientation. Intuitively, one would expect little effect of orientation. The results for tests on the three orientations at 25 and 566°C (77 and 1050°F) are shown in Table 1.10. Specimens from both the as-received and laboratory annealed material were tested.

Table 1.10. Effect of Specimen Orientation (Relative to the Forging Axis) on Tensile Properties[a]

Orientation	Strength, MPa(ksi)		Total Elongation (%)	Reduction of Area (%)
	Yield	Ultimate		
	As Received — 25°C (77°F)			
Tangential	211(30.6)	475(69.0)	32.2	69.2
Radial	261(37.9)	535(77.7)	24.8	57.0
Axial	254(36.9)	522(75.7)	27.8	52.7
	Laboratory Anneal — 25°C (77°F)			
Tangential	263(38.1)	506(73.4)	29.7	78.2
Radial	264(38.3)	520(75.5)	28.2	77.2
Axial	262(38.0)	515(74.7)	30.1	74.9
	As Received — 566°C (1050°F)			
Tangential	182(26.4)	371(53.8)	29.0	71.2
Radial	219(31.8)	447(64.9)	21.1	51.6
Axial	232(33.6)	478(69.4)	23.4	51.6
	Laboratory Anneal — 566°C (1050°F)			
Tangential	196(28.5)	318(46.1)	36.6	88.2
Radial	205(29.8)	327(47.4)	41.5	86.5
Axial	207(30.1)	339(49.2)	33.4	82.5

[a]All tests at 6.67×10^{-4}/sec.

The as-received material very definitely shows an orientation effect. At both 25 and 566°C the tangential specimens are weaker than the radial and axial specimens. This shows up both in the 0.2% yield strength and the ultimate tensile strength. There appears to be little difference between the radial and axial specimens. The ductility measurements reflect the strength differences: total elongation and reduction of area for the tangential specimens are larger than those for the other two orientations. Evidently the laboratory anneal has removed the property differences, for after this anneal, the properties for all three orientations appeared to be the same at either temperature.

Figures 1.12 and 1.13 show the microstructure from the unstressed shoulder regions of the room-temperature test specimens of the as-received tangential and axial specimens, respectively. The radial specimen had a microstructure similar to that of the axial specimen. Obviously, there is a significant difference in the microstructures of these materials. The axial (Fig. 1.13) and radial specimens had significantly more bainite present in the microstructure than the tangential specimen did. The tangential specimen, which had the lowest strength, contained small amounts of pearlite (the black regions of Fig. 1.12) and bainite. The axial and radial specimens showed very little pearlite to be present but contained as much as 25% bainite.

Figure 1.14 is a photomicrograph of the unstressed shoulder region for the laboratory-annealed axial specimen tested at 25°C. There was no difference in the microstructure for the different orientations for these specimens. In this case the microstructure was primarily pro-eutectoid ferrite with some pearlite present. Note in Figs. 1.12, 1.13, and 1.14 that the microstructures contain proeutectoid ferrite grains, some of which etch lighter than others. The dark grains at high magnification can be seen to contain a very high density of a fine precipitate, which gives rise to a mottled appearance and causes them to appear darker at low magnification (the ligher grains contain much less precipitate).

We also made tests over the range 25 to 566°C at 2.67×10^{-6} and 6.67×10^{-4}/sec. For the as-received material, the results along

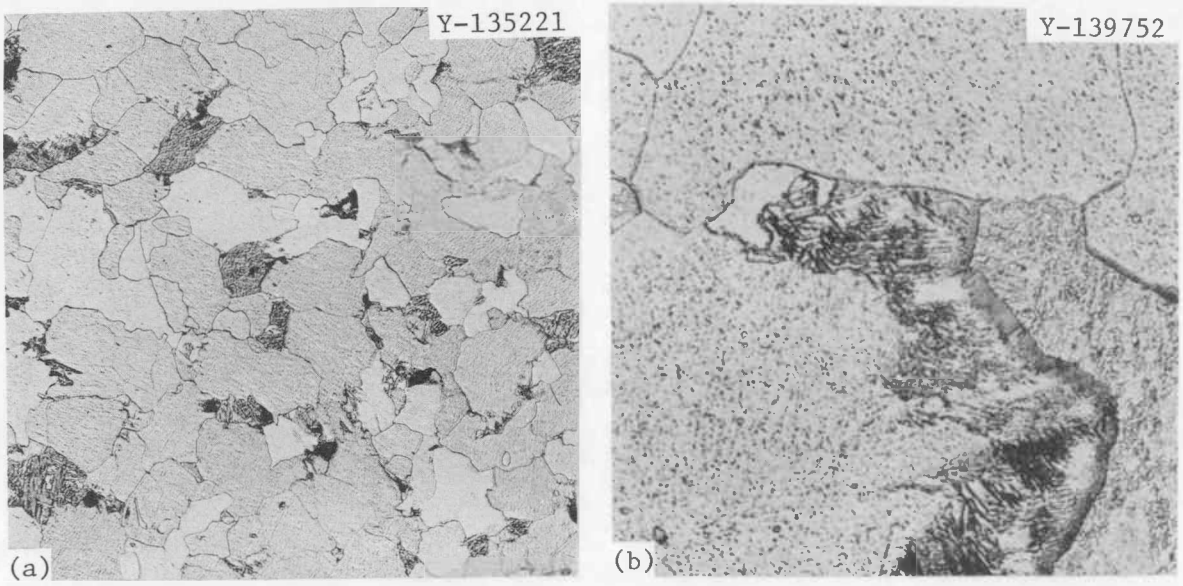

Fig. 1.12. Microstructure of the Unstressed Shoulder Region of the As-Received Tangential Specimens Tested at 25°C. (a) 100×. (b) 500×.

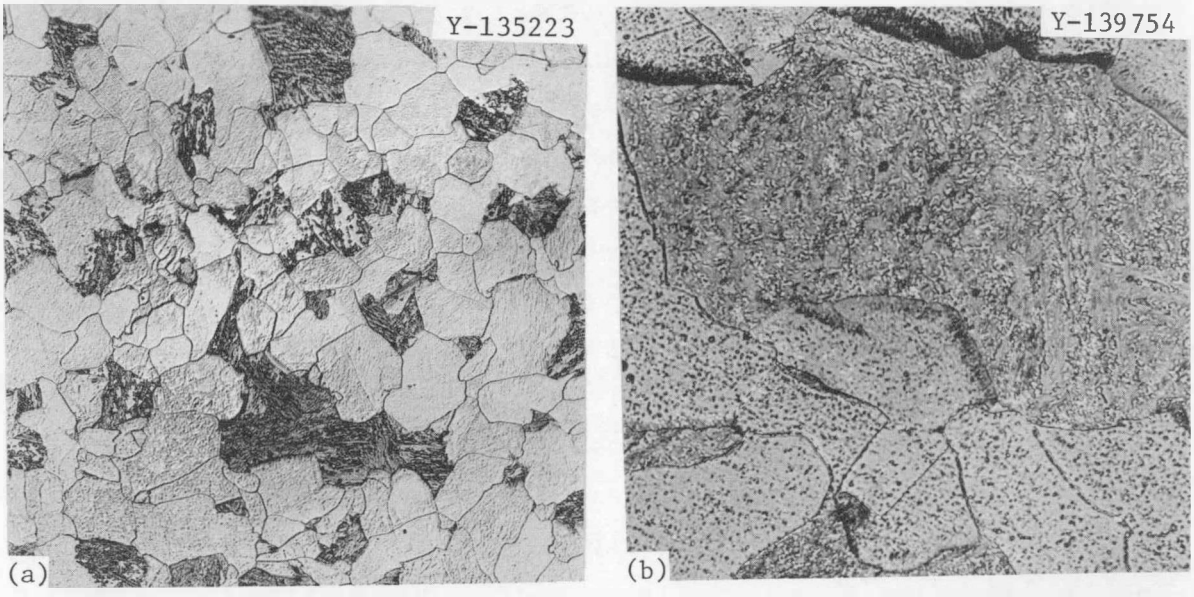

Fig. 1.13. Microstructure of the Unstressed Shoulder Region of the As-Received Axial Specimen Tested at 25°C. (a) 100×. (b) 500×. The radial specimen had a similar microstructure.

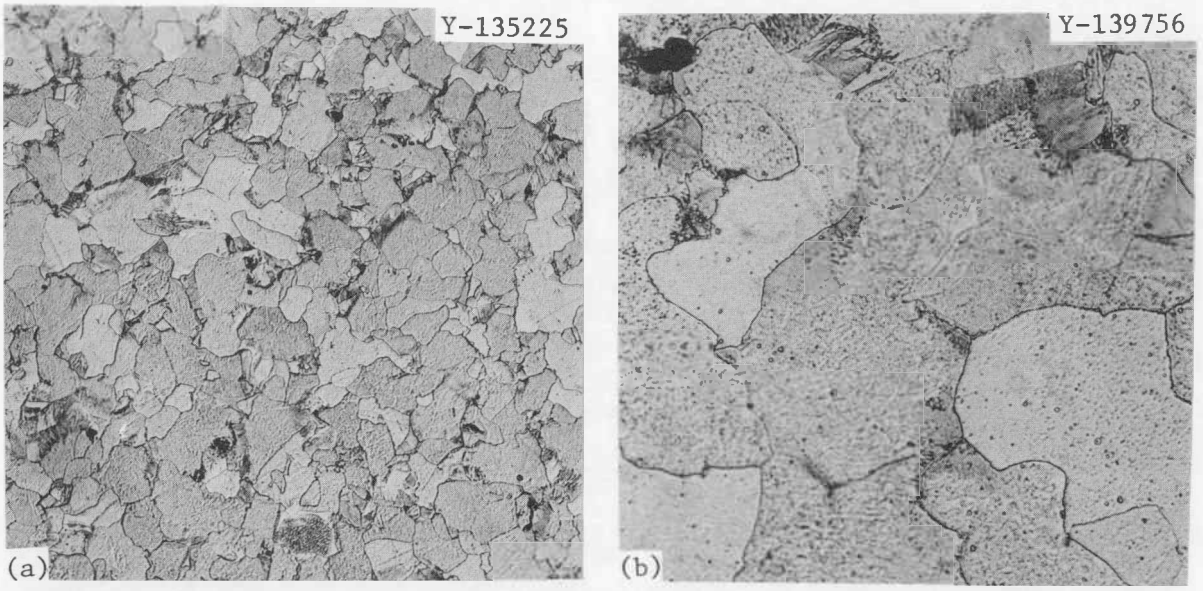

Fig. 1.14. Microstructure of the Unstressed Shoulder Region of the Laboratory-Annealed Axial Specimen Tested at 25°C. (a) 100×; (b) 500×. The radial and tangential specimens had similar microstructures.

with those given previously in Table 1.10 are given in Tables 1.11 and 1.12; Figs. 1.15 and 1.16 show the 0.2% yield strength, the ultimate tensile strength, and the ductility data plotted as functions of temperature for the as-received and laboratory annealed material. The orientation effect for the as-received forging was unexpected; thus not enough axial specimens were available to complete the 2.67×10^{-6}/sec tests. Only a tangential specimen was tested at 566°C, but it is not plotted because of the lower strength for this orientation.

The most significant effect appears when the ultimate tensile strength data are examined [Fig. 1.15(b)]. Data for the as-received and the laboratory annealed material display dynamic strain aging peaks, but there are quite large differences. The peak height for the as-received forging at both strain rates is considerably greater than that for the laboratory annealed material; the peak for the as-received forging also occurs at a higher temperature. This difference in the temperature of the peaks and the magnitude of the peak heights is similar to the heat treatment effects we noted previously[15] for a single heat of steel given different anneal treatments. In those studies we showed that the temperature of the peak and the height of the peak depended on the anneal treatment.

Table 1.11. Tensile Properties for As-Received 2 1/4 Cr-1 Mo Steel Tubesheet Forging

Specimen Orientation	Test Temperature (°C)	Test Temperature (°F)	Strength, MPa(ksi) Yield	Ultimate	Fracture	Elongation, % Uniform	Total	Reduction of Area (%)
			Strain Rate 6.67×10^{-4}/sec					
Tangential	25	77	211(30.6)	475(69.0)	315(45.7)	16.2	32.2	69.2
Radial	25	77	261(37.9)	535(77.7)	393(57.0)	12.6	24.8	57.0
Axial	25	77	254(36.9)	522(75.7)	393(57.0)	14.7	27.8	52.7
Axial	204	400	239(34.7)	473(68.6)	366(53.1)	12.2	22.3	47.5
Axial	316	600	246(35.7)	504(73.1)	416(60.6)	10.2	17.7	43.4
Axial	371	700	230(33.4)	508(73.7)	422(61.3)	9.5	17.8	42.7
Axial	454	850	225(32.6)	521(75.6)	429(62.2)	9.9	18.2	39.7
Axial	510	950	231(33.5)	513(74.4)	387(56.1)	10.5	19.8	42.2
Tangential	566	1050	182(26.4)	371(53.8)	183(26.6)	9.9	29.0	71.2
Radial	566	1050	219(31.8)	447(64.9)	294(42.7)	9.8	21.1	51.6
Axial	566	1050	232(33.6)	478(69.4)	336(48.8)	11.9	23.4	51.6
			Strain Rate 2.67×10^{-6}/sec					
Tangential[a]	25	77	198(28.8)	448(65.0)	299(43.4)	15.7	29.3	64.0
Tangential[a]	93	200	178(25.9)	418(60.6)	275(39.9)	13.7	27.2	68.4
Axial	204	400	218(31.7)	478(69.4)	392(56.9)	11.3	20.3	51.9
Axial	316	600	220(32.0)	552(80.1)	467(67.8)	9.8	19.4	44.6
Axial	371	700	225(32.6)	621(90.2)	508(73.7)	13.3	21.6	40.5
Axial	454	850	229(33.3)	626(90.8)	499(72.4)	21.3	30.5	48.3
Axial	510	950	222(32.2)	558(81.0)	431(62.5)	14.7	26.8	43.1
Tangential[a]	566	1050	169(24.6)	223(32.3)	138(2.0)	4.5	48.7	90.3

[a]Since tangential specimens were decidedly weaker, they are not plotted in Figs. 1.15 and 1.16 even though they were the only ones tested at this strain rate and temperature.

Table 1.12. Tensile Properties for Laboratory Annealed 2 1/4 Cr-1 Mo Steel Tubesheet Forging

Specimen Orientation	Test Temperature (°C)	Test Temperature (°F)	Strength, MPa(ksi) Yield	Ultimate	Fracture	Elongation, % Uniform	Total	Reduction of Area (%)
			Strain Rate 6.67 × 10^{-4}/sec					
Tangential	25	77	263(38.1)	506(73.4)	266(38.6)	13.9	29.7	78.2
Radial	25	77	264(38.3)	520(75.5)	282(41.0)	12.1	28.2	77.2
Axial	25	77	262(38.0)	515(74.7)	289(42.0)	12.1	30.1	74.9
Axial	204	400	221(32.1)	446(64.7)	247(35.9)	10.5	24.2	73.1
Axial	316	600	240(34.8)	491(71.3)	331(48.1)	8.4	20.0	68.5
Axial	371	700	232(33.7)	502(72.9)	336(48.7)	9.6	20.0	60.7
Axial	454	850	234(34.0)	466(67.7)	276(40.1)	9.1	22.8	67.9
Axial	510	950	231(33.5)	423(61.4)	197(28.6)	7.9	24.2	72.4
Tangential	566	1050	196(28.5)	318(46.1)	49(7.1)	7.4	36.6	88.2
Radial	566	1050	205(29.8)	327(47.4)	56(8.1)	7.1	41.5	86.5
Axial	566	1050	207(30.1)	339(49.2)	50(7.2)	6.4	33.4	82.5
			Strain Rate 2.67 × 10^{-6}/sec					
Tangential	25	77	243(35.2)	473(68.7)	245(35.5)	12.5	29.5	77.1
Tangential	93	200	227(33.0)	450(65.3)	241(35.0)	11.7	26.2	79.2
Radial	204	400	234(34.0)	475(68.9)	303(44.0)	9.5	21.6	70.7
Radial	316	600	261(37.9)	555(80.6)	370(53.7)	8.6	22.1	66.6
Radial	371	700	238(34.6)	497(72.2	303(44.0)	9.0	22.2	66.7
Radial	454	850	232(33.7)	433(62.9)	140(20.3)	6.0	22.9	75.1
Radial	510	950	248(36.0)	349(50.7)	35.1(5.1)	3.9	31.6	88.5
Radial	566	1050	183(26.6)	200(29.0)	28.2(4.1)	2.8	50.5	91.9

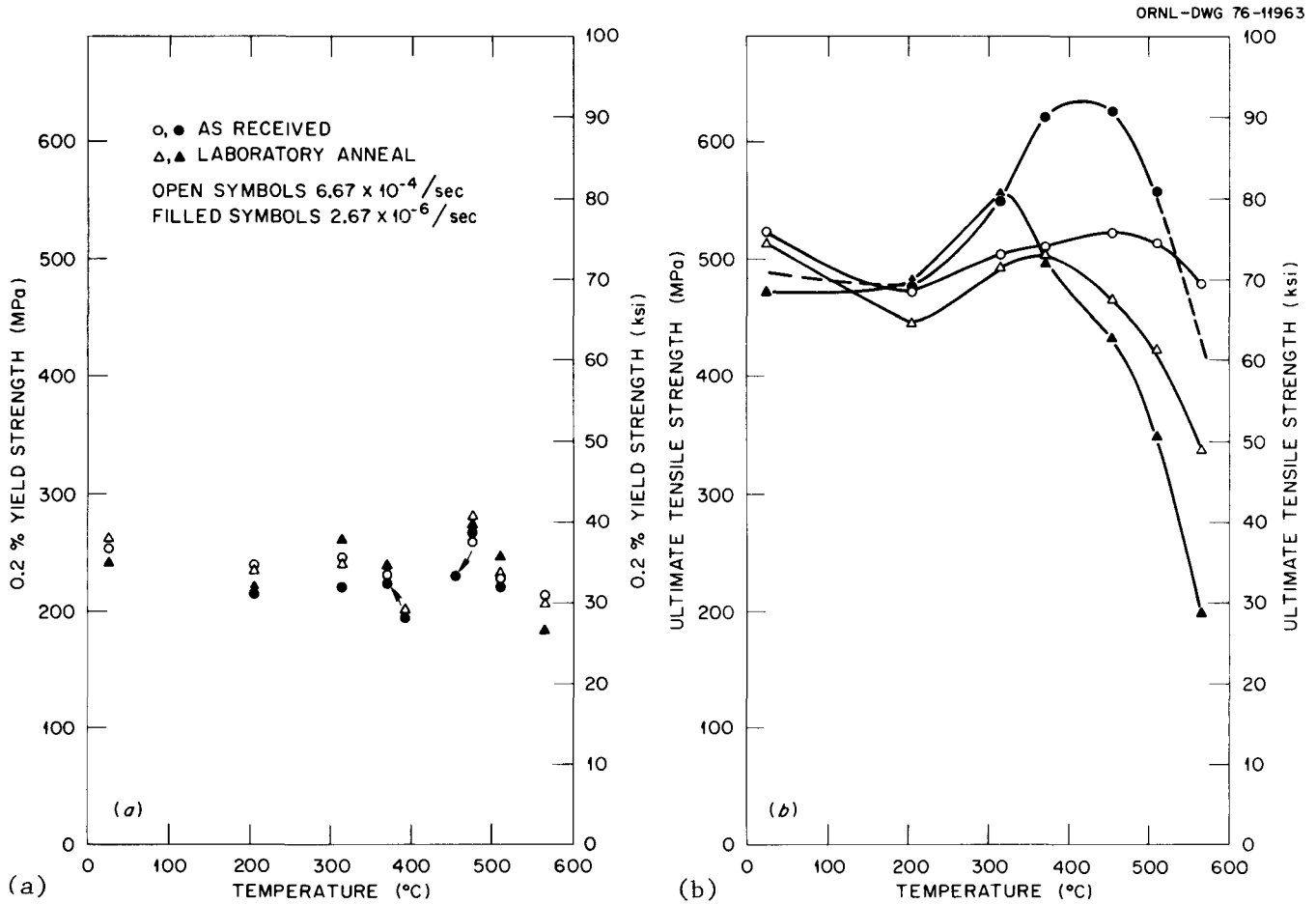

Fig. 1.15. Strength as a Function of Temperature for the As-Received Forging and the Laboratory Annealed Material at two Different Strain Rates. (a) Yield strength. (b) Ultimate tensile strength.

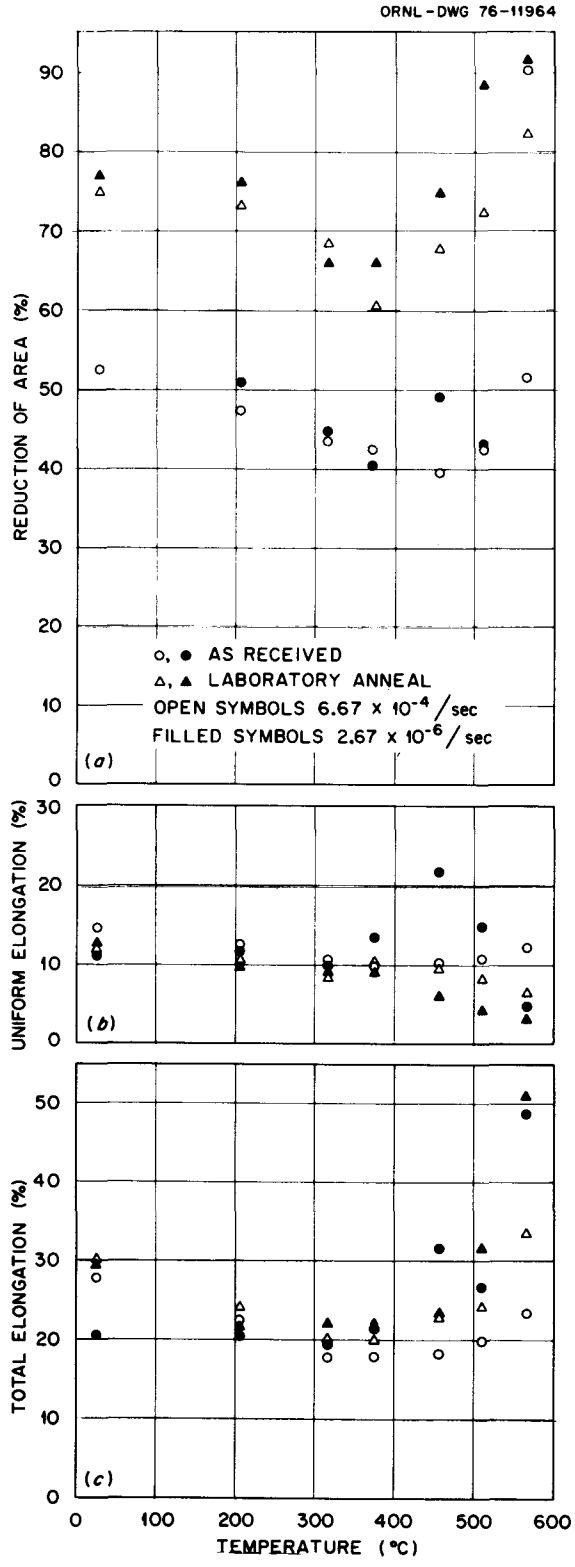

Fig. 1.16. Total and Uniform Elongation and Reduction of Area as a Function of Temperature for the As-Received Forging and the Laboratory Annealed Material at two Different Strain Rates.

The above results lead to some curious, yet interesting and important, results. Consider first the as-received forging. The fact that the microstructure of the tangential specimens was different from the other two orientations indicates that the differences are caused by something other than orientation. We believe this difference is in the position (radial distance from the center of the cylinder) at which the specimens were taken. As stated above, specimens were taken from wedges cut from the cylinder. The tangantial specimens were taken from the wedge edge (i.e., the periphery of the cylinder; 10 to 25 mm (0.5—1 in.) from the edge of the 14-in.-radius cylinder). On the other hand, the radial specimens were taken at approximately 0.25 to 0.28 m (10—11 in.) from the center, while the axial specimens were from less than 0.13 m (5 in.). This would indicate that the strength near the periphery is less than it is at some distance inside the forging as a result of the difference in microstructure. The greater amounts of bainite in the axial and radial specimens would be expected to give a higher strength. It is apparent from these results that the vendor must have taken his tensile and metallography samples (Table 1.9) from the cylinder periphery.

One possible explanation for the difference in microstructure is that the external surface was decarburized during the heat treatment. The lower the carbon content, the less the amount of bainite formed. However, since there is no difference in the microstructure or strength of the laboratory annealed specimens with orientation, this is not too probable. Furthermore, the amount of material machined from the forging after the heat treatment should have included the decarburized material.

The microstructural observations along with the observations on the dynamic strain aging peaks for the as-received material relative to the peaks for the laboratory annealed material [Fig. 1.15(b)] would indicate that although the as-received material was isothermally annealed — held 3 hr at 732°C — it did not transform uniformly. Indeed, if the tranformation was uniform, then the strength of the as-received forging should be less than that of the laboratory annealed material, since the as-received material was transformed at a higher temperature for a longer time.

During the next quarter, we will investigate more closely the variation in microstructure and strength as a function of position in the forging to verify the results reported above. We have also begun creep-rupture tests on these materials, and the preliminary results from those tests will be reported next quarter.

1.4.3 Effect of Sodium on the Mechanical Properties of 2 1/4 Cr-1 Mo Steel — R. L. Klueh

In the demonstration liquid-metal fast breeder reactor, the sodium-heated steam generator is to be constructed of 2 1/4 Cr-1 Mo steel. Under the operating conditions of the steam generator, heated sodium flows from the intermediate heat exchanger, which is to be constructed of an austenitic stainless steel, to the ferritic steel steam generator. As a result of the difference in thermodynamic activity of the carbon in the austenitic and ferritic components, decarburization of the 2 1/4 Cr-1 Mo steel and carburization of the stainless steel can result. Such decarburization could significantly alter the properties of the 2 1/4 Cr-1 Mo steel.

Although the starting microstructure for 2 1/4 Cr-1 Mo steel under most typical heat-treated conditions is microstructurally unstable during elevated-temperature exposure,[17-19] little information is available concerning the effect of prolonged exposure (thermal aging) on the mechanical properties. The bulk of the available creep-rupture data is from material in the as-heat-treated condition[20] (i.e., annealed, normalized and tempered, or quenched and tempered). Similarly, little is known about the effect of a carbon loss combined with thermal aging.

In the present study, the creep-rupture properties of 2 1/4 Cr-1 Mo steel exposed to sodium for 26,500 hr at 566°C (1050°F) are being determined. The properties of specimens simultaneously exposed to a helium atmosphere (aged, but not decarburized) are also being determined. Although 566°C is above the peak temperature of the demonstration plant steam generator [520°C (968°F)], these results are nevertheless of interest because this is the longest time and lowest temperature at which commercial 2 1/4 Cr-1 Mo steel has been decarburized by sodium.

The specimens were exposed to sodium in a large type 316 stainless steel retort by Mine Safety Research Corporation (MSA), Evans City, Pennsylvania; the details of that exposure have been published.[21] Because program funding was discontinued, MSA made only a limited study of the effect of sodium and thermal aging on the tensile properties, metallography, and carbon content after 10,000, 20,000, and 26,500 hr.[22-25]

After 10,000, 20,000, and 26,500 hr, Hiltz and co-workers[23,24] found that the carbon content decreased from 0.11 to 0.093, 0.075, and 0.075 wt % C, respectively. By optical microscopy they found that after 10,000 hr, carbide spheroidization of the original pearlite platelets of the annealed steel was well under way in both the aged and decarburized specimens. The particle density of carbides in the decarburized specimen was slightly less than that in the aged specimen, though there was no noticeable difference in density between the edge and center of the decarburized specimen.[22]

We have previously reported[26] in detail on the carbides present in the sodium-decarburized and helium-aged specimens after 26,500 hr (we were only able to obtain 26,500-hr specimens). For a "starting microstructure" to compare with those obtained after decarburization and/or thermal aging, we annealed end pieces from tensile specimens that had been aged in helium and not decarburized.

With optical microscopy, we found that after 26,500 hr, the carbide particle density of the decarburized and aged specimens was considerably less than reported[23] after 10,000 hr, with the density of the thermally aged specimen being considerably greater than that in the decarburized specimen. For the aged specimen, the density decrease was a result of Ostwald ripening, and the total amount of carbide was not noticeably affected. Decarburization, however, resulted in a gradient in carbide density, with the smallest density near the surface.

The proeutectoid ferrite of annealed 2 1/4 Cr-1 Mo steel contains a large number of small particles — mostly Mo_2C — that are replaced during elevated-temperature exposure by $M_{23}C_6$ and η-carbide.[17,18] (Eta-carbide has generally been referred to as M_6C; however, it was recently found[27] that in 2 1/4 Cr-1 Mo steel, this is more nearly M_4C.) By transmission electron microscopy and electrolytic extraction of

precipitates we found[26] that the precipitates changed from a high density of particles — mostly needles or platelets of Mo_2C — in the annealed steel to a very much smaller density of large globular particles of $M_{23}C_6$ and η-carbide after 26,500 hr.

Tensile specimens were machined from a standard heat of annealed 2 1/4 Cr-1 Mo steel, which was purchased by MSA.[21] According to the vendor's analysis, the steel contained 0.11% C. The specimens, which were aged and decarburized, were in the form of 1.5-mm (0.06-in.) sheet tensile specimens cut from blanks 184-mm-long by 31.8-mm-wide (7 1/4 by 1 1/4 in.) and had a 25.4-mm-long by 12.7-mm-wide (1- × 1/2-in.) gage section. We received from MSA 23 specimens that had been exposed to sodium for 26,500 hr, but only five specimens that had been thermally aged for the same length of time. Unfortunately, none of the starting material was available. Thus, the effect of decarburization and aging will have to be inferred by comparison with literature data.[20]

The tensile properties at 25 and 566°C (75 and 1050°F) were determined by MSA,[24] and after 26,500 hr MSA found that the strength properties of the decarburized and aged specimens had decreased, the greater effect occurring at 566°C (1050°F). At this temperature there was little difference between the specimens decarburized in sodium and those aged in helium. The results are given in Table 1.13.

Because of the large decrease in the strength as a result of decarburization and thermal aging — especially at 566°C — we repeated the tests at 25 and 566°C on decarburized specimens. The results for these tests are also given in Table 3.21. Our results are in good agreement with those obtained by MSA. Because of a lack of specimens, no verification tests were made on helium-exposed specimens. Because of the good agreement on the decarburized specimens, however, no such tests would appear to be necessary.

Creep-rupture tests are now in progress on the decarburized specimens at 510 and 566°C. Selected tests are also being made on the thermally aged specimens at 566°C. Results from these tests will be reported later.

Table 1.13. Changes in Tensile Properties of 2 1/4 Cr-1 Mo Steel After Prolonged Exposure to Helium and Sodium at 566°C (1050°F)[a]

Exposure Time (hr)	Strength, MPa(ksi)		Elongation (%)	Reduction of Area (%)
	Yield	Ultimate		
	Test Temperature 25°C (75°F)			
Helium				
0	241(35)	503(73)	32	68
10,000	276(40)	476(69)	40	68
26,500	234(34)	455(66)	36	59
Sodium				
0	241(35)	503(73)	32	68
10,000	221(32)	428(62)	39	68
20,000	234(34)	434(63)	37	57
26,500	207(30)	414(60)	39	60
26,500[b]	189(27.4)	411(59.6)	42	51
	Test Temperature 566°C (1050°F)			
Helium				
0	186(27)	455(66)	30	56
26,500	138(20)	193(28)	58	72
Sodium				
0	186(27)	455(66)	30	56
10,000	117(17)	200(29)	43	76
20,000	103(15)	166(24)	61	71
26,500	131(19)	200(29)	50	69
26,500[b]	112(16.3)	204(29.6)	66	65

[a]Taken from Reference 24; strain rate was not given.

[b]Tested at ORNL; stain rate 0.05/min.

1.4.4 Fatigue Behavior of 2 1/4 Cr-1 Mo Steel — C. R. Brinkman

1.4.4.1 Time-Dependent Fatigue — Estimates of Worst Effects — M. K. Booker

Last quarter[28] we described our initial attempts to estimate the possible worst effects on fatigue life that can be expected for 2 1/4 Cr-1 Mo steel due to relaxation hold periods at peak strain during strain-controlled cycling. This quarter we will describe additional efforts in that area, including refined calculational procedures and more extensive results.

Actually, this effort consists of two distinct stages: (1) the estimation of fatigue lives with long hold periods (up to 1000 hr); and (2) estimation of shortest fatigue lives that can be expected as a result of hold periods. In Sect. 1.4.4.2 we discuss methods for analyzing the effects of hold periods on fatigue lives in available test data, although practical considerations forced these experimental hold periods to be of relatively short duration. However, those analyses did indicate that the strain range partitioning approach is consistent with the behavior of this material. Therefore, the current projections are based upon that method.

The first step in estimating effects of long hold time is to construct hypothetical hysteresis loops for the tests with long hold periods. The basic method for constructing these loops was discussed last quarter,[28] but it will be briefly described here for completeness. Having chosen a temperature (T) and total strain range ($\Delta\varepsilon_t$), one first estimates the corresponding stress range, $\Delta\sigma$. This estimate is based upon plots such as those shown in Fig. 1.17, which gives estimates of the effect of hold periods on the value of $\Delta\sigma$ at 538 and 593°C. The corresponding plot for data at 482°C was shown last quarter.[28]

Next, one must estimate the magnitude of the stress relaxation, $\Delta\sigma_r$, occurring during the hold period (see Fig. 1.18). Available relaxation curves from the experimental creep-fatigue tests indicate that these curves can be well approximated by the Gittus equation,[29]

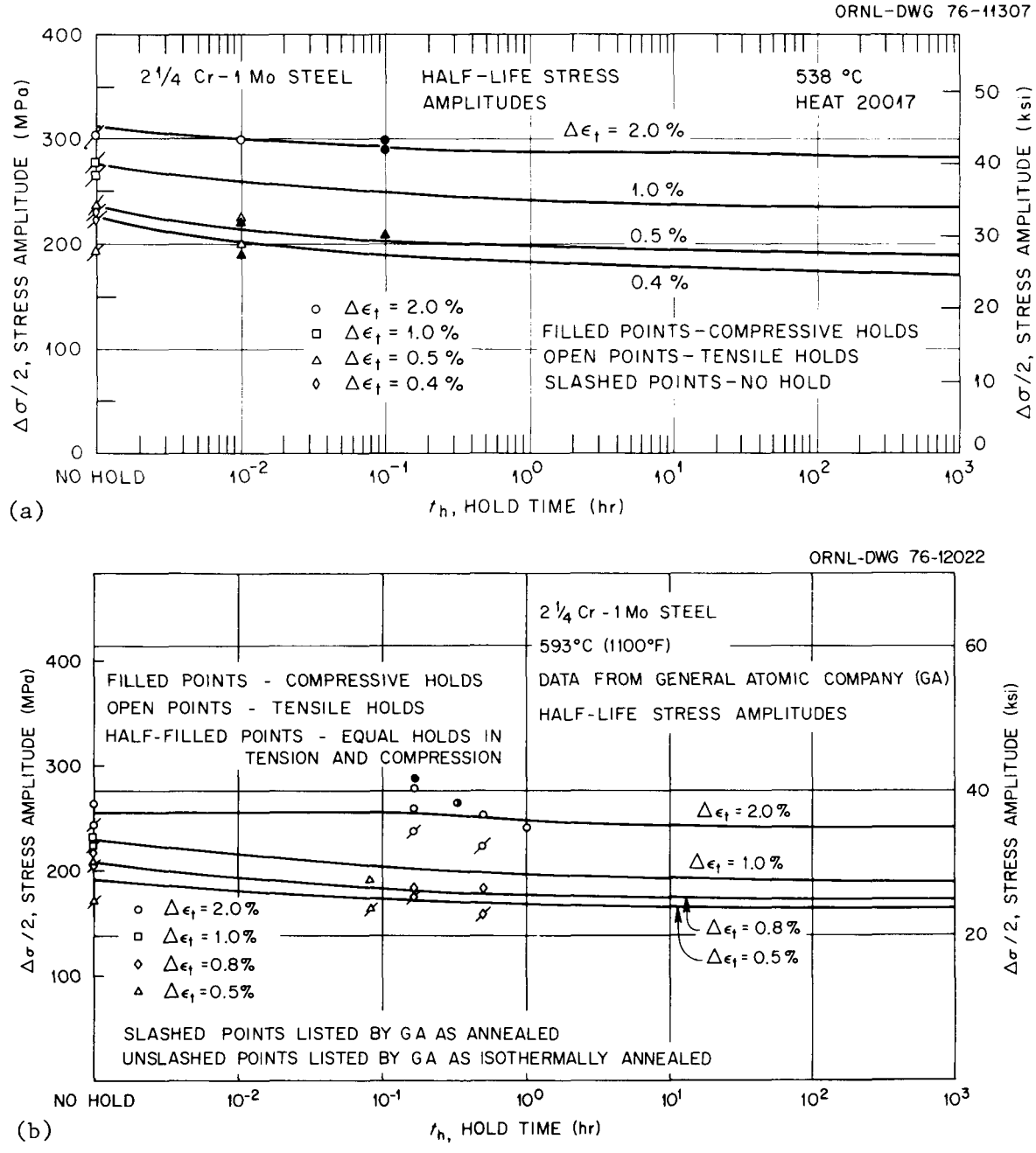

Fig. 1.17. Variation of Half-Life Stress Amplitude with Hold Time for 2 1/4 Cr-1 Mo Steel at (a) 538°C and (b) 593°C.

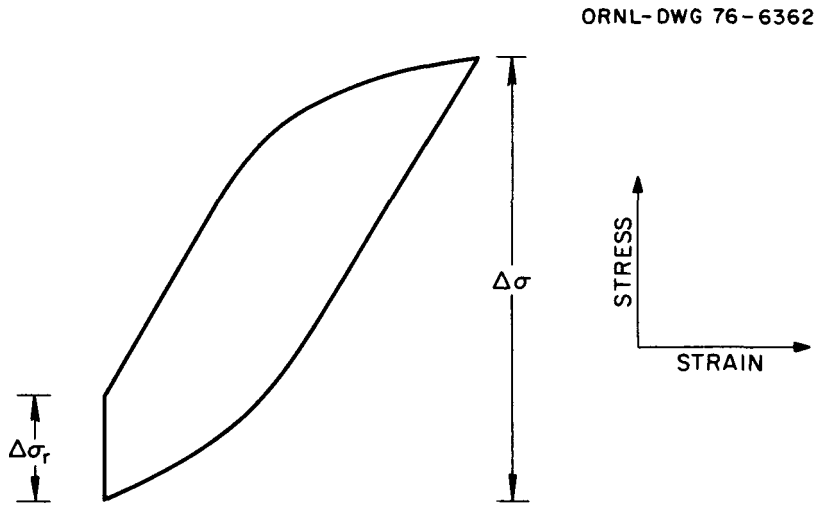

Fig. 1.18. Hysteresis Loop for a Test Involving a Hold Period at Peak Compressive Strain.

which we express as

$$\ln(\sigma_0/\sigma) = Ct^m \ , \tag{1}$$

where σ_0 is the stress at the beginning of the relaxation ($\sigma_0 = \Delta\sigma/2$), and σ and t are the instantaneous stress and time during relaxation. Figures 1.19 and 1.20 illustrate the behavior of the constants C and m from data obtained thus far at 538 and 593°C. (Again, the corresponding plots for 482°C were shown last quarter.) The scatter in the values of C and m is extremely large, although the trends can be estimated as shown in the figures. At each temperature, m appears to be approximately constant. Values of C between strain range levels shown can be estimated by linear interpolation.

Estimates of $\Delta\sigma$, C, and m for a given temperature, strain range, and hold period allow construction of an entire hypothetical hysteresis loop. For example, consider a test with a compressive hold period of t_h. If $\Delta\sigma_r$ is given by $\sigma_0 - \sigma_f$, Eq. (1) shows that

$$\ln(\sigma_0/\sigma_f) = Ct_h^m \tag{2}$$

or

$$\sigma_f = \sigma_0 \exp\left(-Ct_h^m\right) \tag{3}$$

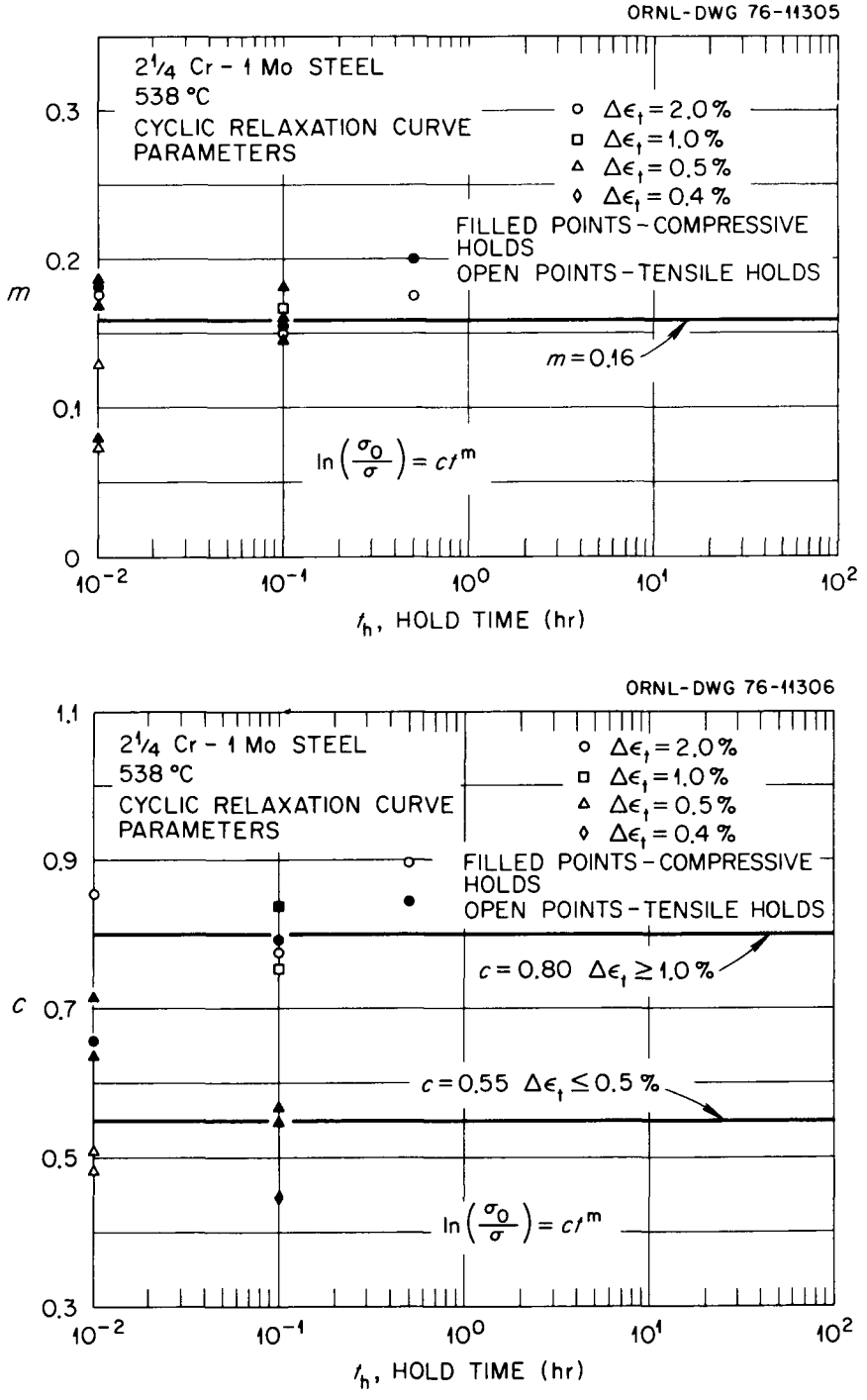

Fig. 1.19. Variation of Gittus Equation Constants with Hold Time at 538°C for 2 1/4 Cr-1 Mo Steel at Various Strain Ranges.

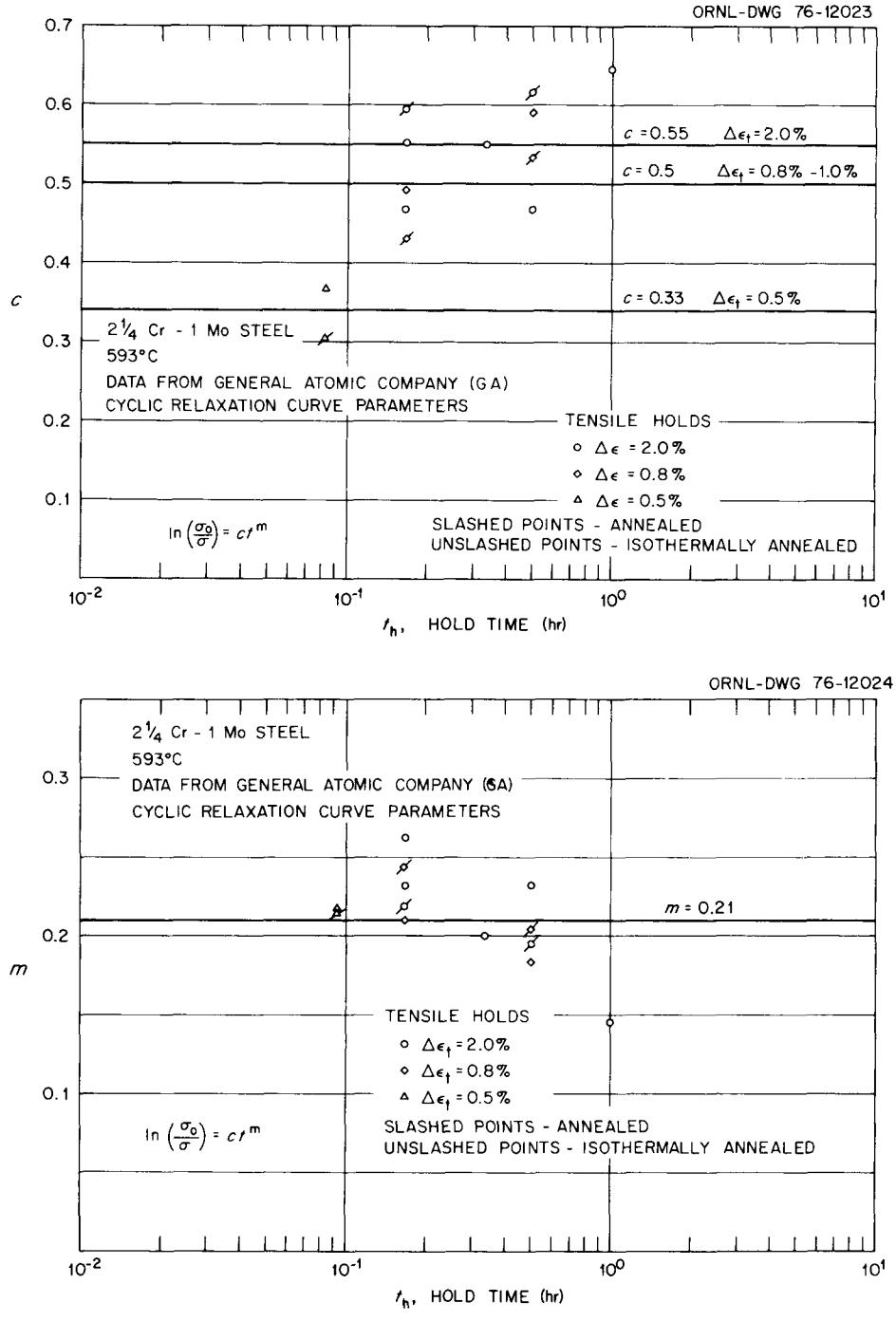

Fig. 1.20. Variation of Gittus Equation Constants with Hold Time at 593°C for 2 1/4 Cr-1 Mo Steel at Various Strain Ranges.

In terms of strain range partitioning,

$$\Delta\varepsilon_{pc} = \Delta\sigma_r/E \ , \tag{4}$$

where E is Young's modulus. The total inelastic strain range is given by

$$\Delta\varepsilon_{\text{inel}} = \Delta\varepsilon_t - (\Delta\sigma - \Delta\sigma_r)/E \tag{5}$$

where $(\Delta\sigma - \Delta\sigma_r)/E$ is merely the total elastic strain range. Finally, one has

$$\Delta\varepsilon_{pp} = \Delta\varepsilon_{\text{inel}} - \Delta\varepsilon_{pc} \ , \tag{6}$$

completing the characterization of the loop.

Tables 1.14 through 1.16 give the hypothetical results constructed by the above method. Several points about these results should be stressed. First, the information at 482°C (Table 1.14) was constructed from data for both heats 20017 and 3P5601 from the ORNL program, although heat 3P5601 generally develops lower values of stress range for a given strain range.[30] At 538°C, the differences between these two heats are even more pronounced, and the $\Delta\sigma$ values (Table 1.15) were estimated from data for heat 20017 only since those were the most numerous at that temperature. All data used at 593°C (Table 1.16) refer to Heat 3 from the program conducted by General Atomic Company.[31] Two heat treatments of this heat were used by Ellis et al.,[31] labelled "annealed" and "isothermally annealed." Their "isothermally annealed" material developed slightly higher stress ranges than their "annealed" material, and the values in Table 1.16 represent estimates of average behavior for this heat of material. Therefore, one must use caution in comparing the values in the tables at different temperatures, since the variations are probably due partially to temperature effects and partially to the fact that the data bases were different at different temperatures.

Table 1.14. Long-Hold-Period Strain Components and Creep Fatigue Lives for 2 1/4 Cr-1 Mo Steel at 482°C (900°F) Calculated from $\ln(\sigma_0/\sigma) = Ct^{0.14}$

Hold Period (hr)	$\Delta\sigma/2$ (MPa)	Partitioned Strain Components (%)		Predicted Lives,[b] Cycles		
				Strain Range Partitioning		Linear Summation of Damage
		$\Delta\varepsilon_{pp}$	$\Delta\varepsilon_{pc}^{a}$	Tensile Hold	Compressive Hold	
			Total Strain Range 0.4%, C = 0.30			
0				93,800	93,800	93,800
0.1	194	0.184	0.021	18,623	12,464	c
1	193	0.186	0.028	15,519	10,105	30,200
10	193	0.186	0.036	12,937	8,228	8,210
100	193	0.186	0.047	10,586	6,641	2,260
300	193	0.186	0.052	9,673	6,052	1,320
1,000	193	0.186	0.059	8,734	5,461	792
			Total Strain Range 0.5%, C = 0.30			
0				25,700	25,700	25,700
0.1	210	0.267	0.023	8,662	7,160	c
1	207	0.270	0.030	7,504	6,089	13,100
10	207	0.270	0.039	6,570	5,213	4,470
100	207	0.270	0.050	5,649	4,406	1,320
300	207	0.270	0.056	5,269	4,087	783
1,000	207	0.270	0.063	4,670	3,639	472
			Total Strain Range 0.75%, C = 0.385			
0				4,120	4,120	4,120
0.1	245	0.478	0.033	3,190	3,006	c
1	238	0.486	0.042	2,941	2,755	3,280
10	238	0.486	0.055	2,700	2,507	2,010
100	238	0.486	0.069	2,479	2,288	969
300	238	0.486	0.077	2,374	2,187	684
1,000	238	0.486	0.085	2,267	2,085	478
			Total Strain Range 1.0%, C = 0.47			
0				2,000	2,000	2,000
0.1	285	0.690	0.045	1,931	1,910	c
1	275	0.702	0.055	1,793	1,778	1,690
10	270	0.702	0.072	1,650	1,640	1,230
100	269	0.702	0.087	1,534	1,529	762
300	269	0.702	0.097	1,463	1,462	595
1,000	269	0.702	0.106	1,407	1,410	432
			Total Strain Range 2.0%, C = 0.47			
0				679	679	679
1	305	1.671	0.061	625	665	603
100	300	1.671	0.097	563	618	319
300	298	1.671	0.105	551	609	257
1,000	296	1.671	0.117	534	595	192

[a] "Creep" component may be $\Delta\varepsilon_{pc}$ or $\Delta\varepsilon_{cp}$.

[b] Values for no hold time calculated from best fits to continuous cycling fatigue data.

[c] Not available.

Table 1.15. Long-Hold-Period Strain Components and Creep Fatigue Lives for 2 1/4 Cr-1 Mo Steel at 538°C (1000°F) Calculated from $\ln(\sigma_0/\sigma) = Ct^{0.16}$

Hold Period (hr)	Δσ/2 (MPa)	Partitioned Strain Components (%)		Predicted Lives,[b] Cycles		
				Strain Range Partitioning		Linear Summation of Damage
		$\Delta\varepsilon_{pp}$	$\Delta\varepsilon_{pc}$[a]	Tensile Hold	Compressive Hold	
			Total Strain Range 0.4%, C = 0.55			
0				93,800	93,800	93,800
0.1	188	0.185	0.034	13,600	8,690	16,200
1	182	0.192	0.044	10,600	6,850	5,530
10	178	0.196	0.056	8,530	5,510	2,170
100	174	0.201	0.068	6,970	4,570	1,240
300	172	0.203	0.073	6,420	4,240	969
1000	171	0.205	0.079	5,940	3,940	652
			Total Strain Range 0.5%, C = 0.55			
0				25,700	25,700	25,700
0.1	203	0.268	0.037	6,890	5,470	8,270
1	198	0.274	0.048	5,710	4,500	3,030
10	194	0.279	0.061	4,630	3,650	1,250
100	191	0.282	0.075	4,090	3,200	668
300	189	0.284	0.081	3,880	3,040	532
1000	187	0.286	0.086	3,690	2,880	[c]
			Total Strain Range 0.75%, C = 0.67			
0				4,120	4,120	4,120
0.1	233	0.484	0.049	2,820	2,630	2,680
1	226	0.492	0.063	2,540	2,360	1,610
10	216	0.503	0.076	2,290	2,130	1,080
100	212	0.507	0.091	2,090	1,940	700
300	208	0.512	0.097	2,020	1,880	544
1000	207	0.513	0.103	1,950	1,820	284
			Total Strain Range 1.0%, C = 0.80			
0				2,000	2,000	2,000
0.1	249	0.716	0.060	1,710	1,700	1,600
1	241	0.724	0.076	1,560	1,560	1,240
10	238	0.728	0.093	1,430	1,440	924
100	234	0.732	0.109	1,330	1,350	612
300	234	0.732	0.116	1,290	1,310	370
1000	234	0.732	0.122	1,260	1,280	[c]
			Total Strain Range 2.0%, C = 0.80			
0				679	679	
0.1	293	1.665	0.071	609	654	
1	289	1.670	0.091	573	626	
10	288	1.671	0.113	539	600	
100	283	1.676	0.131	511	577	
300	283	1.677	0.139	501	569	
1000	283	1.677	0.147	491	561	

[a] "Creep" component may be $\Delta\varepsilon_{pp}$ or $\Delta\varepsilon_{cp}$.

[b] Values for no hold time calculated from best fits to continuous cycling fatigue data.

[c] Not available.

Table 1.16. Long-Hold-Period Strain Components and Creep Fatigue Lives for 2 1/4 Cr-1 Mo Steel at 593°C (1100°F) Calculated from $\ln(\sigma_0/\sigma) = Ct^{0.21}$

Hold Period (hr)	$\Delta\sigma/2$ (MPa)	Partitioned Strain Components (%)		Predicted Lives,[b] Cycles		
				Strain Range Partitioning		Linear Summation of Damage
		$\Delta\varepsilon_{pp}$	$\Delta\varepsilon_{pc}^{a}$	Tensile Hold	Compressive Hold	
			Total Strain Range 0.5%, C = 0.33			
0				10,830	10,830	10,830
0.1	172	0.296	0.019	7,313	6,428	884
1	167	0.303	0.028	5,710	4,951	197
10	165	0.305	0.040	5,027	4,226	51
100	164	0.306	0.056	4,374	3,582	19
300	164	0.306	0.064	4,095	3,323	14
1000	164	0.306	0.073	3,828	3,084	c
			Total Strain Range 0.8%, C = 0.50			
0				2,270	2,270	2,270
0.1	183	0.584	0.029	2,594	2,525	743
1	176	0.592	0.041	2,363	2,291	272
10	173	0.595	0.057	2,139	2,066	110
100	172	0.596	0.075	1,938	1,870	65
300	172	0.597	0.082	1,861	1,796	56
1000	172	0.597	0.089	1,792	1,731	43
			Total Strain Range 1.0%, C = 0.50			
0				1,420	1,420	1,420
0.1	203	0.760	0.032	1,844	1,842	427
1	195	0.769	0.045	1,692	1,695	154
10	192	0.773	0.063	1,543	1,553	62
100	188	0.777	0.081	1,408	1,426	40
300	188	0.778	0.090	1,356	1,377	35
1000	188	0.778	0.098	1,310	1,334	c
			Total Strain Range 2.0%, C = 0.55			
0				556	556	
0.1	255	1.698	0.043	647	677	147
1	248	1.707	0.062	607	647	52
10	241	1.715	0.084	566	616	24
100	241	1.715	0.109	529	587	15
300	241	1.715	0.120	514	576	12
1000	241	1.715	0.129	502	566	9

[a] "Creep" component may be $\Delta\varepsilon_{pc}$ or $\Delta\varepsilon_{cp}$.

[b] Values for no hold time calculated from best fits to continuous cycling fatigue data.

[c] Not available.

Finally, it must be stressed that the values in Tables 1.14 through 1.16 are merely estimates. The values are consistent with available information for very short hold periods, but extrapolation to extremely long hold periods must be done with caution. For instance, Eq. (1) provides a good description of the experimental relaxation curves, but there is no assurance that it adequately describes long-term behavior. Equation (1) predicts that the stress continues to relax with time toward an asymptotic value of zero. However, the asymptotic value could actually be some finite positive stress, in which case Eq. (1) would probably overpredict the amount of relaxation in long hold periods. Fortunately, from the point of view of strain range partitioning, such an overprediction would simply increase the conservatism of the results.

The softening due to hold periods shown in Fig. 1.17 is consistent with previous estimates[32] of the behavior of this material. However, the actual magnitude of this softening is somewhat uncertain. In terms of strain range partitioning, a decreased $\Delta\sigma$ would increase the total inelastic strain but would decrease the amount of "creep" strain due to relaxation. These opposing effects should decrease the sensitivity of the predictions to variations in $\Delta\sigma$. Therefore, we feel that life predictions from Tables 1.14 through 1.16 can yield useful information, even though those data are somewhat subjective.

Each of the hypothetical tests in the tables was analyzed by strain range partitioning assuming the hold period to be in compression or in tension. Based on available information, the mean stress was considered to be zero, so that the compressive and tensile stress amplitudes were equal. (Again, we recognize that this situation may not be the case for very long hold periods. No available data indicate otherwise, however.) The predicted lives from strain range partitioning using the interaction damage rule are given in Tables 1.14 through 1.16.

The linear summation of damage approach has also been used to estimate the cyclic lives of the hypothetical tests in the tables, although no corrections have been made for the increased damage due to compressive hold periods. (These corrections have been ignored here because the linear summation predictions for long hold times appear overconservative already.) Assuming a damage sum of unity, the predicted life can be obtained from the summation

$$N_h/N_f + N_h D_c(1) = 1 \ , \tag{7}$$

where N_f is the expected continuous cycling life. Equation (7) then yields

$$N_h = [D_c(1) + 1/N_f]^{-1} \ . \tag{8}$$

Finally, the tables also contain estimates of the continuous cycling fatigue life, N_f, at each temperature and strain range shown. The values of N_f were calculated from previously reported[33] best-fit fatigue curves. It should be noted that in some cases at high strain ranges (particularly at 593°C) predicted values of N_h by strain range partitioning are greater than the corresponding values of N_f. This occurrence is not to be taken as a prediction that the hold period increases the fatigue life. Rather, it is merely a reflection of the uncertainty in predicting fatigue lives. No cyclic life listed in Table 1.14, 1.15, or 1.16 could possibly be considered accurate within less than a factor of 2. Predicted values of the fatigue life reduction factors (N_f/N_h) from the tables are shown in Figs. 1.21 through 1.23. (Note that Fig. 1.23 was constructed by using N_f = 1842 at $\Delta\varepsilon_t$ = 1.0% for consistency. Otherwise, the values of N_f in the tables were used.)

The predictions from strain range partitioning seem very reasonable. For instance, at low strain ranges, compressive hold periods are predicted to be more damaging than tensile hold periods. The predicted cyclic lives are generally about the length one would expect from a consideration of the available short-term data. On the other hand, predictions from the linear summation of damage approach appear to be extremely conservative, especially for very long hold times ($\geq$100 hr) and particularly at 593°C. It should be noted that because of differences in data sets, more relaxation is generally predicted at 538°C than at 593°C. The smaller amount of relaxation at 593°C would tend to make linear summation predictions relatively more conservative and strain range partitioning predictions relatively less conservative. This effect can be seen from the values in Tables 1.15 and 1.16.

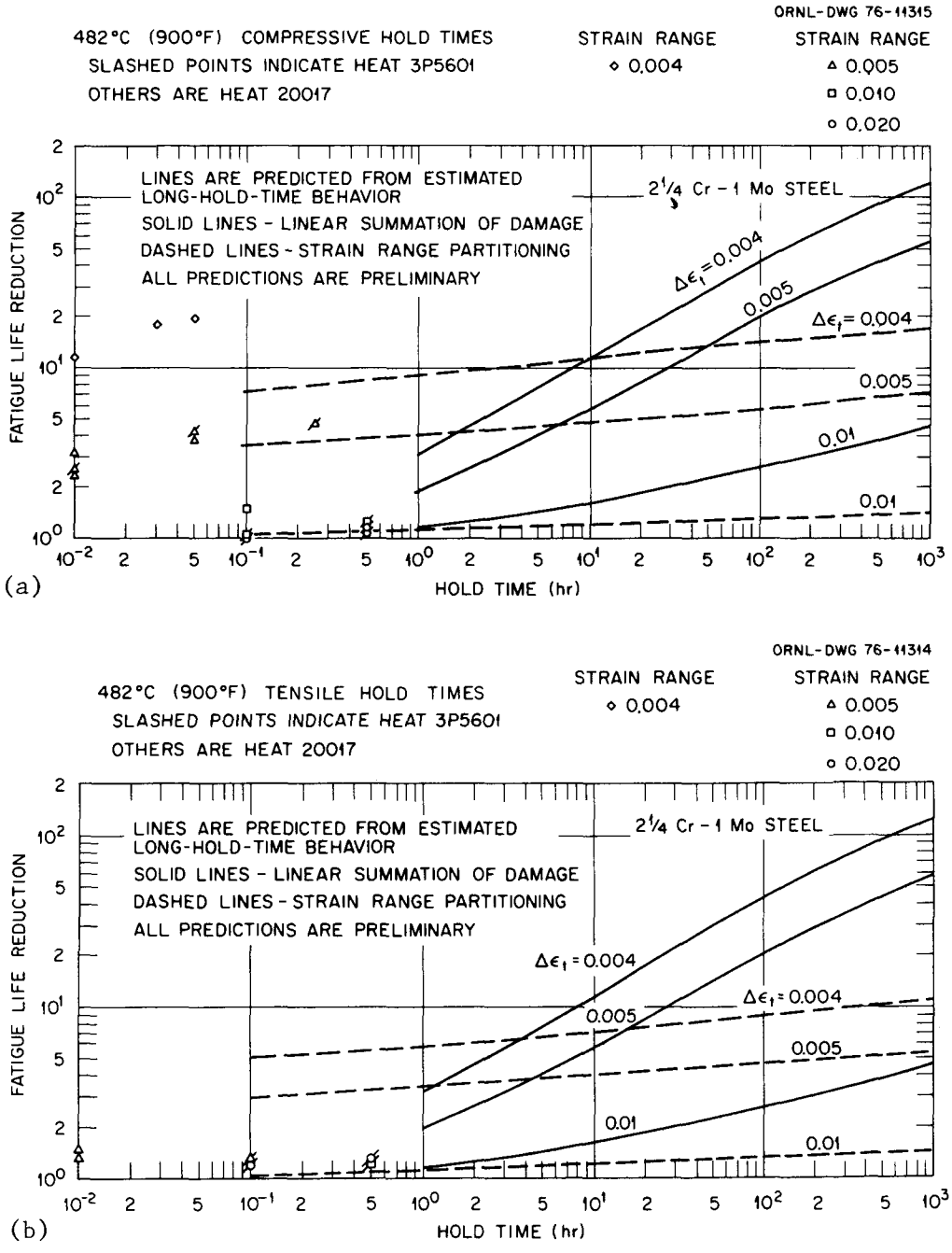

Fig. 1.21. Fatigue Life Reduction Factors, N_h/N_f, for 2 1/4 Cr-1 Mo Steel Subjected to (a) Compressive and (b) Tensile Hold Periods at 482°C (900°F).

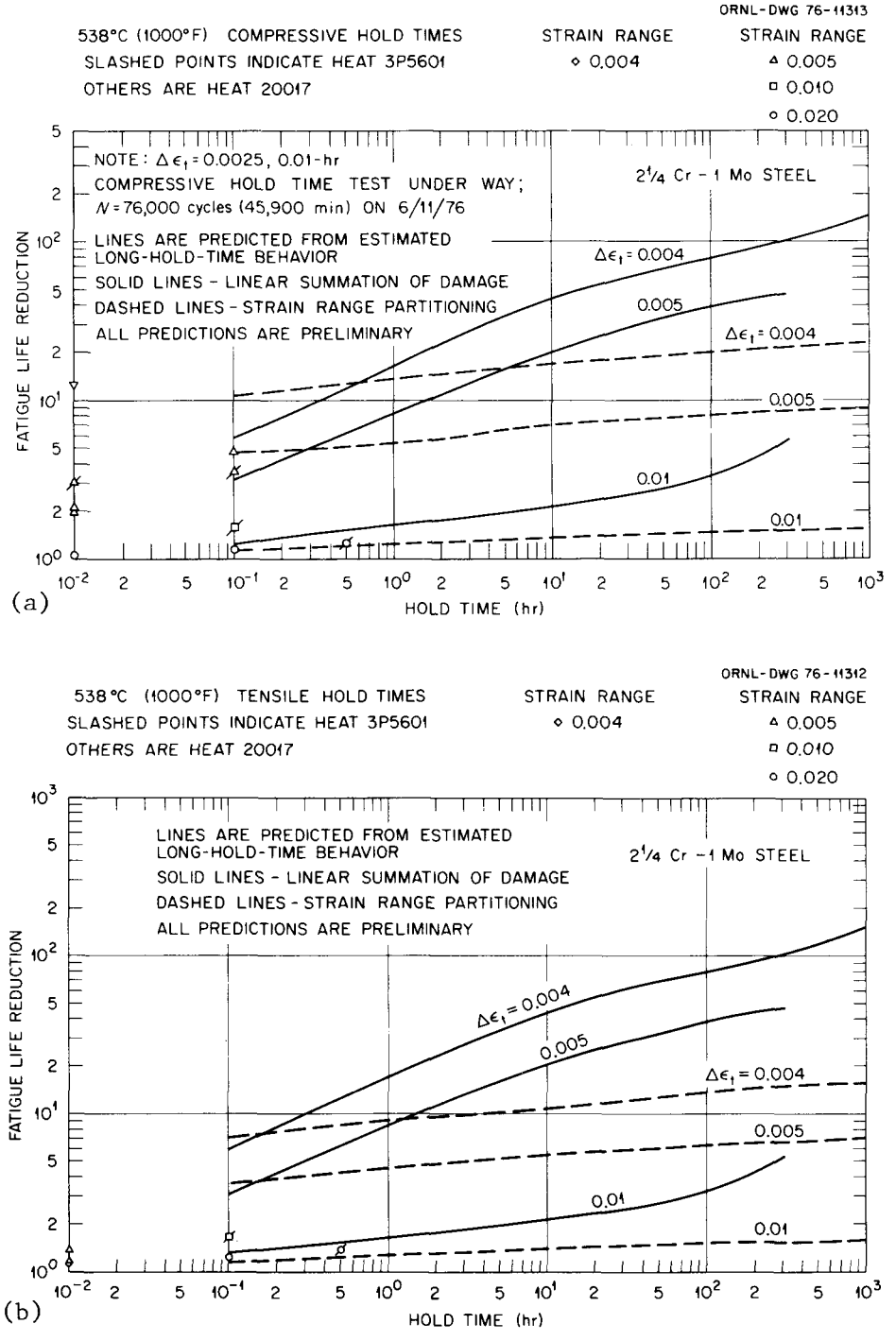

Fig. 1.22. Fatigue Life Reduction Factors, N_h/N_f, for 2 1/4 Cr-1 Mo Steel Subjected to (a) Compressive and (b) Tensile Hold Periods at 538°C (1000°F)

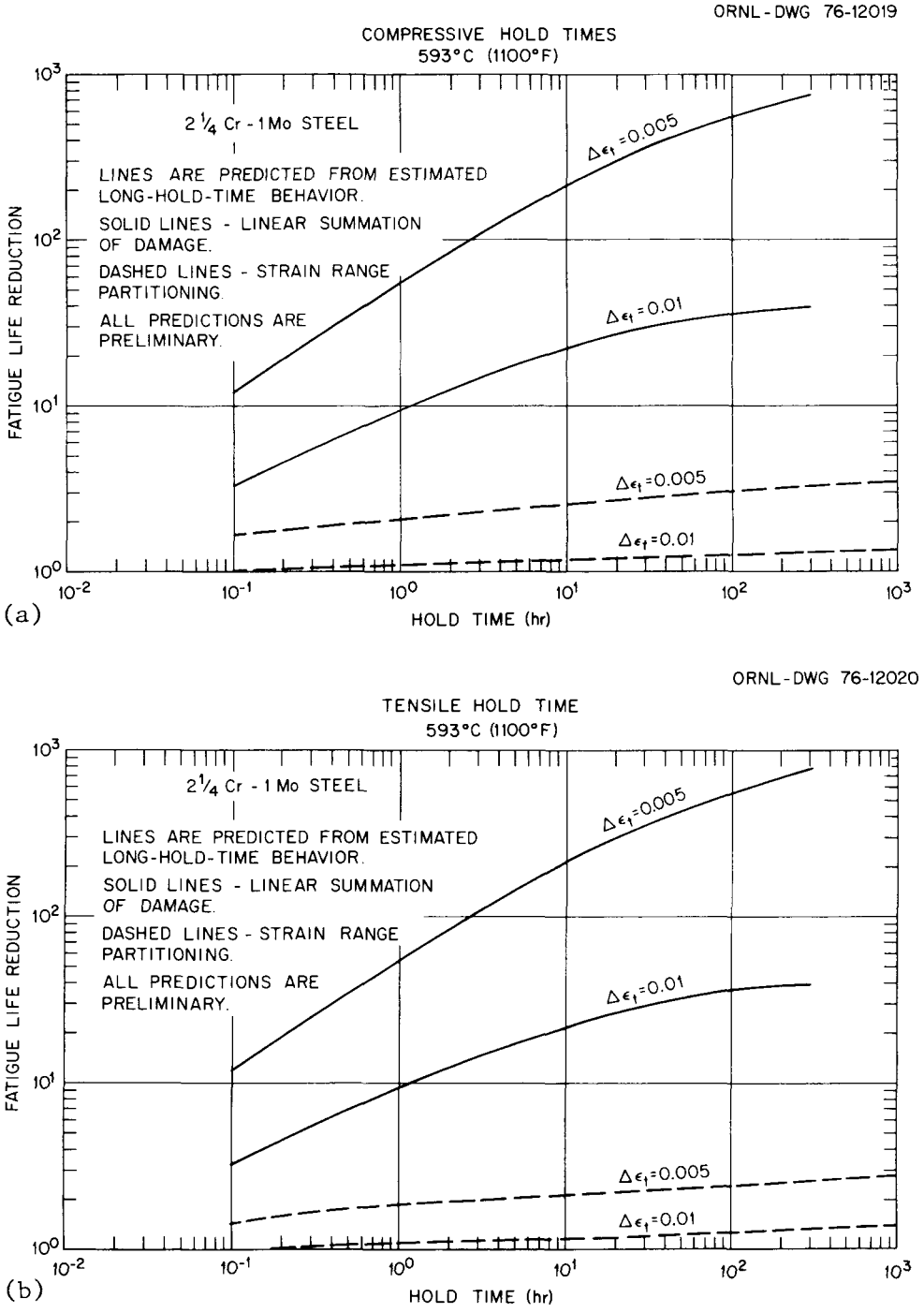

Fig. 1.23. Fatigue Life Reduction Factors, N_h/N_f, for 2 1/4 Cr-1 Mo Steel Subjected to (a) Compressive and (b) Tensile Hold Periods at 593°C (1100°F).

Since the above hypothetical predictions cannot be verified by actual experimental data, it is of interest to attempt to predict conservative lower bounds on cyclic life to avoid problems due to possible inaccuracies in the above predictions. One possible way to do this would be to choose a value for $\Delta\sigma$, and then to assume that relaxation proceeds completely to zero stress in compression, yielding the maximum amount of $\Delta\varepsilon_{pc}$ strain ($\Delta\varepsilon_{pc} = \Delta\sigma/2E$). Actually, this approach is equivalent to using Eq. (1) for relaxation, but letting the hold time go to infinity. The choice of $\Delta\sigma$ is still a problem, but we merely chose the value corresponding to t_h = 0.1 hr in Table 1.14, 1.15, or 1.16. This choice was made because (1) that value is known fairly well since actual test data extend that far, and (2) that value is larger than the values for longer hold times and thus yields a greater amount of $\Delta\varepsilon_{pc}$ strain. (Actually predicted lives using $\Delta\sigma$ from t_h = 1000 hr were only a few percent longer than those for t_h = 0.1 hr, so the above choice of $\Delta\sigma$ is not critical.)

Manson[34] has suggested another possible procedure for estimating worst effects due to creep-fatigue interactions. Since $\Delta\varepsilon_{pc}$ is the most damaging of the inelastic strain range components, a lower bound on life could be defined by the predicted life letting all inelastic strain be of $\Delta\varepsilon_{pc}$ type. For a given inelastic strain range, N_h is merely the value of N_{pc} from the strain range partitioning life relationships,[35] here:

$$N_{pc} = (\Delta\varepsilon_{pc}/215)^{-1.10} \tag{9}$$

The remaining problem is to estimate the total amount of inelastic strain corresponding to a given total strain range. We have performed this estimate in two ways.

The more conservative approach is to estimate the amount of inelastic strain, $\Delta\varepsilon_{inel}$, to be expected in an actual test, and then to set $\Delta\varepsilon_{pc}$ equal to this value. In this case it should be noted that

$$\Delta\varepsilon_{pc} = \Delta\varepsilon_{inel} = \Delta\varepsilon_t - (\Delta\sigma' - \Delta\sigma'_r)/E \ . \tag{10}$$

Thus, in this case, larger stresses correspond to smaller values of $\Delta\varepsilon_{pc}$, and conservatism requires a small value for $\Delta\sigma' - \Delta\sigma'_r$. We proceeded as follows: first, we choose $\Delta\sigma'$ as the value $(\Delta\sigma - \Delta\sigma_r)$ from a 0.1-hr hold period test. (The subtraction of $\Delta\sigma_r$ was merely an arbitrary safety factor and yields $\Delta\sigma'$ values slightly lower than the $\Delta\sigma$ values from the 1000-hr-hold-time tests. We then assumed the maximum amount of relaxation in a compression hold period (i.e., relaxation to zero). Thus

$$\Delta\sigma'_r = \Delta\sigma'/2$$

and

$$\Delta\varepsilon_{pc} = \Delta\varepsilon_t - \Delta\sigma'/2E \ . \tag{11}$$

Equations (9) and (11) thus allow one to estimate a possible "worst effects" cyclic life for each strain range and temperature. (It should be noted that if the above value of $\Delta\sigma'$ were chosen as $\Delta\sigma$ from the 1000-hr hold tests, estimated worst effects lives became only a few percent longer.)

Since relaxation cannot proceed beyond a zero stress, the maximum possible value for $\Delta\varepsilon_{pc}$ is σ_c/E, where σ_c is the compressive stress amplitude. This maximum value is thus $\Delta\sigma'/2E$ above, for the case of a zero mean stress. The above estimates of $\Delta\varepsilon_{pc}$ are always greater than $\Delta\sigma'/2E$, meaning that they can never occur in a real hysteresis loop unless there is a compressive mean stress. Geometric consideration of a hysteresis with an extended compression hold period indicates that, if anything, a tensile mean stress should develop. Therefore, the above estimates for $\Delta\varepsilon_{pc} = \Delta\varepsilon_{inel}$ are probably larger than any that might occur in a real situation, which of course means that the above life predictions should be conservative.

Alternatively, we assumed a zero mean stress and set $\Delta\varepsilon_{pc}$ equal to its maximum value of $\Delta\sigma/2E$, so that $\Delta\varepsilon_{pc} = \Delta\varepsilon_{inel} = \Delta\varepsilon_{el} = \Delta\varepsilon_t/2$. Such a hysteresis loop is shown in Fig. 1.24.

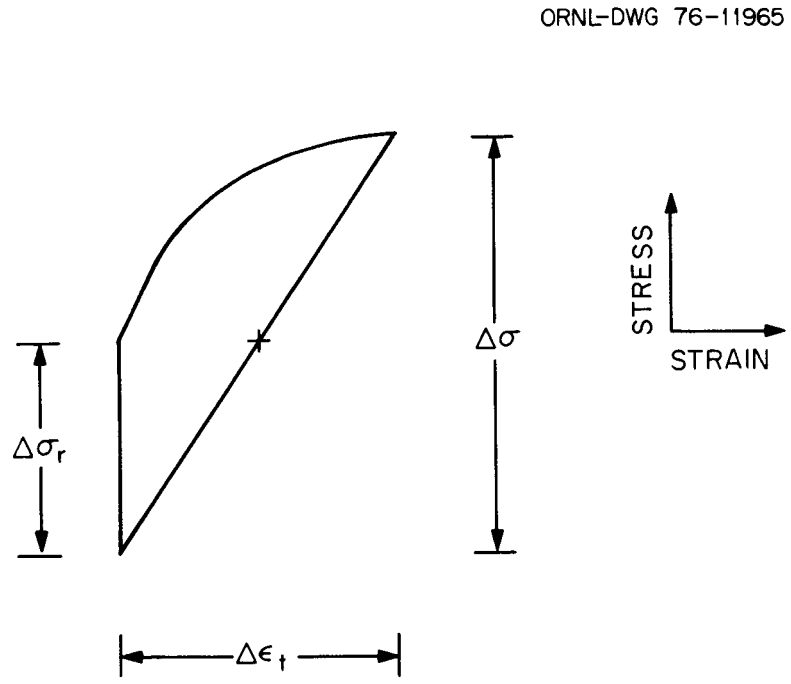

Fig. 1.24. Schematic Hysteresis Loop Illustrating the Basis for Calculation of Worst Effects Curves.

Figure 1.25 compares the two estimates of worst effects curves with the above relaxation to zero stress curves and estimated 1000-hr compression hold period curves with continuous cycling curves at 482, 538, and 593°C. In addition, Fig. 1.26 shows these same predictions for tension hold periods at 538°C. Figure 1.27 compares the two methods of estimating worst effects curves.

The 1000-hr hold period predictions are quite near the relaxation to zero stress predictions — reflecting the fact that Eq. (1) predicts relaxation to near zero stress in 1000 hr. The two "worst effects" curves are considerably more conservative than the relaxation to zero curves, with those constructed by the first method above appearing overconservative at high strain ranges, since the assumptions upon which they are based are least valid at high strain ranges. It should be noted that the first type of worst effects curves is virtually independent of temperature. The second type is independent of temperature, since the strain range partitioning $\Delta\varepsilon_{pc}$ life relationship is independent of temperature.

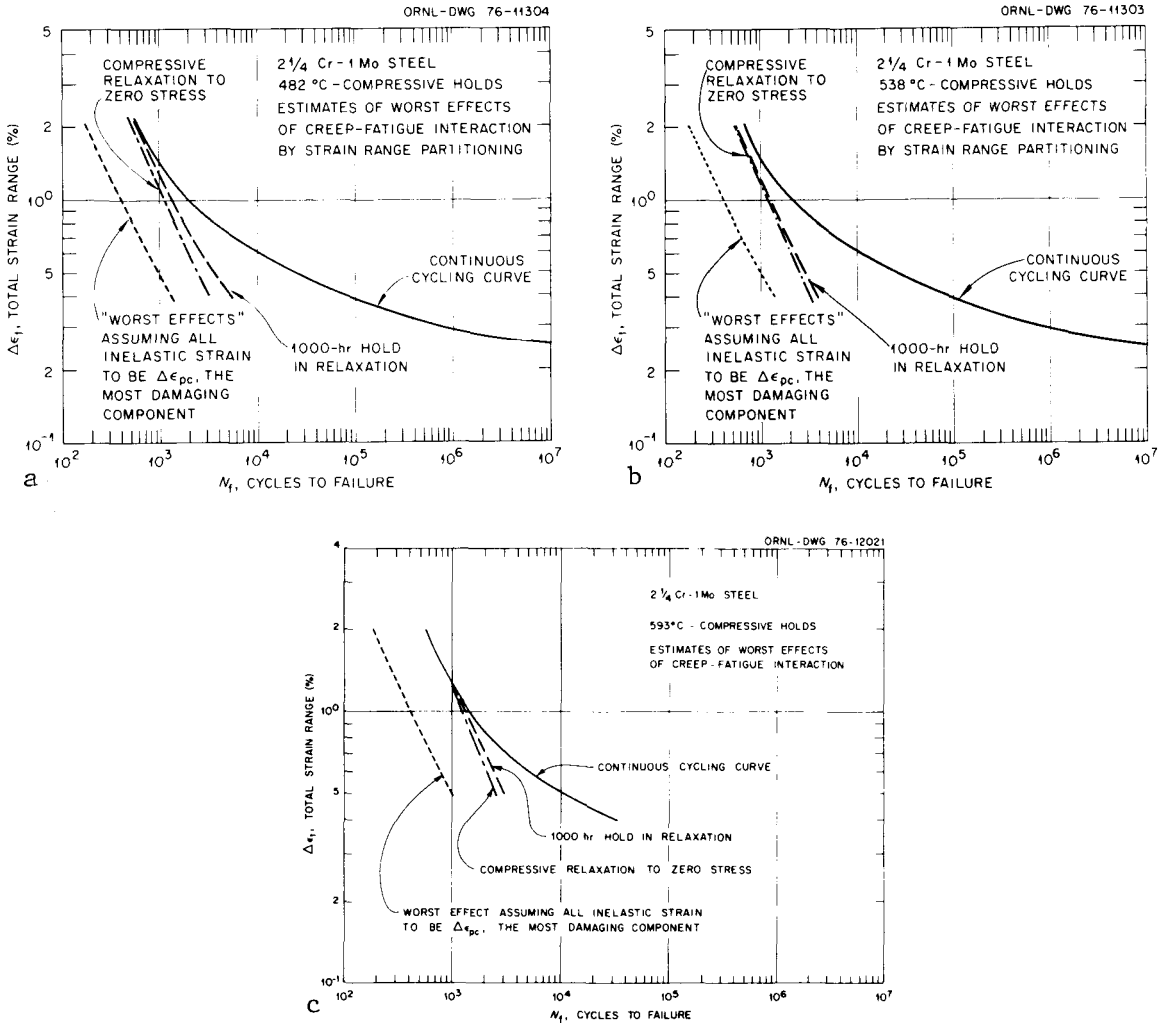

Fig. 1.25. Projected Effects of Long Compression Hold Periods on the Fatigue Life of 2 1/4 Cr-1 Mo Steel at (a) 482°C (900°F), (b) 538°C (1000°F), and (c) 593°C (1100°F).

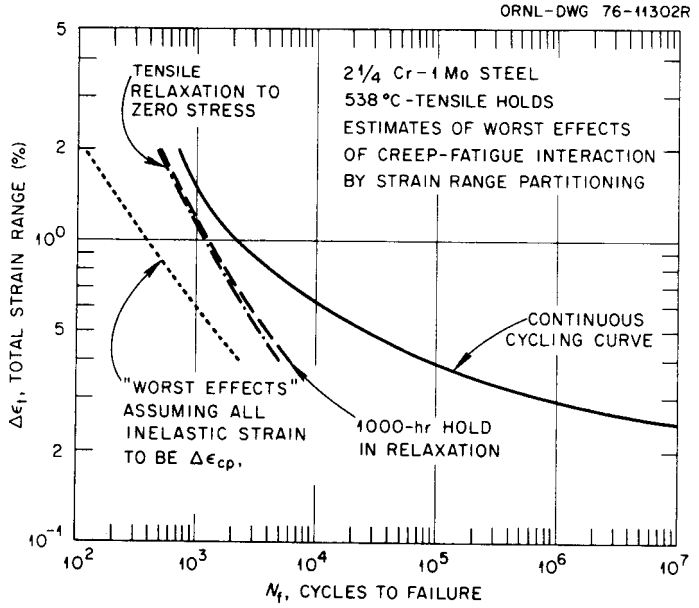

Fig. 1.26. Projected Effects of Long Tension Hold Periods on the Fatigue Life of 2 1/4 Cr-1 Mo Steel at 538°C (1000°F).

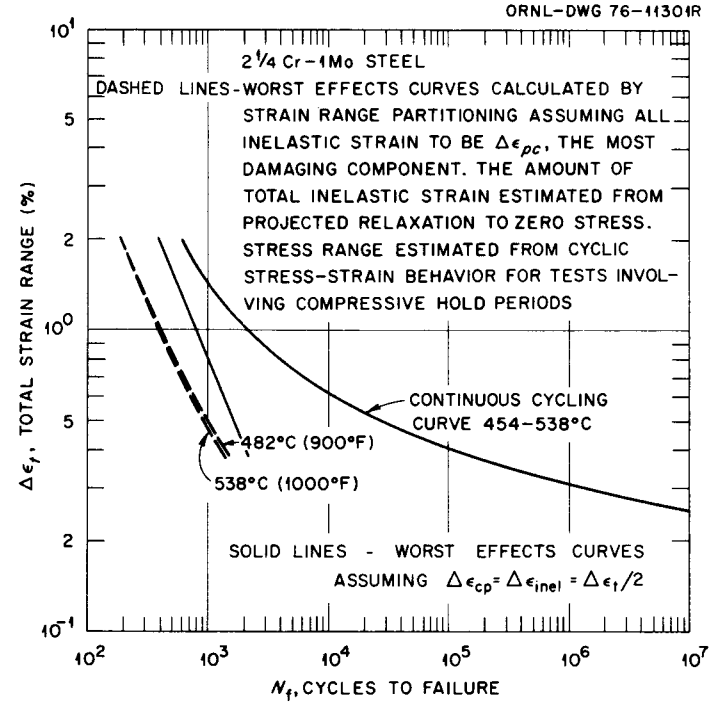

Fig. 1.27. Comparison of Two Methods for Calculating Possible "Worst Effects" Creep-Fatigue Curves for 2 1/4 Cr-1 Mo Steel.

Work is continuing to assess the implications of the above results. The relaxation to zero curves apparently do not represent the worst conceivable situation at low strain ranges. Therefore, the remaining choice is between the two types of worst effects curves. It would appear that the Type II curves are more realistic in terms of actual occurrence. However, scatter and uncertainties in the $\Delta\varepsilon_{pc}$ life relationship mean that the Type II curves may not represent a firm lower bound on life. Still, those curves have several advantages. First, they are independent of temperature, and thus very simple to apply. Second, they merely assume $\Delta\varepsilon_{pc} = \Delta\varepsilon_t/2$ and do not rely on estimates of long-hold-time cyclic stress-strain and relaxation behavior. Work is continuing to assess the possible effects of errors in the estimates of $\Delta\sigma$, C, and m on the other predictions. Also, all results will be extended to lower strain ranges when currently planned low-strain cyclic relaxation tests are completed.

1.4.4.2 Creep-Fatigue Data Analysis — M. K. Booker

Interim results of our analyses of creep-fatigue data for 2 1/4 Cr-1 Mo steel have been presented in several previous reports.[36-38] This quarter we present updated results obtained thus far by the methods of strain range partitioning[35] and the linear summation of creep and fatigue damage.[39]

The strain range partitioning approach involves partitioning the plastic strain range traversed by a cycling specimen into four types:

$\Delta\varepsilon_{pp}$ = tensile plastic strain reversed by compressive plastic strain,

$\Delta\varepsilon_{cc}$ = tensile creep strain reversed by compressive creep strain,

$\Delta\varepsilon_{cp}$ = tensile creep strain reversed by compressive plastic strain,

$\Delta\varepsilon_{pc}$ = tensile plastic strain reversed by compressive creep strain.

Here, "plastic" strain is defined as time-dependent inelastic strain, while "creep" strain is defined as time-dependent inelastic strain. Figure 1.28 illustrates the "life relationships" determined for these four types of strain, whereby $\Delta\varepsilon_{pp}$, $\Delta\varepsilon_{cp}$, $\Delta\varepsilon_{pc}$, and $\Delta\varepsilon_{cc}$ are related respectively to N_{pp}, N_{cp}, N_{pc}, and N_{cc}, where N_i is the expected cycle life of a specimen cycled in pure $\Delta\varepsilon_i$ strain. Shown in the figure are the lines previously determined by Manson et al.,[35] compared with data from the current ORNL program and from the program at General Atomics Corporation.[31] The scatter in the ORNL and GA data is caused partially by the fact that in all cases the creep strain component ($\Delta\varepsilon_{cp}$, $\Delta\varepsilon_{pc}$, $\Delta\varepsilon_{cc}$) was small in comparison with the total plastic strain range.

It should be noted that both the lines and points in Fig. 1.28 were calculated by the linear damage rule, given by

$$\frac{1}{N_{cp}} + \frac{1}{N_{pc}} + \frac{1}{N_{cc}} + \frac{1}{N_{pp}} = \frac{1}{N} \ . \tag{1}$$

Ellis et al.[31] report somewhat unsatisfactory results in the analysis of their data using the above rule, being able to predict the cylic life only within a factor of 3. Moreover, their analysis generally overestimated the cyclic lives. Figure 1.29 shows results of analysis of the ORNL data using the life relationships of Fig. 1.28 and the interaction damage rule, given by

$$\frac{F_{cp}}{N_{cp}} + \frac{F_{pc}}{N_{pc}} + \frac{F_{cc}}{N_{cc}} + \frac{F_{pp}}{N_{pp}} = \frac{1}{N} \ , \tag{2}$$

where, for example, $F_{cp} = \Delta\varepsilon_{cp}/\Delta\varepsilon_{inel}$, $\Delta\varepsilon_{inel}$ being the total inelastic strain range. Results of our analysis of the GA data were reported previously,[30] the margin of error being an acceptable factor of 2 (Fig. 1.30).

The reason for the improvement of our results over those of Ellis et al.[31] can be seen in Fig. 1.31. Comparing Figs. 1.28(d) and 1.31(a), it is clear that the life relationship line used for $\Delta\varepsilon_{cp}$ strain describes the current data significantly better in terms of the interaction

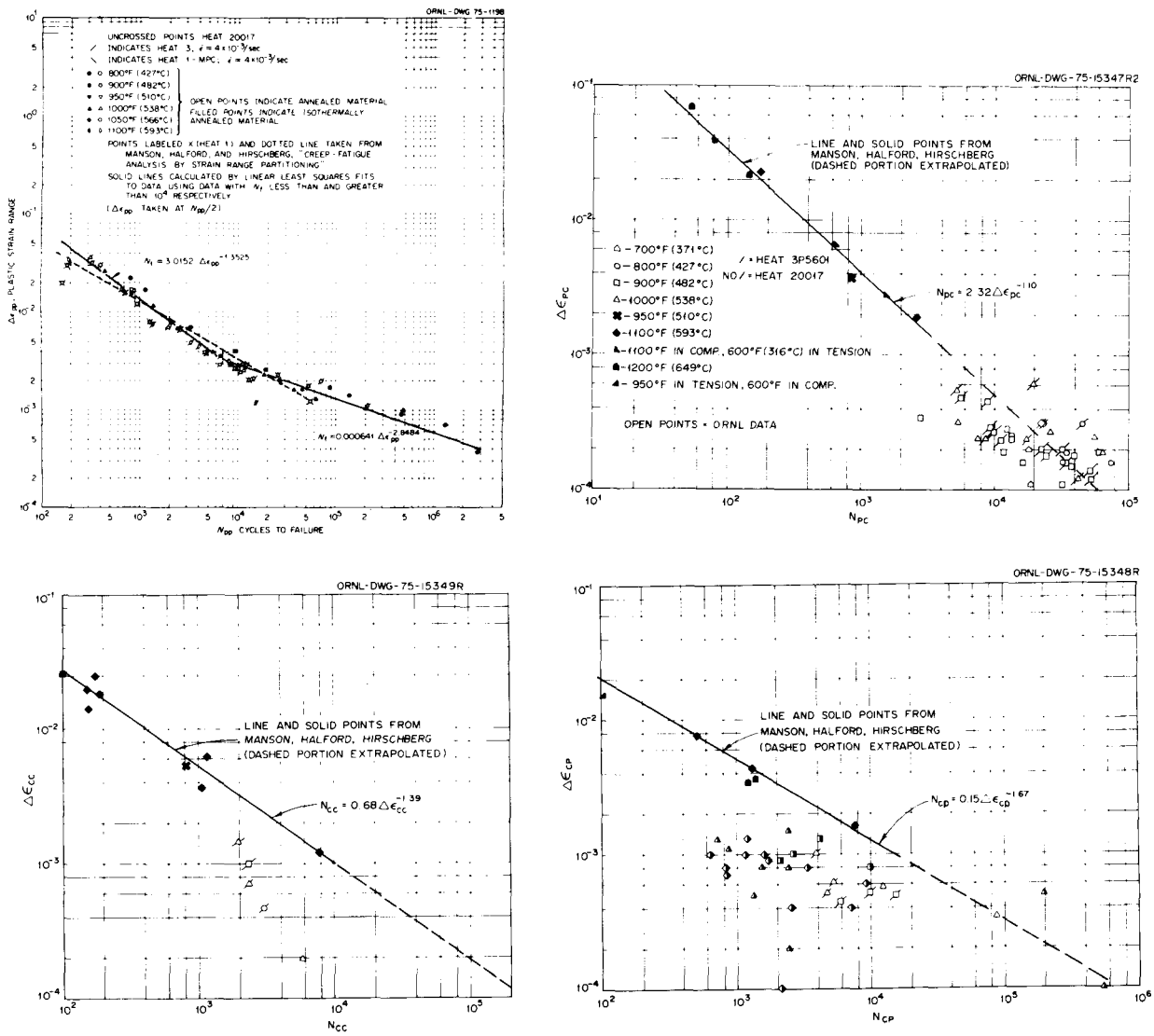

Fig. 1.28. Partitioned Life Relationships for 2 1/4 Cr-1 Mo Steel by the Method of Linear Damage Summation in the Strain Range Partitioning Approach.

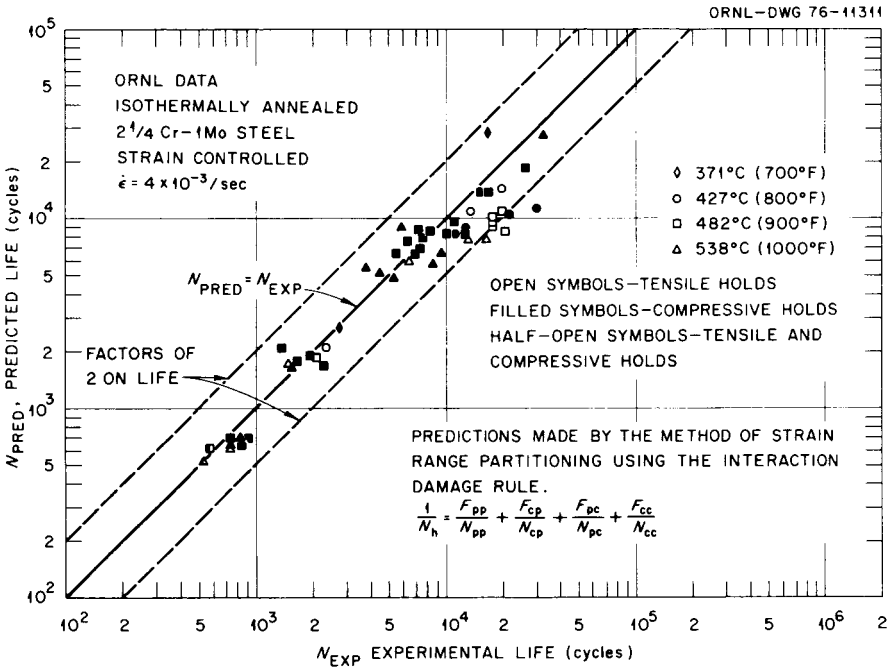

Fig. 1.29. Results of Analysis of ORNL Creep-Fatigue Data for 2 1/4 Cr-1 Mo Steel by the Method of Interaction Damage Summation in the Strain Range Partitioning Approach.

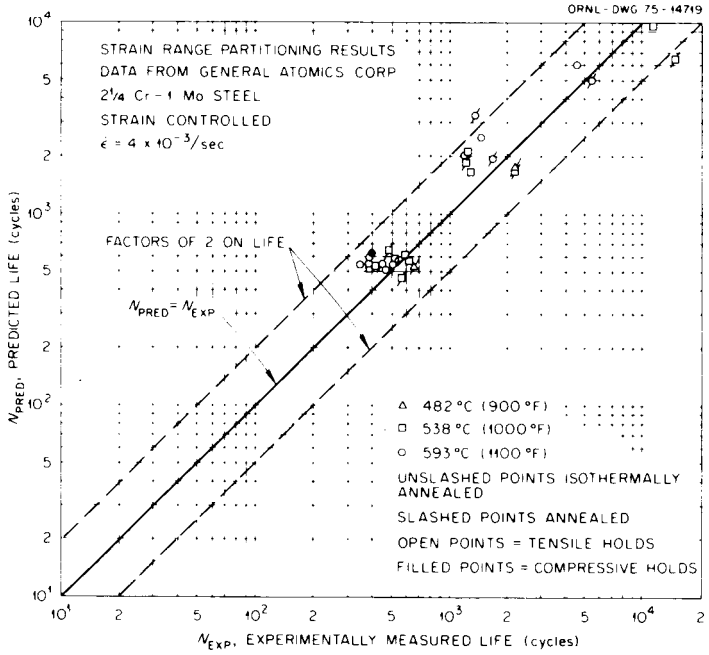

Fig. 1.30. Results of Analysis of GA Creep-Fatigue Data for 2 1/4 Cr-1 Mo Steel by the Method of Interaction Damage Summation in the Strain Range Partitioning Approach.

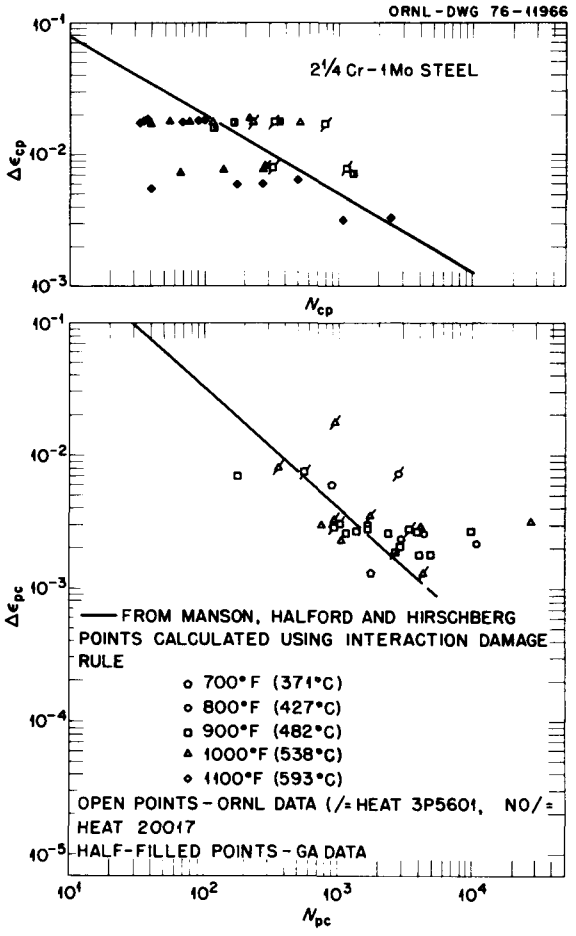

Fig. 1.31. Partitioned *cp* and *pc* Life Relationships for 2 1/4 Cr-1 Mo Steel by the Method of Interaction Damage Summation in the Strain Range Partitioning Approach.

damage rule [Eq. (2)] than in terms of the linear damage rule. On the other hand, data for tests with compressive hold periods seem about equally well-described by either summation procedure. We have used the interaction rule for life predictions in all cases, since most recent results appear to favor that procedure.[40]

A popular method for the analysis of creep-fatigue data in the past has been the method of linear summation of creep and fatigue damage.[39] This method involves numerical integration of a typical relaxation curve during a hold period to calculate the creep damage per cycle as

$$D_c(1) = \int_0^{t_h} dt/t_r \ , \qquad (3)$$

where t_h is the total hold time and t_r is the rupture life. The total creep damage is then

$$D_c = N_h D_c(1) \ , \tag{4}$$

where N_h is the total number of cycles to failure in the given hold-time test.

The fatigue damage is given by

$$D_F = N_h / N_f \ , \tag{5}$$

where N_f is the number of cycles to failure that would have been expected with no hold time. Then, the total damage is given by

$$D = D_c + D_F \ . \tag{6}$$

Figures 1.32 through 1.35 show the results of calculations from Eq. (6) for the currently available data. The smaller data points in the figures were calculated by use of expected values of t_r and N_f. The larger symbols indicate calculations made by use of lower limit values on t_r and N_h (i.e., t_m and N_d). Thus,

$$D_c{}^d + D_F{}^d = D_d \ , \tag{7}$$

where $D_c{}^d$ and $D_F{}^d$ are the values of creep and fatigue damage calculated from t_m and N_d. In these figures, values of N_f were estimated from continuous cycling data[31,41] for these same heats of material, while t_r at each stress was calculated from a previously published[42] equation for that property.

Values of N_d were obtained from the ORNL fatigue design curves for this material,[41] while calculation of t_m is somewhat more complicated. Current creep fatigue design rules[43] specify that

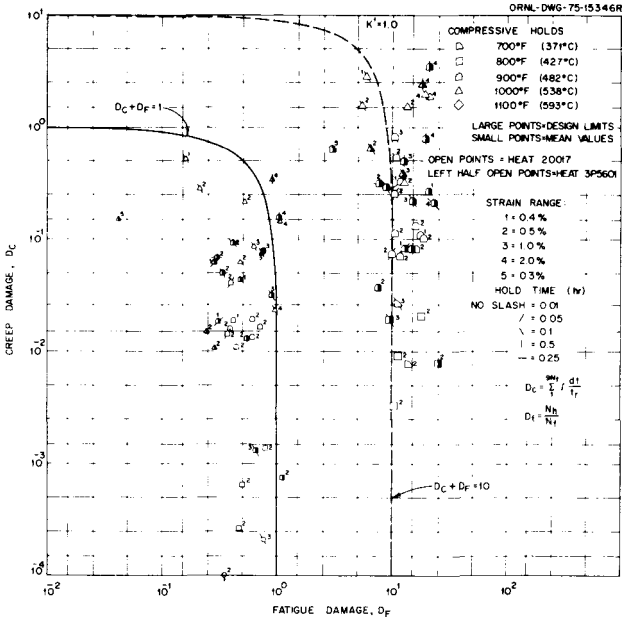

Fig. 1.32. Creep and Fatigue Damage Calculations for 2 1/4 Cr-1 Mo Steel for Use in the Linear Summation of Damage Approach. Data for Tests with Hold Periods at Peak Compressive Strain. $K' = 1.0$.

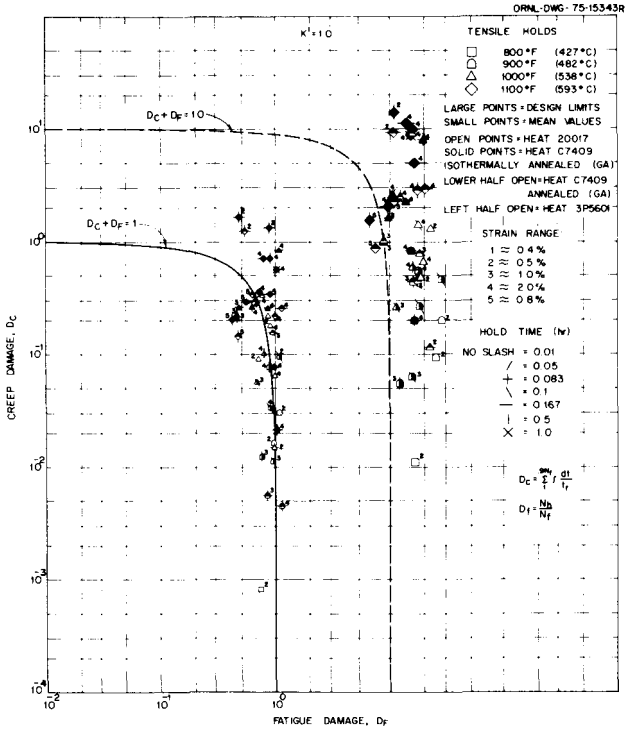

Fig. 1.33. Creep and Fatigue Damage Calculations for 2 1/4 Cr-1 Mo Steel for Use in the Linear Summation of Damage Approach. Data for Tests with Hold Periods at Peak Tensile Strain. $K' = 1.0$.

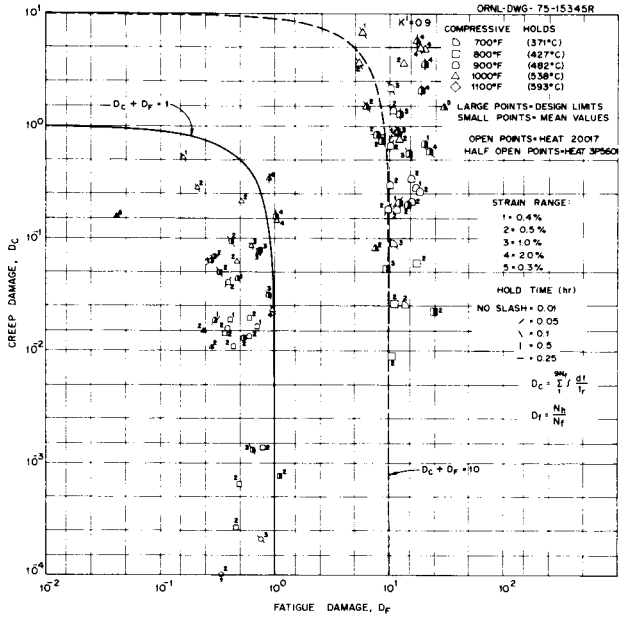

Fig. 1.34. Creep and Fatigue Damage Calculations for 2 1/4 Cr-1 Mo Steel for Use in the Linear Summation of Damage Approach. Data for Tests with Hold Periods at Peak Compressive Strain. $K' = 0.9$.

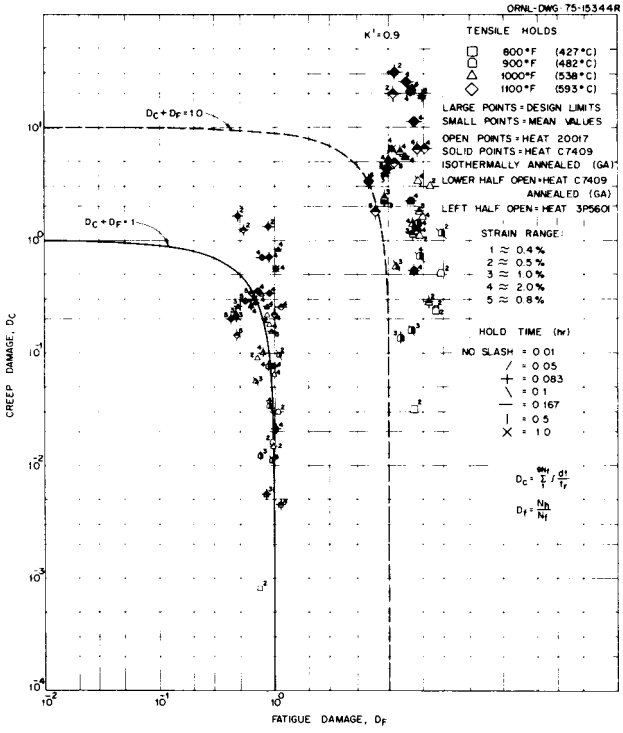

Fig. 1.35. Creep and Fatigue Damage Calculations for 2 1/4 Cr-1 Mo Steel for Use in the Linear Summation of Damage Approach. Data for Tests with Hold Periods at Peak Tensile Strain. $K' = 0.9$.

$$\sum_{j=1}^{P} (n/N_D)_j + \sum_{k=1}^{g} (t/t_m)_k \leq D^* , \quad (8)$$

where

D^* = some specified "damage factor" (currently undefined for 2 1/4 Cr-1 Mo steel),

n = the number of cycles applied under loading condition j,

N_D = the number of design allowable cycles under loading condition j,

t = time duration of loading condition k,

t_m = allowable time under loading condition k.

The value of t_m is calculated as the lower limit time to rupture at the temperature of interest under a stress given by the stress from load k divided by factor K', which is defined as 0.9 for austenitic stainless steels and for Incoloy Alloy 800H.

Based on the minimum stress-rupture curves for 2 1/4 Cr-1 Mo steel,[42] the following equation was used for t_m:

$$\log t_m = 566 \{46.263 - 0.4194 \ln(\sigma/K') - 0.4589 [\ln(\sigma/K')]^2\}/T - 20 \quad (9)$$

where

t_m = allowable time under loading condition k.

σ = stress (MPa),

T = temperature (K),

The values shown in Figs. 1.32 and 1.33 were calculated by use of $K' = 1.0$, while the values in Figs. 1.34 and 1.35 were obtained by use of $K' = 0.9$. Figure 1.36 shows the effect of K' on the minimum stress rupture curves, with $K' = 0.9$ yielding values of t_m roughly half those for $K' = 1.0$, thus approximately doubling the value of D_c^d above.

It should be noted that the values in Figs. 1.32 through 1.35 were actually calculated from

$$D_c = 0.9 N_h D_c(1) \quad (10)$$

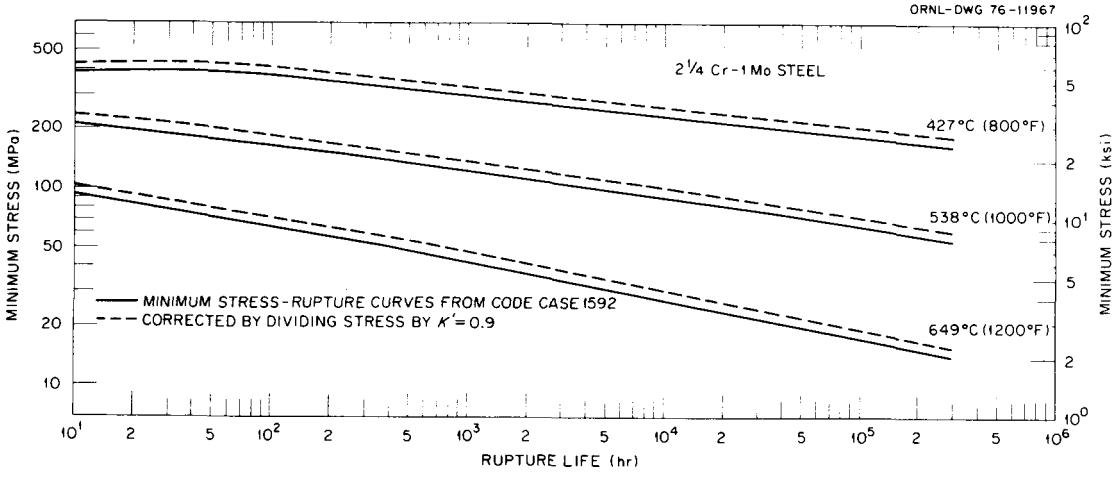

Fig. 1.36. Effect of Using $K' = 0.9$ on Minimum Stress Rupture Curves for 2 1/4 Cr-1 Mo Steel from ASME Code Case 1592.

rather than from Eq. (4). This procedure was based on an estimate that the stress range required to maintain the imposed strain range drops to about 95% of its half-life value at about nine-tenths of the cyclic life. After this point, a sizable crack may exist in the test specimen. However, this correction was found to be a very minor one, and in subsequent life predictions, we used Eq. (4) for simplicity.

Assuming a value of $D = 1$ in Eq. (6), cyclic lives can be predicted by

$$N_h = (1 - D_c)/N_f \ . \tag{11}$$

Figure 1.37 shows the results obtained for the current data by use of this equation. Clearly, the cyclic lives are predicted quite well for the tests involving tension hold periods. However, for this material compressive hold periods are generally more damaging than tension hold periods, especially at low strain ranges. Since the only creep-rupture data available were from tensile creep tests, calculated t_r was in all cases based on these tensile creep-rupture properties. Figure 1.37 shows that the cyclic lives for low-strain-range (long-life) tests involving compression hold periods are generally overestimated at temperatures of 482 to 538°C (900–1000°F).

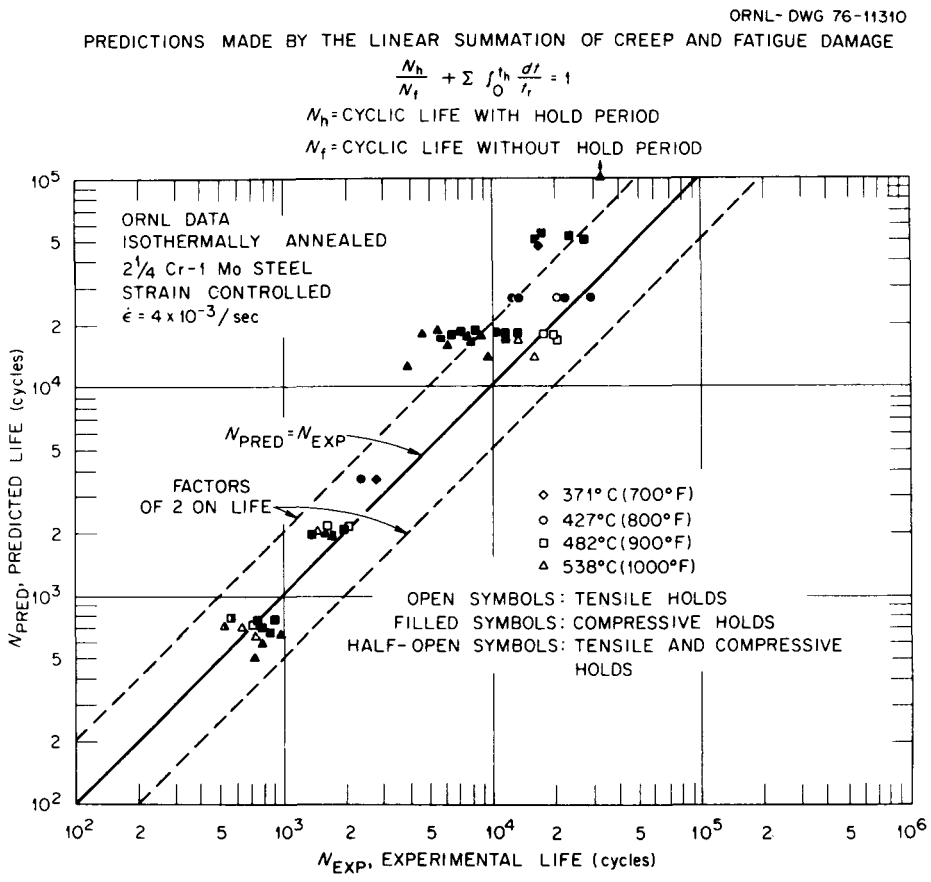

Fig. 1.37. Results of Life Predictions for Creep-Fatigue Tests of 2 1/4 Cr-1 Mo Steel Using the Linear Summation of Damage Approach.

Two possible corrections can be conveniently applied to Eq. (11) to increase the accuracy of the life predictions for compression hold tests. First, the value of the summation of damage can be changed to some number smaller than unity. However, such a correction is probably not warranted. The problem appears to be mainly the inadequacy of predicting compressive creep damage from tensile creep behavior. Thus, a more direct approach would be to attempt to correct D_c to a more realistic value. The simplest way to do this is to correct D_c by some factor β, changing the damage summation equation to

$$D_f + \beta D_c = 1 \ , \tag{12}$$

so that the predicted life is given by

$$N_h = (1 - \beta D_c)/N_f \quad . \tag{13}$$

For each of the available compression hold tests in the range 482–538°C from the ORNL program, values of β were calculated from the experimental values of N_h according to

$$\beta = (1 - D_F)/D_c \quad . \tag{14}$$

Various relationships were attempted to quantify variations in the values thus obtained for β. The most successful correlation found is illustrated in Fig. 1.38, where β is shown to be approximately given by

$$\beta = 0.22 D_c^{-1.24} \quad . \tag{15}$$

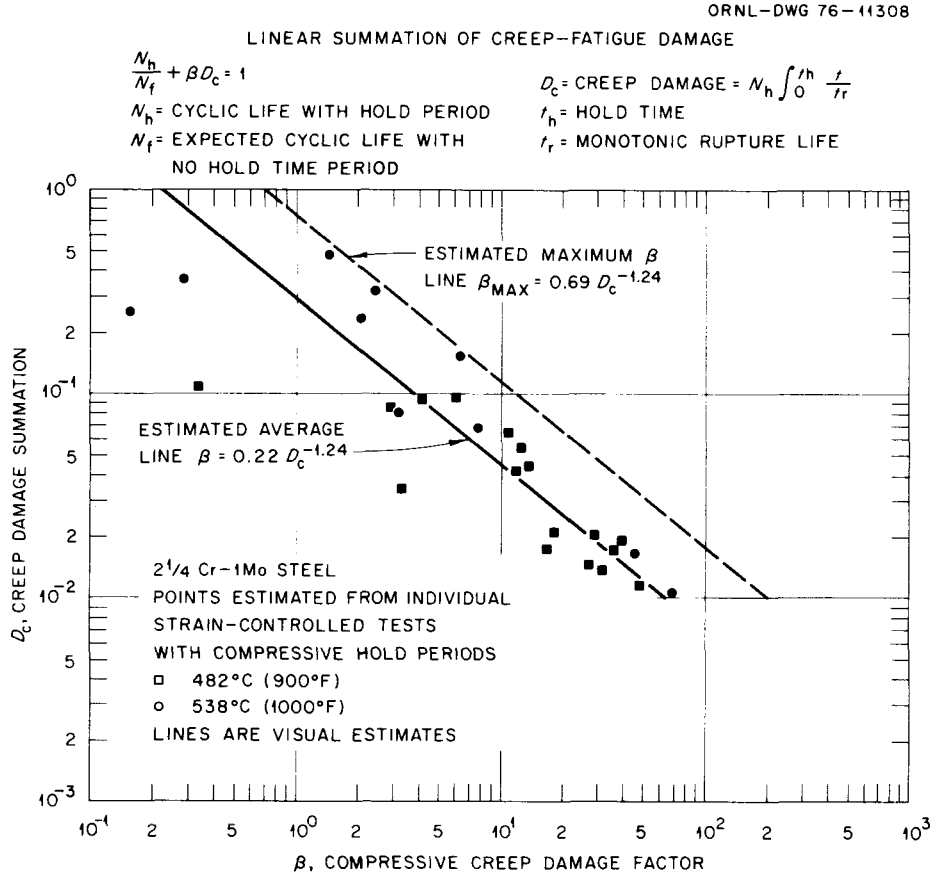

Fig. 1.38. Compressive Creep Correction Factor, β, as a Function of Creep Damage Sum, D_c, for Use in the Linear Summation of Damage Approach.

Clearly, the scatter in Fig. 3.89 is large, although a value of $\beta = 0.69 D_c^{-1.24}$ could be used as a conservative upper limit for the current data.

Figure 1.39 shows the results of life predictions made using Eq. (13) with β estimated by Eq. (15). For completeness, predictions are shown for all ORNL tests, although only compression tests in the range 482 to 538°C were predicted with the β factor.

In terms of fits to data, the method of strain range partitioning clearly provides the best results of the three methods presented above. The coefficients of determination (R^2) given in Table 1.17 show that the β correction significantly improved the fit obtained from the linear summation of damage approach, as is obvious from Figs. 1.37 and 1.39. However, the strain range partitioning predictions are much better still.

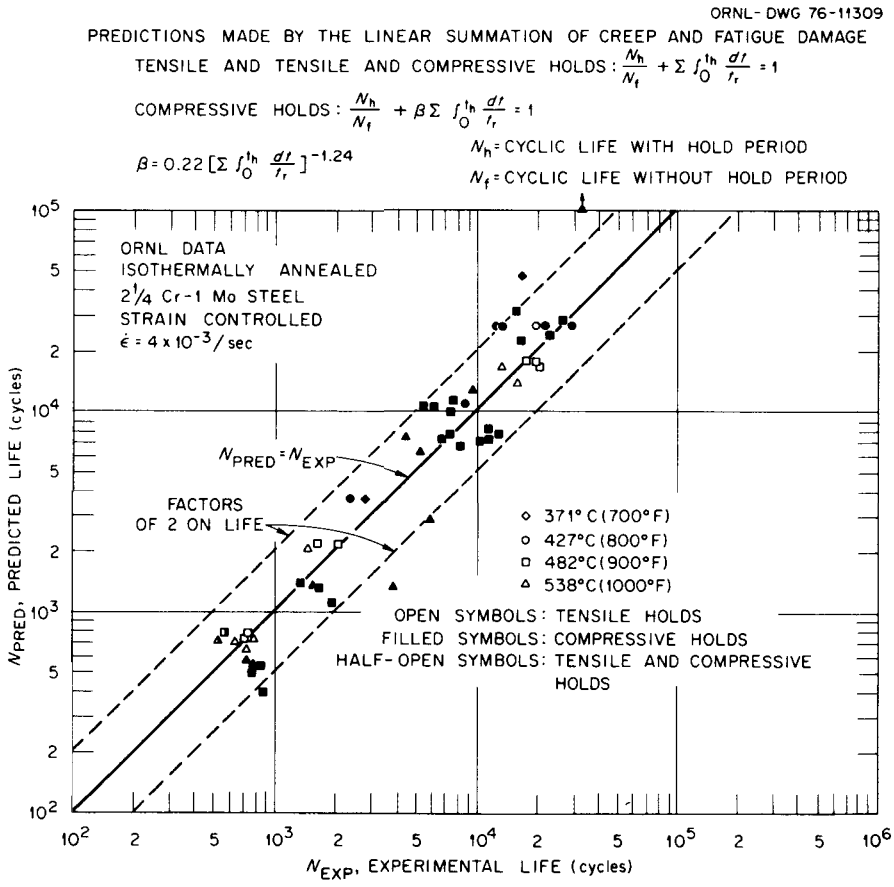

Fig. 1.39. Results of Life Predictions for Creep-Fatigue Tests of 2 1/4 Cr-1 Mo Steel Using the Linear Summation of Damage Approach with Compressive Creep Damage Modified by the β Factor from Fig. 1.38.

Table 1.17. Fits to ORNL Creep-Fatigue Data Using Strain Range Partitioning and Linear Summation of Damage

Method	R^2,[a] Coefficient of Determination, %	
	Compression Hold Data (39 tests)	All Data (56 tests)
Strain Range Partitioning[b]	92.8%	91.7%
Linear Summation[c]	41.1%	67.8%
Modified Linear Summation[d]	63.2%	79.6%

[a]The value of R^2 represents the percentage of variations in the data that are described by the model.

[b]Using the Interaction Damage Rule.

[c]Using $D_F + D_c = 1$.

[d]Using $D_F + \beta D_c = 1$.

The strain range partitioning technique is thus seen to have several distinct advantages in describing the creep-fatigue behavior of this material. These include. (1) good general fit to the available short-term test data; (2) ability to reflect the larger damage due to compressive vs tensile hold periods at low strain ranges; (3) simplicity in application once the life relationships are determined (at least in uniaxial situations); (4) apparent temperature-independence of life relationships; and (5) ability to construct possible "worst effects" curves, as was discussed in Sect. 1.4.4.1.

However, several uncertainties still remain. For instance, we assumed all inelastic strain during continuous cycling at 4×10^{-3}/sec to be of the $\Delta\varepsilon_{pp}$ type. Little information is available at higher strain rates, so it is not possible to fully verify that no significant creep component arises during cycling at this strain rate. Also, in a test with a tensile hold period at peak strain, for example, the amount of $\Delta\varepsilon_{cp}$ strain was calculated by $\Delta\varepsilon_{cp} = \Delta\sigma_r/E$, where E is Young's modulus and $\Delta\sigma_r$ is the total change in stress during the hold period.

However, we have seen some evidence that at the beginning of a hold period, the stress undergoes a sudden rapid decrease, followed by a period of more gradual relaxation. Diercks[44] has attributed a similar decrease for type 304 stainless steel to a strain rate effect caused

by a sudden change from the ramp strain rate to the zero strain rate of the hold period, and has thus suggested that the strain corresponding to this initial stress drop be considered plastic rather than creep strain. Interestingly, the fact remains that even with the above simplifications, the method fits our data quite well. The above effects need to be considered, however.

Uncertainties that need to be resolved concerning the strain range partitioning technique in general include the following.

1. The method has no explicit method for dealing with strain rate effects and therefore may not fully account for these effects. Preliminary results from the method recently developed by Majumdar[45] indicate that strain rate plays an extremely important role in determining the damage caused by a given amount of inelastic strain.

2. The method assumes that the damage caused by hold periods is due totally to creep effects, and does not account for environmental effects or for the effects of metallurgical processes such as strain aging. Recent results reported by James[46] show that crack growth studies indicate that the effects of environmental interactions can be a prime cause of damage during hold periods.

3. The life relationships for 2 1/4 Cr-1 Mo steel are yet to be fully verified. Influences due to temperature, heat-to-heat variations, melting practice, etc. need to be determined. In addition, limits of extrapolation of the relationships and their linearity in log-log coordinates need to be verified. Also, the current relations were derived from the linear damage rule, although they seem consistent with our results from the interaction rule over a limited range.

4. Additional long-term complex-wave-form tests are required for full verification.

The relatively poor fits to the data by the linear summation of damage approach raise the question of whether the creep-fatigue rules[43] in current use for austenitic materials are applicable to 2 1/4 Cr-1 Mo steel. Figures 1.32 through 1.35 indicate that the value of D_d from Eq. (7) is well above unity in all cases, typically being 10 or greater. However, for low-strain-range compression hold tests, the factor of

safety can be considerably reduced. The worst situation occurs in the case of specimen MIL-46, which was tested with 0.01-hr hold periods at peak compressive strain at a strain range of 0.3% at 538°C. The predicted damage summation using average properties was only 0.194 for this test. The design value using $K' = 1.0$ was 3.625, and using $K' = 0.9$ was 4.439. If one applies a conservative value of β from $\beta = 0.69 D_c^{-1.24}$ (where D_c is obtained from average properties) the damage sum becomes 13.32 with $K' = 0.9$ or 7.51 with $K' = 1.0$. Thus, it appears that conservative results can be obtained by using the current procedure with $K' = 0.9$, if D^* from Eq. (8) is unity and if compression hold tests are corrected using $\beta = 0.69 D_c^{-1.24}$, where D_c is given from Eq. (4).

1.4.5 Mechanical Properties Correlations for 2 1/4 Cr-1 Mo Steel — Uniaxial Stress Relaxation of 2 1/4 Cr-1 Mo Steel — M. K. Booker and R. W. Swindeman

From comparisons with limited experimental data for a single heat of isothermally annealed, air-melted plate of 2 1/4 Cr-1 Mo steel, it appears that isothermal, uniaxial relaxation behavior can be estimated from creep behavior by use of the hypothesis of strain hardening. Resonable productions were obtained using strain hardening in conjunction with the creep equation for this material, described by Booker et al.,[42] although this approach tended to overestimate the amount of relaxation at lower temperatures ($\leq$ about 538°C) and higher stresses (> yield strength).

1.4.5.1 Creep Data

For a discussion of the creep data upon which the creep equation for the material was based, see ref. 42. The data consisted of 37 tests from 5 different heats of material meeting the following restrictions:
room-temperature ultimate tensile strength — 483—517 MPa (70—75 ksi);
room-temperature (0.2% offset) yield strength — $\geq$207 MPa (30 ksi);
carbon content — 0.07—0.15 wt %;
chromium content — 2.0—2.5 wt %;
molybdenum content — 0.9—1.1 wt %.

Except for the narrower restrictions on tensile strength, these restrictions are given in the *Nuclear Systems Materials Handbook*. The minimum carbon content of 0.07 wt % is in accordance with ASME Sect. III for components in service above 371°C (700°F). The other restrictions are contained in ASME specifications SA-336-F22A and SA-387-22-Cl I. The equation was developed from data for annealed material from tube-pipe, bar, and plate stock. As far as can be determined, all material was air melted.

1.4.5.2 Relaxation Data

Predictions of relaxation behavior were compared with experimental relaxation data for a single heat of annealed air-melted material. This heat was one of the five used in developing the creep equation. The material had the following composition: 0.11% C, 0.55% Mn, 0.29% Si, 2.13% Cr, 0.9% Mo, 0.014% S, and 0.11% P. Bar specimens having a 6-mm-diam by 32-mm-long reduced section were machined from 25-mm-thick plate after annealing at 927°C and furnace cooling. The microstructure consisted of proeutectoid ferrite with about 5% pearlite and 1% bainite. Tests were performed in an electrohydraulic machine, using servocontrol based on the feedback signal from an extensometer attached to the specimen shoulders. Test temperatures included 450, 482, 510, 538, and 566°C (842, 900, 950, 1000, and 1050°F). At each temperature a specimen was tested for approximately 100 hr (run 1), then reloaded to higher strains for subsequent testing (run 2, etc.). In addition, a series of single loading tests extending to 1000 hr at various strain levels at 510°C was available. Most of the data are shown in Sect. 1.4.5.4.

1.4.5.3 Analytical Procedure

Currently recommended interim design rules[32] suggest that relaxation behavior for 2 1/4 Cr-1 Mo steel be estimated from creep behavior in conjunction with the hypothesis of strain hardening. Some results, however, indicate that strain hardening may not be an adequate representation of the variable load behavior of this material.[32,47] For this reason, the strain hardening approach must currently be regarded as interim.

Basically, the strain hardening approach involves the hypothesis that the instantaneous creep rate, $\dot{e}_c$, is uniquely determined by the instantaneous stress, temperature, and accumulated creep strain,

$$\dot{e}_c = \dot{e}_c(\sigma, T, e_c) \ .$$

Booker et al.[42] recommend an equation for creep strain (e_c) as a function of time (t), stress, and temperature of the form:

$$e_c = \frac{t}{a + bt} + \dot{e}_m t \ , \tag{1}$$

where a, b, and $\dot{e}_m$ are given by

$$\log a = 12.26 - 3.348 \times 10^{-6} T^2 + 9.353 \times 10^{-4} \sigma^2 - 1.167 \times 10^{-4} T\sigma \ , \tag{2}$$

$$\log b = -52.19 + 0.0868T - 3.368 \times 10^{-5} T^2 - 1.152 \ (\log \sigma)^2 \ , \tag{3}$$

$$\log \dot{e}_m = -30.04 + 0.015167T + 2.001 \times 10^{-3} T (\log \sigma)^2 \ , \tag{4}$$

where

T = temperature, °R;
$0.556T - 273$ = temperature, °C
σ = stress, ksi
6.895σ = stress, MPa.

Equations (1) through (4) are valid for stresses of from 7 to 448 MPa (1–65 ksi) from 371 to 593°C (760–1100°F), except that below 438°C (820°F), values of b are given by the value at that temperature.

Equation (1) can be solved for time as a function of creep strain to yield

$$t = \frac{be_c - a\dot{e}_m - 1 + \sqrt{(a\dot{e}_m + 1 - be_c)^2 + 4ae_c b\dot{e}_m}}{2b\dot{e}_m} \ . \tag{5}$$

With Eq. (5) one can use Eq. (1) to predict relaxation behavior via the hypothesis of strain hardening.

The exact procedure used to calculate relaxation behavior was as follows:

First, divide the stresses traversed into small intervals (we used 0.5 MPa = 0.072 ksi), then assume that relaxation occurs as a stepwise process through these intervals downward from the initial stress, as shown schematically in Fig. 1.40.

The stress decrease of 0.5 MPa corresponds to a decrease in elastic strain of $100(0.5/E)$, where E is the static Young's modulus (MPa) as given in ASME Code Case 1592 approximately equal to:[48]

$$E = 6895(30.69 - 0.02169T + 7.492 \times 10^{-5}T^2 - 1.170 \times 10^{-7}T^3) \quad (T = °C) \quad . \quad (6)$$

Thus, it is assumed that the stress remains at each level for a time period long enough to allow a creep strain of $100(0.5/E)$. If $\Delta\varepsilon$ is the total accumulated creep strain at the beginning of a given stress level, then $\Delta\varepsilon + 100(0.5/E)$ is accumulated creep strain at the end of

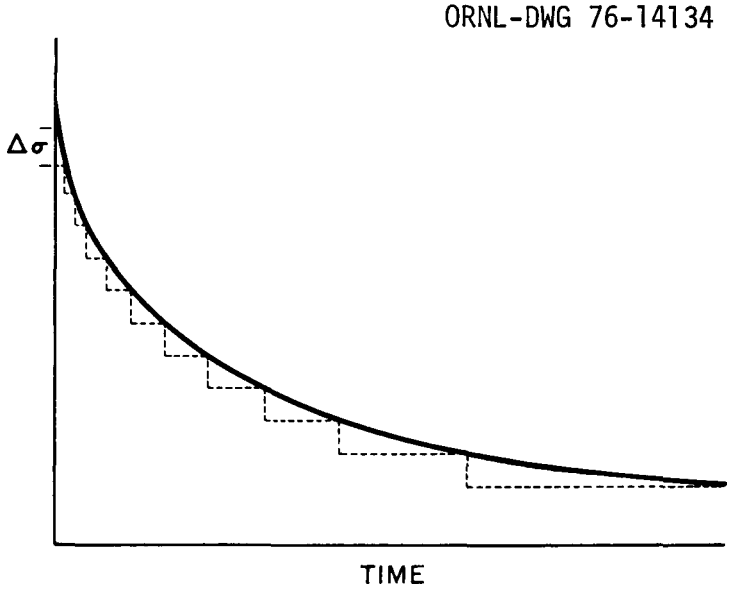

Fig. 1.40. Schematic Illustration of a Relaxation Curve as Approximated in the Numerical Calculation of Relaxation from the Creep Equation Using the Hypothesis of Strain Hardening.

a given stress level. Thus, the time spent at that stress level is $t[\Delta\varepsilon + 100(0.5/E)] - t(\Delta\varepsilon)$, where t is given by Eq. (5) above and where a, b, and $\dot{e}_m$ are defined at the current stress level. For reloadings, the time is reset to zero at the beginning of subsequent relaxation periods, but the creep strain accumulation continues monotonically.

1.4.5.4 Results

Comparisons between predictions made by the above approach and experimental relaxation data are illustrated in Figs. 1.41 through 1.43 at the various temperatures for which data are available. Clearly, at all the higher stress levels the predictions appear to overestimate the amount of relaxation, at least for the times shown in these figures. This problem worsens at lower temperatures ($\leqslant$538°C), where the relaxation response is consistently overestimated. Figure 1.41 shows that at 450 and 482°C (842 and 900°F) the relaxation curves on subsequent loadings are essentially parallel and the predictions always show more relaxation than do the experimental curves, at least to 100 hr. At 510°C (950°F), the material appears to weaken in terms of resistance to relaxation upon reloading. The predictions (Fig. 1.42) are quite good for initial stresses less than about 170 MPa ($\approx$ 25 ksi), but overpredict relaxation at higher stresses, at least for the single run tests in Fig. 1.42(a). Available tests at 538°C (1000°F) again indicate weakening upon reloading; and the predictions again overestimate relaxation for these high-stress tests [Fig. 1.43(a)]. At 566°C (1050°F), available data [Fig. 1.43(b)] indicate that the predictions agree quite well with curves for reloaded specimens, but overpredict the amount of relaxation upon initial loading, at least at high stresses.

1.4.5.5 Limitations

All limitations and restrictions on the creep equation are inherently a part of this correlation as well. The basic range of applicability of the creep equation is as follows:

1. Stress: 7 MPa < σ < 448 MPa (1 ksi < σ < 65 ksi). The equation is limited at low stress by the minimum in the $\dot{e}_m$ equation at σ = 6.9 MPa (1 ksi).

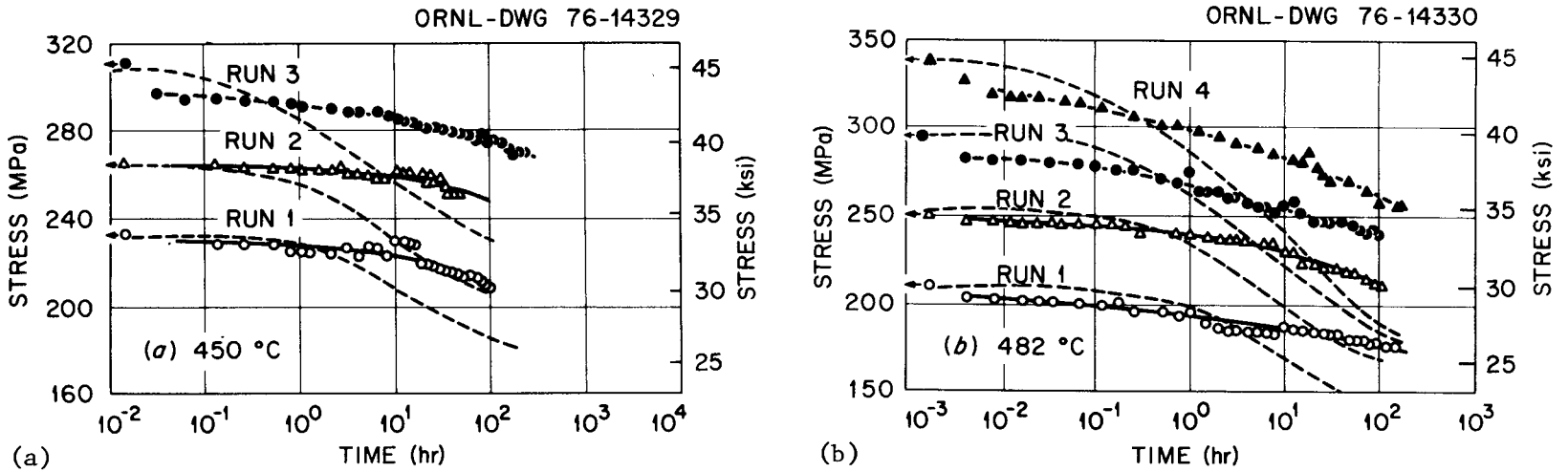

Fig. 1.41. Comparison Between Predicted and Experimental Relaxation Curves in (a) Three Repeated Loadings in a Single Specimen at 450°C and (b) Four Repeated Loading in a Single Specimen at 482°C. Solid lines and points represent experimental data; dashed lines represent predictions.

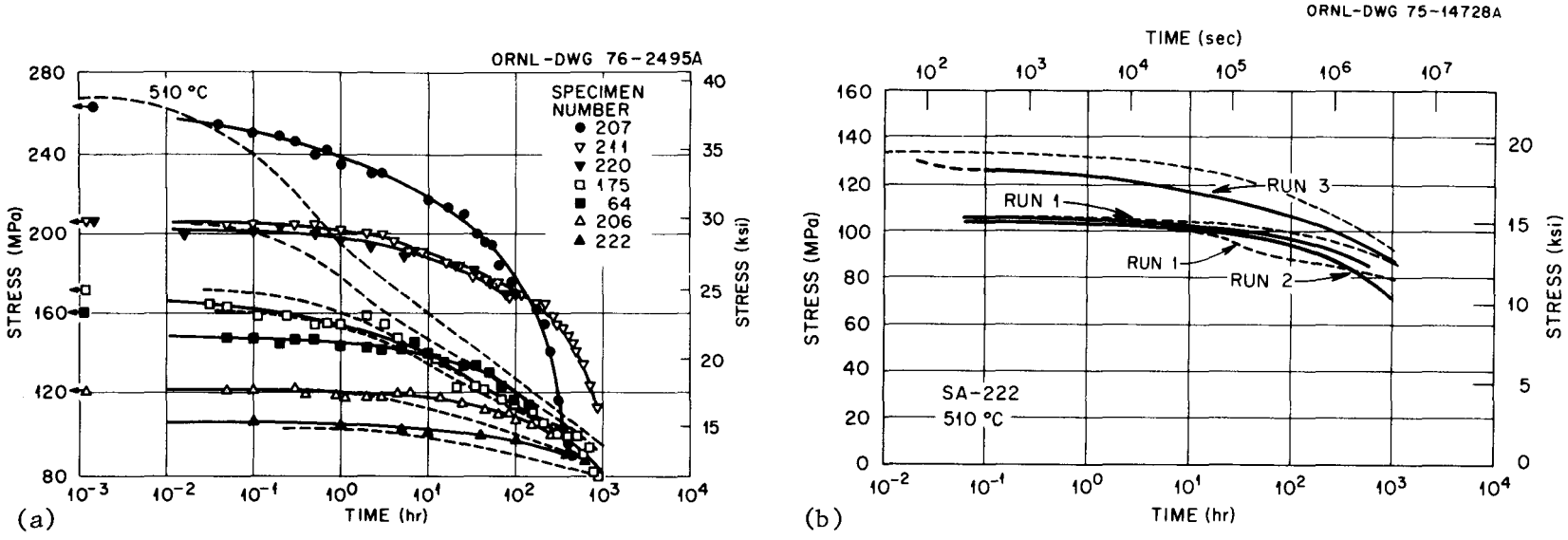

Fig. 1.42. Comparison Between Predicted and Experimental Relaxation Curves at 510°C in (a) Single Loadings of Different Specimens and (b) Three Repeated Loadings of a Single Specimen. Solid lines and points represent experimental data; dashed lines represent predictions.

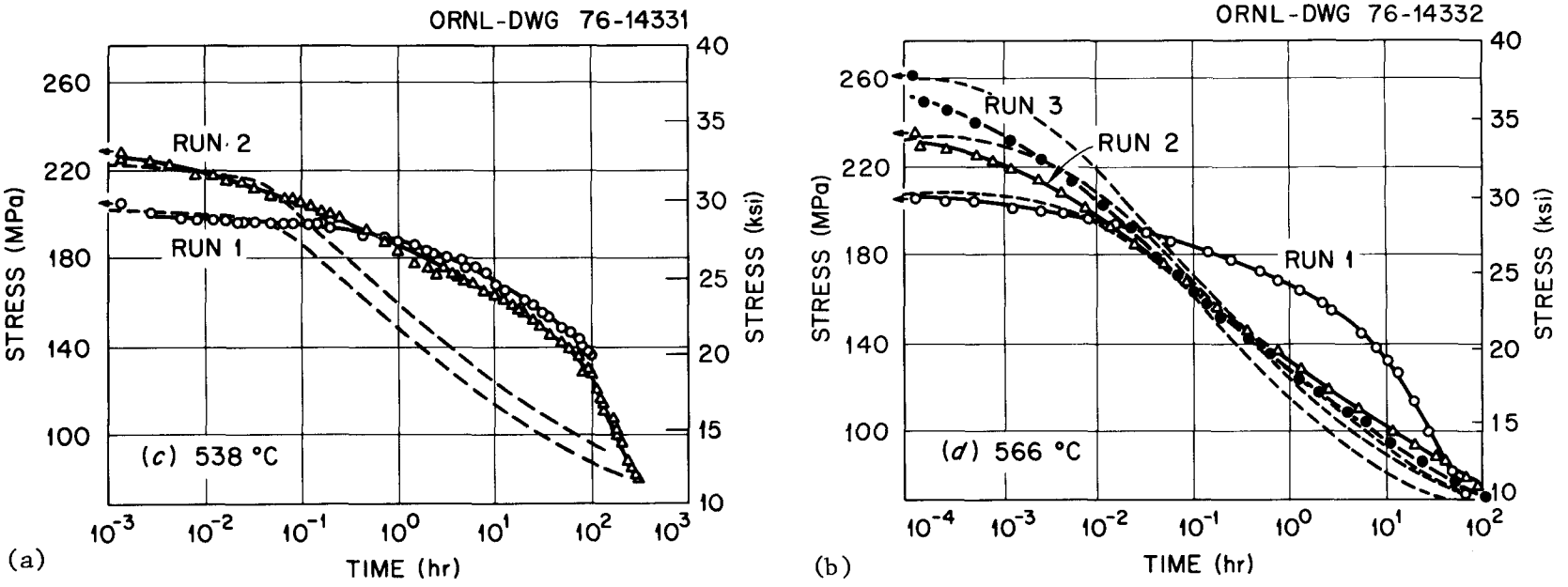

Fig. 1.43. Comparison Between Predicted and Experimental Relaxation Curves in (a) Two Repeated Loadings of a Single Specimen at 538°C and (b) Three Repeated Loadings of a Single Specimen. Solid lines and points represent experimental data; dashed lines represent predictions.

2. Temperature: $371°C \leq T \leq 593°C$ ($700°F \leq T \leq 1100°F$)
3. $t_3 = 0.28 t_r^{1.07}$, where t_r = rupture life; $\log t_r = -31.45 + 39{,}320/T - 19.75 \log \sigma + 0.0164T \log \sigma$

   σ = stress, MPa,

   T = temperature, K,
4. Calculated strain: $\leq$ design criteria strain limits per applicable code or specifications.

Clearly, these restrictions contain some unrealistic regions [e.g., the upper limit of 384 MPa (65 ksi) exceeds the expected ultimate tensile strength]. Also, one must remember the above results, which indicate that the current approach generally overestimates relaxation response at lower temperatures (below about 538°C) and higher initial stresses (> yield strength), although the limited available data do not make it possible to precisely determine the stress-temperature region where problems exist. All results considered, it appears that the current approach will yield reasonably good results for low initial stresses (< yield strength), especially for relaxation after the reloadings. However, the complex nature of this material and the inaccuracies of some predictions indicate a need for further studies of hardening rules.

1.5 NONDESTRUCTIVE TESTING — R. W. McClung

1.5.1 Penetrating Radiation — B. E. Foster

We are continuing our developmental studies for bore-side radiography using the rod-anode microfocus x-ray unit.

After coating the bore of the lens with carbon black to improve stability (mentioned in the last report),[49] we noted a significant improvement in focusing, which severely narrowed the width of the x-ray beam. In fact, the width of the x-ray beam was insufficient to cover the weld bead of the referenced design tube-to-tube joint.

After several experiments of defocusing the electron beam by varying the lens-focusing current in increments of 5 and 10 mA and monitoring the resultant change in usable x-ray beam width, we determined that the electron

beam was much smaller than the 0.2-mm-diam (0.008-in.) flat tip of the tungsten target. This condition effectively eliminated the portion of the beam in the forward direction. To overcome the problem we machined the target (maintaining the 45° included angle of the cone) to a 0.05-mm-diam (0.002-in.) flat tip. The new target configuration provided increased width of the x-ray beam with no loss in penetration or wire sensitivity. In fact, we are now routinely imaging a 20-μm-diam (0.0008-in.) steel wire (placed source side) through the reference design wall thickness of 2.8 mm (0.110 in.). We have, on occasion, imaged a 12.5-μm-diam (0.0005-in.) steel wire through the reference wall. The information on target modification has been communicated to L. A. Fontijn of Technisch Physische Dienst and R. Peugeot of Ridge Instrument Company for incorporation into future production units, if needed.

The series of experiments[49] comparing the sensitivity and resolution obtainable with lead-impregnated vinyl to that obtained with PbO_2 screens has been completed. The lead-impregnated vinyl permitted better contact of the cassette to the specimen and was easier to attach. Because of the better contact, there was slightly better resolution with the lead-impregnated vinyl. A supply of these cassettes, precut to 3.8 × 7 cm (1 1/2 × 2 3/4 in.), has been ordered.

On April 21, C. W. Donnelly of Atomics International (AI) brought 28 tube-to-tube developmental welds of reference design to ORNL for bore-side radiography and, in addition, to observe operation of the microfocus unit. R. A. Hartle of General Electric (GE) arrived on April 22 with 21 tube-to-tube qualification welds associated with the few-tube model.

Each of the 49 sample welds was radiographed in duplicate using the newly fabricated target providing combined forward and reverse throw of the radiation beam. In addition several duplicate radiographs were made of just the tube wall. At the request of C. W. Donnelly several additional radiographs were made utilizing a flat target with back-throw radiation only, which resulted in a projected, distorted image of the weld joint. It was mutually agreed that this latter technique provided less detail of the weld and yielded an image that was extremely difficult to interpret because of the distortion and film density gradient. In total, 163 quality

radiographs were made, including cassette fabrication and film interpretation, in the two-day time period with no equipment malfunction.

The welds for Donnelly were quoted as being developmental and fabricated between Nov. 20, 1975, and April 9, 1976. The welds for Hartle were of two types, one set of ten being the qualification welds previously mentioned and the other set of eleven consisting of a variety of experimental welds and materials.

The distribution of samples according to the largest pore diameter is:

Porosity	Number of Samples	
Maximum diameter, mm (in.)	AI	GE
0	0	10
0.05–0.13 (0.002–0.005)	2	2
0.13–0.25 (0.005–0.010)	17	2
0.25–0.38 (0.010–0.015)	3	0
0.38–0.51 (0.015–0.020)	5	7
>1.3 (>0.050)	1	0

The bulk of the samples brought by Donnelly contains pores in the 0.127–0.254-mm-diam (0.005–0.010-in.) size range and represent the more recently fabricated welds. The samples in the few-tube-model grouping contained either no pores or pores with a maximum diameter of 0.127 mm (0.005 in.). All of the samples were fabricated by AI; the designation of AI indicates the samples were brough by Donnelly, and the samples designated by GE were those brought by Hartle.

The distribution of samples according to the number of pores is:

Pores Imaged on Film	Number of Samples	
	AI	GE
0	0	10
1–10	14	2
11–15	3	0
16–20	5	0
21–30	3	3
31–40	2	2
Over 40	1	4

The bulk of the AI samples contained less than 10 pores and again represents the more recently fabricated welds. The bulk of the GE samples is in the zero porosity category, and these samples are in the few-tube-model category.

In addition, two of the AI samples contained linear indications; one appears to be a classic crater crack; however, this sample had been prepared in mid-December, early in the weld development program. Nine of the GE samples contained linear indications, predominantly lack of fusion; however, these were all in the grouping of experimental welds and materials. Two of the GE samples in the few-tube-model grouping contained a crater, but no definitive crack was visible.

The eight tube-to-tube (T/T) welds[49] from AI have been reradiographed after boring the inner surface to remove excess weld sag. Similar size and distribution of porosity was observed as compared to preboring radiography. We noted linear indications in three of the eight samples. However, we attribute the detection of these linear indications to the improved focusing and resultant smaller focal spot rather than any effects from inner boring.

A report entitled, "A Study of X-Ray and Isotopic Techniques for Bore-Side Radiography of Tube-to-Tubesheet Welds," has been prepared for publication in *Materials Evaluation*.

1.5.2 Eddy Currents — C. V. Dodd

Investigations are continuing of the use of multiple-frequency techniques to detect defects in the presence of variations in other physical properties in steam generator tubing. A computer program (MULPRM) has been written to calculate the material properties from instrument readings for the case where the problem is overdetermined (there are more unique instrument readings than there are material properties). This program has been successfully applied to the calculation of two properties (both conductivity and lift-off) from the magnitude and phase readings at a single frequency. It is currently being applied to the calculation of thickness, conductivity, lift-off, defect size, and defect depth using the magnitude and phase readings at three frequencies. The program also calculates the worst case

error in the material properties due to the maximum measurement error in the magnitudes and phases. This has allowed the three best frequencies for maximum accuracy to be determined. When this application has been successfully completed, permeability variations (as in the steam generator tubing) will be added to the problem.

Due to the complexity of the calculations, we have decided that the calculation of properties that require four or more independent readings could be made more accurately using digital computers rather than analog computers. Therefore, we are replacing the analog computer modules in our present eddy-current instruments with a digital computer. The digital computer is based on the 8080 microprocessor and contains 4 k of random access memory, 4 k of read-only memory, 72 parallel input-output lines, and 1 serial input-output line on a single 158.5 × 236.2 mm (6.25 by 9.3 in.) printed circuit board. The board will fit into the same space in the modular instrument as the display and analog computer module and is expected to cost less than the digital panel meter, which it will replace. The board has been designed and taped and is being photoetched and drilled.

We are developing a monitor system, a simulator, and a capability for programming the read-only memory to go with the computer.

1.5.3 Ultrasonics — K. V. Cook

We are continuing our development of preliminary techniques for inspection of tube-to-tubesheet joints and our feasibility study for the in-service inspection of steam generator tubing. We are developing probes, techniques, and preliminary automated scanners to allow bore-side pulse-echo flaw detection in the reference-size weldments and tubing of 16-mm OD × 2.77-mm wall thickness (0.625 × 0.110 in.).

Our portable scanner for evaluating tube-to-tubesheet (T/TS) joints, short tube-to-tube (T/T) joints, or short tube sections from the bore side has continued to demonstrate reliable performance. The system has been upgraded by motor replacement and appropriate modification so that a 25.4-mm (1-in.) length can be scanned and recordings made in less than 3 min. We are currently scanning the 25.4-mm section to allow precise location of the weld area through the use of slots placed in the tube

section of the T/T mock-up specimens. For the actual weldment inspection 12.7 mm (0.50 in.) of scan should be adequate; thus it is significant to note that with our current system we can inspect the welds in less than 2 min of scanning time.

Three slightly different replaceable probe assemblies were evaluated in the scanner system. All designs utilize stainless steel probe heads, adapters, and handles for stable operation and extensive usage. The particular designs that were evaluated are very versatile and are capable of using either a 4.8-mm-diam (0.190-in.) or a 3.1-mm-diam (0.125-in.) commercial transmitter-receiver tranducer. Fabrication of additional probe heads, if they are required, that use the 3.1-mm-diam transducer instead of the 4.8-mm-diam unit would probably allow inspections in smaller bores [less than the 10.2-mm (0.4-in.) present size].

Our contacts and coordination with commercial transducer manufacturers during our early development stages has been successful in that it is now possible to procure prototype probe heads from commercial suppliers. This will be extremely valuable during transfer of technology to the steam generator fabricator.

The particular probe assembly that we chose to evaluate the T/T mock-up joints from AI has a stainless steel probe head and handle with a brass adapter between the two. We did not feel that the brass adapter warranted the delay required for disassembly and replacement with a stainless steel component. Evaluation has begun on a number of T/T weld joints, which are currently available, with primary emphasis on the reference AI design specimens.

Figure 1.44 shows three samples on which we have been working. Figure 1.44(a) is a piece of reference design tubing, which contains six EDM notches. These notches are 3.1 mm (0.125 in.) long and are machined on both inner and outer surfaces. Three are inner and three are outer notches of three different depths. The depths are 0.2, 0.28, and 0.35 mm (0.008, 0.011, and 0.014 in.), which represent approximately 7, 10, and 13% of the wall thickness. The other two samples will be discussed in following paragraphs along with inspection results. Figure 1.45 shows the electronic system that we have assembled to allow plan-view recording

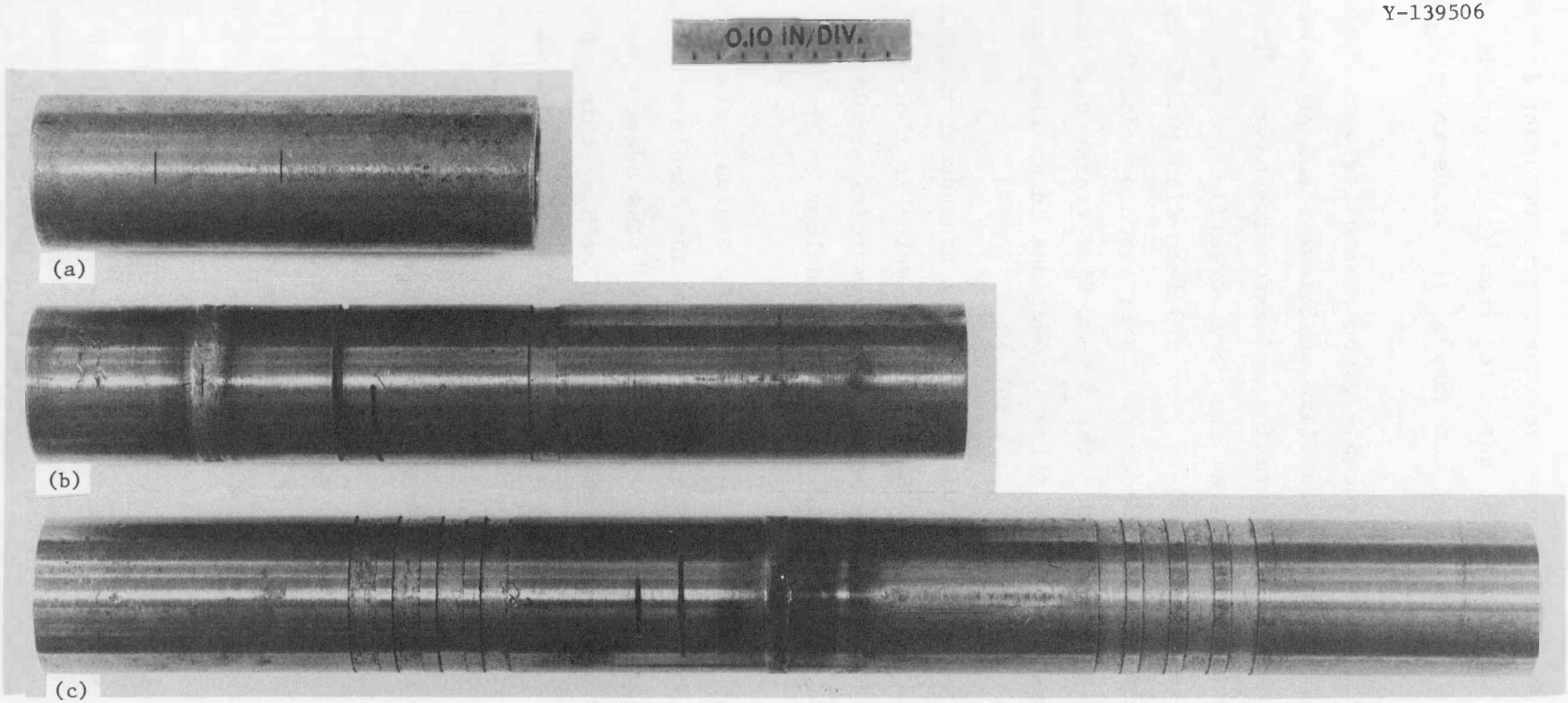

Fig. 1.44. Samples Used for Ultrasonic Inspection of Tube-to-Tube Joints. (a) Tube standard with 0.2-mm-deep × 3.1-mm-long (0.008 × 0.125 in.) reference notches. (b) AI weldment specimen with 0.28-mm-deep × 3.1-mm-long (0.011 × 0.125 in.) reference notches machined in the center and on either side of the weldment. (c) AI weldment typical of mock-up specimens.

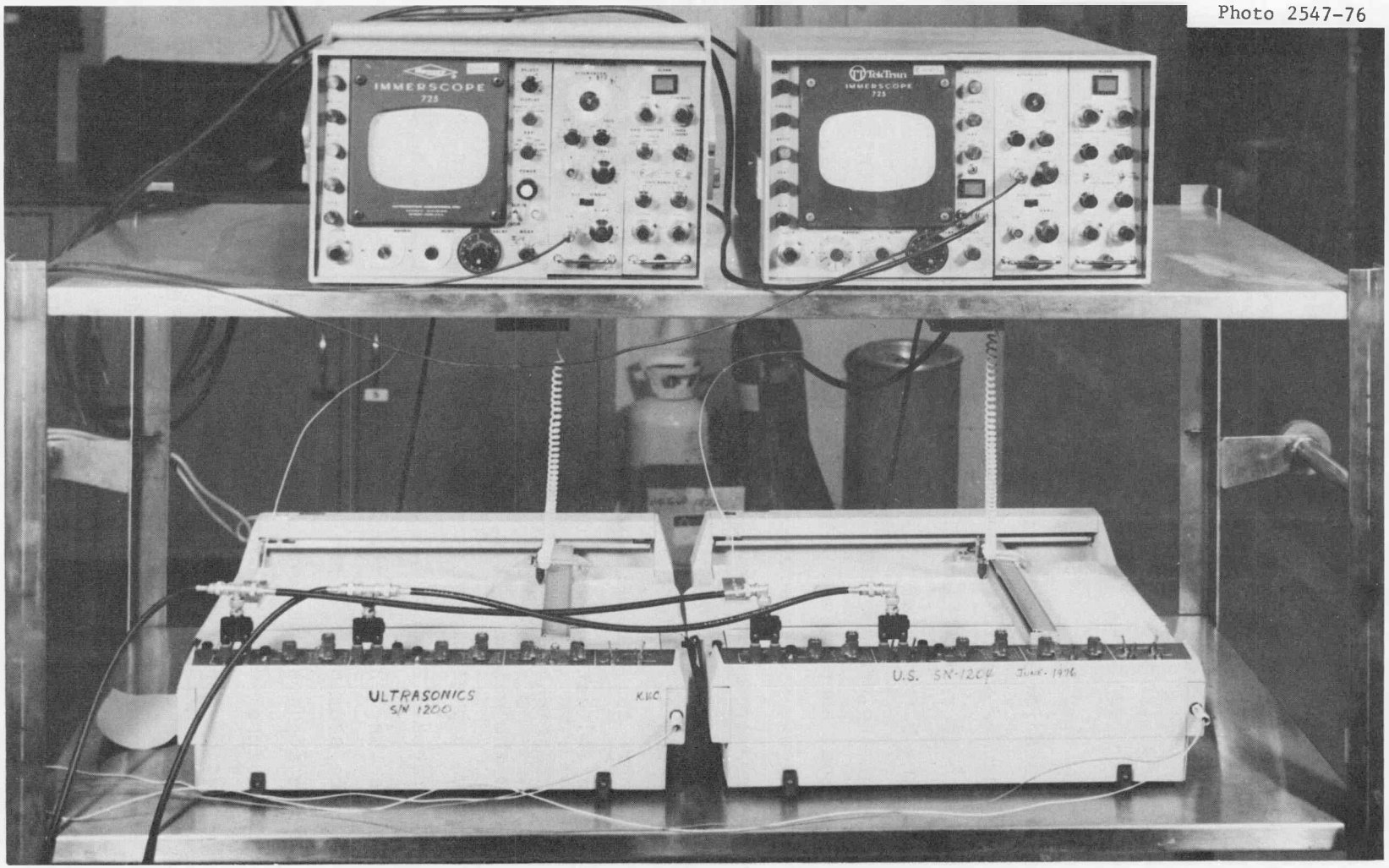

Fig. 1.45. Ultrasonic Electronic System Used to Record Data on a ("C" Scan) Plan View.

of the ultrasonic data. Figure 1.46 is a plan-view recording of the ultrasonic data for the outer- and inner-surface channels, respectively. The long black lines at the beginning of each recording are the responses from the end of the tube section and are representative of a discontinuity extending completely through the wall for one complete rotation. The notch response is evident with the indication farthest from the end of the tube in each figure being the smallest [0.2 mm long by 3.1 mm deep (0.008 × 0.125 in.)]. The other two specimens in Fig. 1.44(b) and (c) are T/T AI weldment specimens. The specimen shown in Fig. 1.44(b) is described later and is used for a preliminary weldment reference. One of the outer-surface EDM notches within the weldment can be seen. The eight T/T specimens had bore restrictions at the weldment (weld sag) that prevented insertion of the 9.8-mm-diam (0.386-in.) ultrasonic probe. These specimens were bore machined and reradiographed prior to ultrasonic testing.

The two best samples, as determined by radiography, were scanned with the ultrasonic system setup at a sensitivity calibrated with 0.2 mm deep by 3.1 mm long (0.008 × 0.125 in.) reference notches in tubing. This size notch represents approximately 7% of wall sensitivity in tubing, but detection in the tube does not necessarily imply detection in the weld where the attenuation is a variable. Both weldments were scanned and no indications were detected in the weldment area; however, gouge-like indications were detected in one tube section about 12.7 mm (0.5 in.) from the weldment [Fig. 1.44(b)]. This particular specimen was selected as a preliminary standard and notches placed on the outer and inner surfaces. The notches are approximately 10% of the wall and were placed in the center of the weld and on each side of the weldment within the tube sections. A preliminary setup and inspection detected all six of the notches. However, we determined with further scanning that the three inner-surface notches were not detectable when placed in a certain rotational position. Further testing indicated that the problem is mechanical in nature. This particular T/T weldment has a nominal inner diameter of 10.2 mm (0.404 in.); whereas, our standard tube has a nominal diameter of about 0.254 mm (0.010 in.) less. Hence, the spring-loaded ball plungers had to be reset to compensate for the test desensitization

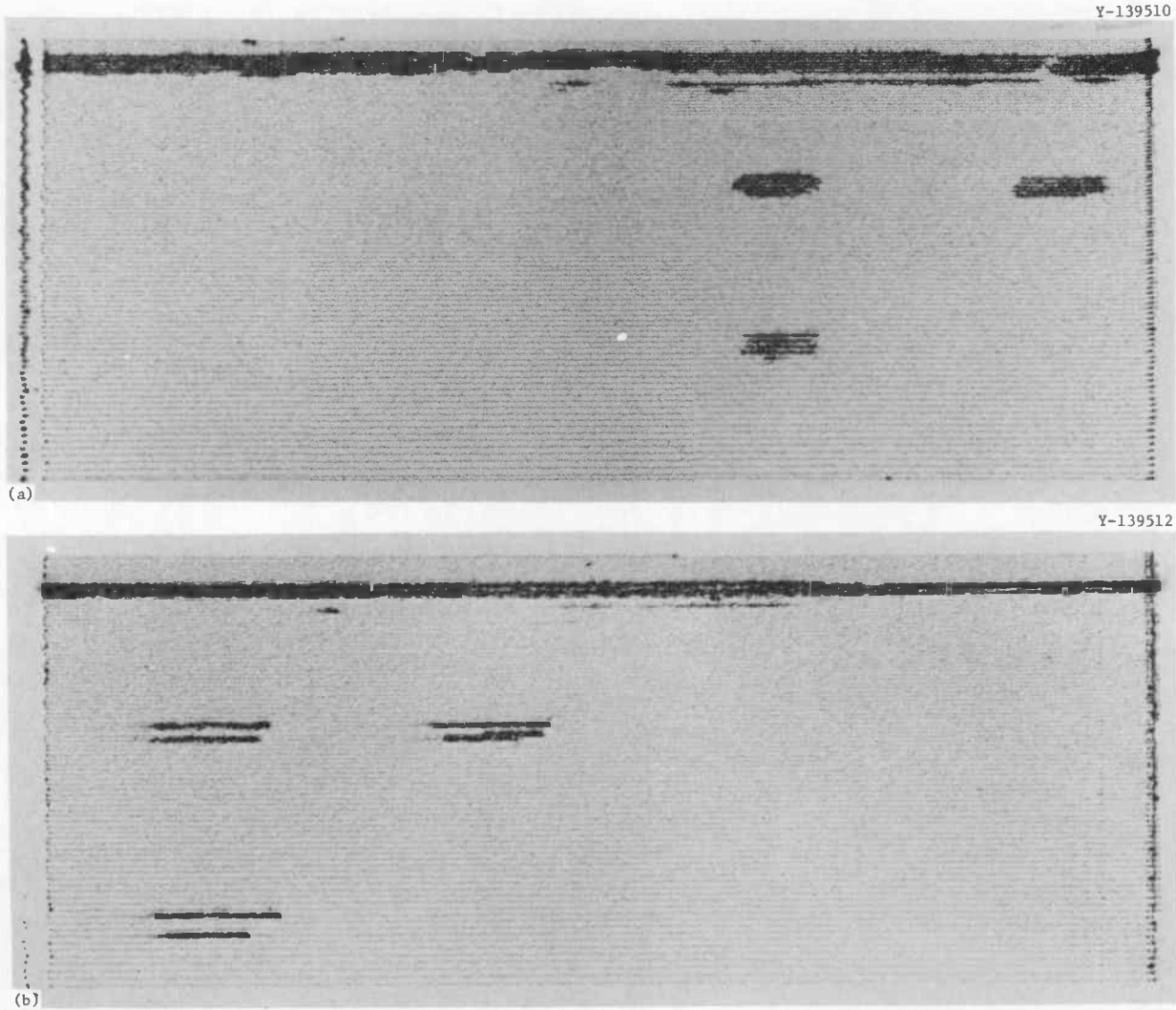

Fig. 1.46. Plan View Recording of Ultrasonic Flaw Response Channel for the Ultrasonic Tube Standard. The long black line represents the end of the tube. The notch response is evident with the indication furthest from the end of the tube being the smallest [0.2 mm deep × 3.1 mm long (0.008 × 0.125 in.)]. 2 1/2×. (a) Outer surface. (b) Inner surface.

due to the mechanical probe instability. This adjustment corrected part of the problem; however, the sensitivity is as yet not completely uniform. We feel that the system is adequate for these preliminary joints and that correction methods are available to upgrade the system later on true prototypic T/TS weld samples.

Figure 1.47 shows representative plan-view recordings of the ultrasonic data for outer- and inner-surface inspections, respectively. Results for the outer-surface channel are extremely good; however, some indications other than the end of the specimen and the three reference notches are evident for the inner-surface inspection [Fig. 1.47(b)]. Many of these indications are located in the tube sections, which indicates that they may be due to inner-surface roughness. The inner surface does appear to have gouge-like and/or machined marks of considerable depth. Similar indications were detected in the other seven specimens that have been machine bored. Approximately half of the specimens had indications in the weld zone but further evaluation is continuing since surface roughness or residual probe misalignment may have contributed to the signals. Current results indicate that a small loss in sensitivity occurs for both ultrasonic test channels when inspecting for discontinuities within or behind the weldment. This loss in sensitivity appears to be rather small and is not as evident in this particular weldment as we might have expected. Further study is necessary before sensitivity levels can be established; however, preliminary results indicate that a sensitivity to notches with depths equivalent to 10% of the wall thickness is realistic.

Six pieces of type 304 stainless steel tubes 22.2-mm-OD by 1.19-mm wall (0.875 × 0.047 in.) have been nondestructively evaluated at the request of ERDA. These tubes are similar to those used in the IHX of the FFTF reactor and were fabricated for Babcock and Wilcox by the Pacific Tube Company. These tubes are part of the commitment by ERDA to the US/USSR steam generator information exchange program. Examinations performed included resonance ultrasonic wall thickness measurements, fluorescent dye penetrant, and ultrasonic flaw detection for longitudinally and transversely oriented flaws (each ultrasonic flaw examination was

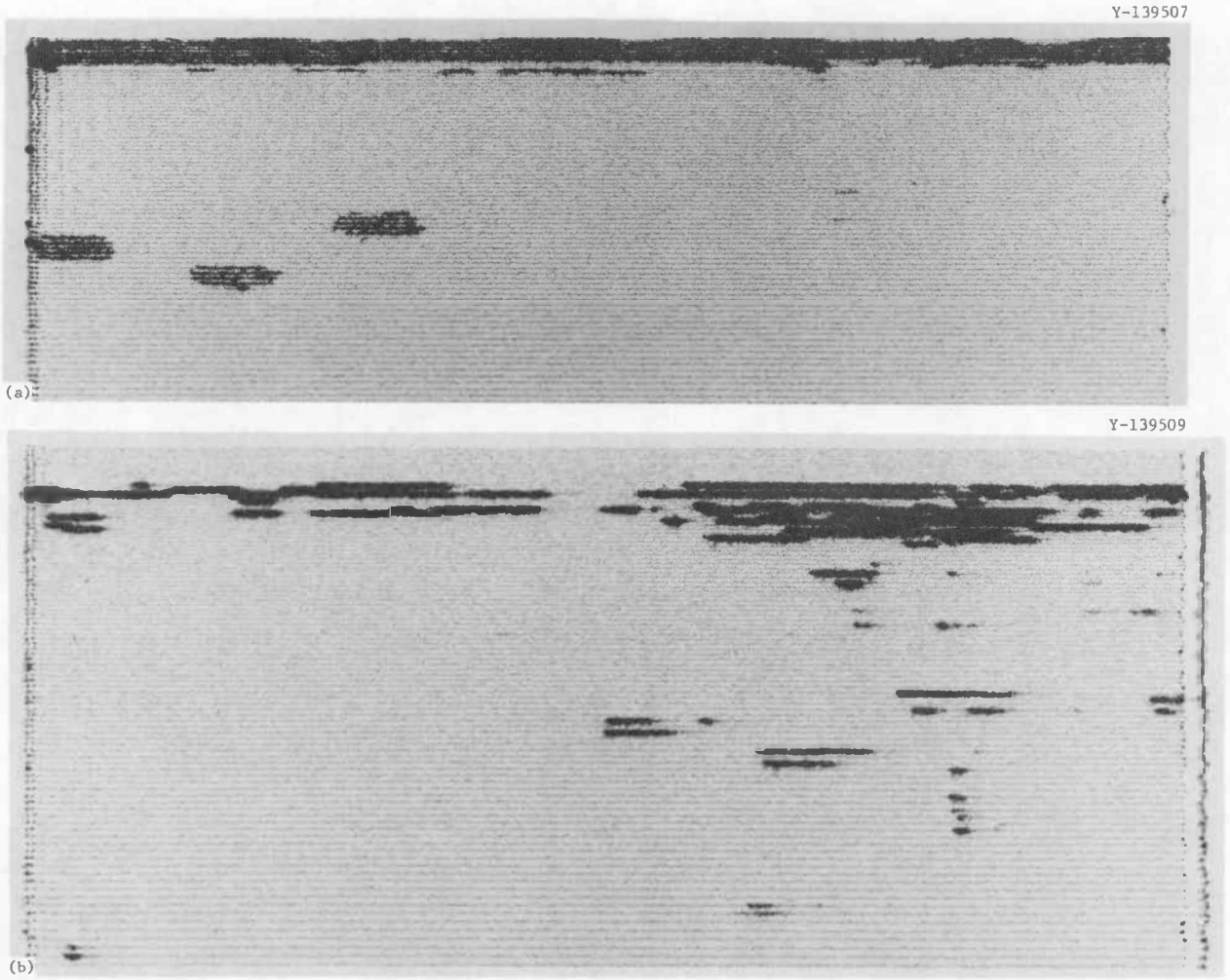

Fig. 1.47. Plan View Recording of the Ultrasonic Flaw Response Channel for the Weld Sample Shown in Fig. 1.44(b). The long black line represents the end of the tube section. (a) Outer surface. The notch response is evident with the indication nearest the end of the tube being the notch which requires examination through the most weldment material. (b) Inner surface. The response for the three 0.28-mm deep × 3.1-mm-long (0.011 × 0.125-in.) notches is the three approximately equal size indications near the center of the right-hand portion of the recording.

performed in two different directions). All of the nondestructive test methods applied to the tubing met or exceeded the previous examination requirements for the tubing procurement, and the tubing was acceptable despite the more stringent inspection. Documentation on the examination methods and results were shipped to Russia along with the tubing in accordance with instructions from ERDA.

1.6 TRANSITION JOINTS

1.6.1 Welding Development — J. F. King

The hot-wire gas tungsten-arc welding process was added to the Welding and Brazing Laboratory this quarter to support the CRBR transition joint program. The low weld dilution rates possible with this process have made it attractive for use on the dissimilar metal joints now under development. All future weld metal deposits for transition joint mechanical property determinations will be made with this process, as will welding procedure development.

The welding equipment shown in Fig. 1.48 comprises the commercially available components that have been obtained for the transition joint

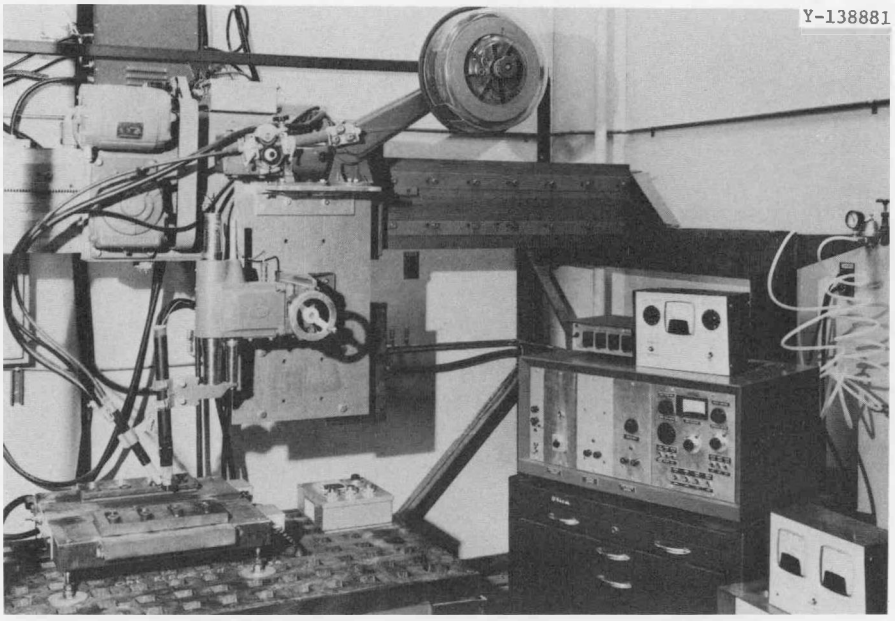

Fig. 1.48. Hot-Wire Gas Tungsten-Arc Welding Equipment for CRBR Transition Joint Welding Development.

welding program. It includes the automatic voltage head, controls, hot wire torch, gas tungsten-arc torch, and two power supplies (not shown). Modifications have been made toward fully automating the process and improving its operating characteristics. A welding head oscillator will be added to complete the welding system. During this period of welding equipment procurement and installation, work continued on making weldments needed for mechanical properties testing. These were made by the cold-wire gas tungsten-arc process and included specimens for all-weld-metal and transverse weld property tests.

1.6.2 Mechanical Properties of Transition Weld Joint Materials

1.6.2.1 Creep Properties — R. L. Klueh and J. F. King

Last quarter[50] we reported on creep-rupture tests on Inconel 82 weld metal at 454, 510, and 566°C (850, 950, and 1050°F). Several more tests were completed at these temperatures, and the data for all completed tests and those in progress are given in Table 1.18. Examination of the data reveals several premature failures at each temperature. As stated last quarter, the reason for such failures is being investigated.

In Fig. 1.49 the creep-rupture curves are given at 454, 510, and 566°C, while Fig. 1.50 shows the stress as a function of minimum creep rate at these temperatures. For both figures the results from the tests that failed prematurely have not been plotted.

During this quarter, several tests were started at 621 and 677°C (1150 and 1250°F). The first results from these tests will be reported next quarter. We have also made a weld from which specimens will be obtained to make creep-rupture tests at 732°C (1350°F).

1.6.2.2 Fatigue Behavior of Transition Joint Materials — J. P. Strizak

Collection of fatigue and creep-fatigue data on Inconel 82 filler metal has begun in support of the LMFBR transition joint technology needs and development program. All-weld-metal specimens were made from large deposits of Inconel 82 filler metal with 19-mm-thick (3/4 in.) 2 1/4 Cr-1 Mo steel plates as a base metal. The plates were prepared

Table 1.18. Creep-Rupture Properties of Inconel 82 Weld Metal

Stress (MPa)	Stress (ksi)	Rupture Life (hr)	Total Elongation (%)	Reduction of Area (%)	Minimum Creep Rate (%/hr)
	Tests at 454°C (850°F) on Welds in 19-mm (3/4-in.) Plate				
414	60	[a]			
434	63	[a]			
455	66	[b]			0.000160
483	70	[c]			0.000273
483	70	68.1	37.0	54.2	0.00769
483	70	75.1	33.4	50.5	0.0187
496	72	1012.6	36.0	38.5	0.000769
510	74	142.3	40.2	52.5	0.013
517	75	3.2	33.7	53.0	0.125
	Tests at 510°C (950°F) on Welds in 13-mm (1/2-in.) Plate				
379	55	[a]			0.000012
396	57.5	[b]			0.0000195
414	60	1645.4	23.6	19.7	0.000463
434	63	1205.1	33.7	29.3	0.000536
448	65	357.1	39.1	35.9	0.00459
455	66	4.0	40.4	39.0	0.150
455	66	39.4	38.7	42.9	0.138
465	67.5	37.1	48.4	51.8	0.209
483	70	10.9	48.4	53.7	0.395
	Tests at 566°C (1050°F) on Welds in 13-mm (1/2-in.) Plate				
328	47.5	[b]			0.0000149
345	50	778.8	14.5	15.6	0.000324
345	50	[a]			0.000031
365	53	1087.5	17.2	18.2	0.000611
379	55	841.1	18.9	18.9	0.00105
396	57.5[d]	448.2	21.4	19.6	0.00280
396	57.5[d]	124.6	21.9		0.0652
396	57.5[d]	63.8	22.2		0.133
414	60	112.8	29.7	27.4	0.0331
434	63	29.5	37.6	36.8	0.231

[a] Test in progress.

[b] Test discontinued before rupture.

[c] Temperature overshot and test failed after 2430 hr.

[d] Tests made on 19-mm (3/4-in.) plates.

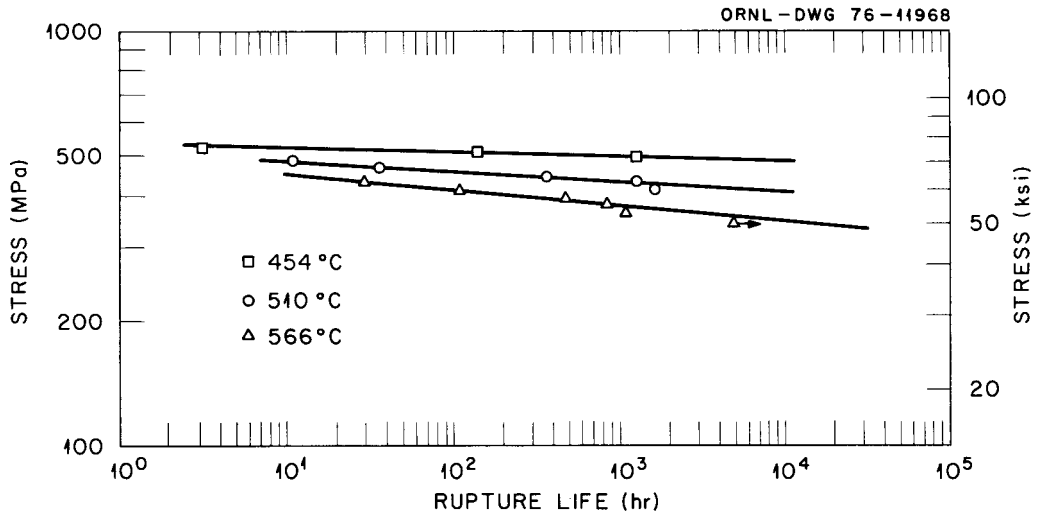

Fig. 1.49. Creep-Rupture Curves for Inconel 82 Weld Metal at 454, 510, and 566°C.

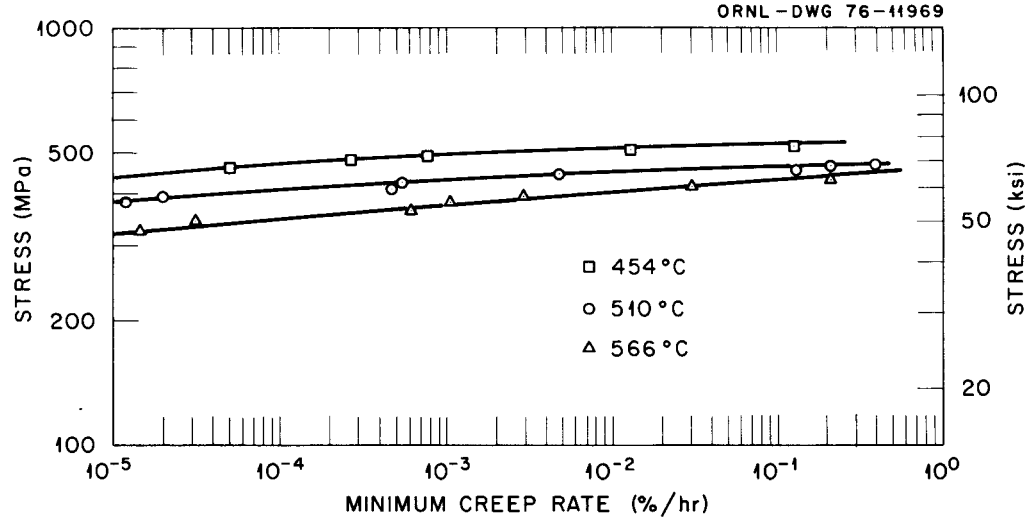

Fig. 1.50. Stress as a Function of Minimum Creep Rate for Inconel 82 Weld Metal at 454, 510, and 566°C.

with a 30°-included-angle V-groove joint geometry with a 32 mm (1 1/4 in.) root opening and a backing strip. Weld deposits were made by the automatic gas tungsten-arc welding process with cold wire filler additions. The welds were stress relieved at 732°C (1350°F) for 1 hr.

Uniform-gage fatigue specimens, 6.35-mm-diam (0.250 in.) by 10.16-mm-long (0.400 in.) gage section, were fabricated with the specimen taken from the center of the weld thickness with its longitudinal axis transverse to the weld direction. The specimens were inspected radiographically, and sound (free from porosity defects) specimens and specimens with defects were identified.

Continuous cycling and creep-fatigue fully reversed strain-controlled tests were conducted on a electrohydraulic closed loop fatigue testing system employing an axial extensometer. Specimens were heated by induction in air. Thermocouples were spot welded to the specimens some distance from the gage area for temperature control and monitoring.

Results of continuous cycling strain-controlled fatigue tests at 538°C (1000°F) are shown in Fig. 1.51. All tests were conducted at a constant strain rate of 4×10^{-3}/sec with a triangular waveform as shown in Fig. 1.52. Comparison of Inconel 82 weld metal with transition weld joint base materials (type 316 stainless steel and 2 1/4 Cr-1 Mo steel) showed that the fatigue behavior of Inconel 82 weld metal was similar to that of the base metals in the low-cycle region. However, Inconel 82 exhibited superior fatigue resistance in the high-cycle region.

In addition to continuous cycling tests, several tests involving hold periods introduced each cycle at peak strain amplitudes (see Fig. 1.52) have been conducted to date to determine the influence of creep-fatigue on the failure behavior of Inconel 82. Results of tests with tensile and compressive strain hold periods of 0.1 hr are shown in Fig. 1.53. Generally, the reduction in fatigue life increased as strain range was decreased. Tests are continuing to determine the most detrimental type of hold period (tensile, compressive, or both) and the influence of increasing hold time on the creep-fatigue behavior of Inconel 82.

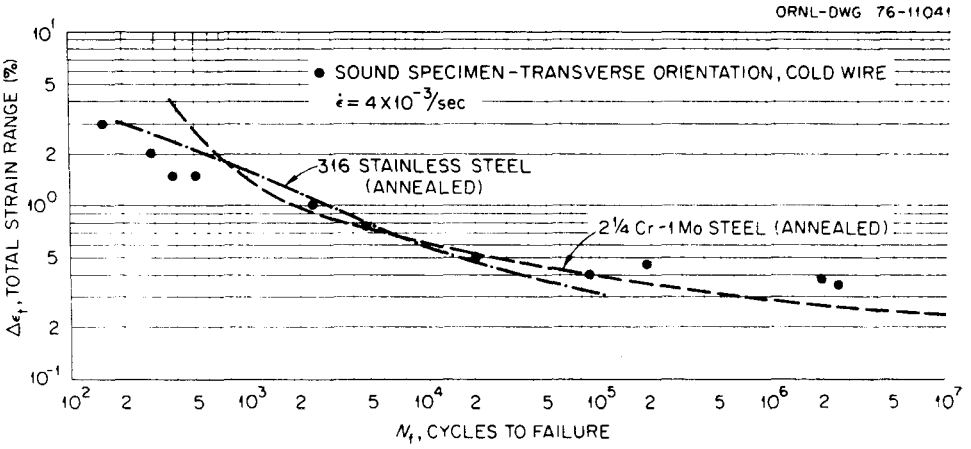

Fig. 1.51. Comparison of the Fatigue Behavior of Inconel 82 Weld Metal with Other Transition Weld Joint Materials at 538°C (1000°F). The type 316 stainless steel curve is for 566°C (1050°F).

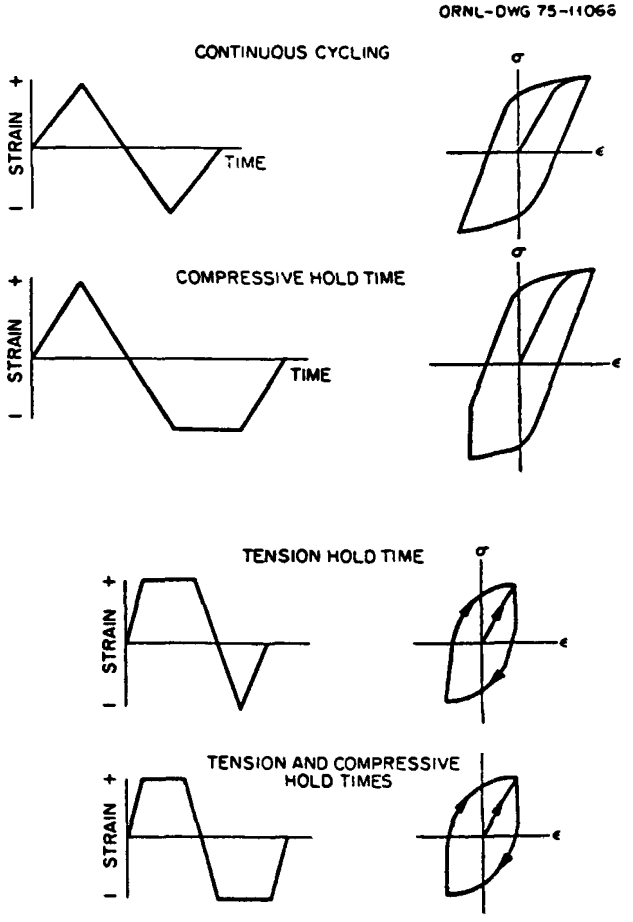

Fig. 1.52. Strain-Time Wave Forms and Associated Stress-Strain Hysteresis Loops for Fatigue and Creep-Fatigue Tests.

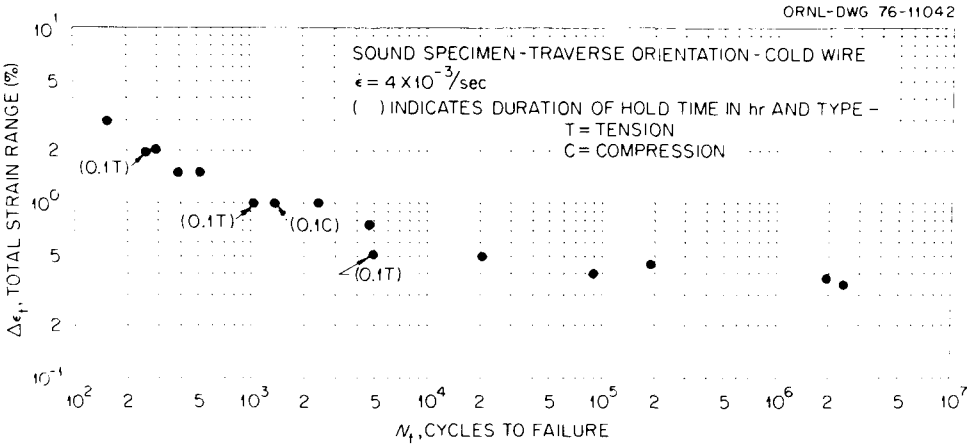

Fig. 1.53. Effect of Hold Periods on the Fatigue Behavior Inconel 82 Weld Metal at 538°C (1000°F).

Several continuous cycling tests at 538°C (1000°F) were repeated with specimens with defects (porosity). Estimates made from radiographic negatives indicated that the pore sizes in the specimens ranged from 0.3 to 0.7 mm (0.012–0.028 in.) in diameter. As shown in Fig. 1.54 fatigue lives were reduced by 80–90% at the elevated temperature. Ishii[51] has shown that porosity up to 5% had little effect on the room-temperature fatigue behavior of mild steel. However, Buchanan and Young[52] showed that in 2 1/4 Cr-1 Mo steel welds at 649°C (1200°F), 5–8 vol % porosity could reduce fatigue life by 98%.

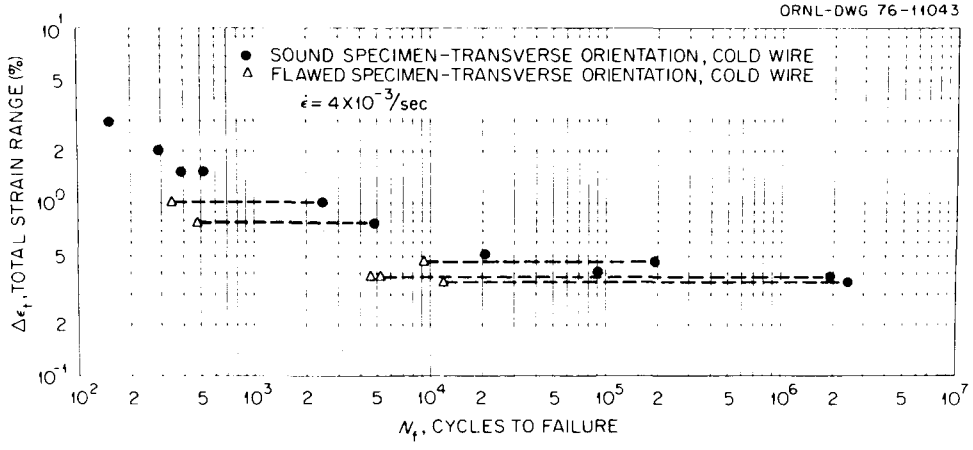

Fig. 1.54. Effect of Material Defects on the Fatigue Behavior of Inconel 82 Weld Metal.

1.6.3 Transition Joints — J. H. Smith

Efforts are continuing to develop ultrasonic inspection techniques for dissimilar metal transition welded joints with emphasis on the base metal—weld metal interface joints.

Six weld samples have been received from GE in San Jose for NDT evaluation. We have four samples of Alloy 800 welded to type 316 stainless steel using 16-8-2 weld wire and a hot-wire gas tungsten arc welding technique. These samples are not prototypic because the root opening [4.762 mm (0.187 in.)] is not the final accepted value [12.70 mm (0.50 in.)]. We also received two weld samples of 2 1/4 Cr-1 Mo welded to Alloy 800 using Inconel 82 weld wire and a hot wire gas tungsten arc welding technique. These samples are supposed to be prototypic. None of the six weld samples received a postweld heat treatment.

Shear and longitudinal wave velocity measurements have been made in three perpendicular directions on samples of each of the base metals used in the transition joint (2 1/4 Cr-1 Mo, Alloy 800, and type 316 stainless steel). No significant directional differences were detected. The base materials appear to be isotropic as far as longitudinal and shear ultrasonic velocities are concerned (for the samples investigated).

Shear and longitudinal wave velocity measurements were made on a sample of Inconel 82 weld metal. A distinct polarization effect has been noted for the shear wave velocity. Two different velocities can be measured depending on whether the particle vibration is parallel or perpendicular to the primary axis of the basic dendritic cell structure in the weld. The two shear wave velocities obtained in the sample examined (a hot wire GTA weld) were 2.97 and 3.73×10^5 cm/sec. No measurements have been made to check the isotropic behavior of the 16-8-2 weld at this time, but a sample is being prepared and measurements will be made as soon as the sample is available. This weldment does have a dendritic cellular structure, therefore a similar anisotropic behavior is expected.

Initial investigations have shown that the Alloy 800 base metal is more attenuative to acoustical energy propagation than either type 316 stainless steel or 2 1/4 Cr-1 Mo. The material also appears to be more nonuniform from sample to sample. Both weldments, 16-8-2 and Inconel 82,

have higher, variable attenuation to sound propagation than either of the base metals. Measurements are being made and it is hoped that number values can be placed on the amounts of attenuation for each material in the near future.

J. H. Smith and R. W. McClung attended the quarterly meeting on the nondestructive evaluation of transition joints held at General Electric Company in San Jose on April 29, 1976. The decision was made that both GE and ORNL will concentrate immediate efforts toward developing an ultrasonic inspection method for smooth machined weld samples. This will eliminate difficulties with surface variations and geometrical reflectors that can be better resolved after the basic inspection technique has been defined.

Emphasis will continue to be placed on the weld metal fusion line (base/weld interface). It has also been determined that conventional ultrasonic weld inspection techniques will not suffice to evaluate the welds and weld interfaces in the steam generator transition joints. We are investigating the use of other approaches, such as the use of longitudinal refracted waves for this inspection. Two weld samples of joint type (2 1/4 Cr-1 Mo/Inconel 82/Inconel 800) have been ground flat and parallel and preliminary investigations have been made using dual crystal, 2 1/4 MHz refracted longitudinal waves. Initial results show that a 2.16-mm-deep (0.085 in.) notch in the Alloy 800 material can be detected through the Inconel 82 weld with sound entering on the 2 1/4 Cr-1 Mo side. These tests were conducted in an immersion setup using water as a couplant. Figure 1.55 shows a copy of the "C" scan recording showing a two-dimensional map of the three-dimensional weld sample. Dark indications are areas that reflect sound. Reflections are obtained from the weldment and from reference reflectors of known size. The "C" scan recorder was set to record only signals exceeding approximately a 50% level on the oscilloscope trace. At this point nothing conclusive can be said about the comparison of relative amplitudes of signals reflected from the weldment and those reflected from the reference reflectors.

The ultrasonic signal reflected from the 2.16-mm-deep (0.085 in.) notch is not proportioned to the size of the notch. It is reduced considerably due to attenuation of sound in the weld metal (when compared with

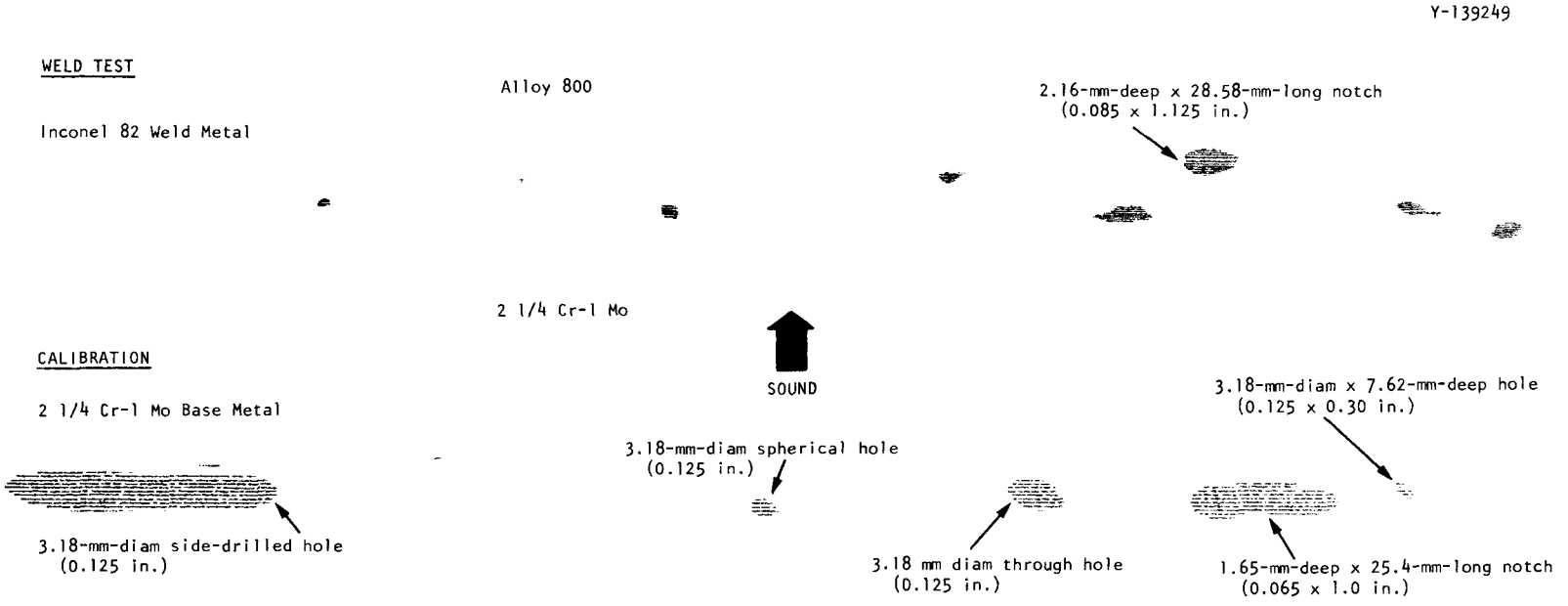

Fig. 1.55. Ultrasonic "C" Scan Recording of Inconel 82 Weld and Calibration Standard.

the size of signal from a notch in the base metal), but the notch is readily detectable. We are also investigating the phase shift of ultrasonic signals in these welds. Since definite phase shifts occur at most discontinuities, it is hoped that this technique can be used to discriminate between flaws and microstructural changes at the interface between the base metal and weldment in the transition joint welds. Further discussion of these studies is provided in the last section of this chapter.

J. H. Smith and R. W. McClung attended a meeting at the CRBRP office in Oak Ridge where a general review was made of the Transition Joint Program. Representatives from ORNL, GE, and ERDA attended the meeting.

1.7 REFERENCES

1. J. C. Griess, J. H. DeVan, and W. A. Maxwell, *The Effect of a High Heat Flux on the Corrosion of 2 1/4 Cr-1 Mo Steel in Superheated Steam*, ORNL-TM-5551 (in press).
2. J. C. Griess, J. H. DeVan, and W. A. Maxwell, *LMFBR Materials Development Program Quart. Prog. Rep. March 31, 1976*, ORNL-5157, pp. 1–5.
3. A. J. Moorhead, "Tube to Tubesheet Welding Development," *LMFBR Materials Development Program Quart. Prog. Rep. March 31, 1976*, ORNL-5157, pp. 5–10.
4. A. J. Moorhead, "Tube to Tubesheet Welding Development," *Steam Generator Materials Technology Program Quart. Progr. Rep. March 31, 1975*, ORNL-TM-4969, pp. 14–17.
5. A. J. Moorhead, "Tube to Tubesheet Welding Development," *LMFBR Materials Development Program Quart. Progr. Rep. Sept. 30, 1975*, ORNL-5117, pp. 12–16.
6. Ibid., *Dec. 31, 1975*, ORNL-5131, pp. 7–10.
7. R. L. Klueh, "Creep-Rupture Properties of 2 1/4 Cr-1 Mo Steel," *Mechanical Properties Test Data for Structural Materials Quart. Prog. Rep. Oct. 31, 1975*, ORNL-5107, pp. 141–54.
8. Ibid., *Apr. 30, 1976*, ORNL-5150, pp. 148–51.
9. F. Garofalo et al., "Creep and Creep-Rupture Relationships in an Austenitic Stainless Steel," *Trans. AIME* 221: 310–19 (1961).

10. W. E. Leyda and J. P. Rowe, *A Study of Time for Departure from Secondary Creep for Eighteen Steels*, ASM Technical Report P9-6.1, American Society for Metals, Metals Park, Ohio, 1969.

11. R. L. Klueh, "The Relationship Between Rupture Life and Creep Properties of 2 1/4 Cr-1 Mo Steel," *Nucl. Technol.* 26: 287–96 (1975).

12. M. K. Booker and V. K. Sikka, *Interrelationships Between Creep Life Criteria for Four Nuclear Structural Materials*, ORNL/TM-4997 (August 1975).

13. R. L. Klueh, "Heat-to-Heat Variation of 2 1/4 Cr-1 Mo Steel," *Mechanical Properties Test Data for Structural Materials Quart. Prog. Rep. July 31, 1975*, ORNL-5106, pp. 131–44.

14. R. L. Klueh, "Heat-to-Heat Variations of 2 1/4 Cr-1 Mo Steel," *Mechanical Properties Test Data for Structural Materials Quart. Prog. Rep. Jan. 31, 1976*, ORNL-5112, pp. 92–101.

15. R. L. Klueh, *Heat Treatment Effects on the Tensile Properties of Annealed 2 1/4 Cr-1 Mo Steel*, ORNL-5144 (May 1976).

16. R. J. Beaver, B. C. Leslie, and G. M. Slaughter, "2 1/4 Cr-1 Mo Steel Tubesheet Forging Development and Characterization," *Fuels and Materials Development Program Quart. Prog. Rep. June 30, 1974*, ORNL-TM-4688, pp. 29–35.

17. R. G. Baker and J. Nutting, "The Tempering of 2 1/4 Cr-1 Mo Steel After Quenching and Normalizing," *J. Iron Steel Inst.* 192: 257–68 (1959).

18. K. F. Hale, "Study of Creep in a Chromium-Molybdenum Steel," *Proc. 4th Intern. Conf. Electron Microscopy*, Vol. 1, 650–58, Springer-Verlag, Berlin, 1960.

19. M. C. Murphy and G. D. Branch, "Metallurgical Changes in 2.25 CrMo Steels During Creep-Rupture Test," *J. Iron Steel Inst.* 209: 546–61 (1971).

20. G. V. Smith, *Supplemental Report on the Elevated-Temperature Properties of Chromium-Molybdenum Steels (An Evaluation of 2 1/4 Cr-1 Mo Steel), ASTM Data Ser. Publ.*, DS 6 S2, American Society for Testing and Materials, Philadelphia, March 1971.

21. E. B. Norris, G. J. Schnabel, and R. D. Wylie, "Properties of Cr-Mo Piping Materials After Service at 1000°F and 1050°F," paper presented at International Conference on Creep and Fatigue in Elevated Temperature Applications, Philadelphia, 1973 and Sheffield, U.K., April 1974.

22. R. H. Hiltz and L. H. Kirschler, *MSAR Evaluation of Candidate Ferritic Alloys for LMFBR Service*, MSAR-69-139, Mine Safety Appliance Research Corp. (July 1969).

23. L. H. Kirschler, R. H. Hiltz, and S. J. Rodgers, *Effect of High Temperature Sodium on the Mechanical Properties of Candidate Alloys for the LMFBR Program*, MSAR-70-76, Mine Safety Appliance Research Corp. (May 1970).

24. R. H. Hiltz, L. H. Kirschler, and R. C. Andrews, *Tensile Strengths of Standard 2 1/4 Cr-1 Mo Steel After 20,000-Hour Exposure in 1050F Sodium*, MSAR-71-78, Mine Safety Appliance Research Corp. (April 1971).

25. R. H. Hiltz, L. H. Kirschler, and R. C. Andrews, *Tensile Strengths of Standard 2 1/4 Cr-1 Mo Steel After 10,000, 20,000, and 26,500 Hour Exposures in 1050F Sodium*, MSAR-72-286, Mine Safety Appliance Research Corp. (December 1972).

26. R. L. Klueh and J. M. Leitnaker, "An Analysis of the Decarburization and Aging Processes in 2 1/4 Cr-1 Mo Steel," *Metall. Trans.* 6A: 2089–93 (1975).

27. J. M. Leitnaker, R. L. Klueh, and W. R. Laing, "The Composition of Eta-Carbide Phase in 2 1/4 Cr-1 Mo Steel," *Metall. Trans.* 6A: 1949–55 (1975).

28. M. K. Booker, "Time-Dependent Fatigue — Estimates of Worst Effects," *Mechanical Properties Test Data for Structural Materials Quart. Prog. Rep. April 30, 1976*, ORNL-5150, pp. 158–64.

29. J. H. Gittus, "Implications of Some Data on Relaxation Creep in Nimonic 80A," *Phil. Mag.* 9: 749 (1964).

30. M. K. Booker, B.L.P. Booker, J. P. Strizak, and C. R. Brinkman, "Cyclic Stress-Strain Behavior of Isothermally Annealed 2 1/4 Cr-1 Mo Steel," to be presented at Second International Conference on Mechanical Behavior of Materials, Boston, Aug. 16–20, 1976.

31. J. R. Ellis et al., "Elevated-Temperature Fatigue and Creep-Fatigue Properties of Annealed 2 1/4 Cr-1 Mo Steel," pp. 213–46 in *Structural Materials for Service at Elevated Temperatures in Nuclear Power Generation*, MPC-1, A. O. Schaefer, ed., American Society of Mechanical Engineers, New York, 1975.

32. C. E. Pugh et al., *Background Information for Interim Methods of Inelastic Analysis for High-Temperature Reactor Components of 2 1/4 Cr-1 Mo Steel*, ORNL/TM-5226 (May 1976).

33. M. K. Booker, "Fatigue Curve Development," *Mechanical Properties Test Data for Structural Materials Quart. Prog. Rep. Jan. 31, 1976*, ORNL-5112, pp. 101–03.

34. S. S. Manson, "The Challenge to Unify Treatment of High Temperature Fatigue — A Partisan Proposal Based on Strain-Range Partitioning," pp. 744–75 in *Fatigue at Elevated Temperatures*, ASTM STP 520, A. E. Carden, A. J. McEvily, and C. H. Wells, eds., American Society for Testing and Materials, Philadelphia, 1972.

35. S. S. Manson, G. R. Halford, and M. H. Hirschberg, *Creep-Fatigue Analysis by Strain-Range Partitioning*, NASA-TM-X-67838 (1971).

36. M. K. Booker, "Creep-Fatigue Data Analysis," *Mechanical Properties Test Data for Structural Materials Quart. Prog. Rep. April 30, 1975*, ORNL-5105, pp. 215–21.

37. Ibid., *July 31, 1975*, ORNL-5106, pp. 144–47.

38. Ibid., *Oct. 31, 1975*, ORNL-5107, pp. 154–58.

39. R. D. Campbell, "Creep Fatigue Interaction Correlation for 304 Stainless Steel Subjected to Strain-Controlled Cycling with Hold Times at Peak Strain," *J. Eng. Ind.* 93: 887–92 (1971).

40. M. H. Hirschberg and G. R. Halford, *Use of Strain-Range Partitioning to Predict High-Temperature Low-Cycle Fatigue Life*, NASA TN D-8072 (January 1976).

41. C. R. Brinkman, M. K. Booker, J. P. Strizak, W. R. Corwin, J. L. Frazier, and J. M. Leitnaker, *Interim Report on the Continuous Cycling Elevated-Temperature Fatigue and Subcritical Crack Growth Behavior of 2 1/4 Cr-1 Mo Steel*, ORNL-TM-4993 (December 1975).

42. M. K. Booker, D. O. Hobson, T. L. Hebble, and C. R. Brinkman, *Mechanical Property Correlations for 2 1/4 Cr-1 Mo Steel in Support of Nuclear Reactor Systems Design*, ORNL/TM-5329 (June 1976). To be published in *International Journal of Pressure Vessels and Piping*.

43. "Case 1592," pp. 327–442 in *1974 Code Cases (ASME Boiler and Pressure Vessel Code)*, American Society for Mechanical Engineers, New York, 1974.

44. D. R. Diercks, "The Application of Strain-Range Partitioning to the Prediction of Elevated-Temperature, Low-Cycle Fatigue Life for Type 304 Stainless Steel," pp. 29–38 in *Advances in Design for Elevated Temperature Environment*, S. Y. Zamrik and R. I. Jetter, eds., American Society of Mechanical Engineers, New York, 1975.

45. S. Majumdar and P. S. Maiya, *A Unified and Mechanistic Approach to Creep-Fatigue Damage*, MS-1843 (Rev. 2), Argonne National Laboratory (September 1975).

46. L. A. James, "Some Questions Regarding the Interaction of Creep and Fatigue," ASME Paper 75-WA/Mat-6, to be published in *Journal of Engineering Materials and Technology*.

47. D. N. Robinson, *A Candidate Creep-Recovery Model for 2 1/4 Cr-1 Mo Steel and Its Experimental Implementation*, ORNL-TM-5110 (October 1975).

48. J. P. Hammond, ORNL, private communication, May 1976.

49. B. E. Foster, "Penetrating Radiation," *LMFBR Materials Development Program Quart. Prog. Rep. March 31, 1976*, ORNL-5157, pp. 39–45.

50. R. L. Klueh and J. F. King, "Mechanical Properties of Transition Weld Joint Materials," *Mechanical Properties Test Data for Structural Materials Quart. Prog. Rep. April 30, 1976*, ORNL-5150, pp. 175–86.

51. Y. Ishii and K. Iida, "Low and Intermediate Cycle Fatigue Strength of Butt Welds Containing Defects," *J. Soc. Nondestr. Test. (Japan)* 18(10), (1969); IIW Document XII-560-69.

52. R. A. Buchanan and D. M. Young, "Effect of Porosity on Elevated Temperature Fatigue Properties of 2 1/4 Cr-1 Mo Steel Weldments," *Weld. J. (Miami)* 54(9): 296-s–301-s (September 1975).

2. ALTERNATE LMFBR STRUCTURAL MATERIALS*

2.1 INTRODUCTION

This work consists of advanced materials development at other sites under the overall direction of ORNL. Two such programs frequently contribute to this report:

1. Advanced Ferritic Alloys Development for LMFBR Steam Generators, under subcontract to C-E Power Systems, Combustion Engineering, Inc., Windsor, Connecticut.
2. Alloy 800 Development for Advanced Steam Generators, under subcontract to Westinghouse Electric Corp., Tampa Division, Tampa, Florida.

2.2 ADVANCED FERRITIC ALLOYS DEVELOPMENT FOR LMFBR STEAM GENERATORS — S. D. Harkness (Combustion Engineering)

2.2.1 Mechanical Property Evaluation — B. Chakravarti and G. Bodine, Jr.

2.2.1.1 Preferred Alloys

Room temperature and short time elevated temperature tensile data have been obtained for heats 3177 and 91887 after tempering for 1 hour at 1400°F (compositions shown in Table 1). The strength levels for these materials are nearly identical and are plotted in Figure 1, along with the tensile strength reported for Sumitoma's alloy HCM9M. Both CE developed alloys exhibit higher strength than HCM9M over the complete range of test temperatures.

2.2.1.2 Aging Studies

Impact test results for a number of heats have been obtained on samples aged for 2000 hours at 950°F. Table 2 lists the identity and composition of a series of 6 low nickel (0.10%) heats (9Cr - 1Mo) which were made to evaluate additions of Si, V, and Mn. These alloys all show 50 ft-lb temperatures below 10°F in the aged condition. The 50 ft-lb temperatures have experienced only minor shifts (5-10°F) to the

---

*Progress on work performed under 189a No. OH038.

TABLE 1
CHEMICAL COMPOSITIONS FOR HEATS 3177 & 91887 (WT. %)

HEAT No.	LOC	C	Mn	Si	S	P	Cr	Mo	V	W	Cb	Ti	Ni	N_2	Al	B	Zr	Cu	As	Sn	O_2	H_2	Cr EQU.
XA 3177	BOT	0.085	0.43	0.21	0.010	0.012	9.69	0.77	0.14	0.48	0.10	0.11	0.07	0.061	0.006						0.009		11.62
ESRXA 3177	TOP	0.087	0.44	0.17	0.010	0.012	9.50	0.78	0.14	0.48	0.11	0.04	0.08	0.066	0.011	<.001	<.001	0.11			0.010		10.16
ESRXA 3177	BOT	0.088	0.44	0.17	0.005	0.013	9.67	0.82	0.15	0.44	0.10	0.04	0.08	0.057	0.032	<.001	<.001	0.11			0.008		10.64

HEAT No.	LOC	C	Mn	Si	S	P	Cr	Mo	V	W	Cb	Ti	Ni	N_2	Al	Cu	B	Zr	Sb		O_2
91887	TOP	0.087	0.38	0.09	0.005	0.007	9.22	1.01	0.22	<.01	0.10	<.01	0.08	0.038		0.01	<0.001	<0.001			0.005
	BOT	0.083	0.39	0.12	0.004	0.007	9.09	0.99	0.21	<.01	0.11	<.01	0.09	0.037		0.02	<0.001	<0.001			0.005

Figure 1
TENSILE PROPERTIES AT ELEVATED TEMPERATURE

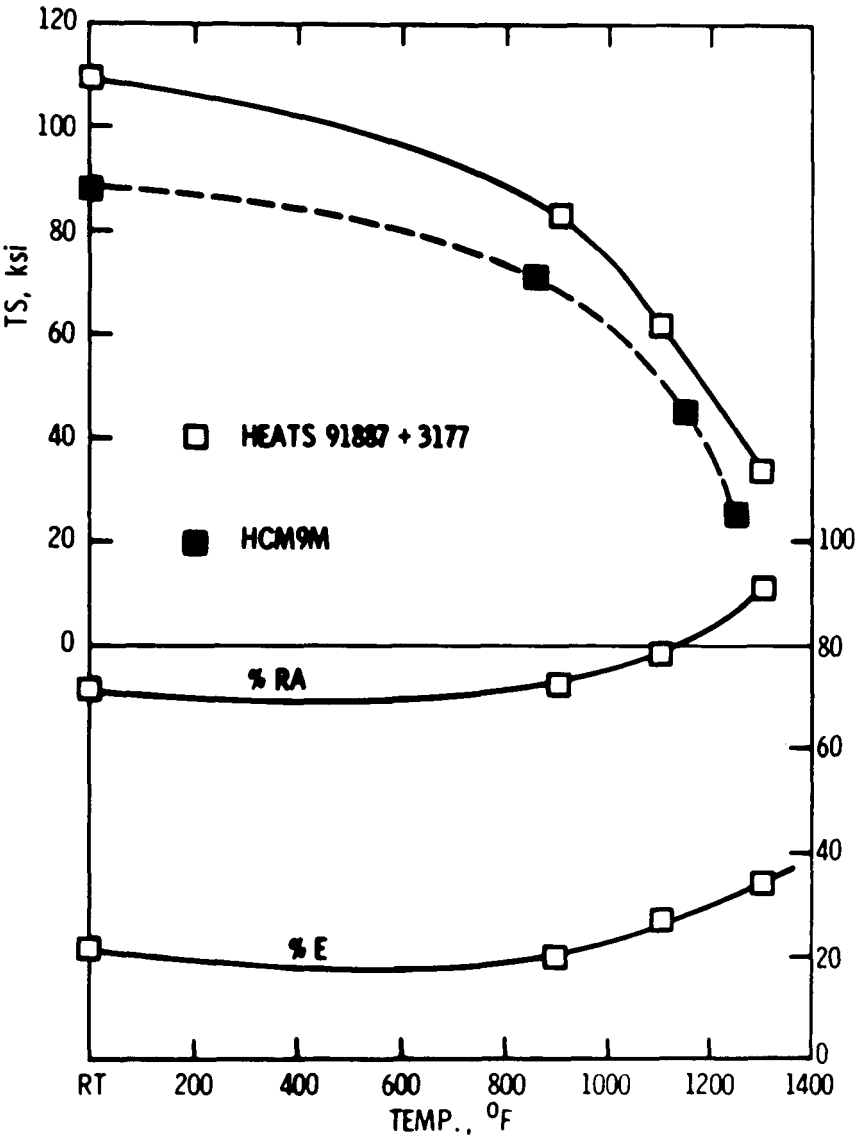

TABLE 2
CVN DATA FOR ALLOYS AGED FOR 2000 HRS AT 950°F
(9 Cr - 1 Mo - 0.10 Ni)

ESR No.	Si	V	MN	50 FT-LB TEMPERATURE	UPPER SHELF ENERGY
3180	0.15	0.25	0.45	- 10°F	112 FT-LBS
3182	0.14	0.26	0.48	10	124
3183	0.08	0.21	0.37	- 20	110
3184	0.08	0.20	0.50	- 45	135
3186	0.10	0.22	0.36	- 20	128
3187	0.06	0.21	0.32	- 45	118

right from their as-tempered values. In addition, these alloys all exhibit an upper energy shelf of at least 110 ft-lbs.

The upper energy shelf value for heat 91887 decreased on aging from 140 to 85 ft-lbs (Figure 2). Further, the 50 ft-lb temperature shifted to the right from a range of (-50/-20) to 94°F. This shift is not considered a serious problem in view of the minimum service temperature expected. However, more tests are required to ensure the stability of this composition with time and temperature.

2.2.2 Creep and Stress Rupture — B. Roberts

2.2.2.1 Preferred Alloy Results

Table 3 summarizes testing as of the end of June 1976. The CE developed alloy (heat 91887) is performing well based on initial short time results. Two tests on this material are compared to the Timken alloy (9Cr - 1Mo) in Figures 3 and 4. The results indicate higher strengths at both 1000 and 1100°F. At this writing, the 1000°F test is in progress and, based on a prediction for the onset of the third stage, should out-perform the Timken alloy.

In contrast to the performance of heat 91887, Sumitoma's recently announced HCM9M alloy is compared to the Timken product in Figure 5. The strength levels are lower for HCM9M over the range of 1000-1200°F.

2.2.2.2 Air/Argon Comparison

Testing in argon has a significant effect on the minimum creep rate. Figures 6 and 7 show this effect on two sets of creep-rupture tests. Another test is currently in progress and will be run to completion. However, no further argon tests are planned at this time. The emphasis of the program will be on obtaining those elevated temperature mechanical properties necessary for the development of a 1592 code case.

2.2.2.3 Weld Metal Testing

The initial stress-rupture tests run on weld metal samples (lot 109) yielded results that were lower than desired. However, test plates welded using lot 111 material (.05Cb added) produced improved results.

Figure 2
CHARPY V- NOTCH IMPACT CURVES OF MATERIAL FROM
FIRST 17 INCH DIAMETER ESR INGOT

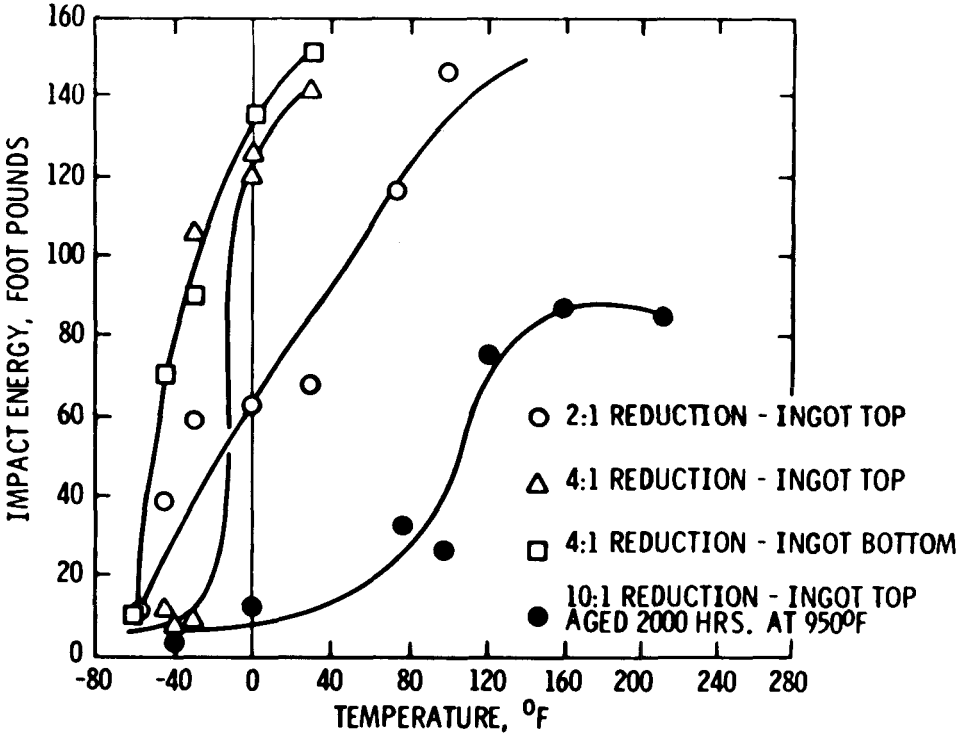

TABLE 3

CREEP AND STRESS RUPTURE RESULTS

SAMPLE IDENT	HEAT No.	STRESS ksi	TEMP °F	ATM.	I.D. STR IN/IN	END PRIMARY		MIN CREEP	ONSET TERTIARY		RUPTURE TIME, HRS	RUPTURE ELONG, %	RED. IN. AREA, %
						STR.IN/IN	Time,hr	RATE, HR^{-1}	STR,IN/IN	Time, hrs			
EXAB	ESR XA 3218	24	1100	ARGON	0.00128	0.0148	207	3.94×10^{-5}	0.0205	347	1043.6	17	79
EXAC	91887	24	1100	ARGON	0.00124	0.0100	810	5.99×10^{-6}	0.0148	1400	>2151		
EXAD	ESR XA 3218	28	1100	ARGON	0.00137	0.0108	17	3.69×10^{-4}	0.0226	56	143.9	26	85
EXAE	ESR XA 3218	28	1100	AIR	0.00134	0.0114	23	2.48×10^{-4}	0.0221	67	165.6	15	82
EXAF	SMA 109 (2088)	28	1100	AIR							13.85	24	80
EXAG	91887	28	1100	ARGON	0.00142	0.0154	38	2.91×10^{-4}	0.0216	70	198.2	27	89
EXAH	SMA 111 (2118)	28	1100	AIR							87.2	16	78
EXAI	SMA 111 (2118)	16	1200	AIR							192.2	(B)	34
ECAJ	91887	28	1100	AIR							485.2	16	85
EXAK	SMA 111 (2128)	40	1000	AIR							300.9	14	74
EXAL	91887	40	1000	AIR							492(A)		
EXAM	SMA 109 (2108)	40	1000	AIR							19.45	(B)	73
EXAO	SMA 109 (2088)	15	1200	AIR							73.1	(B)	56
EXAP	SMA 111 (2128)	25	1100	AIR							40(A)		
EXAQ	91887	28	1100	AIR							40(A)		
EXAR	SMA 111 (2118)	16	1200	AIR							(A)		

NOTE: (A) TEST IN PROGRESS. (B) BROKE OUTSIDE GAGE LENGTH IN SECTION WITH AREA EQUAL TO AREA IN GAGE LENGTH.

Figure 3

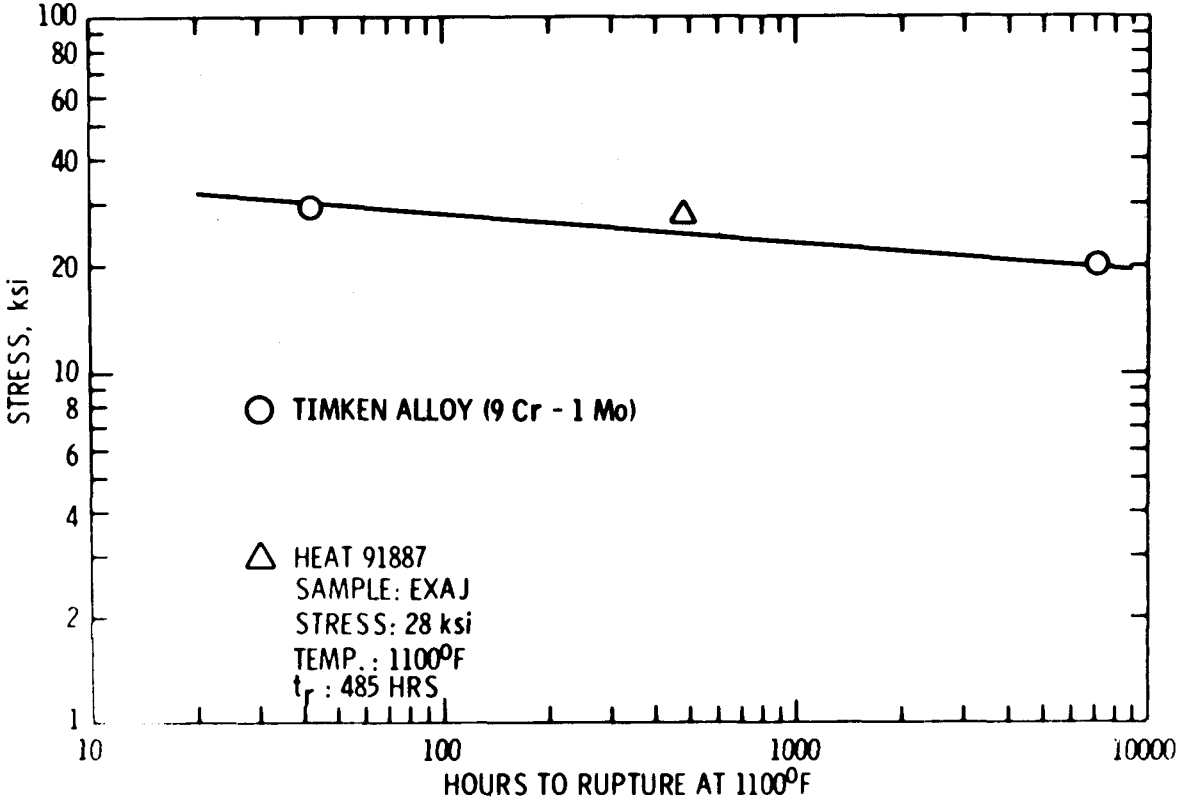
100
80
60
40
20
10
8
6
4
2
1
STRESS, ksi
O TIMKEN ALLOY (9 Cr - 1 Mo)
△ HEAT 91887
SAMPLE: EXAJ
STRESS: 28 ksi
TEMP.: 1100°F
t_r : 485 HRS
10
100
1000
10000
HOURS TO RUPTURE AT 1100°F

Figure 4

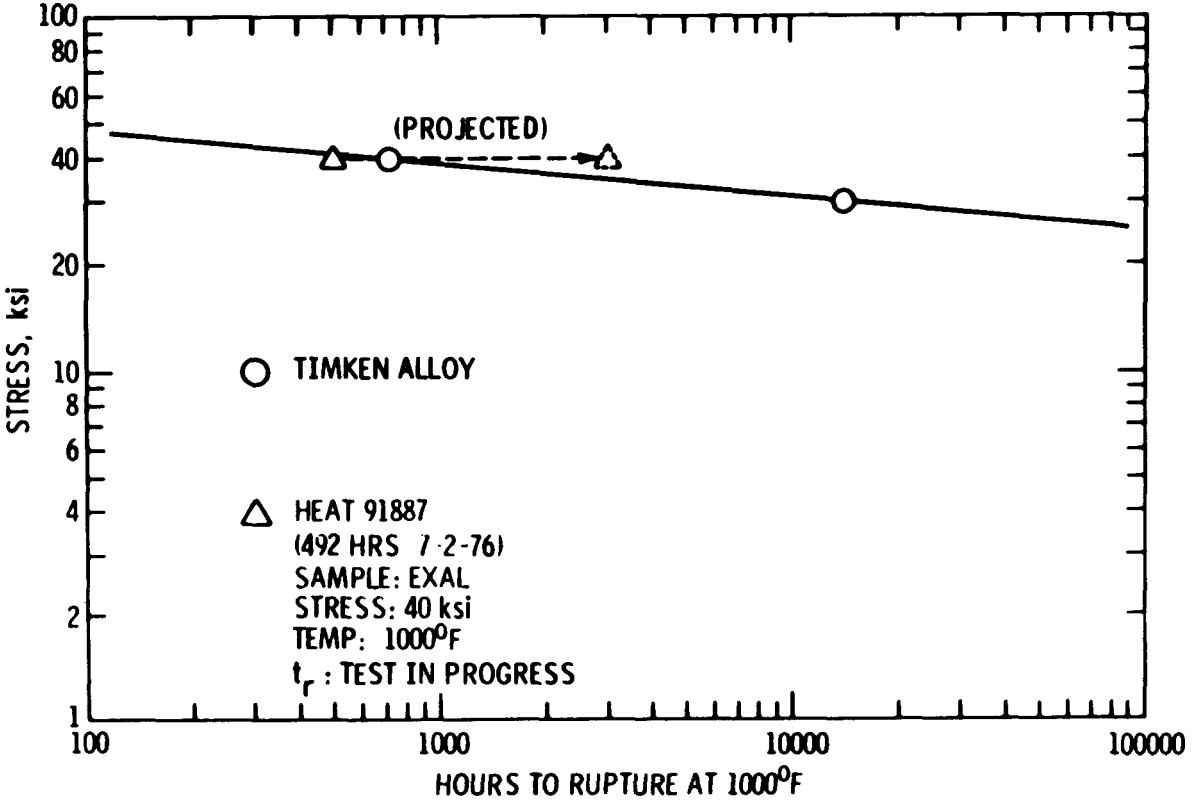
100
80
60
40
20
10
8
6
4
2
1
STRESS, ksi
(PROJECTED)
TIMKEN ALLOY
HEAT 91887
(492 HRS 7-2-76)
SAMPLE: EXAL
STRESS: 40 ksi
TEMP: 1000°F
t_r : TEST IN PROGRESS
100
1000
10000
100000
HOURS TO RUPTURE AT 1000°F

Figure 5

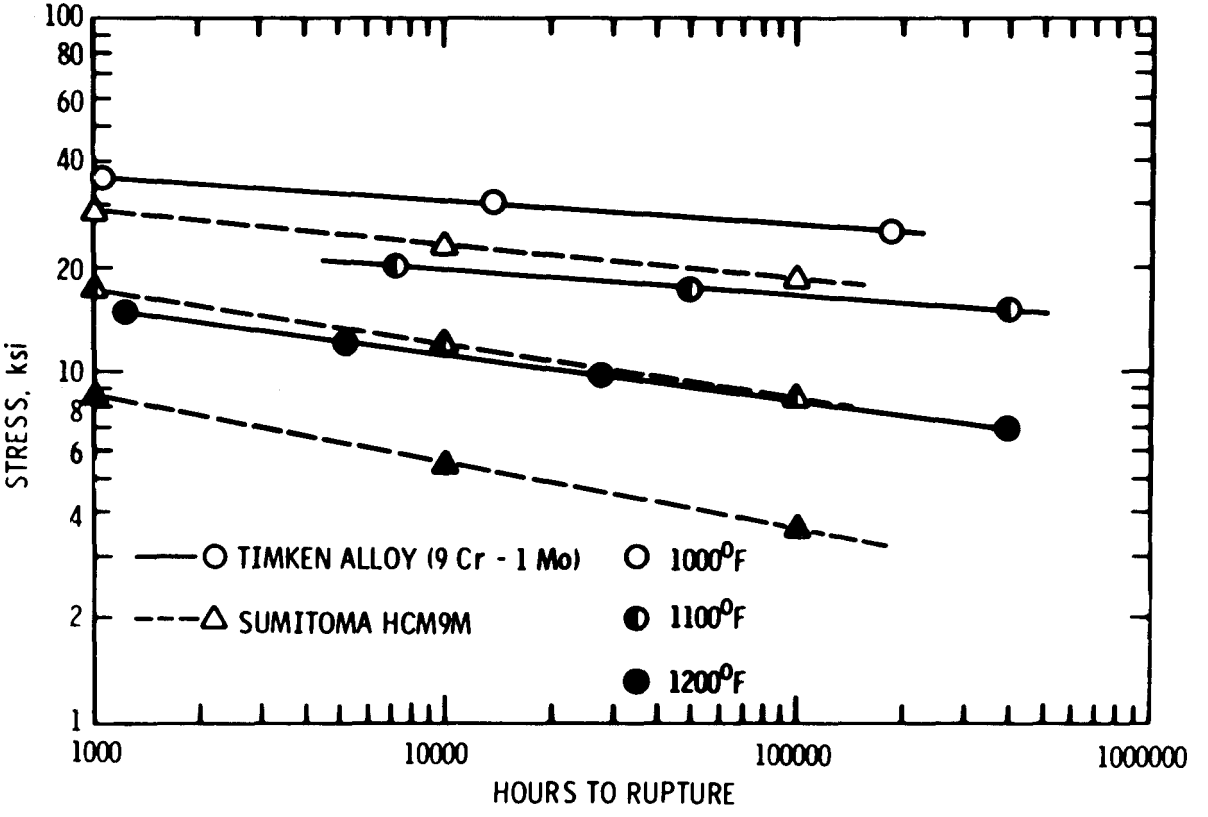
100
80
60
40
20
10
8
6
4
2
1
STRESS, ksi
TIMKEN ALLOY (9 Cr - 1 Mo)
SUMITOMA HCM9M
1000°F
1100°F
1200°F
1000
10000
100000
1000000
HOURS TO RUPTURE

Figure 6

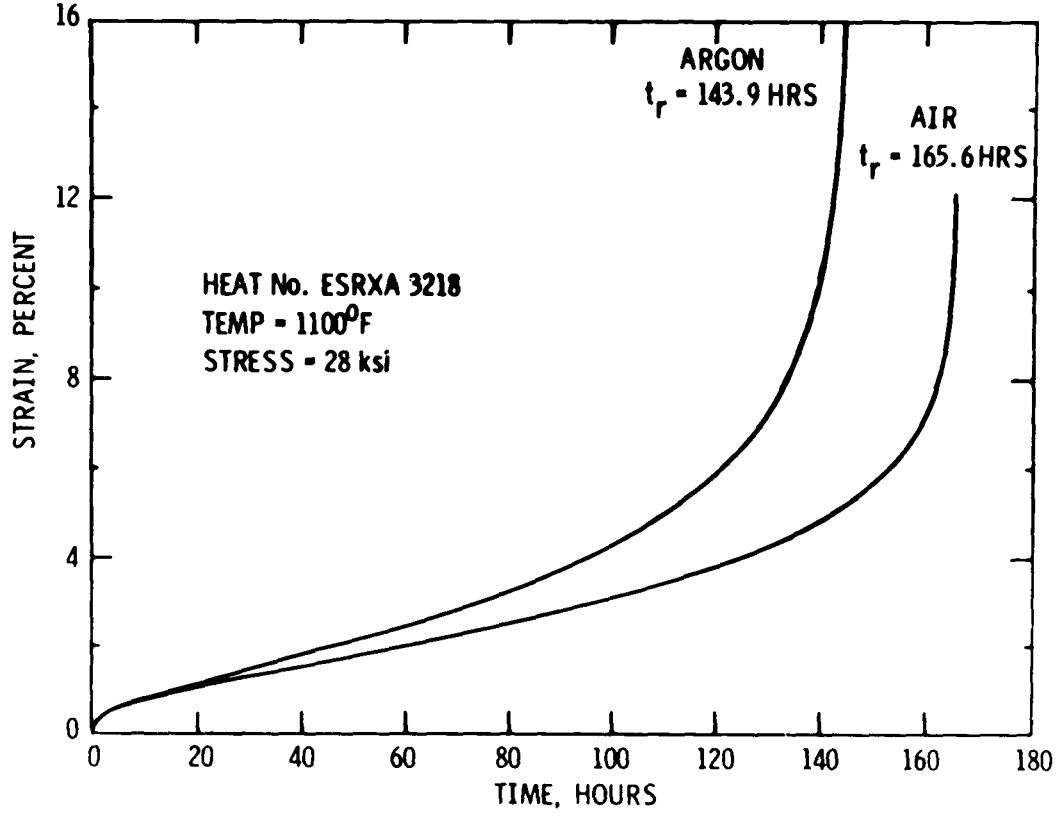
ARGON
t_r = 143.9 HRS
AIR
t_r = 165.6 HRS
HEAT No. ESRXA 3218
TEMP = 1100°F
STRESS = 28 ksi
STRAIN, PERCENT
TIME, HOURS
0
4
8
12
16
0
20
40
60
80
100
120
140
160
180

Figure 7

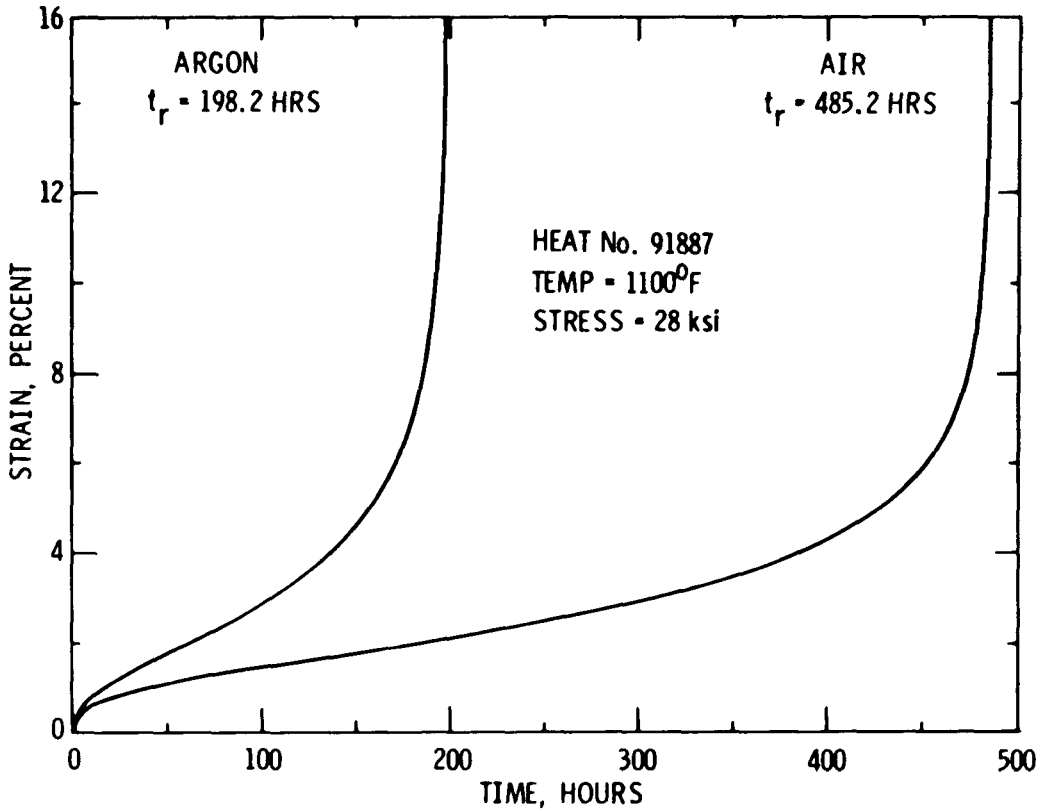
ARGON
t_r = 198.2 HRS
AIR
t_r = 485.2 HRS
HEAT No. 91887
TEMP = 1100°F
STRESS = 28 ksi
STRAIN, PERCENT
TIME, HOURS
0
4
8
12
16
0
100
200
300
400
500

Figures 8 and 9 show initial weld test results plotted in comparison to the Timken alloy. These results are very encouraging and additional specimens are now in test to further characterize this alloy at other temperatures and stress levels.

2.2.3 Welding Development — D. Vandergriff

2.2.3.1 Gas Tungsten Arc (GTA) Welding

Earlier results reported a >240 ft-lb upper energy shelf for 2 GTA welded plates. It was suspected at the time that either carbon loss (.05 to .027%) or microstructural characteristics produced these dramatic results (Figure 10).

Light microscopy did not reveal anything unusual in the microstructure. A Shielded Metal Arc(SMA) electrode was made up duplicating the low carbon level found in the original test material. However, low tensile strength in this special electrode stock indicates that carbon loss cannot explain the exceptional property values.

Transmission electron microscopy will be employed to further characterize the microstructures of these materials.

2.2.3.2 SMA Welding Progress

The pulsed current power supply has been modified to permit pulsed current input up to 50% of the total required current. Test plates are now being made and evaluated.

2.2.4 Melting and Casting — B. Chakravarti

Table 4 lists compositions for 3 pilot heats and the first 17" diameter ingot (91887) purchased from Cartech. Heat 3177 is the original tungsten bearing composition which has exhibited excellent properties as tempered and in the aged condition (2000 hrs at 950°F).

The purpose of making heats 3271 and 3273 was to demonstrate reproducability in making pilot heats and to document the fact that 5" pilot heats are in fact representative of larger diameter ingots.

Figures 11 and 12 compare impact and tensile results for heats 3177 and 3271. The latter is slightly stronger and less ductile and

Figure 8

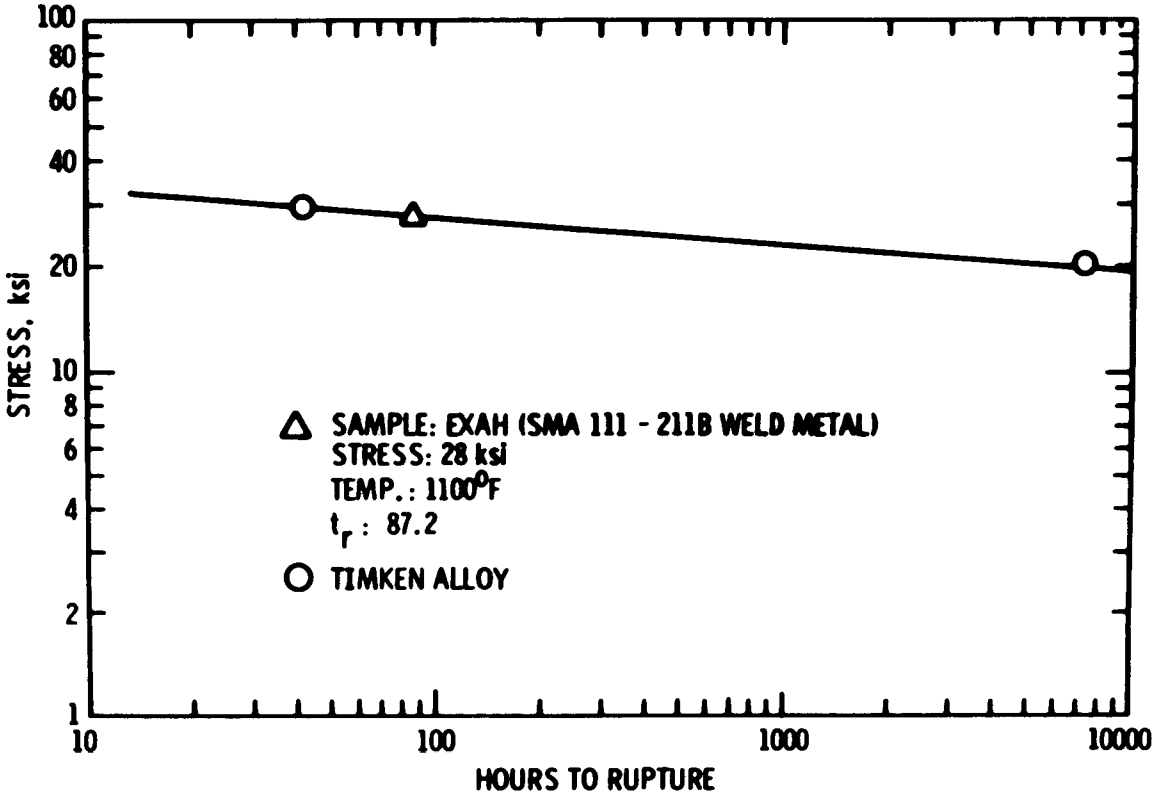
100
80
60
40
20
10
8
6
4
2
1
STRESS, ksi
SAMPLE: EXAH (SMA 111 - 211B WELD METAL)
STRESS: 28 ksi
TEMP.: 1100°F
t_r : 87.2
TIMKEN ALLOY
10
100
1000
10000
HOURS TO RUPTURE

Figure 9

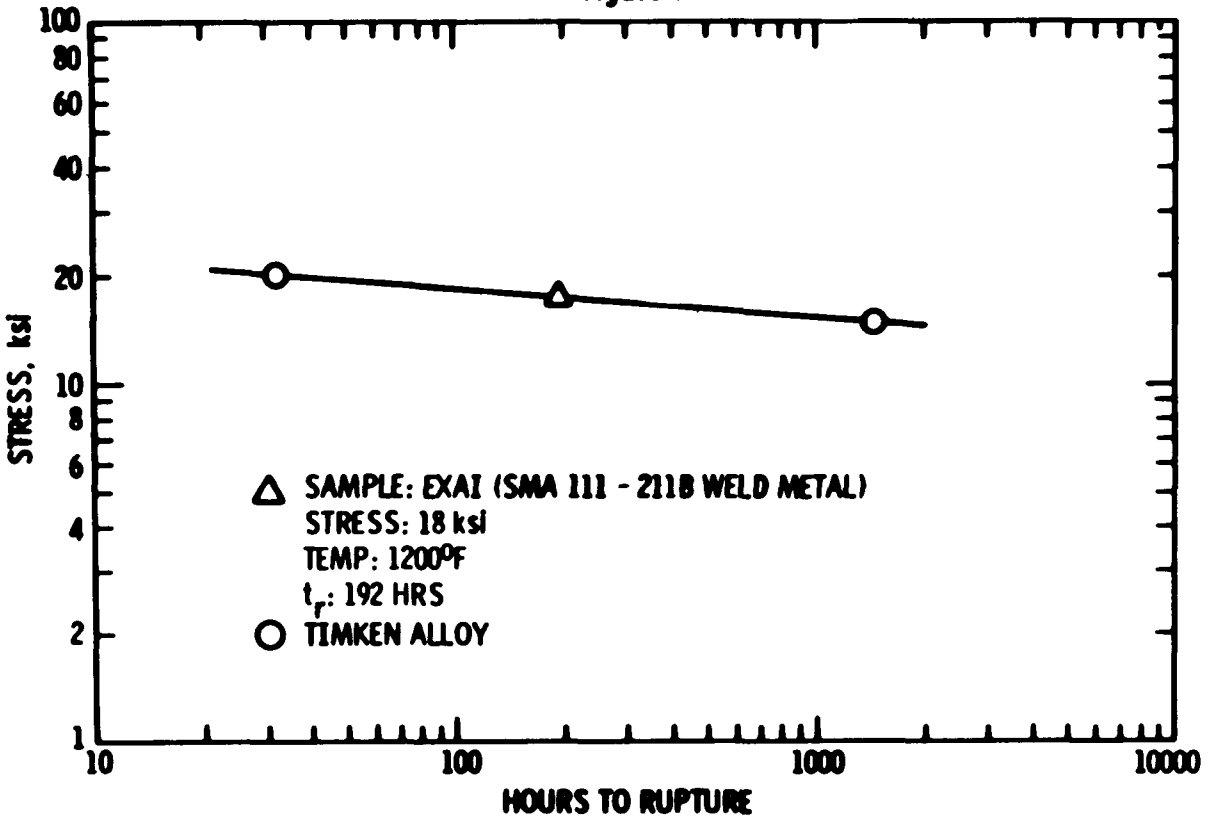
STRESS, ksi
100
80
60
40
20
10
8
6
4
2
1
10
100
1000
10000
HOURS TO RUPTURE
SAMPLE: EXAI (SMA 111 - 211B WELD METAL)
STRESS: 18 ksi
TEMP: 1200°F
t_r: 192 HRS
TIMKEN ALLOY

Figure 10

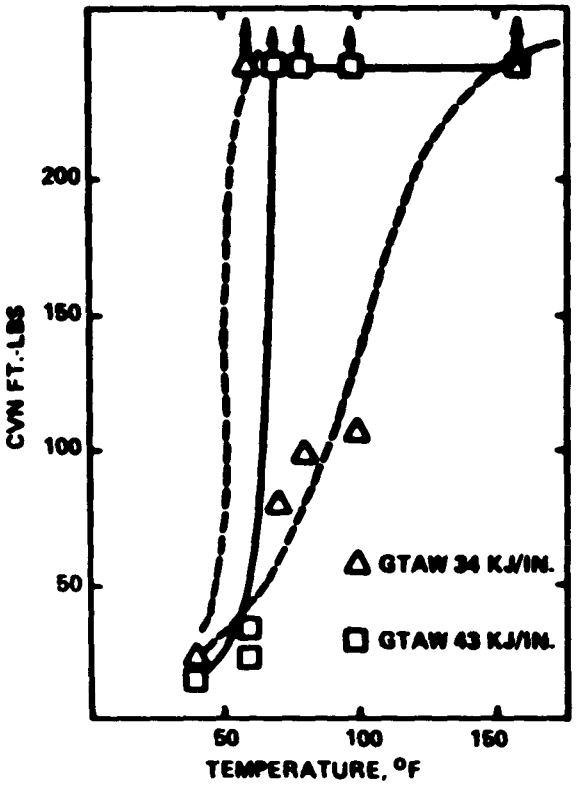

		C	Cr	Mo	V
GTAW ESR INGOT	TOP	0.050	0.15	1.04	0.14
	BOT.	0.061	0.03	1.29	0.14
3/32" ϕ WIRE		0.050	0.11	1.16	0.14
WELD DEPOSIT		0.027	0.21	1.13	0.14

		W	Cb	N_2
GTAW ESR INGOT	TOP	0.14	0.04	0.060
	BOT.	0.13	0.04	0.063
3/32" ϕ WIRE		0.16	0.05	0.066
WELD DEPOSIT		0.16	0.04	0.045

Table 4

HEAT No.	LOC.	C	Mn	Si	S	P	Cr	Mo	V	W	Cb	Ti	Ni	N_2	Al	B	Zr	Cu	As	Sn	Sb	O_2	H_2	Cr EQU
3177	TOP	.087	.44	.17	.010	.012	9.50	.78	.14	.48	.11	.04	.08	.085	.011	<.001	<.001	.11				.010		10.16
3271	TOP	.074	.37	.08	.007	.009	10.27	.75	.14	.45	.09	.01	.21	.087	.004	<.001	<.001	.02						9.853
91887	TOP	.097	.38	.08	.006	.007	9.22	1.01	.22	< .01	.15	< .01	.08	.038	.003	<.001	<.001	.81				.005		10.931
3273	TOP	.10	.32	.06	.007	.011	9.26	1.01	.23	< .01	.13	< .01	.12	.037	.002	<.001	<.001	.02						10.649

Figure 11

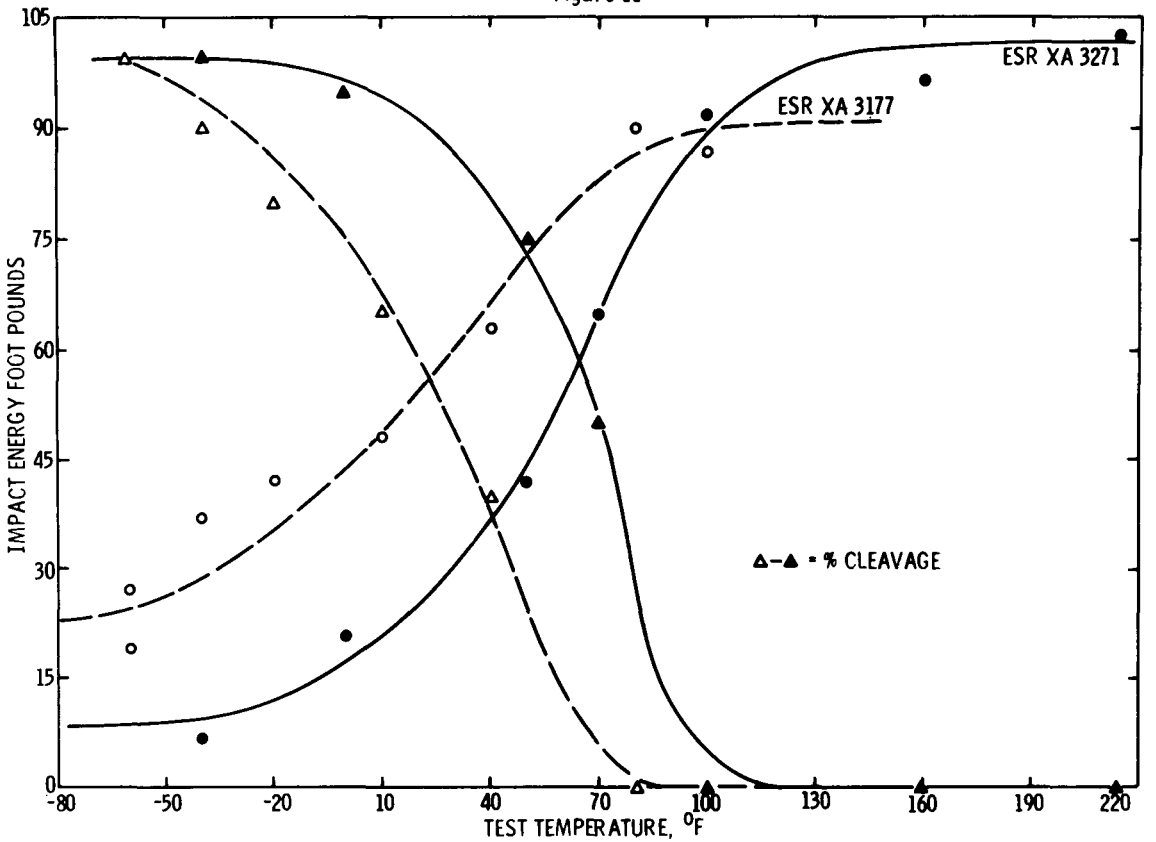
105
90
75
60
45
30
15
0
IMPACT ENERGY FOOT POUNDS
-80
-50
-20
10
40
70
100
130
160
190
220
TEST TEMPERATURE, °F
ESR XA 3271
ESR XA 3177
△–▲ = % CLEAVAGE

Figure 12

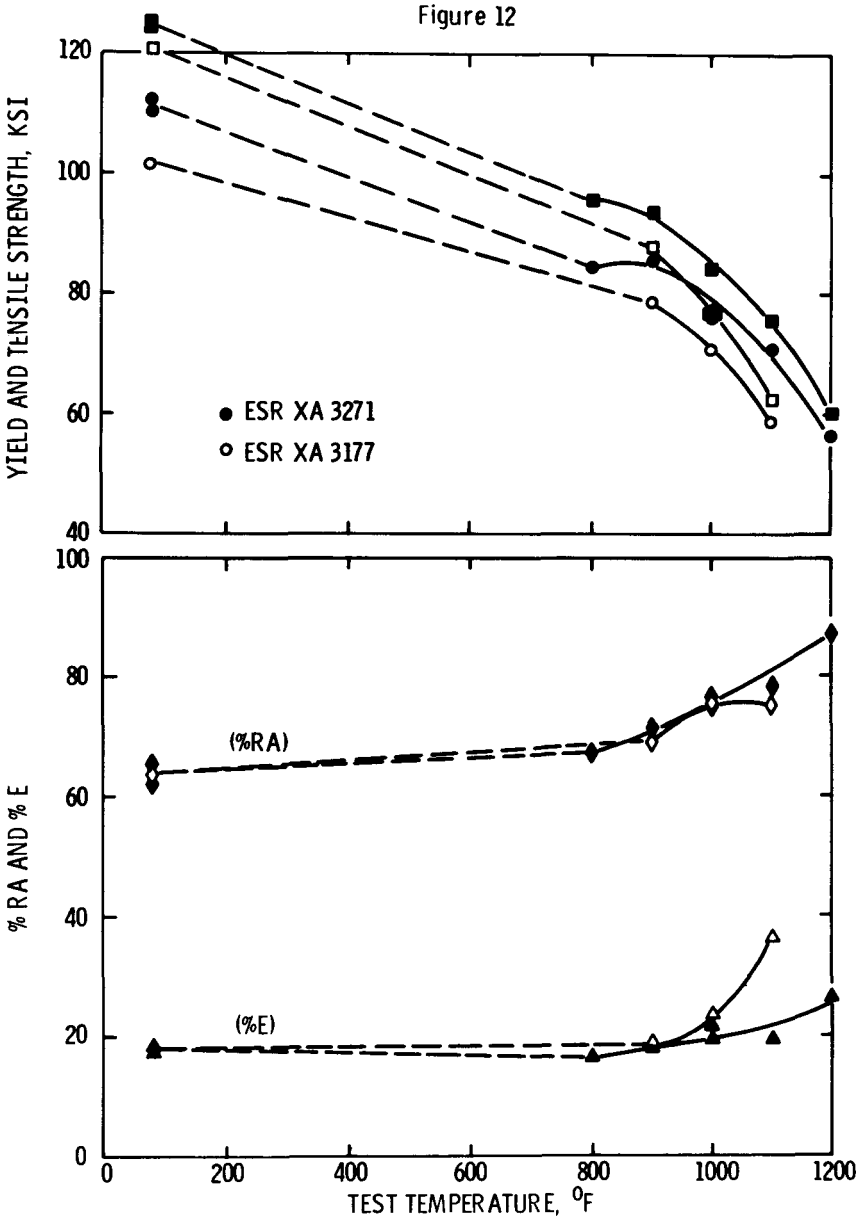
YIELD AND TENSILE STRENGTH, KSI
120
100
80
60
40
● ESR XA 3271
○ ESR XA 3177
% RA AND % E
100
80
60
40
20
0
(%RA)
(%E)
0
200
400
600
800
1000
1200
TEST TEMPERATURE, °F

has experienced a shift to the right in the 50 ft-lb temperature. These differences are not considered abnormal.

The correlation between properties obtained for heats 91887 (17" diameter ingot) and 3273 is shown in Figures 13 and 14. Excellent agreement is seen and it demonstrates that properties obtained on 5" ESR pilot heats are representative of large diameter ingots.

2.2.4.1 Work Planned for Next Quarter

1. Finalize composition for ordering second 5000 lb ingot.
2. Characterize microstructures of alloys retaining toughness after aging for 2000 hours at 950°F.
3. Continue with planned test matrix to obtain stress-rupture data for base and weld metals.
4. Evaluate modified SMA pulsed power supply.
5. Automate GTA welding procedure.
6. Analyze "hammer stopper" weld structures.

2.3 ALLOY 800 DEVELOPMENT FOR ADVANCED LMFBR STEAM GENERATORS - J. M. Duke

The purpose of this program is to develop information on Alloy 800 necessary for the design, analysis, and fabrication of LMFBR steam generators with high reliability. The scope of work includes establishment of a material specification; generation of data for ASME B&PV Code approval, including an assessment of the role of tertiary creep in defining Code Criteria; and subsequent development of mechanical properties, design curves, and mathematical models for inelastic analysis of a reference material. Engineering assessment of the corrosion resistance of both base metal and welds to sodium and non-sodium environments, and development of fabrication and weld processes for prototypic applications are included in the program intended to establish high reliability for LMFBR components through qualifications of an advanced material.

2.3.1. Materials Characterization - C. E. Sessions

The materials characterization task is addressed broadly at defining properties, structures, and composition of Alloy 800 of interest to

Figure 13

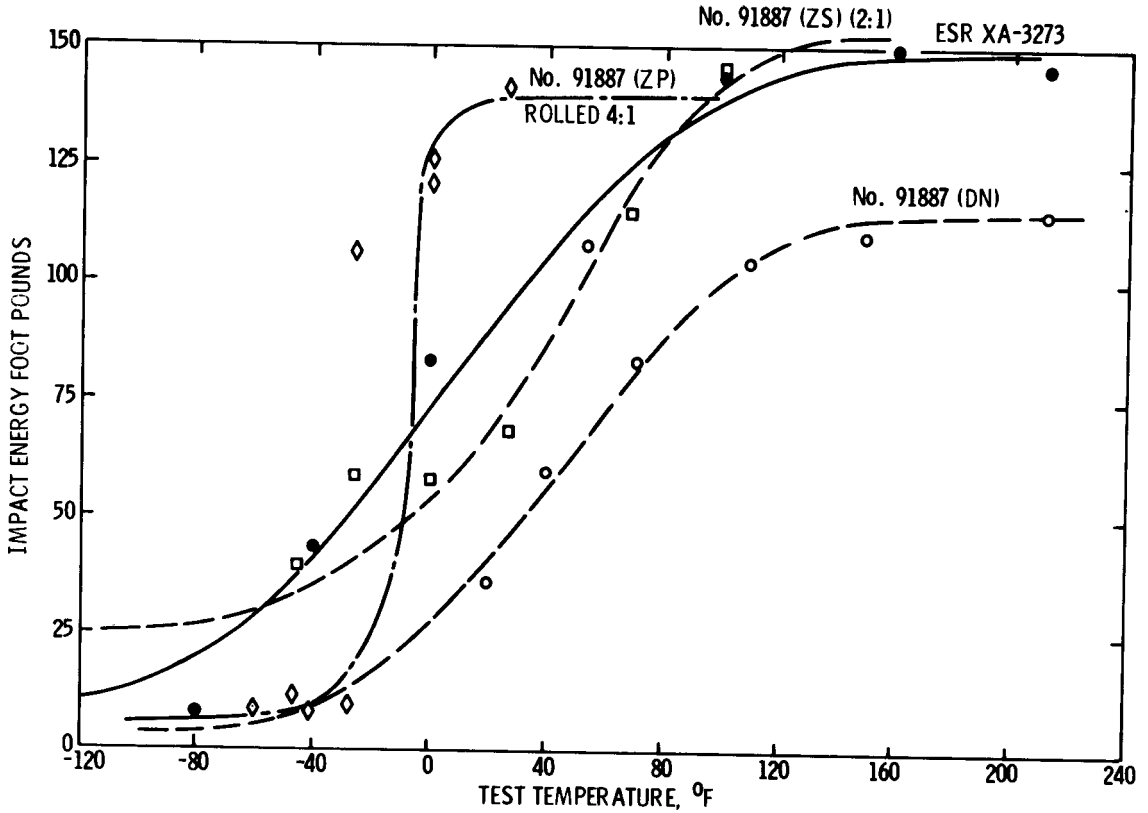
No. 91887 (ZS) (2:1)
ESR XA-3273
No. 91887 (ZP)
ROLLED 4:1
No. 91887 (DN)
IMPACT ENERGY FOOT POUNDS
TEST TEMPERATURE, °F
150
125
100
75
50
25
0
-120
-80
-40
0
40
80
120
160
200
240

Figure 14

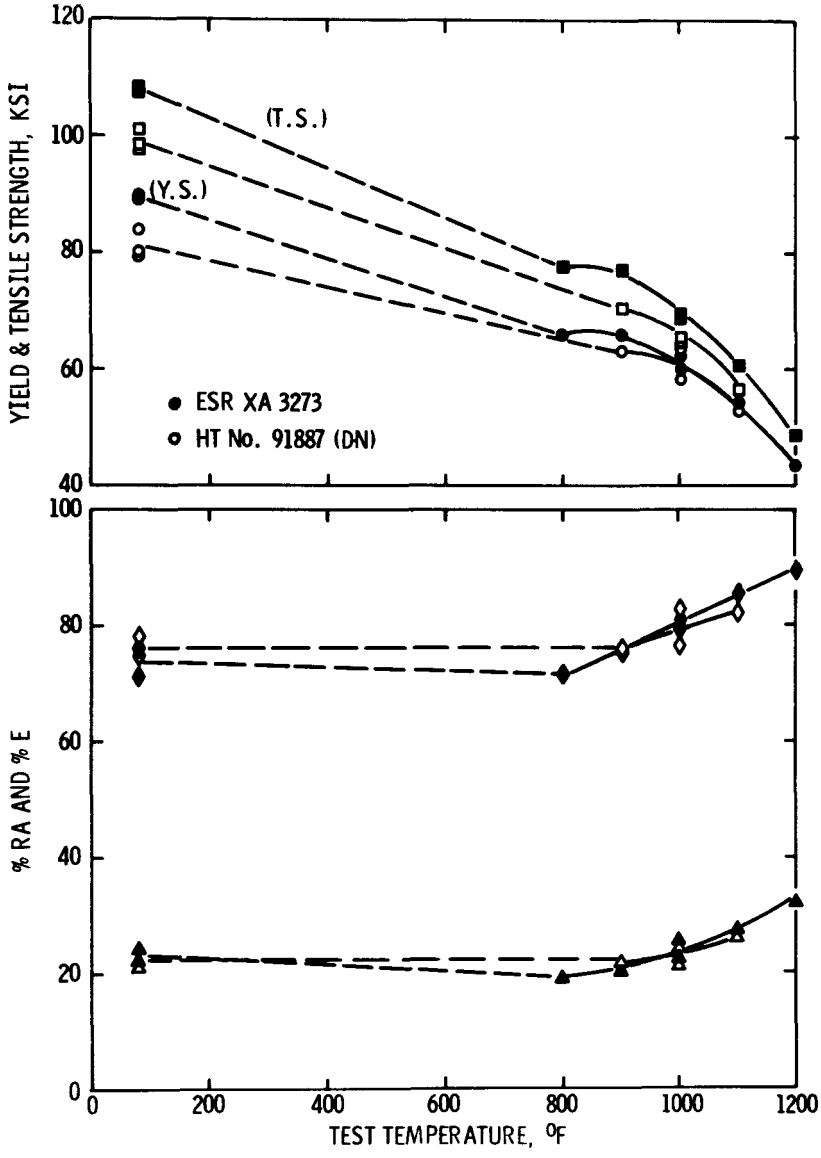
YIELD & TENSILE STRENGTH, KSI
120
100
80
60
40
(T.S.)
(Y.S.)
ESR XA 3273
HT No. 91887 (DN)
% RA AND % E
100
80
60
40
20
0
0
200
400
600
800
1000
1200
TEST TEMPERATURE, °F

designers of LMFBR steam generating equipment. The task specifically addresses the selection of a reference composition of Alloy 800 for subsequent detailed study in the overall program. In this task we will correlate and classify the effects that composition and microstructure have on the physical and mechanical properties. Subsequent effort will be expended toward generation of any mechanical properties data required for Code acceptance of Ni-Fe-Cr Alloy 800 (formerly Grade 1) considering the results of a specific task (2.0) aimed at assessing the role of tertiary creep as a design and materials limit on Alloy 800 application.

2.3.1.1 Specification for Base Material - C. E. Sessions

Background

The variation in mechanical, physical and corrosion properties of engineering alloys is a strong function of the specification relative to heat treatment and chemical composition. For Alloy 800 both a solution anneal (2100°F min) and a mill anneal (1800°F min) are commercially available and the design stresses vary depending upon whether or not a limitation is placed on the carbon content and/or grain size. Since previous users of Alloy 800 have selected different chemistries and heat treatment requirements within the general ASTM specification to fulfill different nuclear system design requirements (PWR, HTGR, etc.), this subtask within the current Advanced Steam Generator Materials Program addresses the selection of a specification for Alloy 800 to specifically meet the LMFBR Steam Generator design requirements and minimize the variability of behavior.

Objective

The overall objective of the specification subtask is to select composition and heat treatment requirements within the allowable ASTM specification (e.g., ASME Section III B&PV Code) for heat exchanger tubing and forgings which will best meet the strength and corrosion resistance anticipated in LMFBR steam generator designs. We accomplished this task through a review of the published literature in three major areas:

(1) Strength requirements at room and elevated temperatures

(2) Corrosion behavior in water/steam, and

(3) Effects on weldability of the base metal.

Completion of this subtask was scheduled for June 30, 1975. Detailed milestones for this and the other two subtasks were given in the original proposal. The preferred combination of chemical composition, microstructure and other pertinent factors was converted into a materials specification considering the present commercial practice and technology in the materials supply industry. Specific input was requested from the International Nickel Company, Sandvik, Sumotomo and other potential suppliers of Alloy 800. The resulting specification will be used to procure additional material and to focus the development activities.

Progress

Work on this task has been completed and the final report[1] will be issued in August. An oral presentation of the conclusion of this work was presented at the International Conference on Liquid Metal Technology in Energy Production on May 3 - 6, 1976 and the paper[2] will be published in the conference proceedings.

2.3.1.2 Physical and Mechanical Properties - C. E. Sessions

Background

The subtle compositional effects on the mechanical properties of Alloy 800 were vividly demonstrated in 1970 by work of Harman[3] at Oak Ridge National Laboratory. Harman showed that both creep rupture life and creep ductility could be radically improved following neutron irradiation. These effects were caused by changing the ratio of titanium to carbon present in the alloy and also the associated grain size for laboratory melts of Alloy 800. Werner[4] further illustrated that the titanium and carbon content of Alloy 800 could significantly affect the unirradiated high temperature tensile ductility. Werner found that titanium, aluminum and carbon were all beneficial when compared to the ductility of high purity laboratory melts of a Fe-Ni-Cr ternary alloy.

Earlier work in 1964 at General Electric Company[7] concluded that Alloy 800 was an excellent candidate fuel cladding for a high temperature superheated steam reactor concept. In this early work the property changes associated with minor alloying additions were illustrated.

A recent detailed discussion of the impact of the specification of Alloy 800 on the design stresses was presented by Moeller and Martin at the BNES Conference in England.[5] They discussed the evolution of the elevated temperature design code for nuclear components (e.g., Code Case 1592 of the ASME Boiler and Pressure Vessel Code). By limiting the data base available for Grade 2 Alloy 800, they were able to define a higher strength Alloy 800 specification as Alloy 800H with a higher allowable stresses for elevated temperature use. Actually the strengthening that is realized is achieved through tightening the range of carbon and the grain size allowed.

These four references simply illustrate the point that materials for use in elevated temperature pressure vessel design must be fully characterized with respect to chemistry, heat treatment and properties to a degree that exceeds that currently available for Alloy 800.

Objective

The primary objective is to evaluate the physical properties (thermal expansion coefficient, thermal conductivity, specific heat, etc.) and mechanical property (tensile, creep, fatigue, crack growth rate and creep-fatigue) data available for Ni-Fe-Cr Alloy 800 within the reference composition range for subsequent use in LMFBR steam generator designs. A secondary objective is to characterize all the test materials being purchased for this program with respect to all properties required for inclusion in the Nuclear Systems Materials Handbook.

Progress

As outlined above, the physical and mechanical properties subtask involves the accumulation of data describing the materials behavior of Alloy 800. The prime effort to date has been the generation of creep information on Alloy 800 of various heats and product forms. Table 2.1

Table 2.1 Status of Creep Testing at Westinghouse Tampa

Heat	Temperature (°F)	Stress	Time to 1% E (hr)	Loading Strain (%)	Current Strain (%)	Time (hr)	Date Started
6729	1000	37500	Loading	3.76	4.51	7386	8/26/75
		34000	Loading	2.97	3.28	7384	8/26/75
		25000	137	0.77	1.01	7335	8/28/75
		20000	-	0.13	0.22	7312	8/29/75
	1100	30000	Loading	2.25	3.47	5892	10/27/75
7094	1000	37500	Loading	2.74	5.13	7001	9/11/75
		30000	Loading	1.25	1.66	4025	1/13/76
	1100	25000	884	0.18	5.03	4672	12/27/75
5501	1000	30000	137	0.71	1.51	5870	10/28/75
		25000	-	0.20	0.47	3997	1/14/76
5475	1000	45000	-	0.23	0.68	10218	4/30/75
		40000	-	0.13	0.29	9735	5/28/75
					TOTAL	80,826 hr	

summarizes the status of twelve creep tests on annealed Alloy 800 that are underway in Tampa. The tests are designed to produce data that describes the properties used in determining the time dependent allowable stress S_t, at the temperature of interest for LMFBR steam generation equipment, namely 1000° and 1100°F. Four of these twelve tests have not yet reached 1% total strain, even though the test duration exceeds 4000 hours in each case. Total testing time to date for these specimens listed in Table 2.1 is 80,826 hours as of July 1, 1976.

Table 2.2 presents a summary of tests which have been terminated either due to failure of the sample or to discontinuation. The total testing time for these twenty-two tests is 29,770 hours. The results in Table 2.2 have not been analyzed to any appreciable extent; however, results include a useful comparison of the short time creep behavior of the two different grades of Alloy 800, (e.g. Grades I and II) for cold drawn tubing of the same heat of material (HH 5475 which contains 0.08% Carbon, 0.57% Aluminum, and 0.42% Titanium). Data of this nature are sparce.

2.3.1.3 Microstructure and Thermal Stability - C. E. Sessions and D. Moon

Background

The classification of the behavior anticipated for Alloy 800 generally and for the chemistry range and product forms anticipated during service should be determined with respect to its microstructure. The mechanical and chemical performance of the alloy depends critically on the microstructure that exists at the start of life and on those structures that develop during the service lifetime. This subtask is devoted to the microstructural characterization of Alloy 800 in general and base line evaluation of all starting heats of materials and product forms used in this program. The characterization will utilize all analytical equipment required to completely analyze the structure. Optical metallography, transmission, scanning electron microscopy, magnetic permeability, x-ray diffraction, and electron probe analysis will be used to assess the structure inherent initially in specific heats of Alloy 800 after thermal aging.

Table 2.2 Test Results Generated To Date For Creep Tests on Alloy 800

Heat	Temperature (°F)	Stress (psi)	Time to 1% Strain (hr)	Loading Strain (%)	Total Strain (%)	Minimum Creep Rate (%/hr)	Time to Failure (hr)	
6729	1000	50000	Loading	9.16	39	.007	1372	
	1100	30000	Loading	1.69	NA	NA	236	(Disc.)
		35000	Loading	1.42	9	.0002	4726	
7094	1100	35000	Loading	2.44	28.2	.0086	753	
5501	1000	58000	Loading	-	30	-	7	
		50000	Loading	8.01	45.7		742	
	1100	35000	Loading	1.64	25	.0034	989	
		25000	Loading	1.36	33	.007	730	
5475 **	900	80000	Loading	11.32	21.8	.021	290	
		80000 *	Loading	-	41.7	NA	0	
		72000 *	Loading	20.6	35	NA	0	
	1000	60000	Loading	1.21	29.5	.014	728	
		60000 *	Loading	18.35	28	.0009	958	
		52000 *	Loading	13.09	26.2	.0003	2321	
		50000	232	0.28	15	.001	4264	
		29200 *	1992	0.98	1.75	.00009	4778	(Disc.)
	1100	50000	21	0.41	20	.030	299	
		50000 *	Loading	8.04	24	.007	220	
		42000	953	0.26	6.7	.0006	2475	
		30000	-	0.17	-	.00007	3070	(Disc.)
	1500	11000	381	0.07	12.8	.001	542	
		9429	160	0.07	14	-	270	

** Specimens machined from wall of either Grade I or Grade II Tubing.
* Specimens of Grade II Tubing - cold drawn and solution treated.

This subtask will also address the broad question of the thermal stability of Alloy 800. Specific attention will be given to the gross effects on the mechanical properties after thermal exposure. These properties will then be used for comparison to deduce the influence of exposures on the mechanical behavior of Alloy 800. Furthermore, this subtask will address the effects of precipitation so that the metallurgical effects can be accounted for and considered in formulating models describing the behavior of Alloy 800 under temperature and stress.

Objective

The objective of this subtask is to characterize the initial microstructure and the thermal stability of Alloy 800 in general and in particular for the specific heats included in this Advanced Materials Program.

Initially a literature review of possible structures achievable in Alloy 800 will be made. Heats of Alloy 800 will be purchased to fill the gap between the literature results and the commercial range of chemistries in Alloy 800. Attempts will be made to produce all desired product forms from a given heat, as well as multiple heats for certain product forms (e.g. tubing). Standardized evaluation will be made of all materials purchased. These evaluations will be based upon the literature review and on criteria established in other subtasks and the measurements made will be used to correlate with the property changes monitored in other tasks. After a catalogue of microstructures has been assembled, interaction with other tasks to solve, correlate or measure other microstructural features will be accomplished.

Using specific heats of Ni-Fe-Cr Alloy 800 purchased for the overall test program, traditional aging studies will be started to measure gross effects of temperature, time and stress on certain mechanical, physical, and corrosion properties. In addition, experiments will be designed to measure the rates of carbide precipitations. Microstructural evaluation of the aged and strained samples will be made to characterize the precipitate distribution and morphology. Detailed interaction with subtasks is anticipated in development of the description of the mechanical behavior.

Progress

Progress under this subtask since our last contribution (December 1975) includes work in three different areas, (1) evaluation of the microstructure of crept samples from HAPD, (2) measurement of the microhardness of aged samples of both annealed (formerly Grade I) and solution treated (formerly Grade II or H) from Heat HH 3539, and (3) continuation of the grain size study. The detailed progress in each of these three areas is discussed separately below.

Since the behavior of Alloy 800 under creep loading conditions is such an important aspect in accomplishing ASME Code acceptance of the annealed grade, an effort was made at the outset of the program to obtain coupons of samples thermally exposed for long times. At our request HAPD supplied five of thirteen samples of various chemistries that were tested at 35,000 psi and 1100°F. Microscopy was performed upon these five coupons from both the strained and unstrained portion of the tested sample in order to correlate the microstructures with the creep behavior measured previously (6). A schematic of the strain-time curve of four of these thirteen tested samples is illustrated in Figure 2.1. The creep response shows a sharp variation with alloy composition over the allowable range of the ASTM specification for Alloy 800. However, the strongest sample (5) in Figure 2.1 does contain a titanium concentration (1.0% Ti) that is outside the range of 0.6% Ti max. allowed, while samples 2, 6, and 9 are within the allowable chemistry range.

The microstructure of the samples 2, 5, and 9 are shown in Figure 2.2, 2.3, and 2.4 respectively. The formation of gamma prime precipitates was easily identified at 100,000 X for samples 9 and 5, but was not apparent for sample 2. Thus the low creep rates, long rupture lives and relatively low rupture ductilities[6] correlate with the samples that contained a high concentration of aluminum and titanium and a fine distribution of gamma prime, Ni_3 (Al, Ti), precipitates. Note that the dislocation cell substructures differ for these three samples. Apparently in sample 2 the dislocations could travel over relatively long distances before interaction leading to the formation of cell boundaries. In contrast, the structure of sample 5 is characterized by bands of non-homogeneous deformation that appear as dense slip bands. Apparently

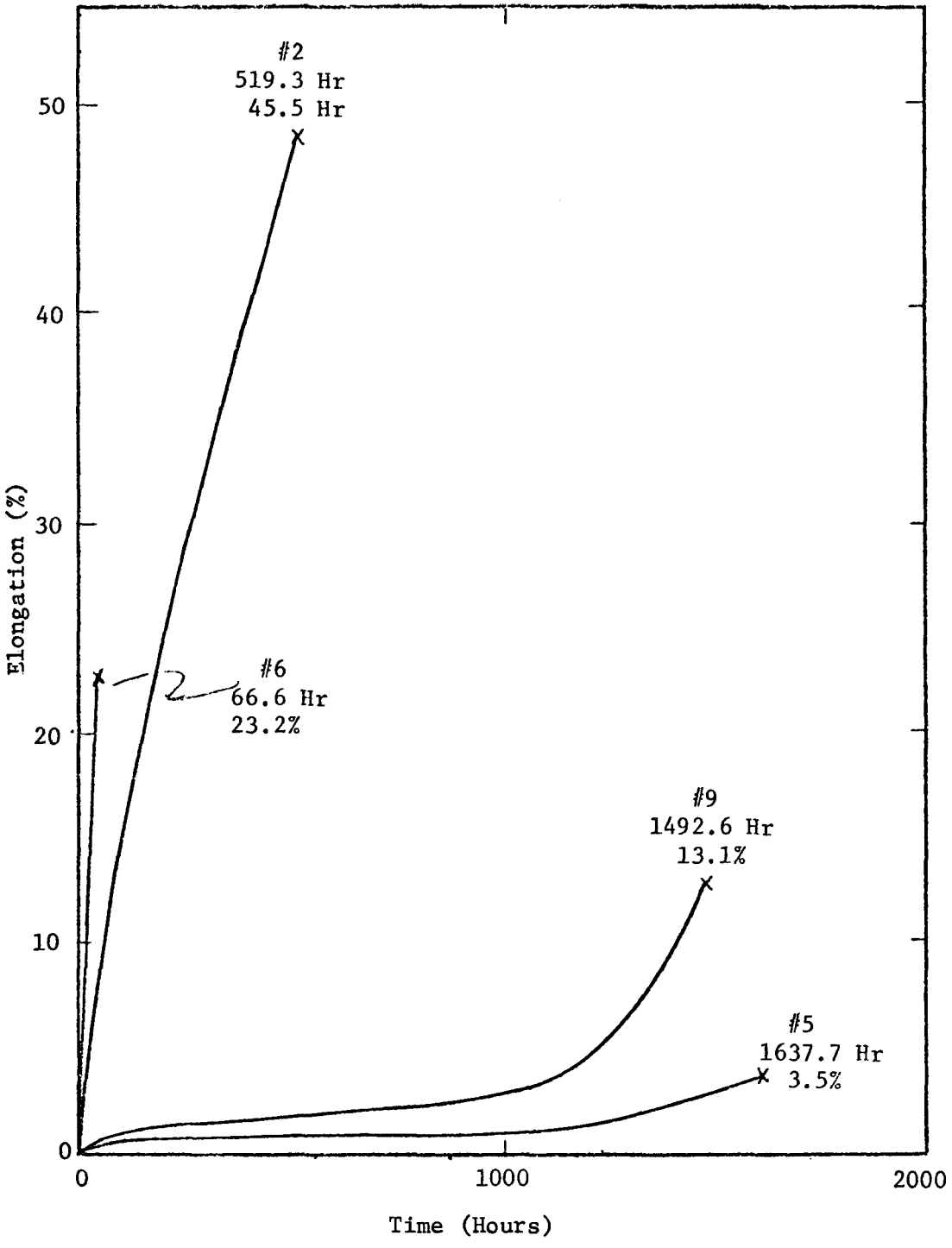

Fig. 2.1 Schematic Creep Curves of Different Chemistries of Annealed Alloy 800 at 35,000 psi and 1100°F (Tested by HAPD and Microscopy by Westinghouse)

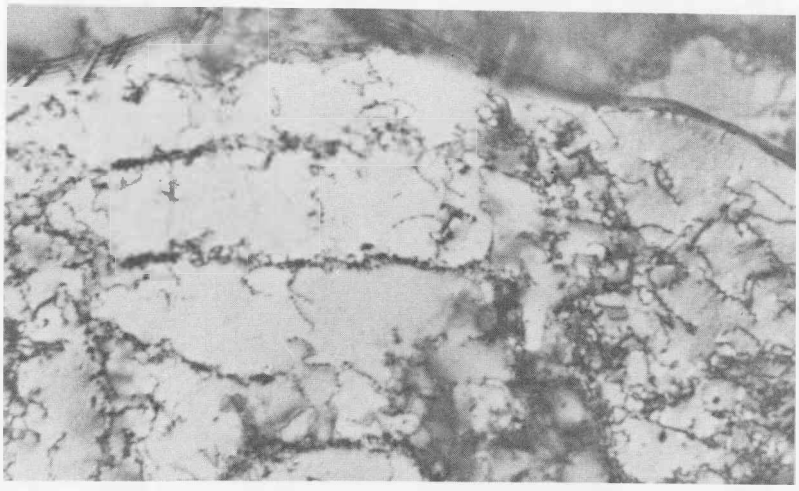

(a)

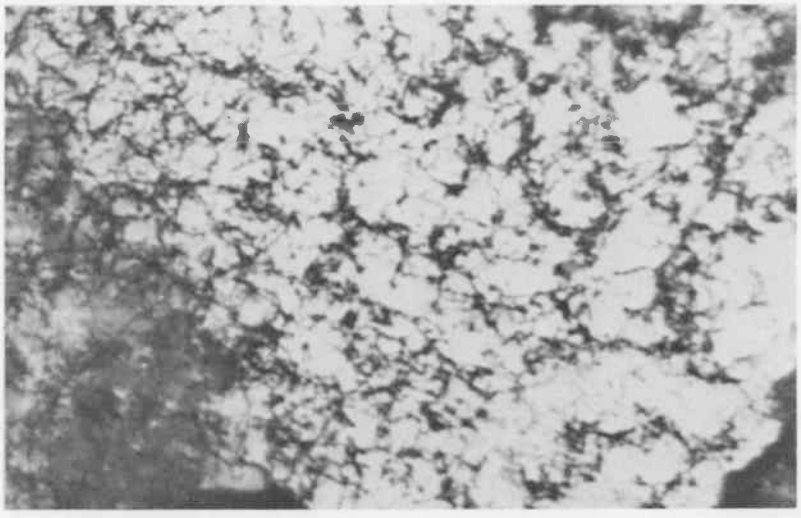

(b)

Fig. 2.2 Transmission Electron Micrograph of Annealed Alloy 800 Sample No. 2 Gage Section after Creep Testing at 35,000 psi and 1100°F. (a) 45,200X Mag. (b) 35,000X Mag.

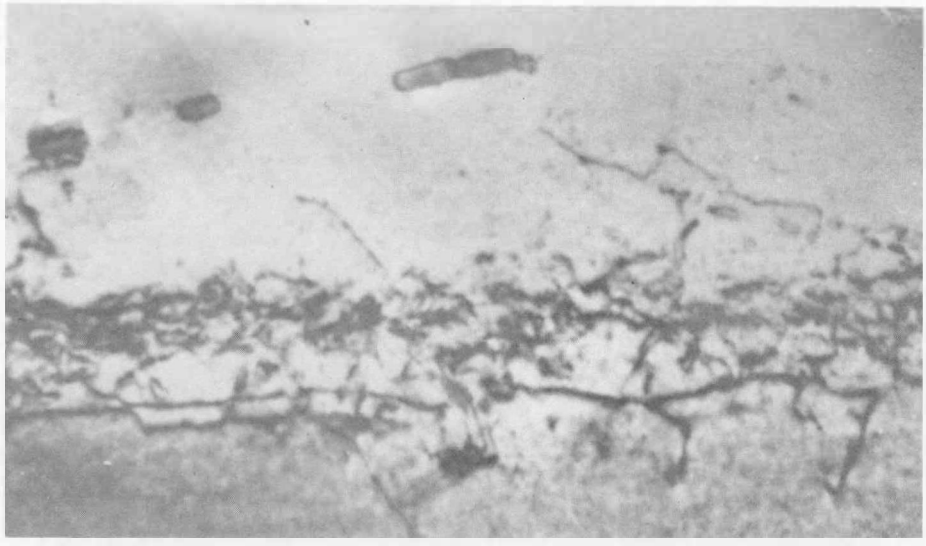

(a)

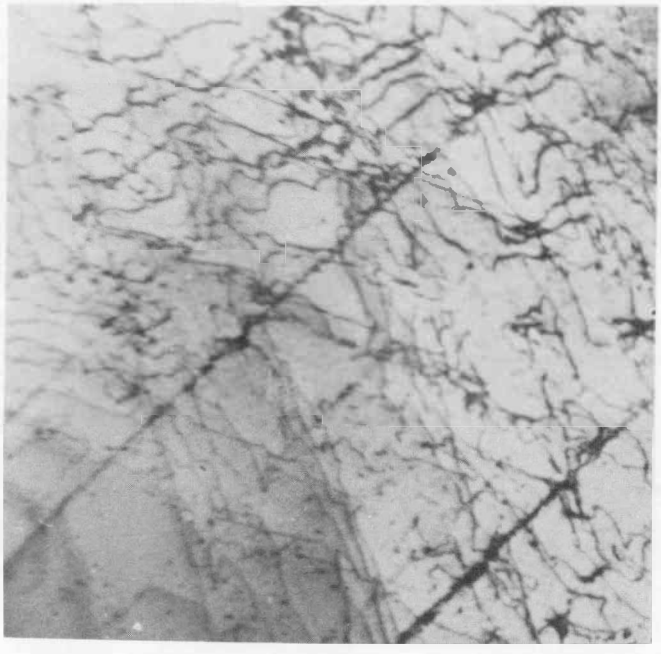

(b)

Fig. 2.3 Transmission Electron Micrograph of Annealed Alloy 800 Sample No. 5 Gage Section After Creep Testing at 35,000 psi and 1100°F. (a) 96,800X Mag. (b) 54,400X Mag.

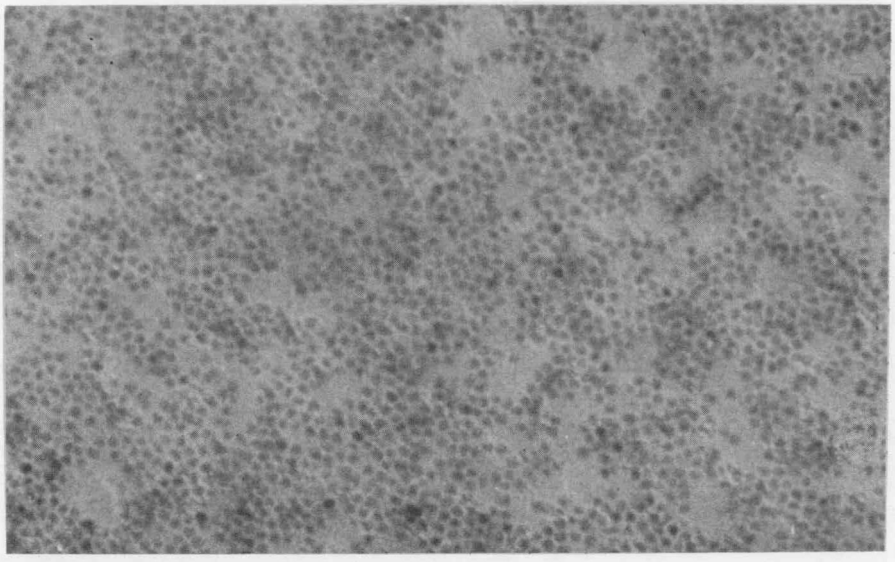

(a)

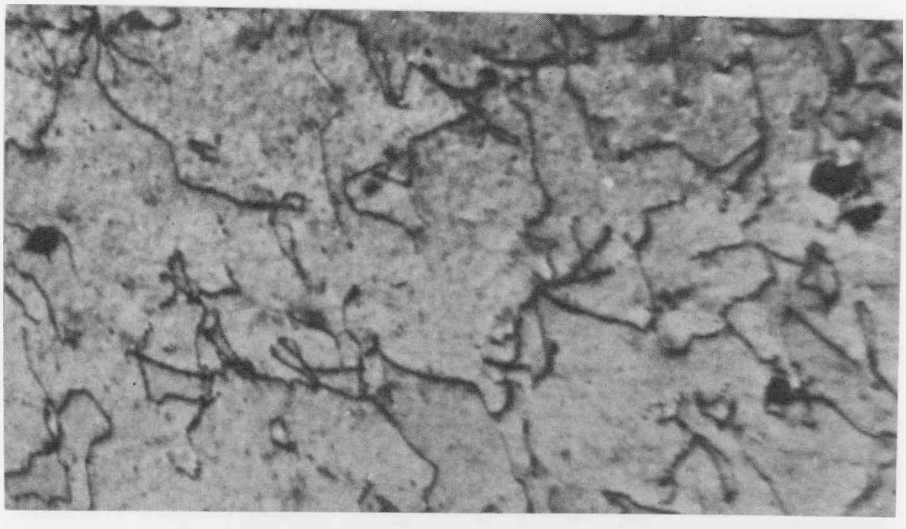

(b)

Fig. 2.4 Transmission Electron Micrograph of Annealed Alloy 800 Sample No. 9 Gage Section After Creep Testing at 35,000 psi and 1100°F. (a) 125,000X Mag. (b) 30,000X Mag.

the fine distribution of gamma prime precipitates in samples 9 and 5 strengthens the material and the dislocations must cut through the precipitate particles, leading to regions of high perferred slip and dense tangles within the slip bands.

Additional analysis of microstructures and creep data[1] is in progress currently that should further aid in interpretation of the role of precipate formation, alloy content and heat-treatment on the mechanical behavior of Alloy 800.

The second area of progress involves an analysis of the aging response of Alloy 800. Coupons of Heat HH 3539 were given laboratory heat treatments at 1825°F and 2100°F to produce an annealed and a solution treated condition of a single heat used in subsequent aging studies. The heat chemistry and details about the heat treatment times and temperatures are presented in Table 2.3. Diamond pyramid microhardness measurements were made on the samples and these results are plotted for the annealed and solution treated conditions in Figures 2.5 and 2.6 respectively. In Figure 2.5 significant hardness increases are shown during aging at 1050°F and 1200°F, but not at higher temperatures. For the annealed condition, hardening was most rapid at 1050°F for the temperatures investigated. In the case of the solution treated materials, the short time hardening is greater for aging at 1200°F than for aging at 1050°F. Also, for a given time at 1050°F, the hardness change appears to be greater for the annealed material compared to the solution treated condition. At the higher temperatures of 1900°F and 2100°F, the hardness decrease is attributed to both precipitate and grain coarsenings.

Based upon both thin film and replica transmission electron microscopy of some of the aged samples, the following general conclusions have been drawn concerning the aging effects in annealed Alloy 800:

1. Gamma prime precipitates in approximately 150 hours at 1050°F.
2. At temperatures above 1200°F there is not much gamma prime precipitation.
3. The relative amounts of MC and $M_{23}C_6$ precipitates are not changed much by aging at temperatures below 1900°F.
4. At 1900°F $M_{23}C_6$ begins to dissolve leaving MC and MN precipitates at 2100°F.

Table 2.3 Chemistry of Alloy 800 Heat HH 3539A Used in Aging Investigation

Alloying Element	Amount Present (%)
Fe	45.76
Ni	30.52
Cr	21.19
Ti	0.42
Al	0.42
C	0.07
Mn	0.79
P	--
S	0.007
Si	0.28
Co	--
Cu	0.52

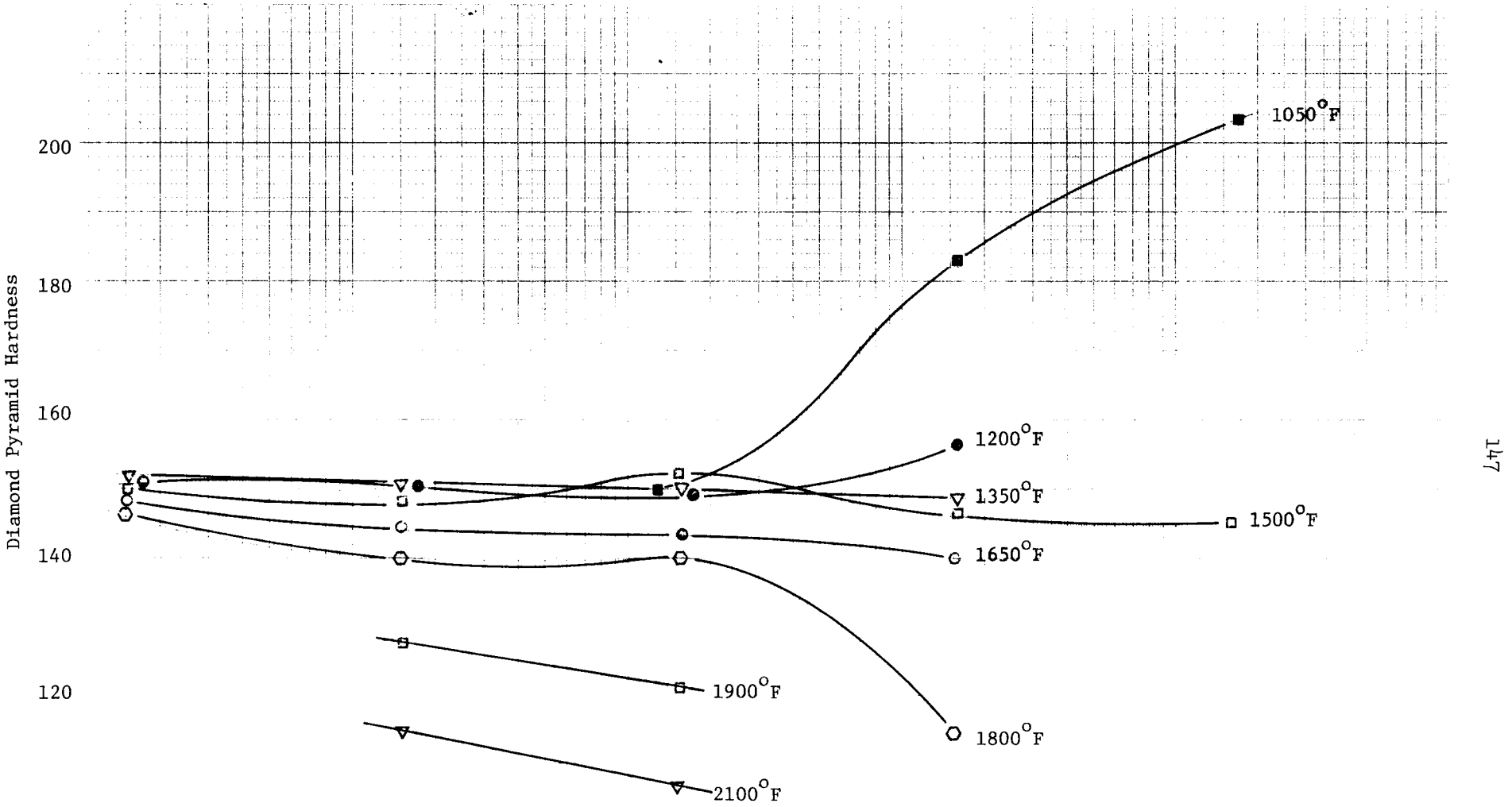

Fig. 2.5 Aging Response of Hot Finished and Annealed Alloy 800 Heat HH 3539. Aged in the "as mill annealed" condition.

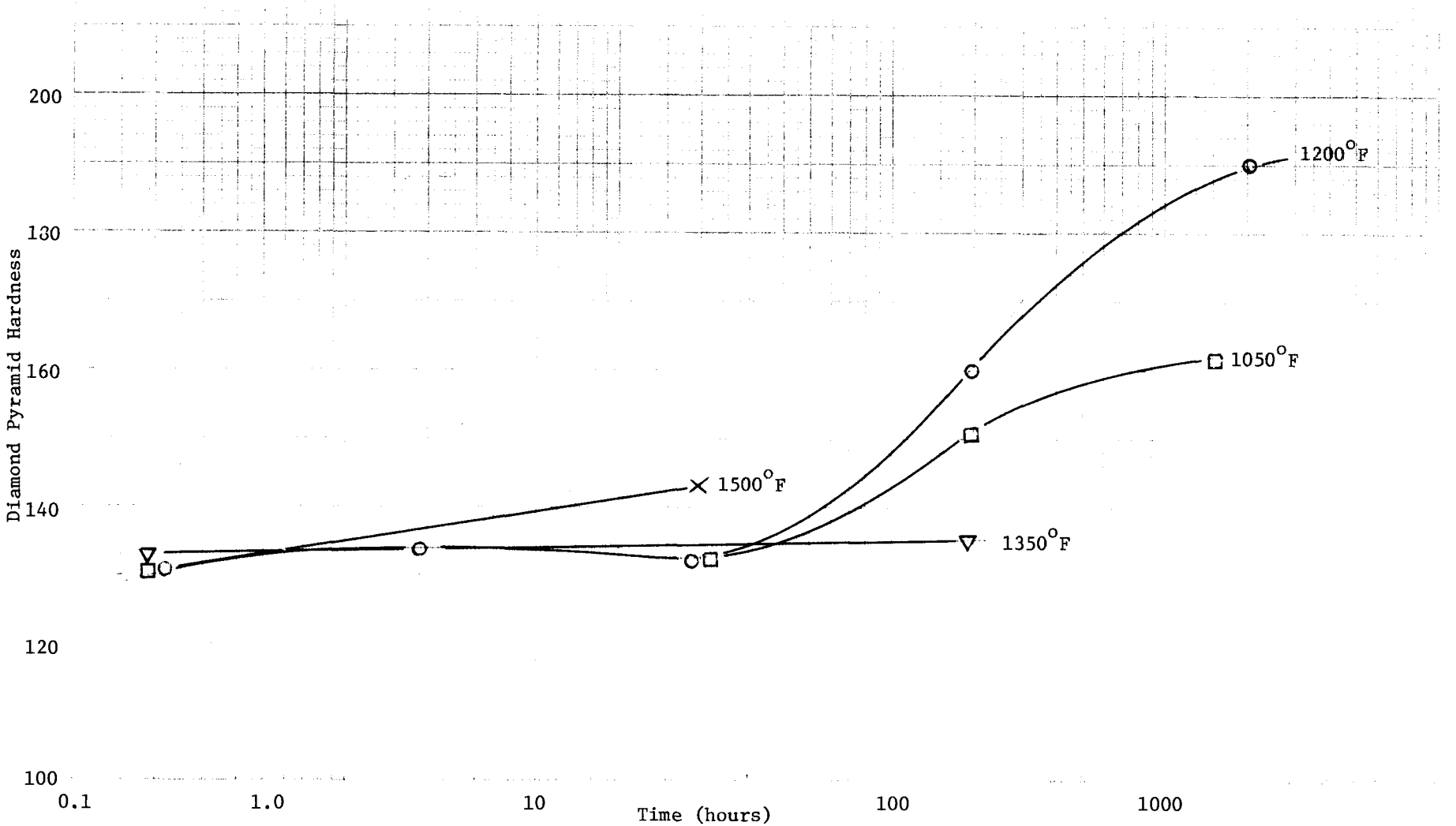

Fig. 2.6 Aging Response of Solution Treated Alloy 800 Heat HH 3539.
Heat treated 1 hour at 2100°F and water quenched prior to aging.

5. Grain growth begins around 1650°F in banded regions, but a duplex grain structure often develops because some fine grained regions do not exhibit grain growth.

Comparable conclusions drawn from the microstructure evaluation of the aged solution treated materials of the same heat are as follows:

1. Gamma prime precipitates in the temperature range 1050-1200°F after 15 hours.
2. The gamma prime precipitate results in increasing hardness as in the prior case for annealed Alloy 800.

Similarities between the aging response of annealed and solution treated Alloy 800 found in this work to date generally agrees with the prior work at General Electric[7] where mechanical property tests and electron microscopy were used to follow the aging behavior.

The third and final item under the microstructure and thermal stability subtask in which progress was made is the grain size study. The hardness response to heat treatment time and temperature was presented previously[8] for most heats under investigation. This quarter we measured the resulting grain size achieved. Longitudinal sections from the tubing samples were mounted and polished prior to measuring the Vickers microhardness with a 2-1/2 Kg load. Coupons of other product forms were polished without mounting and Rockwell hardness measurements made using either the "B" or "C" scales. Comparison of trends were made by plotting the Vickers Hardness Number based upon the ASTM conversion for nickel based alloys[10].

Table 2.4 summarizes the prior hardness response of a low- and high-carbon heat of Alloy 800. The initial hardness of the 35% CW high carbon heat is higher than the low carbon heat. No appreciable softening occurs at either 1500°F or 1750°F for times to 4 minutes; however, in 16 minutes at 1750°F both alloys have VHN of ~ 150. The same time at 2000°F lowers the value slightly from the 150 VHN. On the contrary, within 0.5 minutes at 2000°F the hardness level has decreased to ~ 150 VHN and after 16 minutes the hardness is 135 and 152 VHN for heats HH 7094 and HH 6573, respectively. Thus, the hardness behavior of the high and low carbon heats is quite similar.

Table 2.4 Hardness of Annealed Alloy 800 Following 35% Cold Working and Subsequent Annealing Treatments

Heat	Cold Work (%)	Temperature (°F)	Average Hardness Before Anneal (R_c)	Hardness After Time[a] ½ Min	2 Min	4 Min	16 Min	Converted Vickers Hardness After Time[b] ½ Min	2 Min	4 Min	16 Min
7094	35	1500	22	17 19	93.3 23	96 23	95.7 18.3	225	228	235	225
		1750	22	16 21	14 22	21 100	78 77.7	224	223	248	149
		2000	22	81 78	74.6 74.6	71.6 74.3	73 74	151	135	130	135
6573	35	1500	23.6	99	25	23.3	48.7	241	262	255	245
		1750	23.6	21	22	24	81	238	247	255	155
		2000	23.6	80.3	77.3	81.3	79.7	151	143	151	152

[a] Average of three measurements per samples. Duplicate samples for heat 7094 only.

[b] Conversion of either Rockwell "B" or "C" as per Table 4 ASTM E 140 for Nickel Based Alloys.

The corresponding grain size information for these two heats is presented in Tables 2.5 and 2.6. A few of these data are plotted in Figures 2.7 through 2.10. These two heats of Alloy 800 showed a large range of grain size for the heat treatments at 1500, 1750, and 2000°F. The normal range of grain size observed was from ASTM 4 to 9, with most individual samples exhibiting a duplex grain structure, where both coarse and fine grains coexist. Banding of the precipitated carbides is one factor contributing to this condition, which is fairly typical of nickel based alloys. The duplex grain structure in the starting plate stock reflects the fact that the material was hot finished annealed prior to receipt, which means that during final working some recrystallization and grain growth occurred.

In an effort to summarize the effects of carbon content on the heat treatment response of the two heats of Alloy 800, we concluded an average or predominate grain size number for each sample following the 16-minute annealing treatment, as listed in Table 2.6. The predominate grain size was based simply upon observations of the duplex grain size in three different areas of the sample (e.g. top right, center and bottom left with respect to a longitudinal plane in the direction of cold working). Figures 2.7 through 2.10 are plots of these average grain size numbers as a function of temperature and heat. These figures thus represent a rather "idealized behavior" from which we hope to conclude the overall effects of carbon and temperature on the recrystallized grain size.

The starting grain size of both heats of Alloy 800 was judged to be ASTM 6.5 although, as noted in Table 2.5, the range of grain size for the two differed (ASTM 4-9 and 5-8). Since cold working would simply distort the existing grains, the initial grain size for each level of cold work would be considered as ASTM 6.5. Figure 2.7 shows that neither heat of material changes grain size appreciably when heat treated without prior cold working. Figure 2.8 illustrates a grain size increase (e.g. a decrease in ASTM Grain Size Number from 6.5 to 4.75) for the 0.07% C heat with increasing annealing temperature, but this increase is not reflected in the data taken on the 0.03% C heat. This behavior is not what we would expect based upon published literature; however, we have not attempted to resolve the conflict to date.

Table 2.5 Grain Size Measurements of Annealed Alloy 800 Following 35% Cold Working and Subsequent Annealing Treatments

Heat	Cold Work (%)	Temperature (°F)	Grain Size Before Cold Working (ASTM No.) Range	Grain Size Before Cold Working (ASTM No.) Average	Range of ASTM Grain Size After Annealing Time[a] ½ Min	2 Min	4 Min	16 Min
HH 7094	35	1500	4-9	6.5	6-7	6-7	4-8	4-8
					3-7	7	5-8	4-7
		1750	-	6.5	5 & 7	3-7	7-8	6-9
					-	1-8	6-7	6-8
		2000	-	6.5	6-7	4-7	6 & 8	4-8
					8	5-8	7-8	4-8
HH 6573	35	1500	5-8	6.5	5,6&8	2,3&8	4-8	4-8
		1750	-	6.5	5-6	6 & 8	6-7	6-7
		2000	-	6.5	5 & 8	5-6	6	6-8

[a]Range of grain size concluded based upon 100X observation of three areas of samples with duplex grain structures.

Table 2.6 Grain Size Measured for Heat Treated Samples of Alloy 800 Containing Zero, 15, and 60% Cold Work

Heat	Cold Work (%)	Temperature (°F)	Range of ASTM Grain Size After Annealing Time (ASTM No.) ½ Min	2 Min	4 Min	16 Min	Predominate Grain Size After 16 Min Anneal
HH 7094	0	1500	5-8	8	5-8	5-8	6
		1750	6-8	8-9	4-8	5-8	6.5
		2000	6-7	7-8	4&8	2-8	5.5
	15	1500	7-8	5-7	7-8	4-8	6.25
		1750	6&8	5-7	6	7-8	7.5
		2000	7-8	5-8	7-8	5-8	6.5
	60	1500	6-7	4-5	6-7	7-8	6.5
		1750	6-7	7	6-7	8-9	8.5
		2000	8	-	5-9	4-8	6
6573	0	1500	6&8	8	7-8	7-8	5.5
		1750	8	7-8	-	4-7	5.5
		2000	8	5-7	-	8	7
	15	1500	6-7	6	6-7	3-7	5.5
			4-5	3&6	-	3-8	-
		1750	6	7-8	5-6	3-7	4.75
			-	6	6	3-6	-
		2000	6-7	5-7	6	2-7	4.75
			6-7	5-6	6	5-7	-
	60	1500	5	4,6,7	4-6	4-5	6.5
		1750	5-6	-	5	9	9
		2000	4-7	8-9	8-9	8-9	8.5

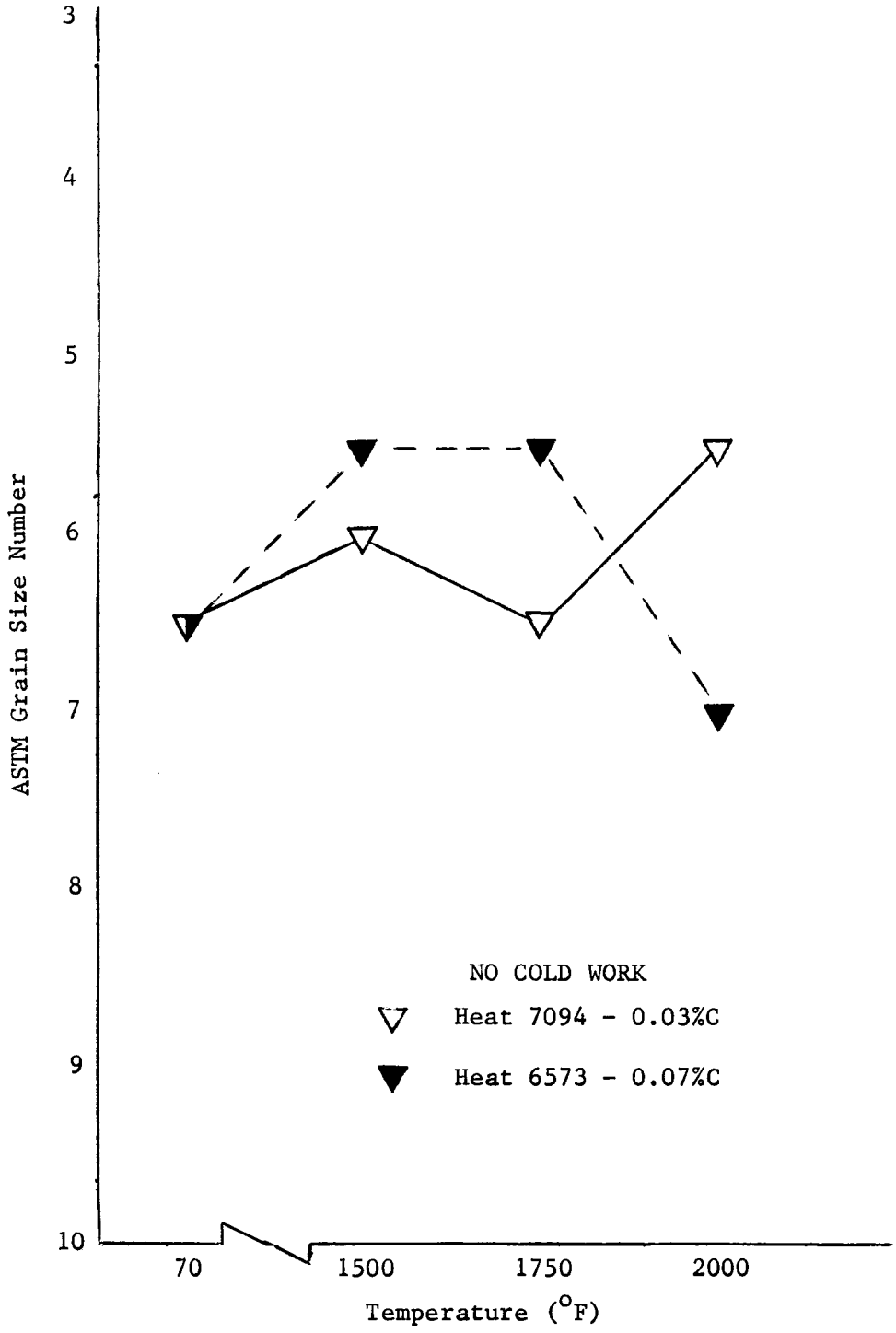

Fig. 2.7 Average Grain Size for Non-Cold Work Alloy 800 Following a 16 Minute Anneal

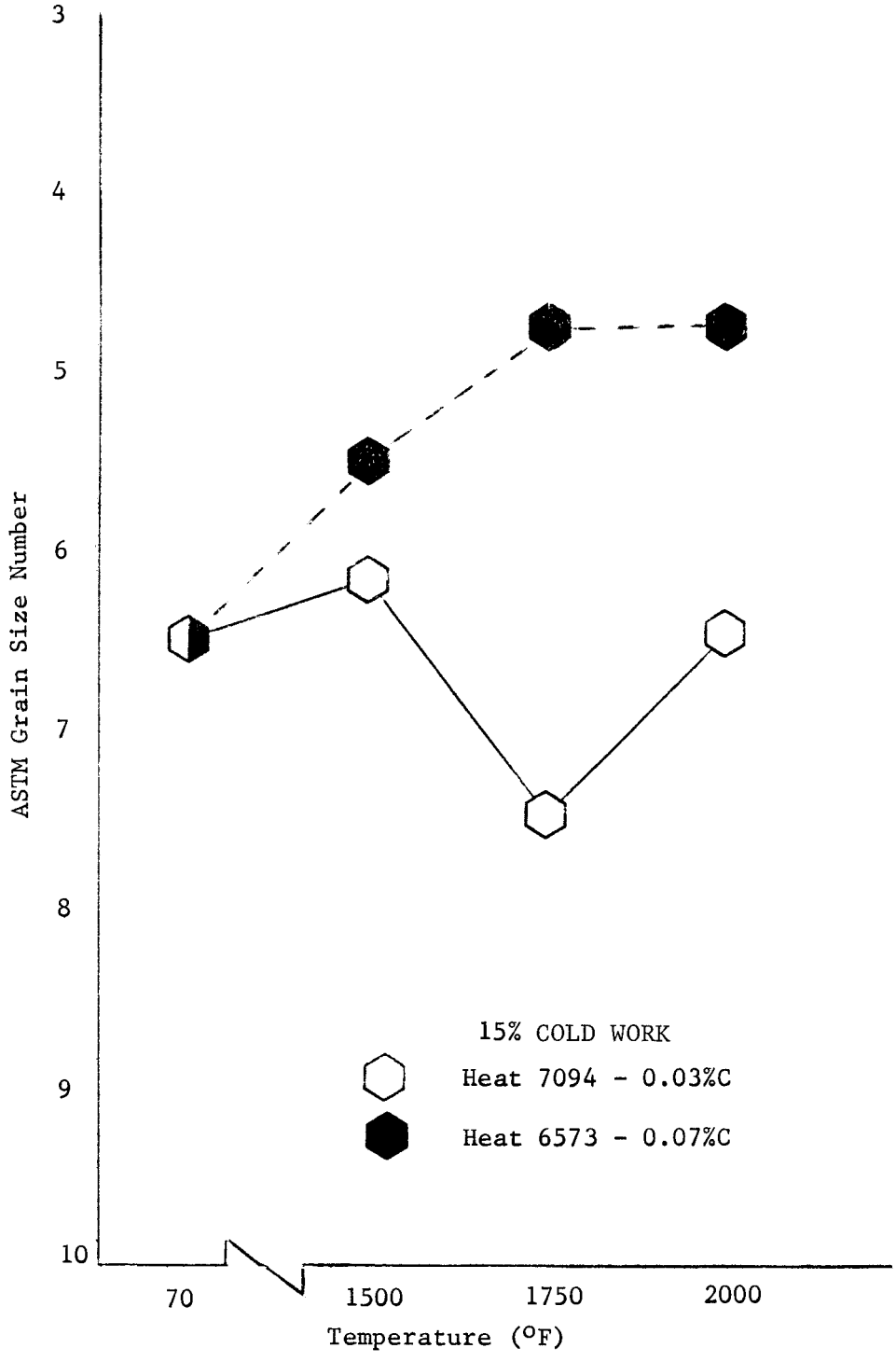

Fig. 2.8 Average Grain Size for 15% Cold Work Alloy 800 Following a 16 Minute Anneal

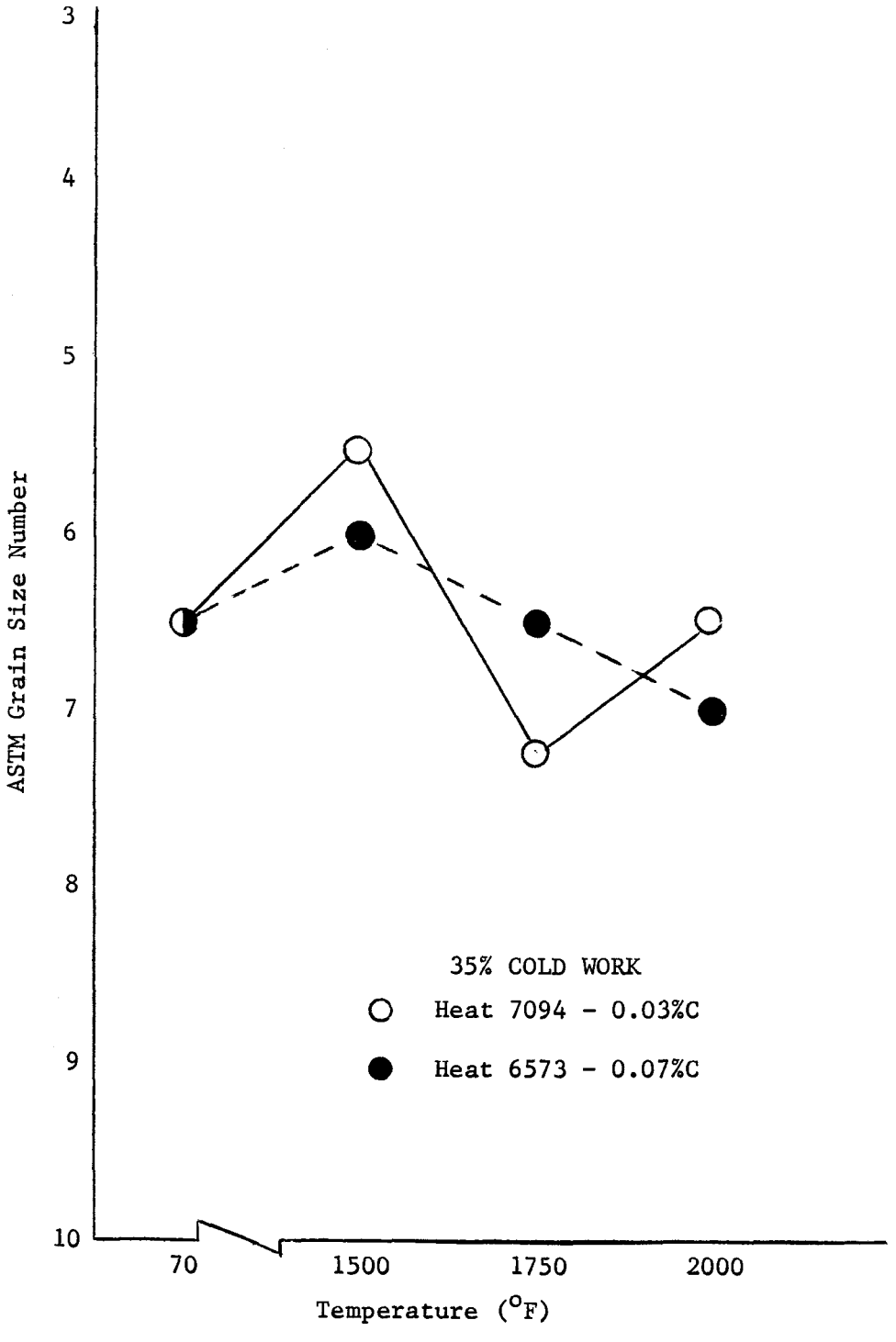

Fig. 2.9 Average Grain Size for 35% Cold Work Alloy 800 Following a 16 Minute Anneal

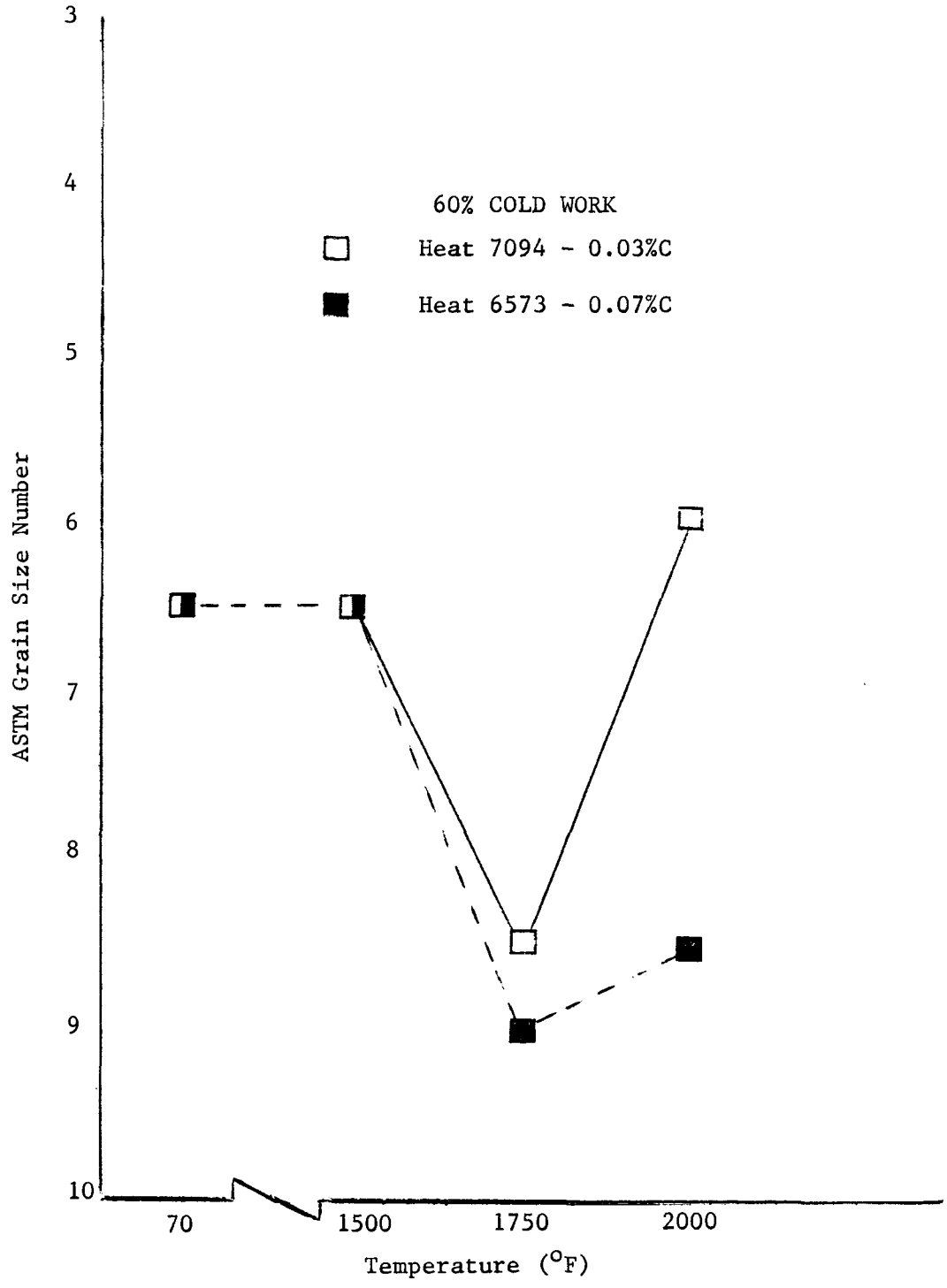

Fig. 2.10 Average Grain Size for 60% Cold Work Alloy 800 Following a 16 Minute Anneal

Figure 2.9 illustrates the results obtained for the heats containing 35% prior cold work that could be correlated with hardness data in Table 2.4. The figure indicates that there is only a small change in the average size when the starting grain size is compared to that obtained after annealing 16 minutes at 1500°, 1750° or 2000°F. Based upon the abrupt hardness drop with annealing temperature at 1450°F reported previously[8] and the observation that some grain growth occurs at 1650°F in fine grain regions of heat HH 3539 (previous section), the results in Figure 2.9 are rather surprising. Since the measured grain size at 1500°F averaged 5.5 and 6.0, respectively, then obviously neither heat recrystallized. Since the hardness dropped sharply at 1450°F for heat HH 7094[8], then we must conclude that the major change in the hardness during annealing of 35% cold worked Alloy 800 is attributable to recovery processes rather than to recrystallization per se. At 1750°F the recrystallization process in the low carbon heat is reflected in the grain size measurements, but not for the 0.07% C heat. At 2000°F both heats reflect a recrystallized microstructure.

The behavior of the two heats for 60% cold work is typical of that suggested in the published literature. Both heats exhibit a large decrease in grain size at 1750°F which correlates with complete recrystallization. At 2000°F the data suggest grain coarsening for the low carbon heat with little or no change in the recrystallized grain size of the 0.07% C heat as compared to the response at 1750°F. Again the observations suggest that recrystallization does not occur in 16 minutes at 1500°F for either heat.

Microstructures of a few of the heat treated coupons are illustrated in Figures 2.11 through 2.13. There is little apparent difference between Figure 2-11 (a) and (b) for Heat 7094 before and after heat treatment for 16 minutes at 1350°F. Both samples received 35% cold deformation. Figure 2.12 is the same heat for 60% cold work after annealing 16 minutes at 1750° and 2000°F. A grain size difference is readily apparent. Identical histories are shown in Figure 2.13 for the 0.07% C heat (HH 6573). Notice the "ghost" boundaries caused by precipitation on prior grain boundaries and the newly recrystallized grains which are much finer. Also note the finer grain size in

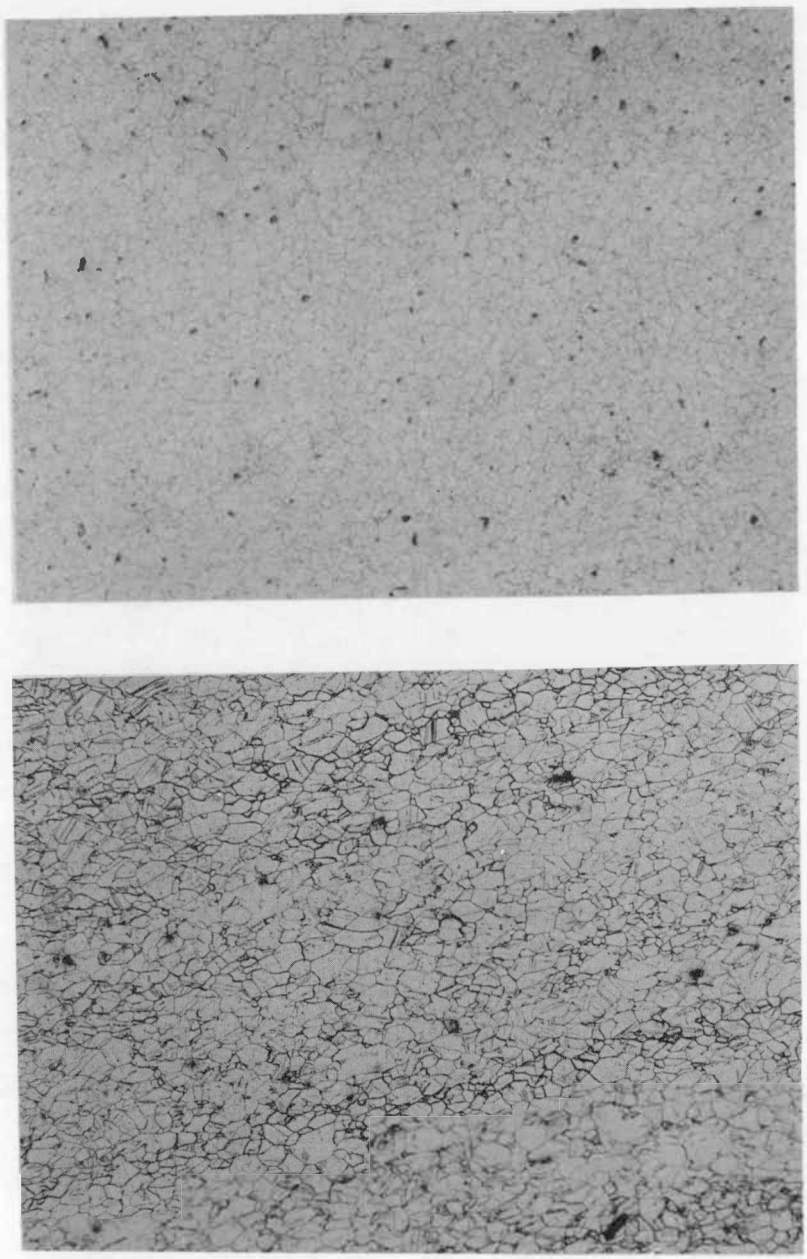

Fig. 2.11 Alloy 800 Heat HH 7094 Samples Containing 35% Cold Work. (a) Coupon after cold working (100X), and (b) Coupon after 16 mins. at 1350^{O}F (100X).

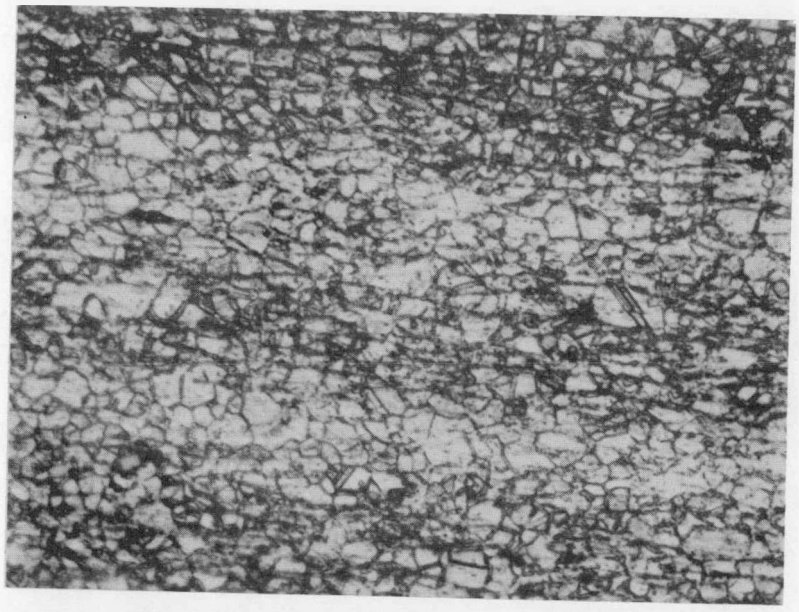

(a)

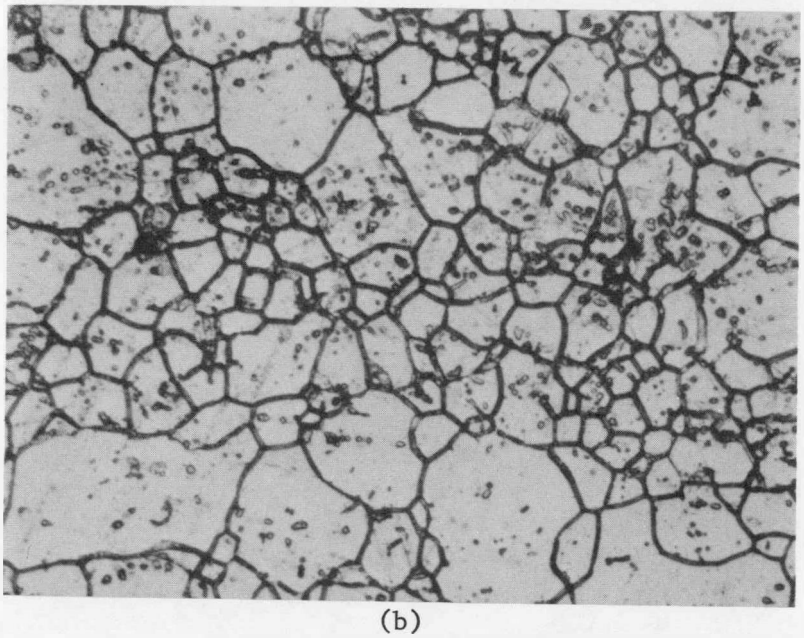

(b)

Fig. 2.12 Samples of 60% Cold Worked Heat HH 7094 Following Heat Treatment for
(a) 16 Min. at 1750°F (400X), and
(b) 16 Min. at 2000°F (400X).

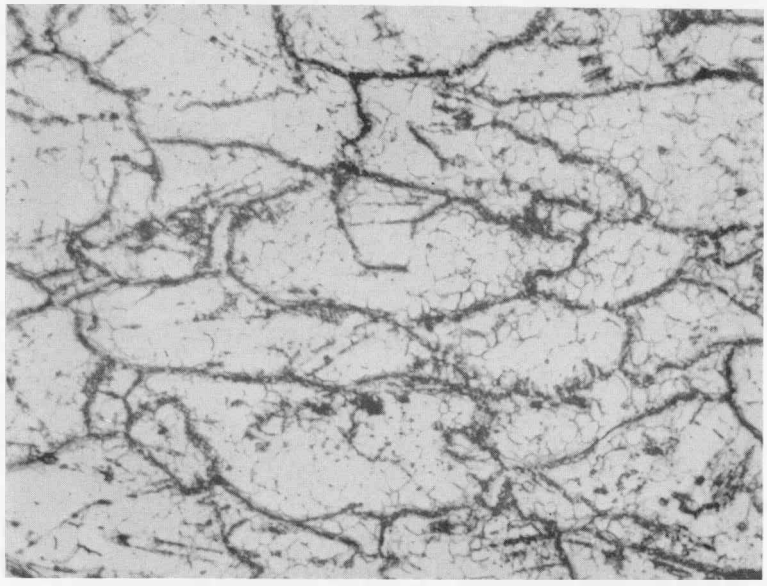

(a)

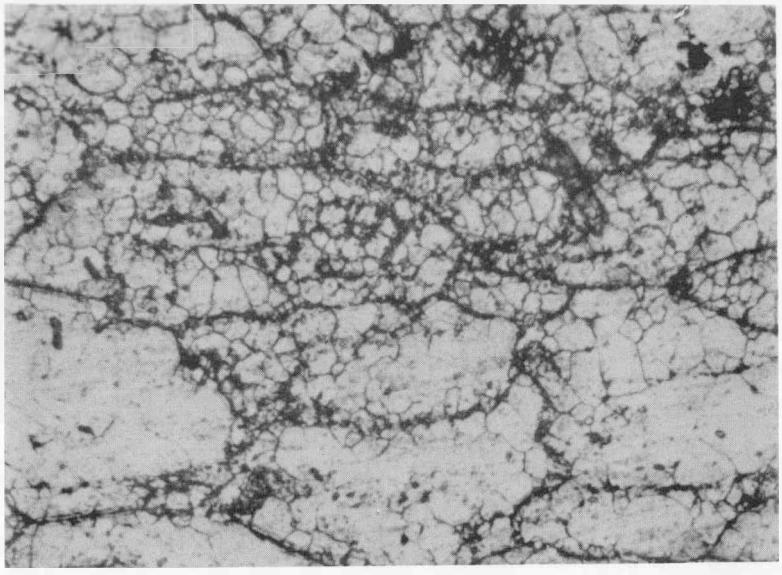

(b)

Fig. 2.13 Samples of 60% Cold Worked Heat HH 6573 Following Heat Treatment for
(a) 16 Min. at 1750°F (400X), and
(b) 16 Min. at 2000°F (400X)
Note the Ghost Grain Boundaries and Recrystallized Grains.

Figure 2.13(b) as was illustrated in the plot of average grain size for the 60% cold worked conditions in Figure 2.10 at 2000°F.

2.3.1.4 Package for Code Acceptance - (Scheduled for FY-1977 Initiation)

2.3.1.5 Mathematical Models for Design Analysis - (Scheduled for FY-1978 Initiation)

2.3.1.6 Prototypic Weld Metal Behavior - (Scheduled for FY-1979 Initiation)

2.3.2 Role of Tertiary Creep - P. J. Langford

Code Case 1592 of Section III of the ASME Boiler and Pressure Vessel Code contains limiting values of stress intensity applicable to both time-independent and time-dependent loading of Class 1 vessels intended for elevated-temperature service. Code approval for use of Alloy 800 as a material for advanced LMFBR steam generators requires establishment and justification of basic allowable limits for each loading category. The criteria to establish the basic time-dependent stress allowable, S_t, reference (1) creep rupture, (2) accumulation of a total strain of 1% and (3) the initiation of tertiary creep. When applied to annealed Alloy 800, extrapolation of time to initiation of tertiary creep from the available test data yields low stress allowables relative to those based on the time to rupture and remaining ductility. Establishment of reasonable allowables will require additional test data justifying a less conservative extrapolation and/or modification or deletion of the existing design criterion.

Extrapolation of creep tests at temperatures above 704°C (1300°F) drastically underpredicts the rupture life at 593°C (1100°F). Consequently, much longer test times and tests at low temperatures are needed to obtain Code approval of Alloy 800. Because of the time and cost associated with obtaining the data, and due to the lack of technical justification and/or consensus of the use of the tertiary creep criterion, the program includes both data generation as part of the Material Characterization task (Section 2.3.1), and a review and evaluation of

the Role of Tertiary Creep in establishing the design allowables for the annealed material.

The criterion considering tertiary creep was imposed based on concerns related to 1) metallurgical factors, 2) failure in multiaxial conditions, and 3) design analysis techniques. Each of these concerns is addressed separately. Completion of this three-part task is expected to insure Code acceptance of annealed Alloy 800 with reasonable time-dependent allowables. Progress to date supports attainment of objectives for each of the three developmental efforts.

1. In terms of metallurgical implications, the onset of tertiary creep was assumed to indicate the initiation of the fracture process. Concerns of microcrack formation and coalescence of voids leading to material failure contributed to inclusion of the present criterion restricting material usage following deviation from the minimum creep rate. Subsequent usage of material following initiation of tertiary creep therefore was postulated to correspond to use of damaged material. These concerns were unsubstantiated, and the objective of the initial subtask is to demonstrate material acceptability subsequent to the present definition of tertiary creep initiation for those allowables limited by the existing criterion.

   The shape of creep curves, and hence the limiting allowable, has been related to material composition, operative deformation mechanism, temperature, and loading stress. No implications of material damage can be ascribed to these factors well beyond the point where the current arbitrary limit is imposed because of deviation from linearity in a constant load test. Further, the existing criterion has no consistent interpretation for nonclassical creep curves which do not have three well defined stages of creep. Low times to initiation of tertiary creep resulting in time-dependent allowables restricted by the existing criterion have been shown to result from a range of curve shapes which are predominantly nonclassical. The existence of competing creep deformation mechanisms also has been established, and the difficulties previously encountered in extrapolation are to be expected, particularly at temperatures around $1100^{o}F$ ($593^{o}C$).

The present initiation of tertiary creep criterion therefore is concluded to be related to arbitrary metallurgical factors controlling the shape of constant load creep test strain-time curves, and not to be related to material damage or necking.

2. The second concern leading to inclusion of the present criterion as a factor for limiting primary time-dependent allowables was related to the correlation of failure of multiaxial creep test capsules to the onset of third-stage creep exhibited in uniaxial tests. Local necking and cracking in a uniaxial test were presumed to correspond to leaking in tubular creep tests, and again the onset of tertiary creep was assumed to be related to a failure process without consideration of the kinematics of material creep response. The objective in this case is to demonstrate that the present criterion does not correlate multiaxial creep failure with deviation from second-stage creep in uniaxial tests.

   Results of tests from the only located reference reporting correlation have been discounted owing to specimen design. The reported cylinder wall thickness was comprised of less than four grains, and continuum assumptions inherent in correlation of resulting biaxial leak/failure data with results of uniaxial creep tests therefore are violated. No justifiable basis for correlation of multiaxial creep failure with the existing tertiary creep criterion has been identified.

3. The final factor proposed as justification for the present criterion was related to the effect on design and analysis if deviation from second-stage creep were allowed. A postulated physical mechanism of accelerated strain concentration due to increasing strain in the tertiary region of a uniaxial test was precluded in design to primary loading allowable limits. The criterion was included to prevent excessive strain accumulation resulting from cycling weakened material due to strain softening as well as to prevent tensile instability due to elevated temperature loading. Related concerns of inability to analyze material response having increasing strain rates with increasing strain contributed to use of the criterion in establishing primary time-dependent allowables. The objective of the third

subtask is demonstration that design and analysis can be performed beyond deviation from the minimum creep rate without material or analytical instability and the accumulation of error in analysis.

Preclusion of tensile instability at elevated-temperature loads is considered to be effected by criteria based on rupture and total strain. Existing references demonstrate the capability of analyses considering accelerated strain rates for noncyclic loading. The capability for such analysis for general cyclic, nonradial history-dependent loading considering hardening and creep-plasticity interaction is not considered to be an appropriate factor for establishing allowables as long as creep strain is accounted for in design and analysis. A consistent means of accounting for strain beyond the existing limit in establishing allowables and in formulation of constitutive theories used in analysis has been proposed, and the need for the present arbitrary criterion for its impact on design analysis is negated.

The existing criterion is consequently either not related to or overly conservative with respect to prevention of the phenomenon for which it was intended and revision of the current definition and interpretation should be pursued.

Further details of progress related to evaluation of each of the three regions of concern are provided in the following three subsections.

2.3.2.1 Metallurgical Implications - P. J. Langford, D. M. Moon, and D. H. Harrod

In terms of metallurgical factors, the onset of tertiary creep was assumed to be the initiation of the fracture process. This subtask addresses the acceptability of use of the material after the onet of tertiary creep as presently defined. Consideration is given to the specific alloy as well as the behavior of materials currently accepted for use in Class 1 Nuclear Components in Elevated Temperature Service.

Background

One of the three general factors responsible for inclusion of a tertiary creep criterion in establishing design allowables for elevated-

temperature service was the metallurgical concern of microcrack formation and coalescence of voids leading to material failure. Subsequent usefulness of a material following initiation of third-stage creep was therefore postulated to be related to observable phenomena considered to indicate material damage. The onset of tertiary creep therefore was assumed to be directly related to a failure process, but no reflection of the kinematics of the material creep response was considered explicitly.

Definition of a criterion to preclude such material damage was arbitrarily set at the point of deviation of second stage creep in a uniaxial creep test. However, this approach was subject to uncertainties in definition of second stage creep, and a modification was adapted wherein the limit was set by using 0.2% strain offset from the linear portion of the creep curve. This technique allowed for more consistent selection of the "onset of tertiary creep" for a given curve, but the results are not consistently reproducible as are yield stresses defined by an offset approach. The present criterion therefore is somewhat arbitrary in that it does not correspond to a readily measurable property of the constant load creep response.

Consideration of metallurgical implications in defining the proper role of tertiary creep also is required regardless of damage or material property implications. The practical impossibility of obtaining all long-time low-temperature strain data directly from constant-load creep tests requires use of extrapolation procedures to predict this data from short-time high-temperature and/or high-load test results. Based on existing data, extrapolative procedures which predict reasonable tertiary creep limits cannot be justified and those which are considered conservative yield unreasonably low basic allowable S_t values. A sufficient understanding of the metallurgy of the material to allow justifiable extrapolation into the temperature-stress range of intended use is imperative.

Objectives

Determination of the acceptability of using Alloy 800 after the onset of tertiary creep, as presently defined, based on relevant metallurgical implications, is the objective. Demonstration of acceptability is to be

achieved through 1) metallographic observations, 2) mechanical testing, and 3) phenomenological observations related to the shapes of constant load creep curves. Following a review of literature from which 1) conventionally acceptable or potential causes of third-stage creep initiation, and 2) mechanical properties indicative of material usefulness will be identified, a testing and evaluation program will be completed to identify the viability of Alloy 800 for subsequent use after the existing Code limit is exceeded. Conditions for which 1) no acceptable metallurgical bases connoting material instability or damage are observed, and 2) no significant reduction in mechanical properties occurs will be considered to imply material viability in the absence of substantiated indications of damage.

Results of these observations and tests then will be correlated with available information on creep behavior kinematics for Alloy 800 as well as for other currently Code approved materials. Implications of a proper role of tertiary creep thereby will be demonstrated in relation to the creep response of other materials as exhibited by constant load creep curves.

Progress

Previous development has resulted in identification of possible phenomenological explanations for early initiation of tertiary creep as presently defined. In particular, the shapes of creep curves are noted[12] to be a function of the type alloy, prior thermomechanical history, the operative deformation mechanism, and the external variables of temperature and loading stress. Expectations that a typical or classical creep curve exhibiting well defined stages of primary, secondary, and tertiary creep will be obtained for all test conditions are considered to be unjustified. A basic allowable criterion for which material damage is implicitly related to such an assumption therefore may be unduly restrictive.

These observations were related to the referenced creep curve shapes shown on Figure 2.14 and the factors contributing to the shapes as described by Bird, Mukherjee, and Dorn[12] and Harrod[13]. They were further

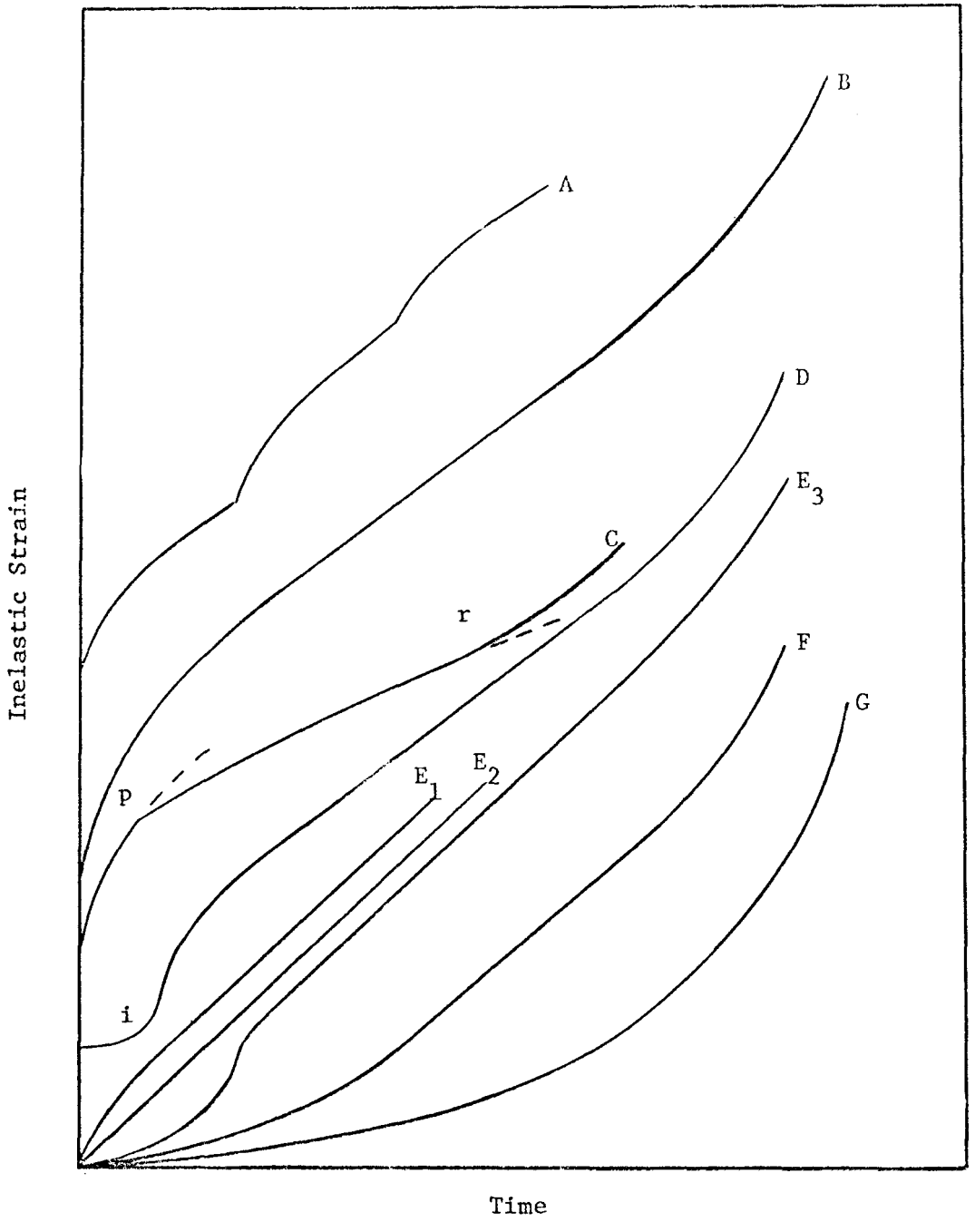

Fig. 2.14 Typical Creep Curves with Assigned Type
(After Bird, Mukherjee, and Dorn[12])

related to the existence of gamma prime $Ni_3(Al, Ti)$ precipitation as a creep strengthening[14-17] mechanism in Alloy 800 as described in the literature and as observed[18] in testing and metallographic observations. The shape of constant load creep curves, and hence the current limit, therefore was related to composition, deformation mechanism, and the test variables of temperature and stress with no implications of material damage.

Similar observations have been reported for other materials. Non-classical creep curve shapes for 2-1/4 Cr-1 Mo have been related[19] to precipitation reactions and deformation mechanisms. The present tertiary creep criterion also is not coincident with necking or crack formation for 2-1/4 Cr-1 Mo, and is not indicative of useful life of the material.[20] It has also been noted[21] that four stages of creep have been identified in a Russian works and damage is considered to begin at the fourth stage rather than at the point of deviation from linearity.

Additional testing and metallography of results of 13 tests on 11 heats of material crept at 1100°F (593°C) and 35 ksi (241.3 MPa) are completed and evaluation is in progress. Implications of these results which extends those reported previously for 4 of the 11 heats will be addressed in subsequent reports.

Previous development of phenomenological explanations for the impact of the present tertiary creep criterion has continued. The existing criterion has been shown to have no consistent interpretation for non-classical creep curves. Further, low ratios of tertiary creep initiation times to rupture lines for Alloy 800 have been shown to result from a range of nonclassical curves (see Figures 2.10 - 2.13) (Ref. 22). Figure 2.15 is illustrative of this fact: rupture data for which the ratios of tertiary to rupture times are less than 0.4 are indicated by denoting the curve shape by the data point where the curve shape is as shown on Figure 2.14. The consistency of the illustrated rupture data in spite of the random shapes of creep curves is of interest. Table 2.7 is the corresponding chemistry and specimen identification legend. The relationship of creep deformation mechanisms and test conditions such as strain on loading to the noted curve shapes and tertiary initiation times

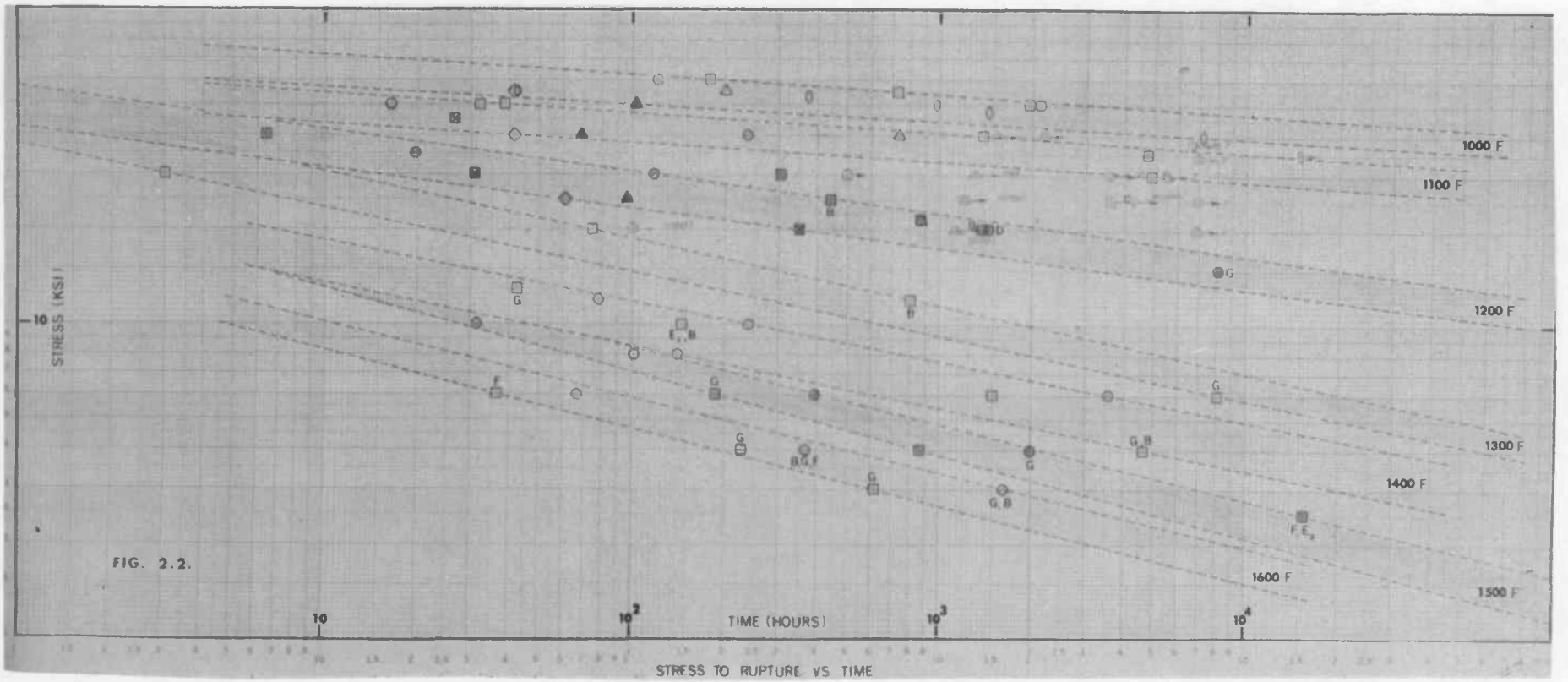

Fig. 2.15 Stress-Rupture Data for Annealed Alloy 800 Including HAPD and Westinghouse Results

Table 2.7 Specimen and Chemistry Identification Legend

Symbol	Heat*	Specimen Type	Composition (Weight Percent) C	Ti	Al	Nb	Al+Ti	Effective (Al+Ti) (Atomic Percent)
◇	2658	Cold-Drawn Tube	.08	.32	.21	-	0.53	0.68
⬡	8311	Cold-Drawn Tube	.09	.40	.42	-	0.82	0.94
▽	7382	Cold-Drawn Tube	.07	.52	.52	-	1.04	1.38
○	8735	Cold-Drawn Round	.04	.39	.29	-	0.68	0.88
□	8808	Hot-Rolled Plate	.05	.51	.51	-	1.02	1.44
⊠	1929	Cold-Drawn Tube	.04	.41	.42	-	0.83	1.18
△	5959	Cold-Drawn Tube	.04	.50	.43	-	0.93	1.06
⛢	5341	Cold-Drawn Tube	.03	.37	.46	-	0.83	1.27
✡	6625	Cold-Drawn Tube	.06	.56	.54	-	1.10	1.52
⊕	7391	Cold-Drawn Round	.07	.53	.52	-	1.05	1.39
⬯	5464	Cold-Drawn Tube	.06	.45	.44	-	0.89	1.14
◇	5475	Cold-Drawn Tube	.08	.42	.57	-	0.99	1.28
▱	7097	Cold-Drawn Tube	.03	.38	.30	-	0.68	0.91
△	6451	Cold-Drawn Tube	.02	.54	.34	-	0.88	1.23
⌂	6729	Hot-Finished Round	.02	.54	.27	-	0.81	1.08
◺	5501	Hot-Finished Round	.07	.44	.38	-	0.82	0.96
◇	7094	Hot-Finished Round	.03	.41	.38	-	0.79	1.11

*Huntington Alloys Products Division designation HH.

will be addressed in subsequent development following more accurate identification of the gamma prime precipitation regime and receipt of additional data.

One further important conclusion evolves from consideration of the role of $Ni_3(Al,Ti)$ precipitation in establishing the creep response of this material: available data for which the tertiary creep criterion adversely affects setting basic allowables have been shown[22] to apply to a time-temperature-stress regime for which the creep strengthening mechanism is solid solution hardening alone, whereas the intended use conditions are in a regime for which precipitation hardening plays a major factor in establishing creep properties. Extrapolation of data from one regime into the other is therefore to be avoided without metallurgical justification and earlier Alloy 800 data packages were severely penalized in this respect. Penalties are expected to be particularly severe at about 1100°F (593°C) where the strengthening effects of gamma prime are a maximum. It should be noted that precipitation kinetics and composition influence the fit of empirical correlations relating rupture and creep properties of 2-1/4 Cr-1 Mo steel.[23]

2.3.2.2 Correlation with Multiaxial Failure - R. L. Flury and P. J. Langford

The second concern leading to the present tertiary creep criterion relates to the correlation of failure in multiaxial creep tests to the onset of tertiary creep obtained in uniaxial tests. This is based on a rationale that local necking and cracking occur during tertiary creep such that a leak would be experienced in a tubular creep test at the corresponding time. Again, the onset of tertiary creep is assumed to be directly related to a failure process rather than a reflection of the kinematics of the material creep response. The design criteria must protect against this type of failure in fast reactor systems, particularly when the heat transfer fluids are as reactive as sodium and water. The second subtask addresses the relationship of the existing tertiary creep definition with material failure or rupture in multiaxial stress states. Demonstration that the existing criteria is not required or is overly conservative for such design criteria is the objective.

Background

One principal explanation offered in defense of inclusion of the existing tertiary creep criterion is that material rupture under multiaxial stress conditions may be related to the initiation of tertiary creep rather than to rupture as obtained from a uniaxial test. Limiting code allowables are based upon uniaxial data. Relating such data to the physical world of multiaxial stress states typical of biaxial conditions in vessel shell and steam generator tubing, and multiaxial conditions common to head-shell junctions, nozzle-head junctions, tube-tubesheet weld zones, and other discontinuities exhibiting strain concentration requires the use of proven failure theories. These theories typically relate time to rupture (t_R) and/or strain at rupture (ε_R) using appropriate failure and damage criteria. Concerns that multiaxial failure may be more properly related to initiation of third-stage creep than to rupture data obtained from uniaxial tests can be resolved with multiaxial test data. This second subtask addresses resolution of these concerns.

Objective

The objective of this task is to demonstrate that the existing definition of the initiation of tertiary creep does not correlate with material failure or rupture for multiaxial stress states. Test results will be compared with cumulative damage theories in order to achieve this goal.

Progress

Demonstration that the existing definition of tertiary creep initiation is not correlable with failure in multiaxial stress states began with a review of literature and initiation of a biaxial creep test program. Only one reference[24] was located in which multiaxial creep failure was correlated with tertiary creep as determined from uniaxial tests. However, validity of conclusions based on this frequently cited reference to 316 stainless test capsules are at least questionable as a result of specimen configuration: the reported cylinder wall thickness of 20 mils is so thin that less than four grains (ASTM 3) on the average comprised the wall thickness. Continuum assumptions inherent in

correlation of resulting biaxial leak/failure data with results of uniaxial creep tests are therefore violated. Resulting influences of grain boundary orientation and differences in local ductility at triple points and the surrounding matrix could possibly account for correlation in this one instance.

No additional effort has been expended on multiaxial failure correlation during the last two reporting periods. Annealed Alloy 800 specimens of two types had been machined and instrumented for biaxial creep testing along with supporting uniaxial tests on specimens of the same material. These included three basic thin flat plate specimens that assume different biaxial stress states through end constraint when tested with uniaxial test machines. Secondly, four tubular creep rupture specimens (see Figure 2.16) were rough-machined, and qualifications for welding the end caps were essentially completed. Only welding and final machining of these specimens to a wall thickness of 50 mils are required to initiate testing. Additional details are given in the previous report.[25]

2.3.2.3 Effect on Design Analysis - C. F. Uber, R. L. Flury, and P. J. Langford

The third concern regarding design analysis deals with a postulated physical mechanism of accelerated strain concentration due to the increasing strain in the tertiary region of a uniaxial creep test. A second related concern involves the increasing error in prediction of the strain with use of the current model of material behavior representing primary and secondary creep.

Background

The final factor proposed as justification for the present criterion was related to the effect on design and analysis if deviation from second-stage creep were allowed. A postulated physical mechanism of accelerated strain concentration due to increasing strain in the tertiary region of a uniaxial test was precluded in design to primary loading allowable limits. The criterion was included to prevent excessive strain accumulation resulting from cycling weakened material due to strain softening as well as to prevent tensile instability due to long-term

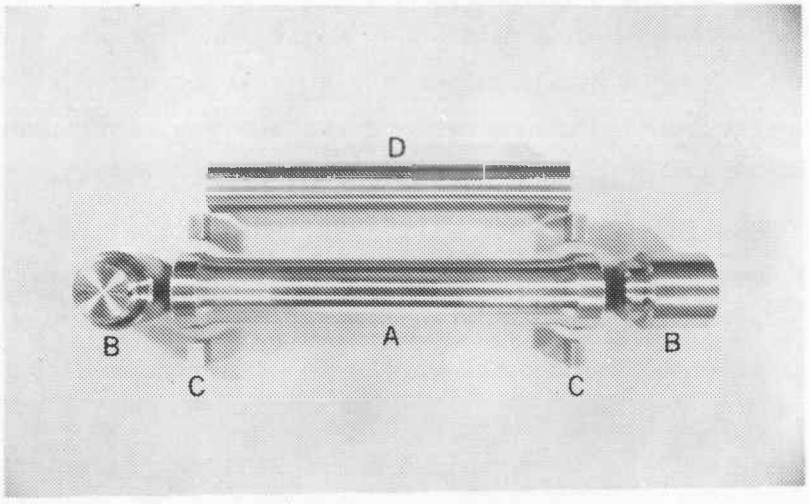

Fig. 2.16 Sample Tubular Creep Rupture Specimen of Annealed Alloy 800 Prior to Welding End Caps and Final Machining (1.25 mm wall x 39 mm dia.).
A. Specimen Body, B. End Plugs,
C. Extensometer Tabs, D. Volumetric Reduction Bar

elevated temperature loading. Related concerns of inability to analyze material response having increasing strain rates with increasing strain contributed to use of the criterion in establishing primary time-dependent allowables.

Objective

The objective of the third subtask is demonstration that design and analysis can be performed beyond deviation from the minimum creep rate without material or analytical instability and the accumulation of error in analysis. Inclusion of accelerating creep strain rates with increasing strain as a part of constitutive theories for design analysis is not necessarily implied by elimination of the existing criterion: accounting for straining beyond deviation from second stage creep can be accomplished without recourse to such an approach unless the strains are excessive (they need not be since all that is required to eliminate need for the criterion is to demonstrate the ability to account for nonlinear strains up to the one percent total strain limit). However, use of such capability for this limited application will demonstrate that modification of the existing criterion does not imply significant instability or error for Alloy 800 and that a more proper role of tertiary creep in establishing allowables is not precluded by analytical limitations.

The approach will be to establish a mathematical relationship to characterize tertiary creep behavior as a function of stress and temperature. It is therefore the intention of this development to demonstrate that the material retains its usefulness beyond the present definition for initiation of tertiary creep and that accounting for creep strain beyond this limit prior to the start of the sharp increase in strain softening is possible. Steps to be followed in implementing this approach include: 1) generation of an analytical model incorporating accelerating creep in the creep equation, 2) demonstration of capability of analysis without instability beyond deviation from second-stage creep, and 3) use of this model to show that excessive strain accumulation or instability is not incurred by relaxing the existing criterion.

Progress

This third subtask concerning the effect of tertiary creep initiation on design analysis has not been addressed in recent development. Previously, an equation was generated[16] for the creep strain which includes a strain-softening term representative of the tertiary creep behavior exhibited by Alloy 800. The equation was then incorporated into a library of user creep subroutines compatible with the major inelastic analysis programs ANSYS and MARC. The strain softening (increasing strain rate with increasing strain) features of this equation are invoked when a function of stress and temperature exceeds the time-to-initiation-of-tertiary-creep function.

Existing references[27,28] demonstrate the capability of noncyclic loading without instability or error. Pugh et al. reported plane strain analysis of thick walled cylinders subjected to constant internal pressure loadings using creep response characteristic of 2-1/4 Cr-1 Mo. Numerically stable results were obtained at increased cost. Hayhurst et al.[28] computed the formation and growth of regions of damage in uniaxially loaded plates containing circular holes as described in relation to the effects of stress concentrations in tension panels.[29] Although the capability of such analyses for general cyclic, nonradial, history dependent loading considering hardening and creep plasticity interaction has not been demonstrated, there has been no motivation for such extensive development. Further, the need for such an approach is eliminated provided that additional strains beyond second stage creep strains are accounted for in design and analysis.

A recent proposal at the meeting of the Ad Hoc Task Group on Tertiary Creep (June 15, 1976) is illustrative of an approach which precludes the need for general strain softening analytical capability associated with an upsweeping creep curve. The critical aspect of the existing tertiary creep criterion was identified to be related to the need for consistent accounting for creep strain in design and analysis. At present the onset of tertiary creep factor used in establishing allowables precludes creep strain which is inconsistent with a classical creep curve. Creep strains are computed using primary plus secondary creep correlations which are

identical to those used in generating isochronous stress-strain curves, and no inconsistency is possible. If deviations from linearity are permitted in establishing allowables, i.e., if the existing criterion is modified, the only requirement is that the increased strain be accounted for in constitutive theories used in analysis.

Figures 2.17 and 2.18 are illustrations of a proposed method for accounting for this strain without requiring creep strain softening capability in analysis. Given a typical nonclassical creep curve response for which the 0.2% offset rate is restrictive in setting allowables such as curve 1 in Figure 2.17, the creep response used in setting allowables can be arbitrarily taken from a modified curve such as curve 2. Improvement in the "time to initiation of tertiary creep" from t_1 to t_2 thereby is afforded, and the assumed creep rate is slightly higher (conservative with respect to strain). Use of this proposal indicates that tertiary creep can in effect be deleted as a criterion for establishing allowables if the corresponding isochronous curves used in analysis are consistently modified to reflect the increased strain at a given load, or the reduced stress for a given strain, as indicated on Figure 2.17. Where modifications of the isochronous curves are required, allowables based on the stress for one percent total strain must be consistently modified. The impact of using this approach on Alloy 800 should yield reasonable allowables since the shape of the creep curves yielding low tertiary creep limits are similar to that illustrated. It should be noted that presentation of the creep characteristics of 2-1/4 Cr-1 Mo at this meeting indicated marked similarities with Alloy 800 with respect to the nonclassical creep response and the proposed method of establishing primary time-dependent allowables also has application to 2-1/4 Cr-1 Mo.

2.3.3 Non-Sodium Environmental Effects - (Scheduled for FY-1978 Initiation)

2.3.4 Sodium Exposure Effects - (Scheduled for FY-1978 Initiation)

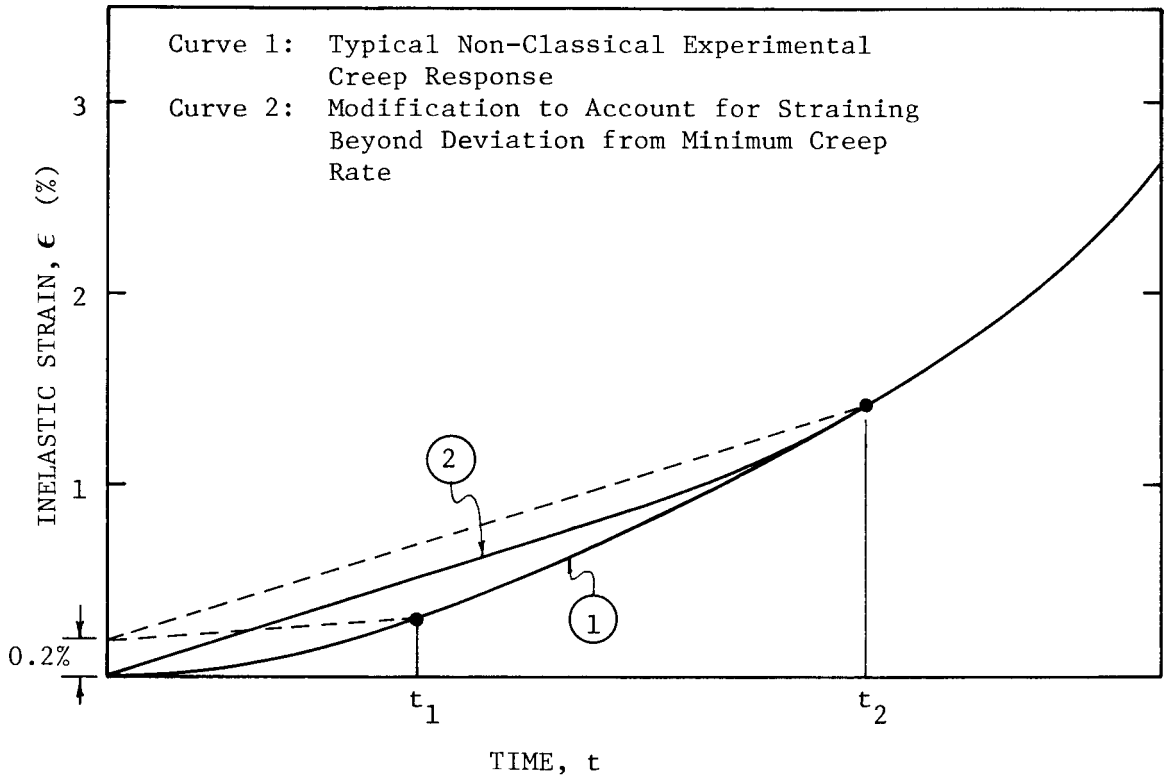

Fig. 2.17 Constant Load Creep Curves

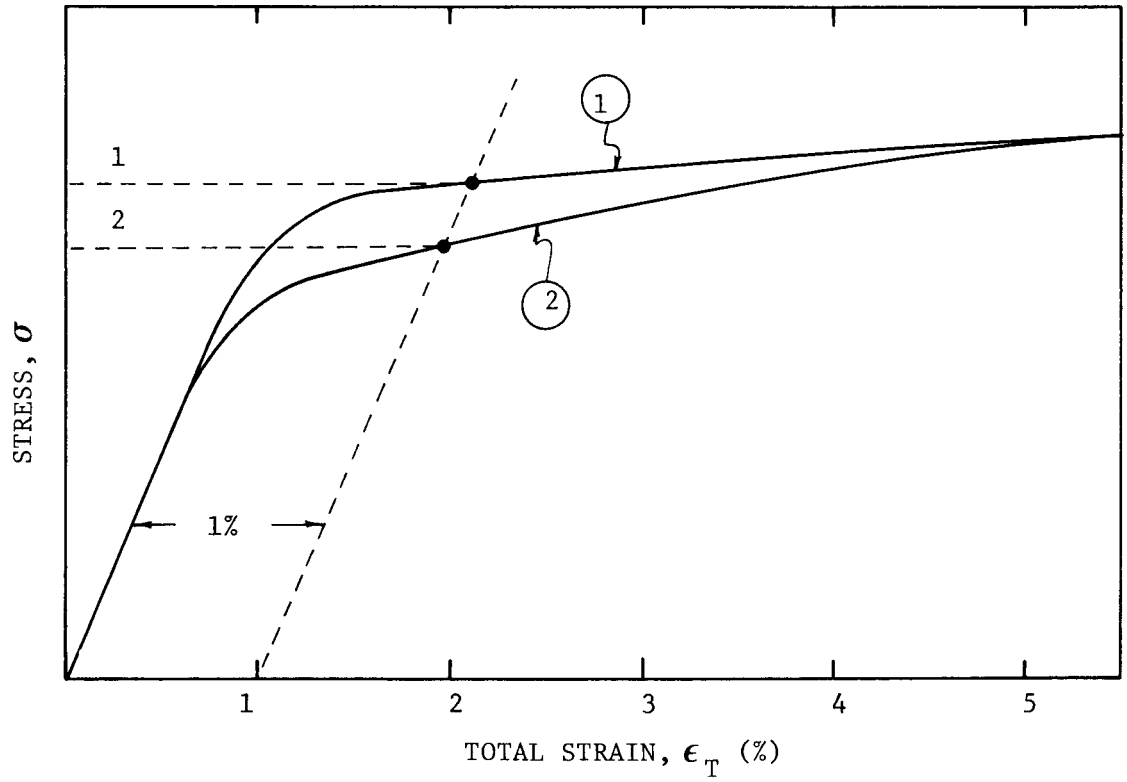

Fig. 2.18 Isochronous Stress-Strain Curves Consistent with Creep Curves

2.3.5 Fabrication and Weld Process Development - (Subtask 2.3.6.1 on Selection of Weld Filler Metal was completed. The remaining tasks are scheduled for FY-1978 Initiation)

2.4 REFERENCES

1. C. E. Sessions, G. Grotke, A. R. Vaia, and I.L.W. Wilson, Review of the Behavior of Alloy 800 for Use in LMFBR Steam Generators, Westinghouse Tampa Division, WNET-115-R1 (February 1976).
2. J. M. Duke, C. E. Sessions, and W. E. Ray, Qualification of Alloy 800 for Sodium Heated Steam Generators, paper presented at International Conference on Liquid Metal Technology in Energy Production, May 3-6, 1976 in Seven Springs, Pa.
3. Fuels and Materials Development Program Quarterly Progress Report for Period Ending December 31, 1968, Oak Ridge National Laboratory, ORNL 4390, pp. 127-134.
4. W. J. Werner, "An Investigation of the Effect of Certain Minor Elements on Elevated Temperature Ductility of Incoloy 800," ORNL 4504 (1971).
5. R. H. Moeller and J. M. Martin, "Optimization of Incoloy Alloy 800 Mechanical Properties for Various Power Plant Requirements," The British Nuclear Energy Society Materials Conference, Status Review of Alloy 800, University of Reading, England, September 25-26, 1974.
6. T. H. Bassford, "Effect of Chemistry and Thermo-Mechanical Processing on the Mechanical Properties of Incoloy Alloy 800 for Nuclear Reactor Steam Generator Tubing," Personal Communication, J. M. Martin, Huntington Alloys, Inc. to J. M. Duke, Westinghouse Tampa Division, March 10, 1975.
7. H. H. Klepfer, K. C. Antony, and U. E. Wolff, "The Influence of Impurities on the Properties of Two Nuclear Reactor Structural Alloys" in Materials Science and Technology For Advanced Application, Vol. II 1964 Golden Gate Metals Conference, San Francisco, California.
8. C. E. Sessions and D. Moon, Liquid Metal Fast Breeder Reactor Materials Development Program, ORNL 5131, pp. 104-119, (December 1975).

9. Summary Status Report - Role of Tertiary Creep, (February 27, 1976) presented to ASME Ad Hoc Task Force on Tertiary Creep.
10. 1973 Annual Book of ASTM Standards, Part 31, Specification ASTM E-112.
11. P. J. Langford, D. M. Moon, and D. H. Harrod, "Metallurgical Implications," Steam Generator Materials Technology Program Quarterly Progress Report for Period Ending June 30, 1975, ORNL-TM-5027, pp. 162-163 (October 1975).
12. J. E. Bird, A. K. Mukherjee and J. E. Dorn, "Correlations Between High-Temperature Creep behavior and Structure", Quantitative Relation Between Properties and Microstructure, Israel University Press, Jerusalem, pp. 255-341 (1969).
13. D. L. Harrod, "Preliminary Analysis of the Creep Behavior of Incoloy Alloy 800 and Recommendations for Specific Analytical/ Experimental Research Programs," Research Report 75-1D4-HTRFC-R1, Westinghouse Research Laboratories, Pittsburgh, Pennsylvania, March 3, 1975.
14. L. Egnell and N. C. Persson, "Creep Rupture Ductility of Alloy 800," Paper presented at the 18eme Colloque de Metallurgie - Le nickel et son role specifique dans certains types d'alliage - Saclay, June 23-25, 1975.
15. A Plumtree and N. G. Persson, "Influence of γ' - Precipitation on the Creep Strength and Ductility of an Austenitic Fe-Ni-Cr Alloy," Paper presented at the Fourth Inter-American Conference on Materials Technology, Caracas, VEnezuela, June 29 - July 4, 1975.
16. P. G. Stone, J. Orr, and J. C. Guest, "The Metallurgy of Alloy 800," The British Nuclear Energy Society Materials Conference, Status Review of Alloy 800, University of Reading, England, September 25-26, 1974, and J. Br. Nucl. Energy Soc., 1975, 14, Jan., No. 1, pp. 25-34 (1975).
17. J. Orr, "Effect of Titanium and Aluminum on High Temperature Properties," The British Nuclear Energy Society Materials Conference, Status Review of Alloy 800, University of Reading, England, September 25-26, 1974.

18. P. J. Langford, D. M. Moon, and D. H. Harrod, "Metallurgical Implications," Steam Generator Materials Technology Program Quarterly Progress Report for Period Ending June 30, 1975, ORNL-TM-5027, pp. 128 (October 1975).

19. R. L. Klueh, "The Relationship Between Rupture Life and Creep Properties of 2-1/4 Cr-1 Mo Steel," ASME Paper 74-PVP-20, pp. 2-4, March 20, 1974.

20. R. L. Klueh, "The Relationship Between Rupture Life and Creep Properties of 2-1/4 Cr-1 Mo Steel," ASME Paper 74-PVP-20, pp. 8-9, March 20, 1974.

21. M. K. Booker, C. R. Brinkman, and V. K. Sikha, "Correlation and Extrapolation of Creep Ductility Data for Four Elevated - Temperature Structural Materials," ORNL-TM-4992, pp. 30-31, August 1974.

22. P. J. Langford, D. M. Moon, and D. H. Harrod, "Metallurgical Implications," Steam Generator Materials Technology Program Quarterly Progress Report for Period Ending June 30, 1975, ORNL-TM-5027, pp. 132-145 (October 1975).

23. R. L. Klueh, "The Relationship Between Rupture Life and Creep Properties of 2-1/4 Cr-1 Mo Steel," ASME Paper 74-PVP-20, p. 9, March 20, 1974.

24. G. H. Rowe, J. R. Stewart, and K. N. Burgess, "Capped End, Thin-Wall Creep-Rupture Behavior of Type 316 Stainless Steel," J. Basic Eng. 85: 71-86 (1963).

25. R. L. Flury and P. J. Langford, "Correlation with Multiaxial Failure," Steam Generator Materials Technology Program Quarterly Progress Report for Period Ending June 30, 1975, ORNL-TM-5027, pp. 168-185 (October 1975).

26. R. L. Flury and P. J. Langford, "Correlation with Multiaxial Failure," Steam Generator Materials Technology Program Quarterly Progress Report for Period Ending June 30, 1975, ORNL-TM-5027, pp. 169-186 (October 1975).

27. C. E. Pugh et al., "Interim Guidelines and Background Information for Inelastic Analysis of High-Temperature Reactor System Components Made of 2-1/4 Cr-1 Mo Steel," Appendix C, "Analytical Considerations for the Treatment of Tertiary Creep Behavior," ORNL-TM-5226 Draft, December 1975.

28. D. R. Hayhurst et al., "Estimates of the Creep Rupture Life of Structures Using the Finite-Element Method," to be published Journal of the Mechanics and Physics of Solids.

29. D. R. Hayhurst, C. J. Morrison, and F. A. Leckie, "The Effect of Stress Concentrations on the Creep Rupture of Tension Panels," Paper No. 75-APM-R, Journal of Applied Mechanics, September 1975.

Blank Page

3. MECHANICAL AND METALLURGICAL BEHAVIOR OF WELDMENTS FOR LMFBR*

P. Patriarca G. M. Slaughter C. R. Brinkman

3.1 INTRODUCTION

We are evaluating the behavior of weldments in austenitic stainless steel at 370 to 650°C (700–1200°F) as a function of both welding process and the variables within a process for application to liquid-metal-cooled fast breeder reactor (LMFBR) vessels and components. The investigation covers both heavy-section weldments, which are applicable to reactor vessels as well as other components, and thinner section weldments, which are applicable to piping. Major portions of both the heavy-section and piping weldments studies are concerned with the development and evaluation (including the determination of elevated-temperature design data) of improved filler metals that contain controlled additions of minor elements for increased strength and ductility.

An investigation is under way to determine the influence of deposition procedures on the microstructure and properties of hardfacing materials. Also, the post-test examination of the intermediate heat exchanger from the Sodium Components Test Installation has been completed. The main emphasis was to look for evidence of tube-to-tubesheet weld defects, mass transfer deposits, caustic corrosion, and carbon transfer.

3.2 WELDING DEVELOPMENT AND MECHANICAL TESTING OF WELDMENTS FOR STAINLESS STEEL COMPONENTS

3.2.1 General Stainless Steel Welding Development — D. P. Edmonds, R. T. King, and E. Bolling

We are continuing to investigate and characterize austenitic stainless steel weld materials for high-temperature sodium applications. Our primary objective at this time is to develop bare stainless steel filler wires for gas tungsten-arc (GTA) and submerged-arc (SA) welds with improved high-temperature mechanical properties. These welding materials are intended for use in critical LMFBR stainless steel pressure vessel, thermal liner, and piping applications.

*Progress on work performed under 189a No. OH024.

Previous work[1] has shown that the addition of 0.5% Ti, 0.042% P, and 0.006% B [referred to as controlled residual elements (CRE)] to types 316 and 308 stainless steel weld wires produces GTA weld deposits with improved creep properties. We previously reported[2] the procurement of several large commercial heats of types 316, 16-8-2 (modified), and 308 stainless steel with the CRE modification. Six of these heats have been fabricated into 3.97- and 1.14-mm-diam (0.0156 and 0.045 in.) wires for SA and GTA welding. We had also procured 44 small heats of stainless steel CRE materials with minor variations of the residual elements. Of these heats, 22 are being fabricated into welding wire.

We have made GTA and SA test welds (Table 3.1) using each of the six large heats of filler wire. The GTA welds were made in 13-mm-thick (0.50-in.) material and SA welds were made in 25-mm-thick (1.00-in.)

Table 3.1. Test Welds Made With Stainless Steel CRE Wires From Large Commercial Heats

Weld	Alloy Type			Manufacturer[a]	Heat	Flux
	Base	Filler				
			Gas Tungsten-Arc Welds			
V168	304	308	CRE	E	A2283	
V171	304	308	CRE	A	035046	
V172	316	16-8-2	CRE	A	035047	
V173	316	316	CRE	A	035048	
V174	316	17-8-2	CRE	A	035049	
V175	304	308	CRE	A	035050	
			Submerged-Arc Welds			
SA-E12[b]	316	316	CRE	A	035048	Arcos S-11
SA-E13	316	16-8-2	CRE	A	035047	Arcos S-11
SA-E14	316	16-8-2	CRE	A	035047	Arcos S-4
SA-E15	316	316	CRE	A	035048	Arcos S-4
SA-E16	304	308	CRE	A	035046	Arcos S-11
SA-E17	304	308	CRE	A	035050	Arcos S-11
SA-E18	316	17-8-2	CRE	A	035049	Arcos S-11
SA-E19	304	308	CRE	E	A2283	Arcos S-11

[a]The manufacturer designations are keyed to the descriptions of the filler metals in Tables 3.1 and 3.2 of ref. 2.

[b]This weld hot cracked.

material by use of single-V-joint configurations. Longitudinal all-weld-metal buttonhead creep specimens with a 3.2-mm-diam by 28.6-mm-long (0.13- by 1.13-in.) gage section have been machined from each test weld. Creep-rupture tests at 649°C (1200°F) are in progress for the welds listed in Table 3.1, and results from the short-time tests that have been completed are shown in Table 3.2. Results are inconclusive at this time; however, the following general trends can be observed. First, the SA welds tend to be significantly weaker than the GTA welds made with the same materials and also to have very good ductility. For example a specimen from weld E13, which was tested at 138 MPa (20.0 ksi), failed

Table 3.2. Creep-Rupture Properties at 649°C (1200°F) of GTA and SA Welds Made With Commercial CRE Stainless Steel Filler Wires

Weld	Filler Wire Type	Test Stress (MPa)	Test Stress (ksi)	Time to Rupture (hr)	Elongation (%)	Reduction of Area (%)
			GTA Welds			
V168	308 CRE	138	20.0	>1598[a]		
		172	25.0	523.8	11.5	17.4
		207	30.0	130.5	20.5	22.8
V171	308 CRE	138	20.0	>1219[a]		
		207	30.0	15.2	55.7	66.9
V172	16-8-2 CRE	172	25.0	>904[a]		
		241	35.0	19.1	46.3	64.3
V173	316 CRE	276	40.0	37.7	26.3	47.1
V174	17-8-2 CRE	241	35.0	80.8	24.4	b
V175	308 CRE	207	30.0	95.7	34.4	63.3
			SA Welds			
E13	16-8-2 CRE	104	15.0	>1219[a]		
		138	20.0	1287.1	31.4	70.0
		172	25.0	184.2	23.6	75.7
E14	16-8-2 CRE	172	25.0	38.9	34.7	66.1
E15	316 CRE	172	25.0	340.9	23.9	59.4

[a]Test in progress.

[b]Reduction of area could not be accurately measured.

after 1287.1 hr with a total reduction of area of 70.0% and a total elongation of 31.4%. Except weld V168, the GTA welds have reasonably good creep ductility. The creep strengths of the GTA welds are comparable to those of earlier experimental heats of CRE materials produced at ORNL.[1] Longer time tests are currently in progress to fully characterize these materials.

3.3 MECHANICAL AND METALLURGICAL BEHAVIOR OF WELDMENTS FOR LMFBR — P. Patriarca, G. M. Slaughter, W. R. Martin, and C. R. Brinkman

3.3.1 Effect of Postweld Heat Treatment and Creep Prestraining on the Creep-Rupture Behavior of Type 308 Stainless Steel Submerged-Arc Welds — E. Bolling and R. T. King

Two related creep experiments at 649°C are being performed on a single type 308 stainless steel weld made by the submerged-arc process in 51-mm-thick (2-in.) type 304 stainless steel plate. First, the creep-rupture properties at 138 and 172 MPa (20 and 25 ksi) of as-deposited longitudinal weld and transverse weldment specimens are being compared with those of longitudinal weld and transverse weldment specimens that have been heat-treated for 4 hr at 607 or 982°C (1125 or 1800°F) in air. The rationale for expecting the latter heat treatment to partially dissolve and agglomerate ferrite, thereby reducing the continuity of sigma phase formed in testing and improving ductility, has been discussed in an earlier report.[3] The materials and testing methods for this experiment were also presented in the earlier report.[3] A second experiment is aimed at examining whether prestraining in creep at 649°C at low stress [110 or 124 MPa (16 or 18 ksi)] for short fractions of the rupture life has a detrimental effect on ductility when the stress is increased (incremented) to cause rupture in a short time at 172 MPa. If sigma phase is formed at low stress, then incrementally stressed specimens should be less ductile than specimens ruptured in short time without prestrain. The testing in the second experiment was performed by methods identical to those used in the first experiment,[3] except that the load was incremented at temperature by supporting the load train, adding weight to the load, and continuously reapplying the load. Thus

the high-stress (172 MPa) tests from the first experiment served as no-prestrain controls for the second experiment.

The data from all the tests are combined in Tables 3.3 and 3.4. All terms are as defined previously.[3] The basic creep-rupture data are combined in Figs. 3.1 thorugh 3.4 for specimens from near the surface (L1, T1 types) and at a position intermediate to the surface and root pass regions (L2, T2 types). With the exception of one transverse weldment specimen that apparently failed in the heat-affected zone, all failures were in weld metal and involved substructural separations typical of sigma-phase-affected ruptures.

From the creep-rupture plots (Figs. 3.1 and 3.2), we estimate that prestraining 500 hr at 110 MPa (16 ksi) consumes from 0.01 to 0.02 of the rupture time at that stress, while prestraining 500 hr at 124 MPa (18 ksi) consumes between 0.03 and 0.05 of the rupture time at that stress. The effect of these prestrain treatments is judged by the ratio of total elongation for prestrained specimen to that of a nonprestrained control specimen. These ratios are shown in Fig. 3.5.

The significant results from testing at constant load at 649°C are:

1. Creep-rupture times for this weld metal in all conditions investigated tend to be slightly longer than average rupture times for annealed type 304 stainless steel base metal.

2. At 172 MPa (25 ksi), transverse weldment specimens have longer rupture times than longitudinal all-weld-metal specimens, but at 138 MPa (20 ksi) no distinction can be made.

3. The time to the onset of tertiary creep is between 0.5 and 1.0 times the rupture time at 172 MPa (25 ksi) and between 0.18—0.62 times at 138 MPa (20 ksi).

4. The strain at the onset of tertiary creep is 0.1 to 0.4 of the total fracture strain for as-welded metal and welds heat-treated at 607°C and 0.2 to 0.6 for welds annealed at 982°C.

5. The rupture strains for all the conditions decrease with increasing rupture time from about 100 to about 1000 hr. The lowest rupture strains, in the 2—3% range, occur for transverse as-deposited and 607°C-heat-treated specimens.

Table 3.3. Creep Test Times to Various Events for Type 308 Stainless Steel Submerged-Arc Welds Tested at 649°C (1200°F)

Specimen Orientation and Level	Stress (MPa)	Stress (ksi)	Approximate Time, hr, to Various Events: End First Stage	End Second Stage	0.2% Offset Third Stage	Fracture	0.5% Creep Strain	1% Creep Strain	2% Creep Strain	0.5% Total Strain	1% Total Strain	2% Total Strain	$\frac{t_{III}}{t_r}$
						As Welded							
Longitudinal 1	138	20	43	211	325	530.6	16	66	195	0.9	31	149	0.61
	172	25	1.0	10.2	15.0	69.1	0.8	2.8	6.8	0.08	1.2	5.2	0.22
	110[b]	16	82.6			a	255			59.8			
	172[b]	25	6.5	24.3	48	95.3	8.5	20.1	55	8.5	20.1	55	0.57
	124[b]	18				a							
	172[b]	25				45.0							
Longitudinal 2	138	20	65.1	233.2	593.3	786.4	76.5	432.7	754.2	1.0	167.4	686.2	0.75
	172	25	8.0	35.0	56.0	144.9	6.1	15.6	40.0	0.1	7	30.5	0.39
Transverse 1	138	20	202.5	473.9	695	757.8	92.4	372.7	740	13.7	215.5	686.8	0.92
	172	25	2.7	30.6	42	113.2	4	10	23	0.8	6	20	0.37
Transverse 2	138	20	74.5	444.9	620	623.9	368.2	615	621	57.5	602	620	0.99
	172	25	2.0	58.2	102.7	204.5	30.5	70.9	121.6	0.05	33.2	101.1	0.50
						Annealed 4 hr at 607°C (1125°F), Water Quenched							
Longitudinal 1	138	20	73.9	370	550	728.1	54	241	550	3.9	114	473	0.75
	172	25	1.0	17.5	22.5	71.9	1.0	3.2	7.5	0.2	1.1	5.4	0.31
Longitudinal 2	138	20	100	650	800	957.0	200	622	902	12	344	845	0.84
	172	25	2.4	31.6	43.5	147.9	5.2	16	35	0.25	6.5	29	0.29
Transverse 1	138	20	43.2	403.6	675	774.9	137	386	706	124	370	701	0.87
	172	25	0.8	12.5	23	81.9	2.2	6.5	14	0.1	2.6	11	0.18
Transverse 2	138	20	66	839	1190	1190.4	791	1172	1175	189	1103	1173	1.00
	172	25	7.5	66.2	120	217.1	26	67	123	1.3	36	105	0.55
						Annealed 2 hr at 982°C (1800°F), Water Quenched							
Longitudinal 1	138	20	100	498	714	1346.7	9.2	73.9	401	0.2	14.6	271	0.53
	172	25	7.1	25.0	32.5	79.2	0.2	0.7	2.2	∿0	0.01	0.7	0.41
	110[b]	16	a				a						
	172[b]	25	∿4	∿32	∿39	108.9	1.2	5	14	1.2	5	14	0.36
	124[c]	18				a				∿27			
	172[b]	25				97.8	13	20	22	13	20	22	∿0
Longitudinal 2	138	20	46	721.5	905.7	1320.4	5.2	40	386	0.3	6.5	244	0.69
	172	25	6	82.3	89.7	166.2	0.4	1.2	3.5	0	0	0.1	0.54
Transverse 1	138	20	114.6	618.5	955	1278.1	5.6	193	655	∿0	∿0	167	0.75
	172	25	12	54	68	112.5	0.6	2.1	7.2		0.07	2.8	0.60
Transverse 2	138	20	187	803.9	1027	1973.1	9.7	64	336	0.05	10.3	181	0.52
	172	25	27.8	107.5	131.5	211.4	0.5	2.2	6.9	∿0	∿0	0.9	0.62

[a] Load increased to 172 MPa (25 ksi) after 500 hr.

[b] Same specimen as shown on line above at lower stress. Times are measured from the time the stress was increased.

[c] No sense can be attached to the results because the specimen strained 0.21% on load, jumped from 0.24 to 0.53% strain between 18.4 and 35.5 hr, and then exhibited no significant strain before the load was increased.

Table 3.4. Creep Test Strain Data for Type 308 Stainless Steel Submerged-Arc Welds Tested at 649°C (1200°F)

Specimen Orientation and Level	Stress (MPa)	Stress (ksi)	Strain, % Loading ε_L	ε_I Stage I	Stage II Real	Stage II Offset	Rupture ε_r	Strain Rate, %/hr $\dot{\varepsilon}$ Stage II Real	$\dot{\varepsilon}$ Stage II Offset	ε_r/t_r	Reduction of Area (%)	Total Rupture Time, t_r (hr)	$\frac{\varepsilon_{III}}{\varepsilon_r}$
						As Welded							
Longitudinal 1	138	20	0.23	0.51	0.856	1.57	7.5	0.0051	0.0056	0.014	12.6	530.6	0.39
	172	25	0.26	0.35	1.44	2.4	29.0	0.160	0.17	0.34	29.1	69.1	0.13
	110[b]	16	0.13	0.37			a	0.00048				a	
	172[b]	25	0.14	0.23	0.39	0.92	8.2	0.020	0.020			595.3	
	124[b]	18					a					a	
	172[b]	25										545.0	
Longitudinal 2	138	20	0.25	0.31	0.128	0.52	6.3	0.00072	0.0009	0.006	6.3	786.4	0.21
	172	25	0.23	0.45	0.72	1.48	15.2	0.0261	0.031	0.085	26.7	144.9	0.18
Transverse 1	138	20	0.18	0.45	0.28	0.68	5.0	0.0010	0.0013	0.0052	3.8	757.8	0.33
	172	25	0.24	0.34	1.67	2.46	11.2	0.060	0.062	0.185	16.5	113.2	0.31
Transverse 2	138	20	0.144	0.19	0.168	0.06	3.0	0.00048	0.0073	0.0039	2.5	623.9	0.30
	172	25	0.29	0.10	0.41	0.896	6.7	0.0075	0.008	0.026	8.0	204.5	0.24
						Annealed 4 hr at 607°C (1125°F), Water Quenched							
Longitudinal 1	138	20	0.20	0.36	0.49	9.2	4.7	0.0016	0.0019	0.0054	4.8	728.1	0.40
	172	25	0.34	0.31	2.56	3.6	24.2	0.157	0.166	0.27	33.4	71.9	0.22
Longitudinal 2	138	20	0.268	0.24	0.43	0.69	5.7	0.0008	0.0009	0.0074	5.0	957.0	0.25
	172	25	0.28	0.21	0.912	1.46	20.4	0.031	0.035	0.68	25.7	147.9	0.11
Transverse 1	138	20	0.024[c]	0.17	0.52	1.21	5.6	0.0013	0.0002	0.0057	8.2	774.9	0.27
	172	25	0.28	0.36	0.75	1.76	14.5	0.064	0.079	0.144	25.7	81.9	0.21
Transverse 2	138	20	0.16	0.12	0.22	0.46	2.5	0.00025	0.00040	0.0019	1.0	1190.4	0.37
	172	25	0.25	0.17	0.45	1.04	7.5	0.0078	0.0093	0.026	14.0	217.1	0.24
						Annealed 2 hr at 892°C (1800°F), Water Quenched							
Longitudinal 1	138	20	0.26	0.71	0.74	1.28	9.6	0.0018	0.0020	0.0059	7.2	1346.7	0.29
	172	25	0.64	2.48	3.88	5.84	33.7	0.22	0.23	0.34	36.5	79.2	0.33
	110[b]	16	0.02	0.24			a	0.00023				a	
	172[b]	25		0.73	2.34	3.21	25.3	0.106	0.0942	0.18	26.3	608.9	0.2
	124[d]	18	0.21				a					a	
	172[b]	25					27.3				22.3	597.8	
Longitudinal 2	138	20	0.24	0.66	1.22	1.73	10.1	0.0018	0.0020	0.0060	10.9	1320.4	0.33
	172	25	1.2	1.75	9.92	11.04	45.6	0.130	0.132	0.23	42.4	166.2	0.36
Transverse 1	138	20	1.00	0.60	0.73	1.36	6.9	0.0014	0.0016	0.0043	9.5	1278.1	0.52
	172	25	0.53	1.72	3.2	4.53	16.5	0.076	0.180	0.12	31.4	112.5	0.52
Transverse 2	138	20	0.304	0.99	1.11	1.65	11.3	0.0018	0.0020	0.0045	8.5	1973.1	0.33
	172	25	1.2	2.96	4.8	6.4	22.4	0.060	0.062	0.085	46.0	211.4	0.59

[a] Load increased to 172 MPa (25 ksi) after 500 hr.

[b] Same specimen as shown on line above at lower stress.

[c] Value questionable because of apparent dial gage or specimen bending problem.

[d] No sense can be attached to the results because the specimen strained 0.21% on load, jumped from 0.24 to 0.53% strain between 18.4 and 35.5 hr, and then exhibited no significant strain before the load was increased.

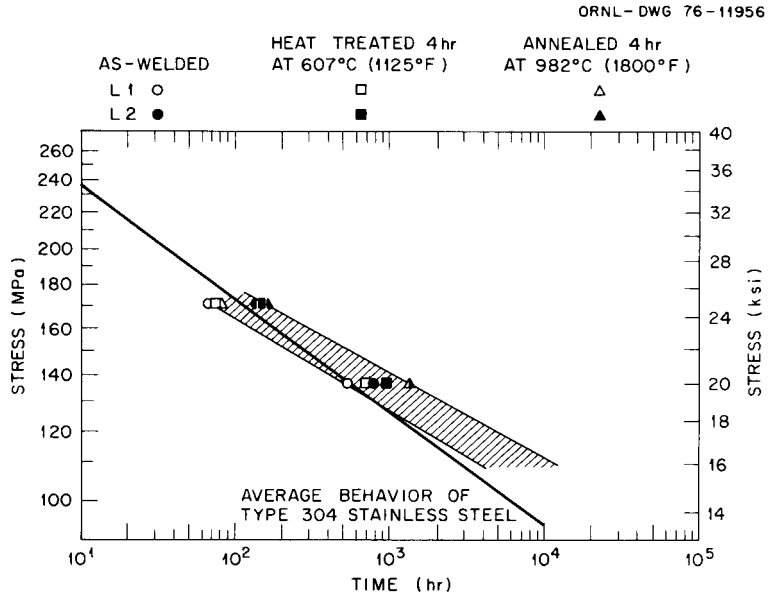

Fig. 3.1. Creep-Rupture Behavior of Longitudinal All-Weld-Metal Specimens of Type 308 Stainless Steel Submerged-Arc Welds at 649°C (1200°F).

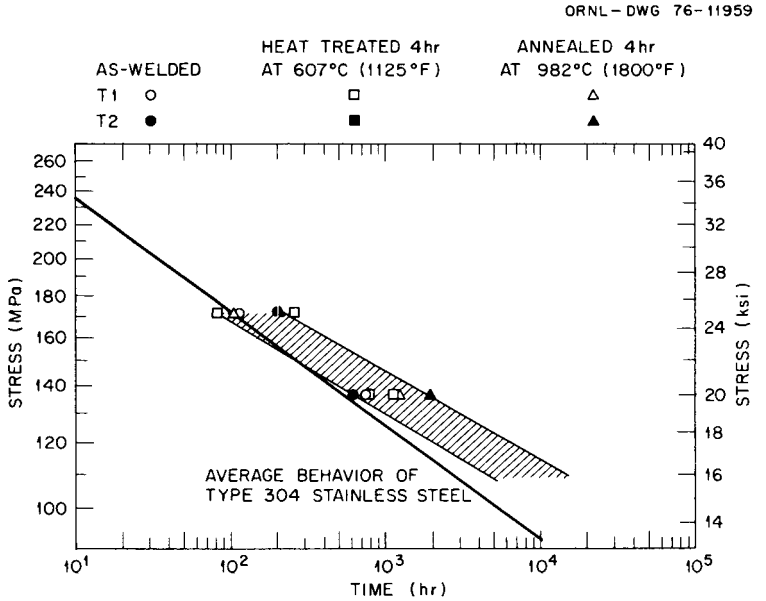

Fig. 3.2. Creep-Rupture Behavior of Transverse Weldment Specimens of Type 308 Submerged-Arc Welds in Type 304 Stainless Steel Base Metal, Tested at 649°C (1200°F).

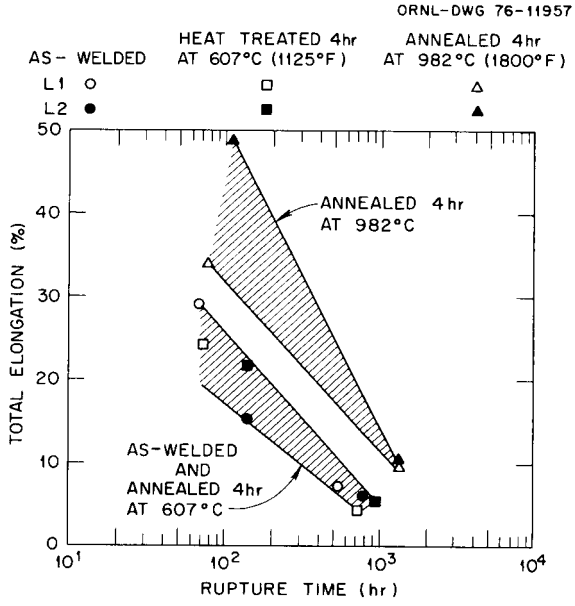

Fig. 3.3. Creep-Rupture Strain Behavior of Longitudinal All-Weld-Metal Specimen of Type 308 Stainless Steel Submerged-Arc Welds at 649°C (1200°F).

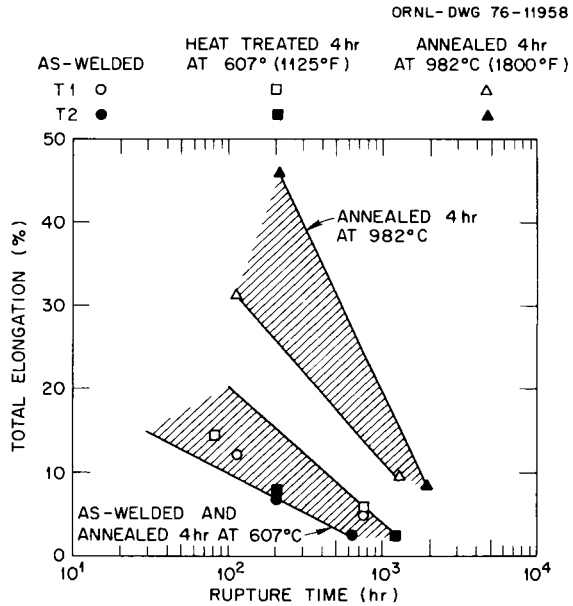

Fig. 3.4. Creep-Rupture Strain Behavior of Transverse Weldment Specimens of Type 308 Submerged-Arc Welds in Type 304 Stainless Steel Base Metal, Tested at 649°C (1200°F).

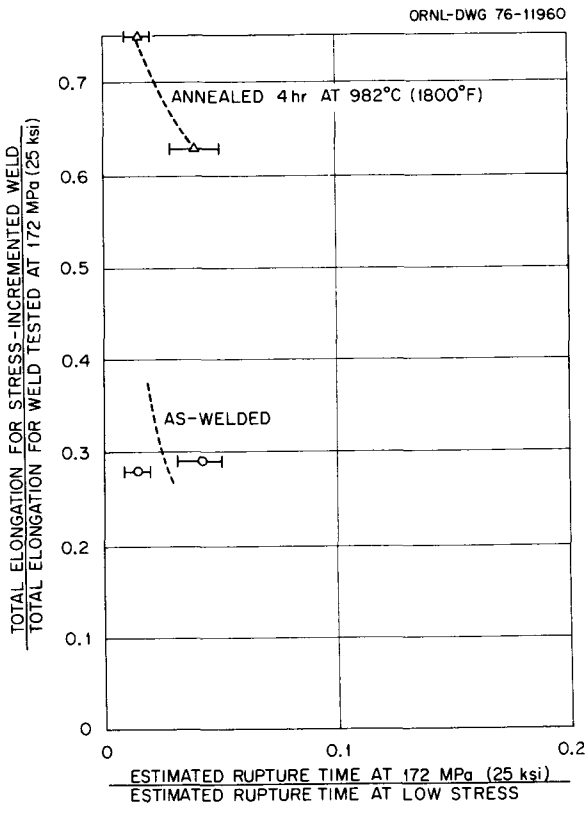

Fig. 3.5. Effect of Prestraining at Low Stress [110 and 124 MPa (16 and 18 ksi)] on Strain for Specimens Incremented to 172 MPa (25 ksi) After 500 hr.

6. Weld metal annealed 4 hr at 982°C has greater ductility than as-deposited weld metal or welds heat-treated 4 hr at 607°C.

The significant results from incremented stress tests performed on longitudinal all-weld-metal specimens in the as-deposited condition or after annealing for 4 hr at 982°C are:

1. Prestraining at 110 and 124 MPa (16 and 18 ksi) for times to about 0.01 to 0.05 of the total estimated rupture times at those stresses has no experimentally significant effect on the rupture time when the stress is later raised to 172 MPa (25 ksi).

2. Prestraining as-deposited weld metal reduces the total rupture strains to about one-third the values observed in tests at 172 MPa only.

3. Prestraining weld metal annealed at 982°C reduces the total rupture strains to about 0.7 times the values observed in tests at 172 MPa only.

4. Such testing results in fracture morphologies commonly associated with transformation of ferrite to sigma phase and failures that propagate along sigma phase austenite boundaries. The 500-hr period of prestraining allows the sigma phase to form and causes relatively low-ductility failures when the stress is incremented. Welds annealed at 982°C are suspected of having less continuous ferrite; metallography to demonstrate this point is in progress.

3.3.2 Status of Creep Testing on 16-8-2 Submerged Arc Welds — R. T. King, D. P. Edmonds, and E. Bolling

A preliminary report[4] has given details on the materials, experimental and testing methods, and certain characteristics of type 16-8-2 submerged-arc welds made in 25-mm-thick (1-in.) type 316 stainless steel plate. Here we simply update the creep-rupture test data of Table 3.9 of that report and make some corrections. Table 3.5 gives the status of creep-rupture tests together with some of the more important test data that have been obtained.

With two exceptions, all the specimens tested have failed in weld metal. The exceptions are specimens 775-T3 and -T7, both of which were intended to be transverse weld metal specimens. Some base metal was inadvertently included in the gage length, and the fracture surface includes both regions of intergranular separation in the HAZ very near to the fusion line and apparently trans-substructural tearing in the weld metal. Because of possible stress concentration effects near the geometrical discontinuity at the fillet at the end of the gage length and near the metallurgical discontinuity at the fusion line, this failure path does not necessarily imply higher strength for weld metal or HAZ under these test conditions.

We are now preparing impact and aging specimens for characterization. Preliminary results will be reported later.

3.3.3 Demonstration on Importance of Anisotropy in Welded Pipe Calculations — B. R. Dewey

Work is continuing in the development of constitutive equations that recognize anisotropy in weld metal. To demonstrate the use of some

Table 3.5. Creep-Rupture Test Data for Babcock and Wilcox Type 16-8-2 Stainless Steel Submerged-Arc Welds

Stress (MPa)	Stress (ksi)	Specimen Type and Number	Test	Rupture Time (hr)	Time to Tertiary Creep		Total Strain, %			Reduction of Area (%)
							Onset of Tertiary Creep		Rupture	
					Linearity	0.2% Offset	Linearity	0.2% Offset		
				Tests at 649°C (1200°F)						
172	25	L1 776-L35	FWB-239	31.5	1.2	1.75	1.37	1.7	44.2	58.4
138	20	L1 775-L1	FWB-249	478.5	25	58	1.46	3.0	42.5	54.0
110	16	L1 775-L6	FWB-250	>2485.4					>17.9	
172	25	L2 776-L37	FWB-237	73.9	∿4	∿5.7	∿0.8	∿1.1	48.5	50.1
138	20	L2 775-L14	FWB-254	609.4	34	73	0.6	1.1	44.2	56.1
110	16	L2 775-L10	FWB-257	>2243.9					>12.3	
172	25	T1 776-T3	FWB-240	121.3	6	11.5	∿0.96	∿1.6	30.7	37.7
138	20	T1 776-T1	FWB-252	1334.6					30.3	32.5
110	16	T1 775-T5	FWB-253	>2363.6					>5.96	
172	25	T2 776-T6	FWB-246	111.8	11.4	20	0.9	1.75	34.7	49.0
138	20	T2 775-T6	FWB-256	1009.0	250	300	1.1	1.39	15.7	36.9
				Tests at 566°C (1050°F)						
310	45	L1 776-L34	FWB-241	45.8	29	31	9.8	11.0	44.1	45.6
276	40	L1 775-L2	FWB-255	209.3	105	124	7.9	9.2	23.3	29.3
276	40	L1 775-L3	FWB-259	174.0	85	95	17.0	18.4	40.3	38.0
310	45	L2 775-L5	FWB-248	78.8	27.5	29	8	8.4	34.7	36.2
241	35	L2 775-L3	FWB-259	699.8	323	395	4.4	5.4	26.2	62.0
310	45	T1 776-T1	FWB-238	75.3	37.5	41.8	19.9	21.2	42.8	25.6
276	40	T1 775-T3	FWB-263	201.5	137.5	198	7.6	9.5	14.0	15.6
241	35	T1 775-T7	FWB-260	1279.5						
310	45	T2 776-T2	FWB-245	109.6	2.8	38.4	1.6	3.0	11.5	13.9
310	45	T2 775-T4	FWB-264	142.5	38	55	2.6	3.5	14.0	18.4

recently presented data,[5] a finite element program was modified to accept orthotropic elastic constants and has been used to conduct stress analysis in a hypothetical weld joint in a pipe.

3.3.3.1 Description of Finite Element Program

With finite element programs, the user ordinarily inputs the elastic modulus E and Poisson ratio ν as discrete functions of temperature for each material. Internally, the program takes the values of E and ν and forms an elastic stiffness (or compliance) matrix for the material in each element. This computation typically takes the following form, as an example, for the compliance matrix in a three-dimensional solid:

$$[S] = \begin{bmatrix} 1/E & -\nu/E & -\nu/E & 0 & 0 & 0 \\ -\nu/E & 1/E & -\nu/E & 0 & 0 & 0 \\ -\nu/E & -\nu/E & 1/E & 0 & 0 & 0 \\ 0 & 0 & 0 & 2(1+\nu)/E & 0 & 0 \\ 0 & 0 & 0 & 0 & 2(1+\nu)/E & 0 \\ 0 & 0 & 0 & 0 & 0 & 2(1+\nu)/E \end{bmatrix} \quad (1)$$

Hence, a matrix of the form of Eq. (1) can be input directly (instead of just E and ν) in the case of anisotropic material. This has been done using the numerical values for a type 308 stainless steel electroslag weld reported[5] previously.

For the example that follows, axisymmetric welds with two preferential orientations have been compared with one assumed to be isotropic. The mesh shown in Fig. 3.6 was used to model a symmetric pipe segment with a ratio of outside diameter to thickness d/h = 8.0. The r axis represents the center line of a symmetric V-weld with an included angle of 53°. The Z axis represents the center line of the pipe. The mesh in Fig. 3.6 contains 210 elements (linear quadrilaterals and triangles) and 231 nodal points. Loading is by uniform pressure on the inside of the pipe.

Room-temperature elastic properties were used for the base metal and the electroslag weld metal. For the base metal, type 304 stainless steel, E was assumed to be 195 GPa and ν, 0.283. For the weld metal,

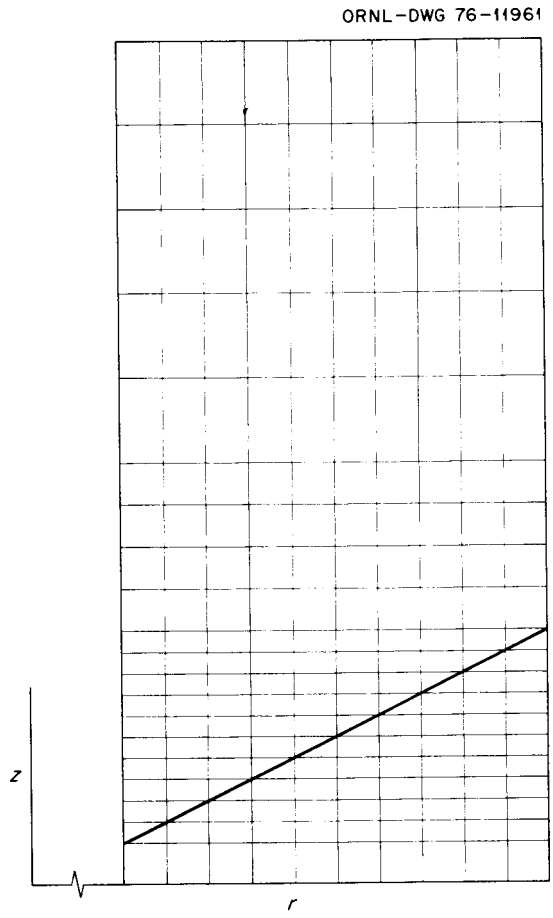

Fig. 3.6. Finite Element Mesh for Idealized Pipe Weld. Weld metal is on lower right.

the properties in Table 3.6 were used, where the subscripts correspond to the unprimed coordinates on the idealized weld shown in Fig. 3.7.

Table 3.6. Engineering Constants for Specially Orthotropic Model of Electroslag Weld Metal

Modulus[a]	Value (GPa)	Poisson's Ratio	Value
$E_{11} = E_{22}$	142	$\nu_{12} = \nu_{21}$	0.24
E_{33}	104	$\nu_{13} = \nu_{23}$	0.53
$G_{44} = G_{45}$	82	$\nu_{31} = \nu_{32}$	0.39
G_{66}	57		

[a] E denotes Young's modulus, G shear modulus.

ORNL-DWG 75-13166R

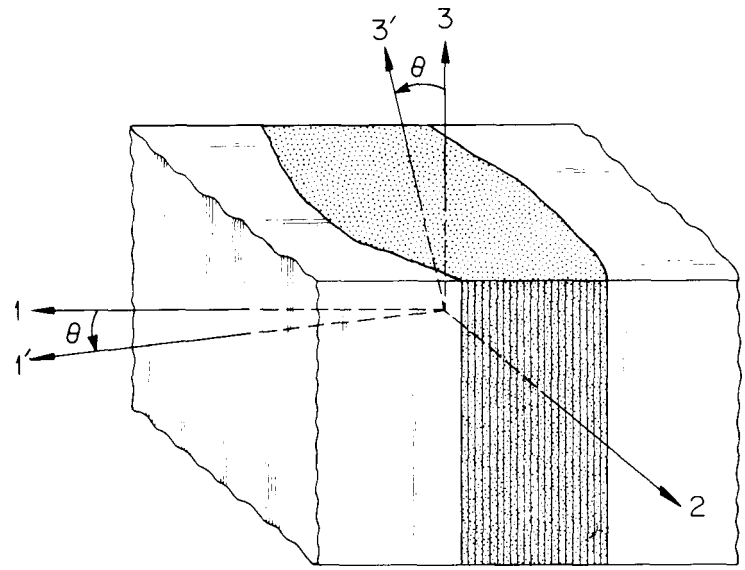

Fig. 3.7. Idealized Electroslag Weld with Coordinate Axes. The elongate subgrains are in the 3-direction. Also shown is a positive rotation around the 2-axis.

Three different elastic symmetry conditions were used in the finite element demonstrations:

Case 1. Properties of Table 3.6 with the r direction (direction of elongated subgrains) in the weld in the pipe corresponding to the 3-direction in Fig. 3.7, the z direction to the 1-direction, and the t direction (hoop) to the 2-direction.

Case 2. Same as case 1 except that θ (Fig. 3.7) equals 126.9°, which places the elongated subgrains perpendicular to the fusion line.

Case 3. Isotropic weld metal with same E and ν as base metal.

3.3.3.2 Results

Displacements, stresses, and strains are routinely available from the finite element calculations for the three cases. Comparisons among the hoop strain ε_θ distributions on the inner and outer surfaces of the pipe are given in Fig. 3.8. Here, we see that the mismatch between weld metal and base metal causes an increase in strain in the vicinity of the weld. Furthermore, the orientation of the weld grains significantly affects the magnitude of the strain increase.

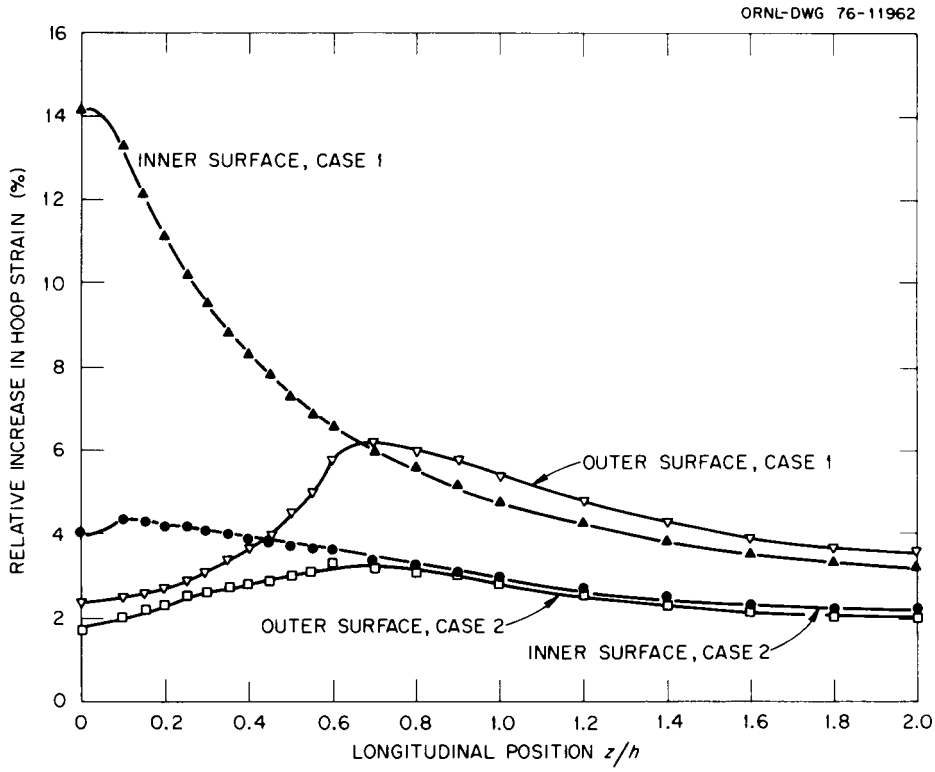

Fig. 3.8. Effect of Orientation of Weld Metal.

An interesting observation is that the apparent E for weld metal can be much lower than that for base metal. One should note that the transformation equations, when applied to the values given in Table 3.6, give a value of E at $\theta = 45°$ close to the value of E for isotropic material. The directional variation of properties of the weld metal do significantly affect stress analysis. With such properties routinely incorporated in finite element analysis, improved accuracy and confidence in the design of weld joints will result.

3.3.4 Novel Measurement of Ultrasound Velocity in Type 308 Stainless Steel Weld Metal — L. Adler* and K. V. Cook

Studies of mechanical properties of austenitic stainless steel weld metal have shown that the elastic properties of weldments are anisotropic. Recent measurements[5] with both longitudinal and shear wave ultrasonic

*Consultant from the University of Tennessee.

techniques detected velocity changes along special planes of the weldment. The macrostructure of specimens of a single-pass stainless steel (type 308) electroslag weld leads us to expect either orthotropic or special orthotropic (transversely isotropic) symmetry for the elastic constants. Altogether nine elastic constants are required to relate stress and elastic strain for orthotropic symmetry. The relationship between the elastic stiffness constants and the ultrasonic velocity may be obtained in matrix form by use of the Christoffel relations. By measuring ultrasonic velocities the component of the elastic stiffness matrix may be obtained. For our initial work, sections were taken from the weldment, and contact methods were used to measure velocity changes in directions governed by the planes of the sections. This approach is slow and costly and limits the information that can be obtained. Therefore we devised a special mechanical goniometry system that uses immersion techniques for coupling the transducer to the test weld.

Ultrasonic velocity was measured in various orientations of the weld structure with this immersed ultrasonic through-transmission system, on cylindrical specimens taken from the three orthogonal directions in the weld. In each cylindrical sample velocity changes were measured as a function of rotation (or angle). Both longitudinal and shear wave velocities vary with sample rotation. The longitudinal velocity varies by as much as 15% and the shear 30% in the 1-3 plane for the type 308 stainless steel weld metal, as shown in Fig. 3.9. The solid curves in Fig. 3.9 are calculated from Christoffel's equation for the assumed orthotropic symmetry, and the points are experimental. Data such as those presented in Fig. 3.9 can be applied to deformation analyses for real weldments, as we previously indicated.[5] These results have significance in the field of ultrasonic inspection of weld material, where variation of the ultrasonic velocities with structure, material, and orientation can be important.

The interface between base metal and weld metal may introduce two very important variables not presently considered in routine angle beam testing. These variables are sound transmission changes and angle changes. Thus, both amplitude reflection (apparent attenuation) and

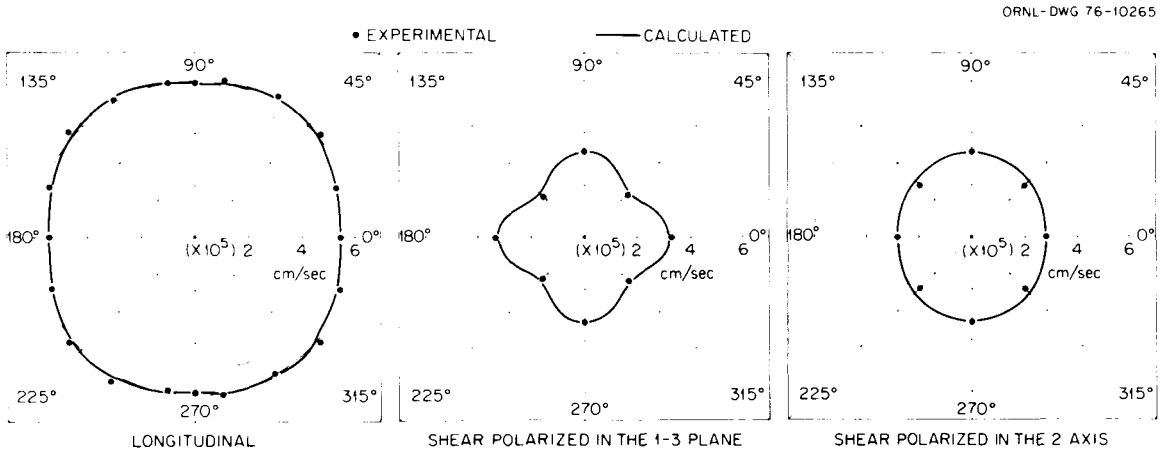

Fig. 3.9. Variation of Ultrasonic Velocities with Orientation in a "Single Pass" Stainless Steel Weldment in the 1-3 Plane.

location of signals from reflectors (time changes) such as flaws are affected. These variations must be determined for each weldment material to assure meaningful testing.

3.4 REFERENCES

1. D. P. Edmonds, R. T. King, and E. Bolling, "Creep-Rupture Behavior of Gas Tungsten-Arc Types 308, 316, and 16-8-2 Stainless Steel Welds Made With Special Filler Materials," *LMFBR Materials Development Program Quart. Prog. Rep. Sept. 30, 1975*, ORNL-5117, pp. 103–07.
2. D. P. Edmonds and R. T. King, "General Stainless Steel Weld Development," *LMFBR Materials Development Program Quart. Prog. Rep. Dec. 31, 1975*, ORNL-5131, pp. 161–66.
3. E. Bolling and R. T. King, "Preliminary Report on Effect of Postweld Heat Treatment on Type 308 Stainless Steel Submerged-Arc Welds," *LMFBR Materials Development Program Quart. Prog. Rep. Dec. 31, 1975*, ORNL-5131, pp. 175–82.
4 R. T. King and D. P. Edmonds, "Structure and Properties of a 16-8-2 Submerged-Arc Weld," *LMFBR Materials Development Program Quart. Prog. Rep. March 31, 1976*, ORNL-5157, pp. 106–17.
5. B. R. Dewey, L. Adler, R. T. King, and K. V. Cook, "Measurements of Anisotropic Elastic Constants for Weld Metal," Society for Experimental Stress Analysis Paper WR-11-1975, May 1976, presented at the 1976 SESA Spring Meeting, Silver Spring, Md., May 9–14, 1976; submitted for publication to the *Journal of Experimental Mechanics*.

4. LARGE-DIAMETER PIPING AND FITTING DEVELOPMENT*

G. M. Slaughter

4.1 INTRODUCTION

A program has been initiated with the objective of evaluating welded and seamless pipe and fittings currently manufactured by qualified suppliers. The seamless pipe phase is confined to pipe made by reduction of centrifugally cast pipe into wrought pipe (ASME SA-452 basic specification) and the reduction of welded pipe into pipe where the cast structure of the weld is reduced to grain structure capable of ultrasonic inspection. The welded pipe phase of the program consists of evaluating type 316 stainless steel pipe welded by (1) the GTA process with 16-8-2 filler; (2) the GTA process autogenously; and (3) the submerged-arc process with a choice to be made between 16-8-2 filler and ER 316 filler.

4.2 PROCUREMENT OF PIPE AND ELBOWS — R. J. Beaver

Large-diameter type 316 stainless steel welded pipe, 0.914 m (36.0 in. OD) by 12.7 mm (0.50 in.) wall thickness, and a large-diameter elbow, also 0.914 m by 12.7 mm with a 90° bend, are being procured from industrial sources for evaluation of metallurgical and dimensional characteristics and comparison of current commercial practices. Table 4.1 summarizes the current status of the pipe procurement. Requests for bids for the welded elbow to be manufactured in accordance with MET-WB-MS-7 Specification (ASME SA-403 with Additional Requirements) revealed that the only supplier interested in providing one elbow was Swepco Tube Corporation at a cost of $22,500. This elbow will be manufactured by Swepco's commercial practice of GTA welding with ER 316 filler metal. Delivery is anticipated in October 1976.

The status of procurement of seamless pipe from the Airite Division of Sargent Industries is summarized in Table 4.2. This pipe represents a developmental effort consisting of reducing 38.1-mm-wall (1.50 in.)

---

*Progress on work performed under 189a No. OH0103.

Table 4.1. Status of Large-Diameter Welded Pipe Procurement[a]

Specification	Process	Filler Metal	Supplier	Delivery	Cost ($)
ORNL-MET-WB-MS-2 (ASME SA-348 With Additional Requirements)	GTA	16-8-2	Youngstown Welding and Engineering	July 1976	7000
	GTA	16-8-2	Trent Tube	September 1976	9100
	SA	ER 316	Swepco	September 1976	8200
	SA	16-8-2	[b]	October 1976	
ORNL-MET-WB-MS-4 (ASME SA-312 With Additional Requirements)	GTA	None	Swepco	August 1976	5900

[a] 0.914 m (36.0 in.) OD by 12.7 mm (0.50 in.) wall.

[b] Request for quotation issued.

Table 4.2. Status of Wrought Austenitic Stainless Steel Large-Diameter Pipe to be Made by Spin Forging[a]

	Centrifugally Cast Pipe	Welded Pipe
Specification	ORNL MET-WB-MS-6 (ASME SA-452 With Supplementary Requirements)	ORNL MET-WB-MS-8 (ASME SA-376 With Supplementary Requirements)
Material	Type 316H stainless steel	Type 304H stainless steel
Supplier of Preform	Wisconsin Centrifugal	National Annealing Box
Manufacturing Cost		
Preform	$8000	$17,000
Pipe	$16,000 (includes mandrel cost)	$9500
Delivery Dates		
Preform	August 1976	September 1976
Pipe	September 1976	October 1976

[a] 0.876 m (34.5 in.) OD by 12.7 mm (0.50 in.) wall.

centrifugally cast and welded preforms into wrought seamless pipe by spin-forging with the aim of complying to the ASME SA-452 standard (for the centrifugally cast preform) and ASME SA-376 (for the welded preform). A quotation received for production quantities of large-diameter welded pipe and discussions with Wisconsin Centrifugal, Inc., relative to decreases in the cost of centrifugal castings made in production quantities indicates that wrought seamless austenitic stainless steel pipe produced from a centrifugal casting and meeting the requirements of the SAME SA-452 standard is very likely to be economically competitive with large-diameter welded pipe produced to the ASME SA-358 standard.

4.3 EFFECTS OF COLD WORK AND ANNEALING ON WELDED PIPE — G. M. Goodwin and J. D. Hudson

We are investigating the effects of cold work and annealing on the structure and resultant mechanical properties of welded austenitic stainless steel pipe. The information generated in this portion of the program will be useful in determining desirable working schedules for fabrication of pipe by spin-forging of rolled and welded blanks.

The starting material for this study is 0.46-m-diam by 25-mm-wall (18 by 1 in.) type 304 stainless steel pipe, procured to the requirements of ASTM A 358, Class I. It has a long submerged-arc seam weld and was solution heat-treated at 1066 ± 14°C (1950 ± 25°F) following fabrication. Chemical analyses (wt %) of the base metal and weld metal are as follows:

	C	Mn	P	S	Si	Cr	Ni
Base Metal	0.060	1.07	0.028	0.024	0.46	18.20	9.50
Weld Metal						19.90	10.28

The macrostructure of the seam weld in the as-welded and solution annealed condition is shown in Fig. 4.1. The root pass was deposited from inside the pipe. In this condition, the base metal contains no ferrite and the fusion zone shows 0—1.4 FN (ferrite number, as measured by Ferritescope), with essentially all the ferrite located in the final outer pass. The hardness of the base plate is R_B 85 to 89, and that of the weld zone R_B 80 to 84.

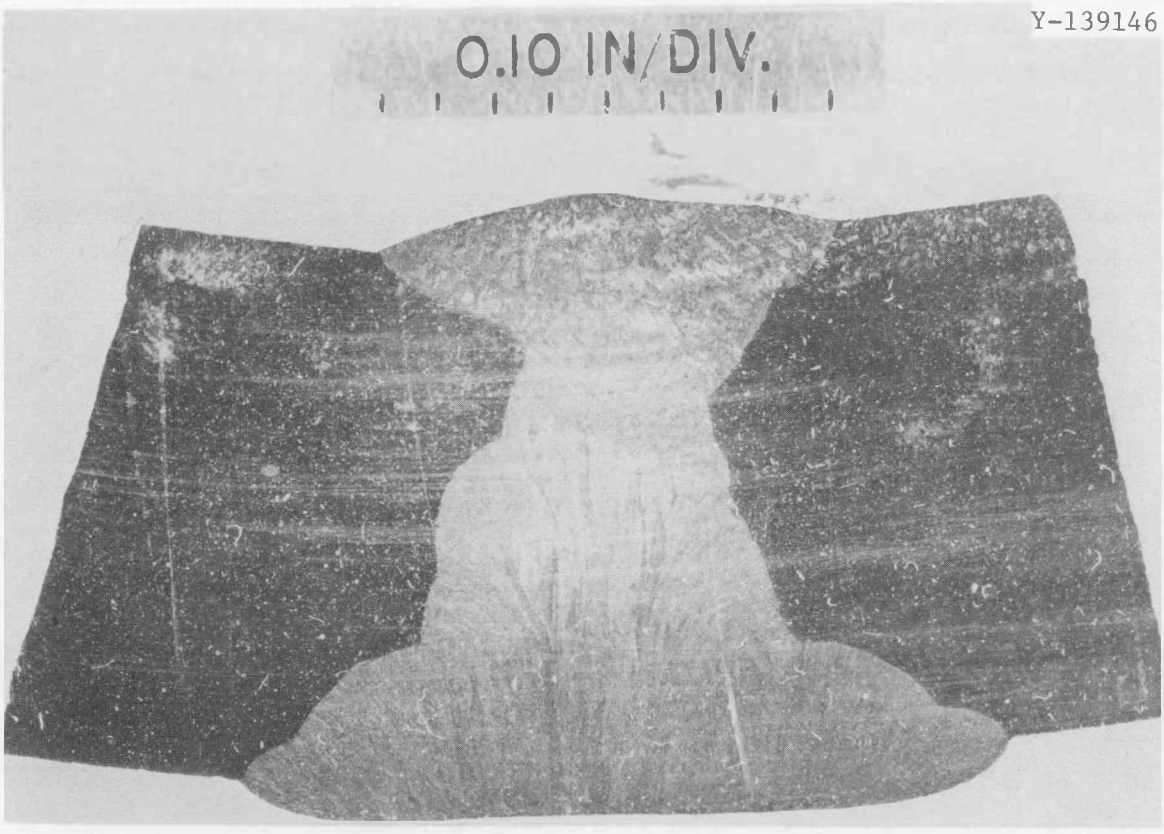

Fig. 4.1. Macrostructure of As-Received Type 304 Stainless Steel Pipe. Etchant: 50% HCl—10% HNO_3. Scale is 2.5 mm per division.

The microstructure of the as-received pipe is shown in Fig. 4.2. Note that the ferrite measured on the outer pass of the weld is readily apparent in the microstructure (d) and is agglomerated. The absence of ferrite in the root pass region (b) permitted significant grain boundary migration during solution heat treatment. Most of the fusion zone contains a mixture of these two structures, as shown in (c). The base metal (a) is, of course, fully annealed and has a relatively coarse grain size.

After removal of the weld reinforcement, a section of the pipe was reduced 10% in thickness by cold rolling perpendicular to the weld direction. The macrostructure is shown in Fig. 4.3. Although little change can be observed in the overall structure, martensite is observed in both base metal [Fig. 4.4(a)], and weld metal [Fig. 4.4(b)]. The hardness increases to approximately R_B 93. Ferritescope measurements confirm the presence of a small amount of martensite, with typical readings of 0.1 FN in the base metal.

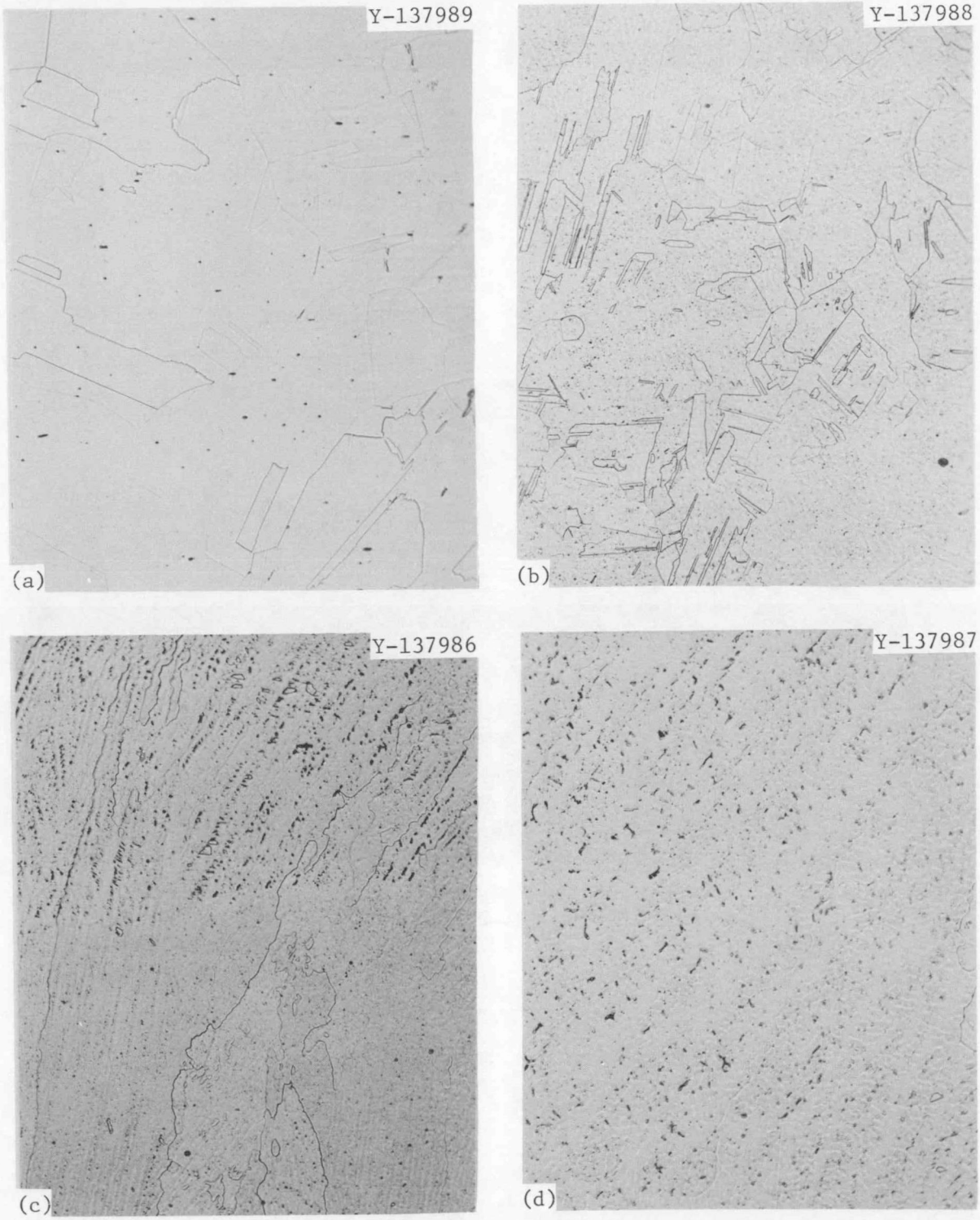

Fig. 4.2. Microstructure of As-Received Type 304 Stainless Steel Pipe. 100×. Etchant: 50% HCl—10% HNO_3. (a) Base metal. (b) Root of weld. (c) Middle of weld. (d) Outside of weld.

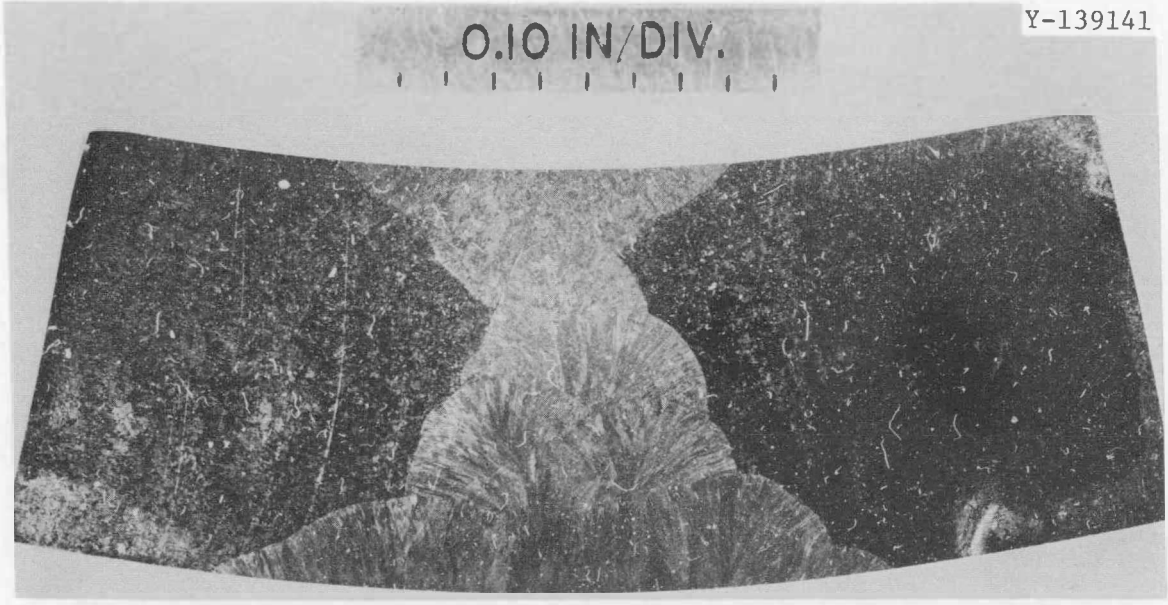

Fig. 4.3. Macrostructure of Type 304 Stainless Steel Pipe Cold Worked 10%. Etchant: 50% HCl—10% HNO_3. Scale is 2.5 mm per division.

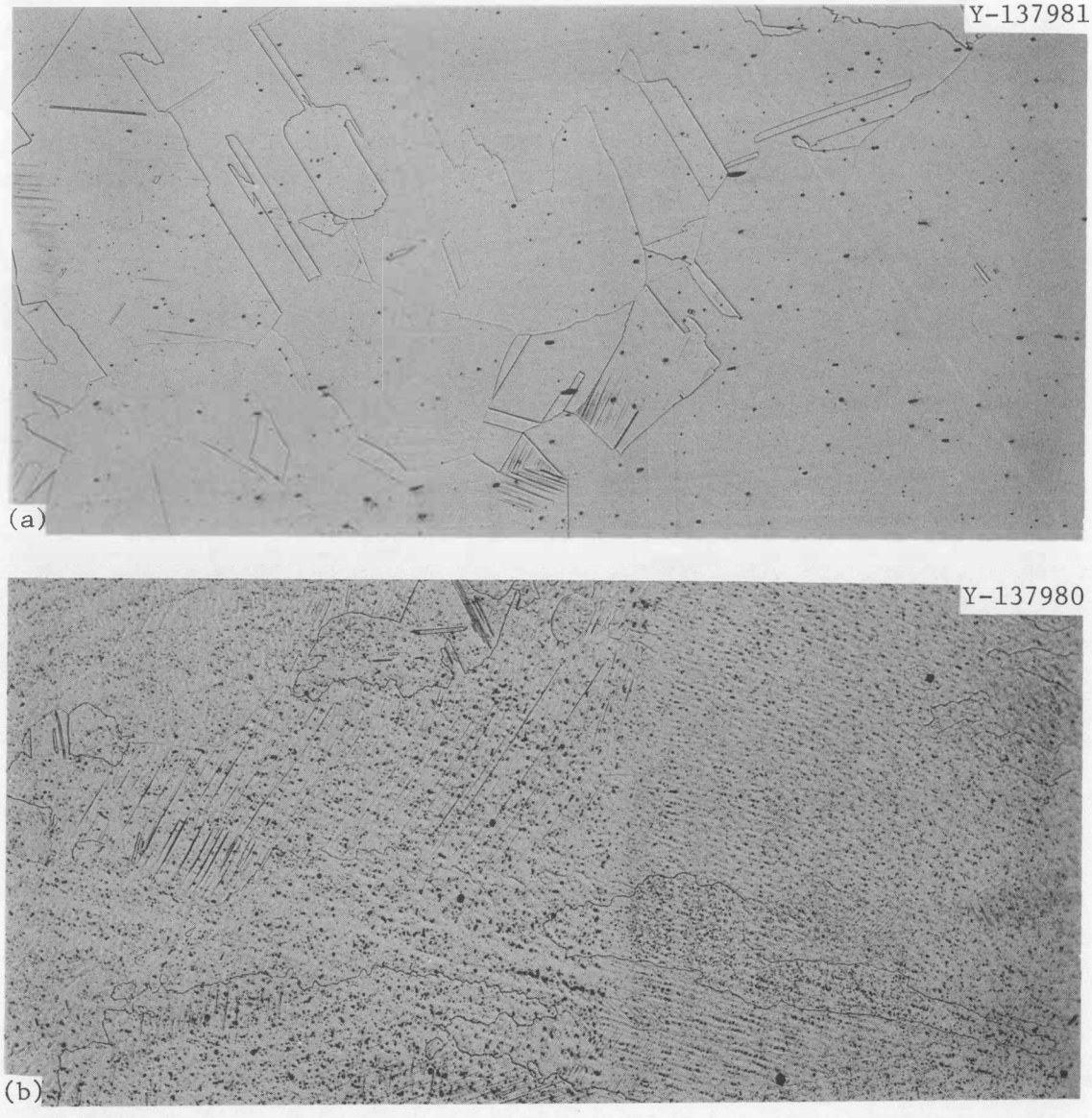

Fig. 4.4. Microstructure of Type 304 Stainless Steel Pipe Cold Worked 10%. 100×. Etchant: 50% HCl—10% HNO_3. (a) Base metal. (b) Fusion zone.

Additional cold work, to 20% reduction in thickness, gives the macrostructure shown in Fig. 4.5. Hardness was increased to approximately R_C 24. The as-cold-worked microstructure is shown in Fig. 4.6. The increased amount of martensite noted in the figure is again confirmed by Ferritescope measurements, with typical base metal readings of 0.2 FN.

Fig. 4.5. Macrostructure of Type 304 Stainless Steel Pipe Cold Worked 20%. Etchant: 50% HCl—10% HNO_3.

Annealing the 20%-cold-worked material at 1066 ± 14°C (1950 ± 25°F) results in the microstructures shown in Fig. 4.7. All martensite is removed from both the base metal and fusion zone, and the ferrite level in the fusion zone is reduced to approximately 0.2 FN, compared with approximately 1.5 FN in the as-welded and solution annealed condition. It is also noted that although the base metal grain size shows little change, the fusion zone grain size is significantly reduced by solution annealing [compare Figs. 4.7(b) and 4.2(b)].

Additional reduction in thickness to 30% cold work (Fig. 4.8) increases the hardness to approximately R_C 29 and shows a martensite level in the base metal of 0.2 to 0.6 FN. The microstructure of

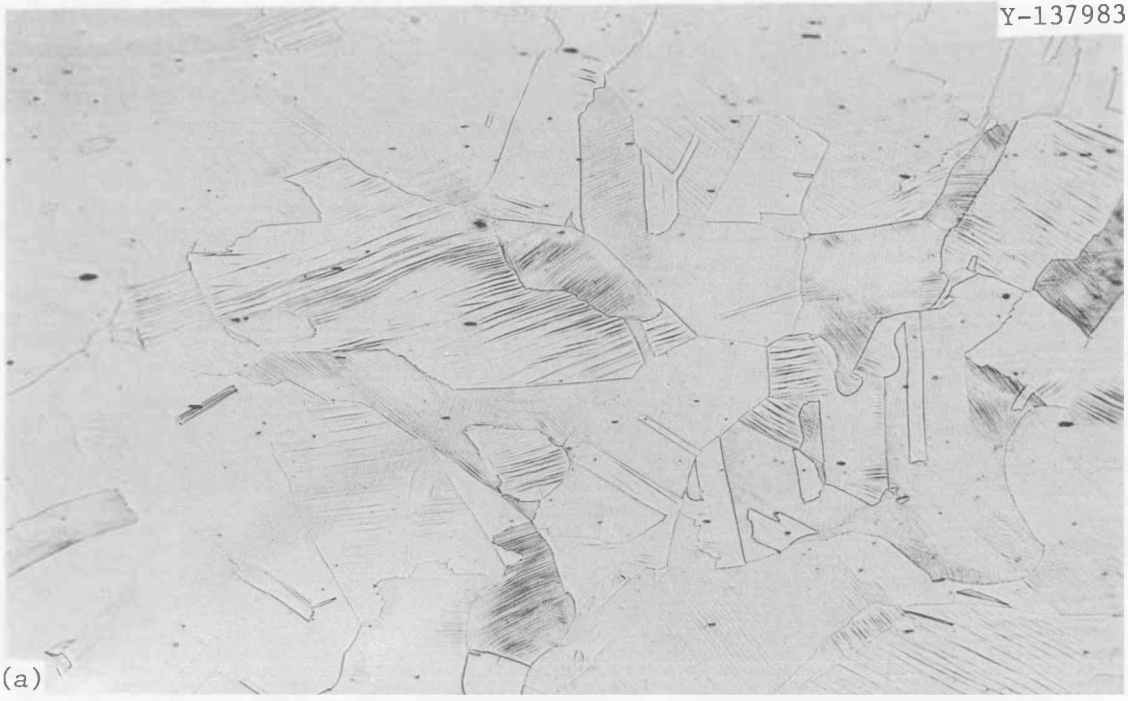

Fig. 4.6. Microstructure of Type 304 Stainless Steel Pipe Cold Worked 20%. 100×. Etchant: 50% HCl—10% HNO_3. (a) Base metal. (b) Fusion zone.

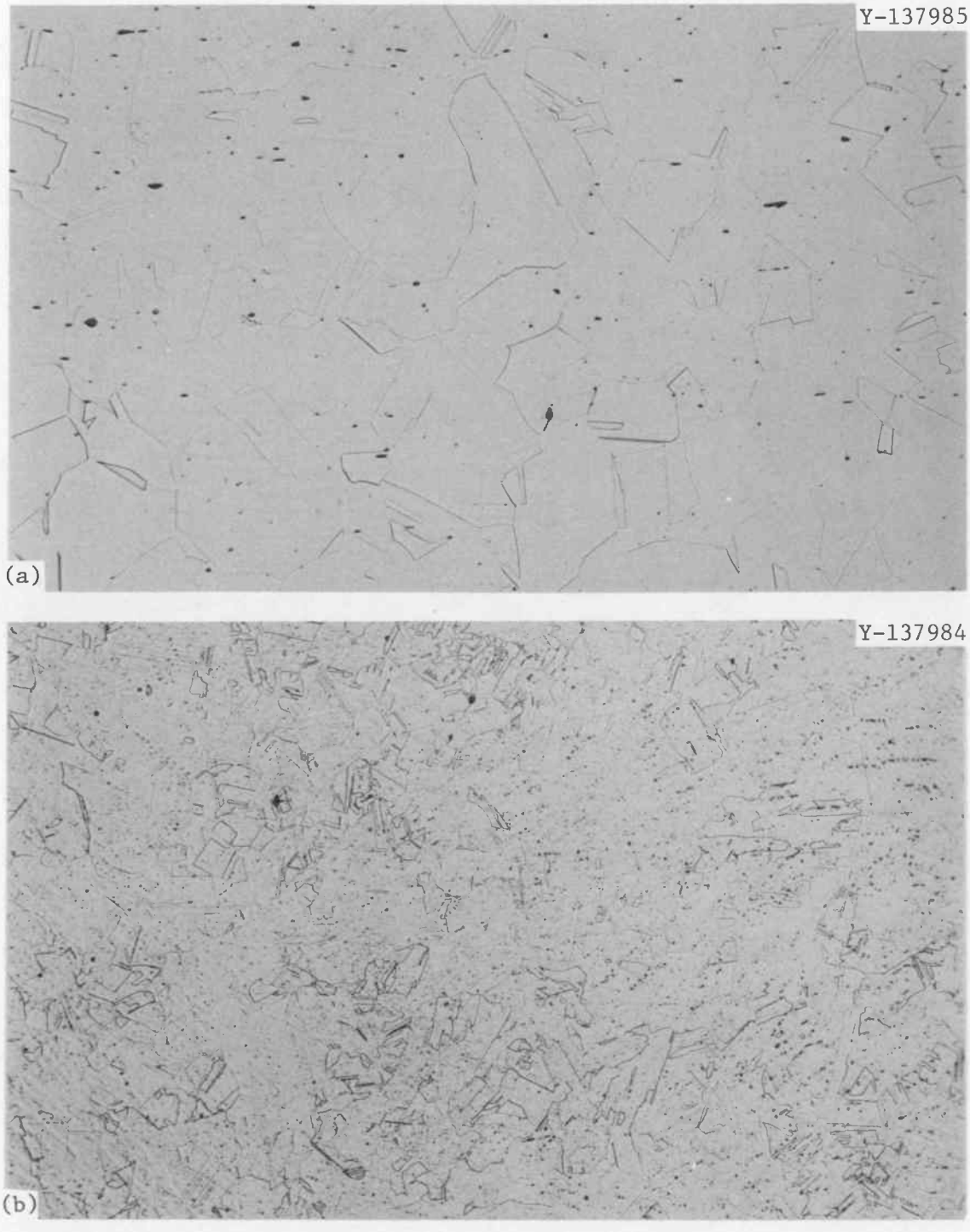

Fig. 4.7. Microstructure of Type 304 Stainless Steel Pipe Cold Worked 20% and Solution Annealed at 1066°C (1950°F). 100×. Etchant: 50% HCl—10% HNO_3. (a) Base metal. (b) Fusion zone.

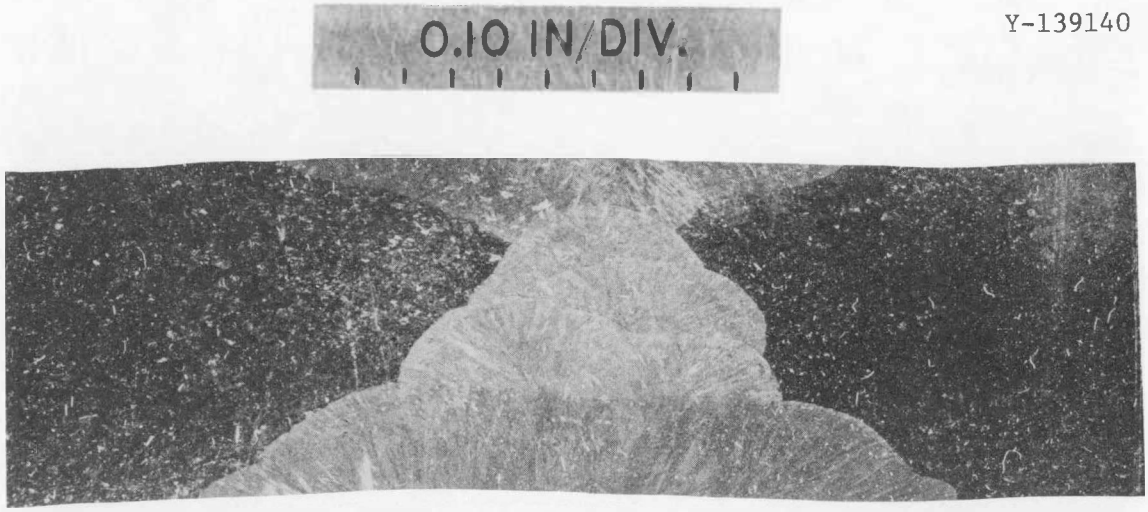

Fig. 4.8. Macrostructure of Type 304 Stainless Steel Pipe Cold Worked 30%. Etchant: 50% HCl—10% HNO_3. Scale is 2.5 mm per division.

30%-cold-worked material is shown in Fig. 4.9. Note in Fig. 4.9(b) that the martensite forms in local areas, depending at least in part on substructural orientation.

Further reduction to 43.7% cold work initiates edge cracking and represents the practical limit in this instance for cold work without an intermediate anneal. Hardness is increased to R_C 37 to 38. The macrostructure is shown in Fig. 4.10. The martensite level of the base metal reaches a level of 1.0 to 1.5 FN. The microstructure at this level of cold work (Fig. 4.11) confirms the presence of larger amounts of martensite.

Annealing at 1066 ± 14°C (1950 ± 25°F) results in the microstructures shown in Fig. 4.12. As was the case with 20% cold work [Fig. 4.7(a)], the base metal is returned to approximately the same grain size, but the fusion zone shows significant grain refinement [compare Figs. 12(b), 7(b), and 2(b)]. Ferrite level is further reduced to 0.1 FN. Little evidence of the as-welded structure remains.

Plans for further work in this area include sequential cold work and annealing to the same levels discussed here to determine the effect of intermediate anneals, and then characterizing the mechanical properties of several representative structures.

(a)

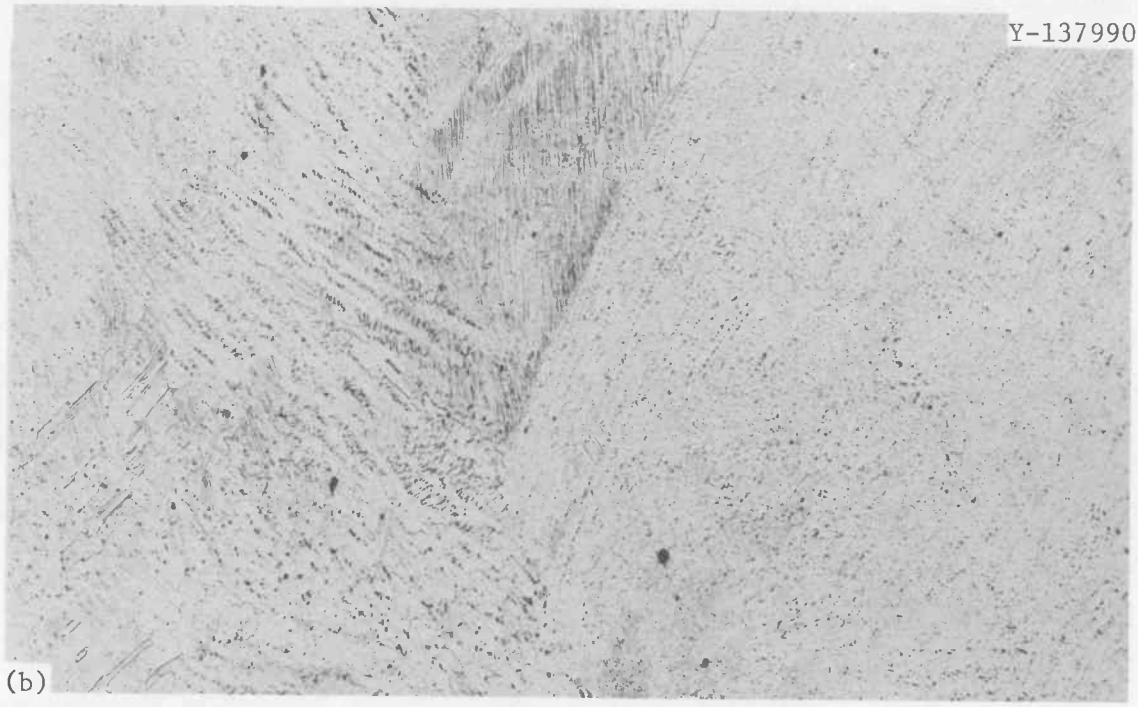

(b)

Fig. 4.9. Microstructure of Type 304 Stainless Steel Pipe Cold Worked 30%. 100×. Etchant: 50% HCl—10% HNO_3. (a) Base metal. (b) Fusion zone.

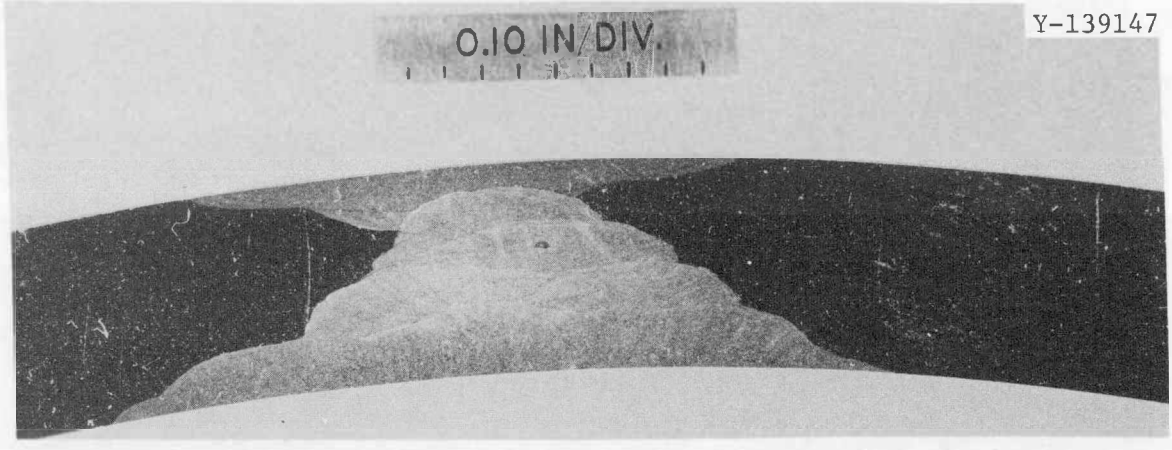

Fig. 4.10. Macrostructure of Type 304 Stainless Steel Pipe Cold Worked 43.7%. Etchant: 50% HCl—10% HNO_3. Scale is 2.5 mm per division.

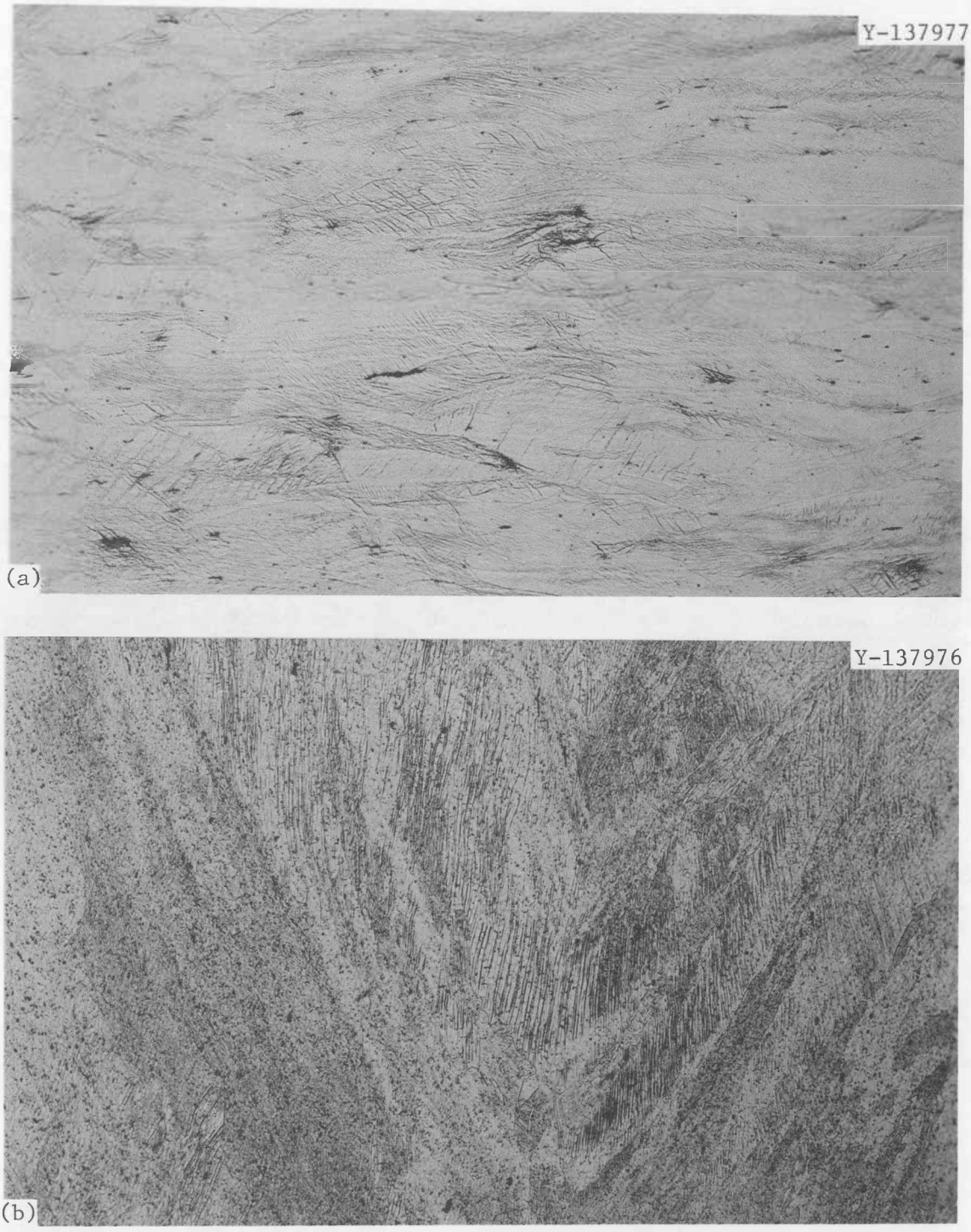

Fig. 4.11. Microstructure of Type 304 Stainless Steel Pipe Cold Worked 43.7%. 100×. Etchant: 50% HCl—10% HNO_3. (a) Base metal. (b) Fusion zone.

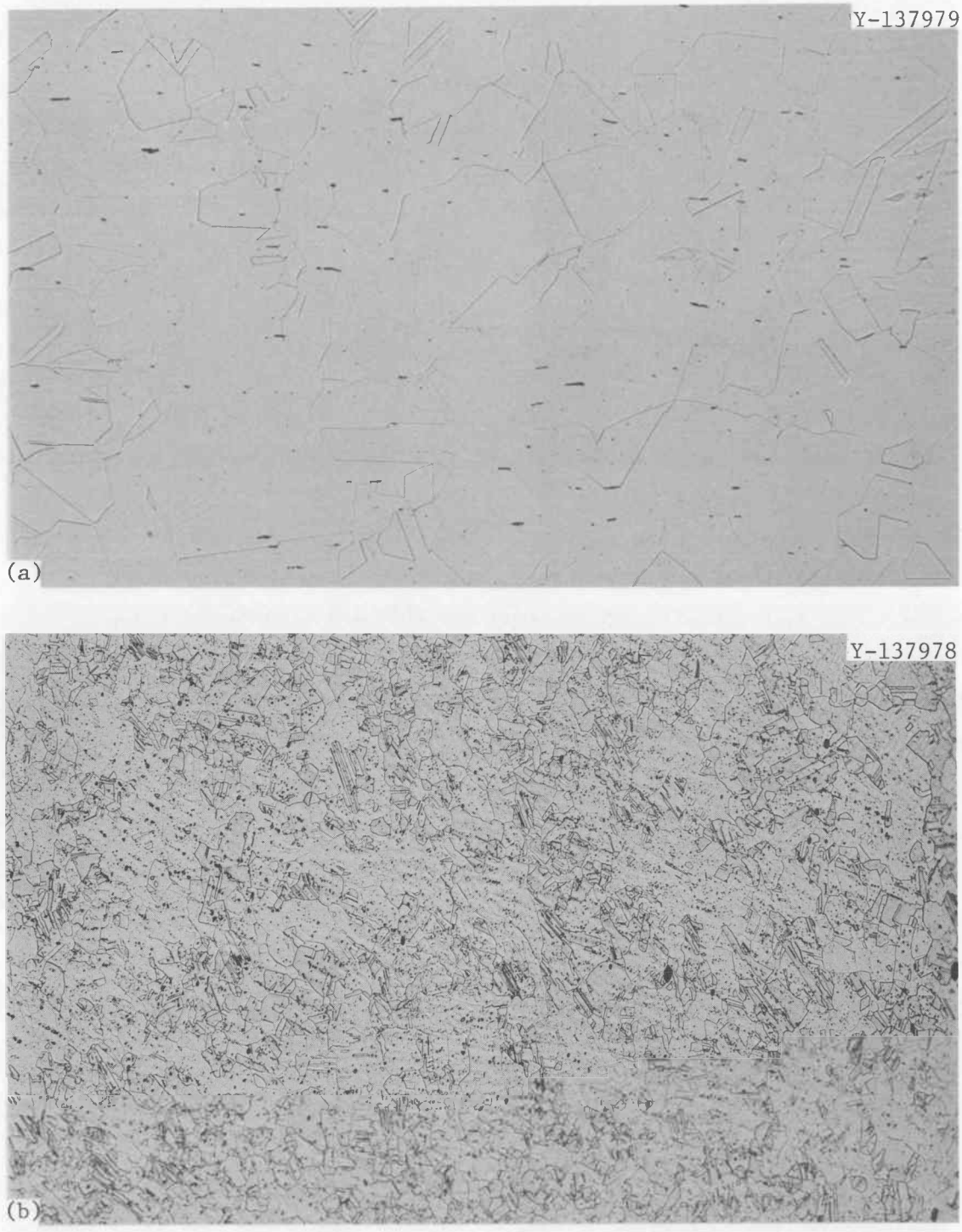

Fig. 4.12. Microstructure of Type 304 Stainless Steel Pipe Cold Worked 43.7% and Solution Annealed at 1066°C (1950°F). 100×. Etchant: 50% HCl—10% HNO_3. (a) Base metal. (b) Fusion zone.

4.4 CHARACTERIZATION OF CENTRIFUGALLY CAST PIPE SECTIONS FOR WORKING AND RECRYSTALLIZATION EXPERIMENTS — R. T. King and G. M. Goodwin

Making wrought thin-wall stainless steel piping for primary piping of LMFBRs from centrifugally cast pipe appears to be an attractive process, both economically and technically. We are therefore performing a series of experiments designed to demonstrate optimum schedules of working and annealing, and to characterize the effects of processing on the structure and properties of the material. This report gives initial characterization of the centrifugally cast pipe that is being used in the experiments.

Four sections of pipe have been supplied for the work by Sandusky Foundry and Machine Co., Sandusky, Ohio. Each pipe is 0.589 m (23 3/16 in.) OD by 0.486 m (19 1/8 in.) ID × about 0.5 m (2 ft) long. The chemical compositions and characterizations of the materials are given in Table 4.3. A 0.1-m-long (4-in.) ring was cut from each pipe, and a 100 by 50 by 25-mm slab was sawed from each ring. The slabs were polished on three sides and etched to reveal the macrostructure. (See Figs. 4.13, 4.14, and 4.15.) Approximate ferrite numbers (FN) were measured with a Ferritescope on the outer surface of the pipe, the inner surface of the pipe, and points about 5 mm from each surface. These results are compared with ferrite contents calculated by the vendor from the Schaeffler Diagram in Table 4.4.

Further characterization work will involve microstructural and chemical analyses. A limited amount of mechanical testing to provide base-line data is contemplated.

Table 4.3. Chemical Composition and Character of Centrifugally Cast Pipe

Designation	Pipe Heat	Material	Vendor Chemical Analysis, wt %								
			C	Mn	Si	Cr	Ni	P	S	Co	Mo
CF8(L)	154344	CF8 low ferrite	0.04	1.13	0.92	19.0	8.5	0.02	0.02	0.02	
CF8(H)	154345	CF8 high ferrite	0.04	0.54	1.48	20.5	8.5	0.01	0.02	0.03	
CF8M(L)	154581	CF8M low ferrite	0.04	1.16	1.00	19.7	10.2	0.02	0.02	0.04	2.2
CF8M(H)	154348	CF8M high ferrite	0.05	1.03	0.98	20.0	9.2	0.02	0.02	0.03	2.7

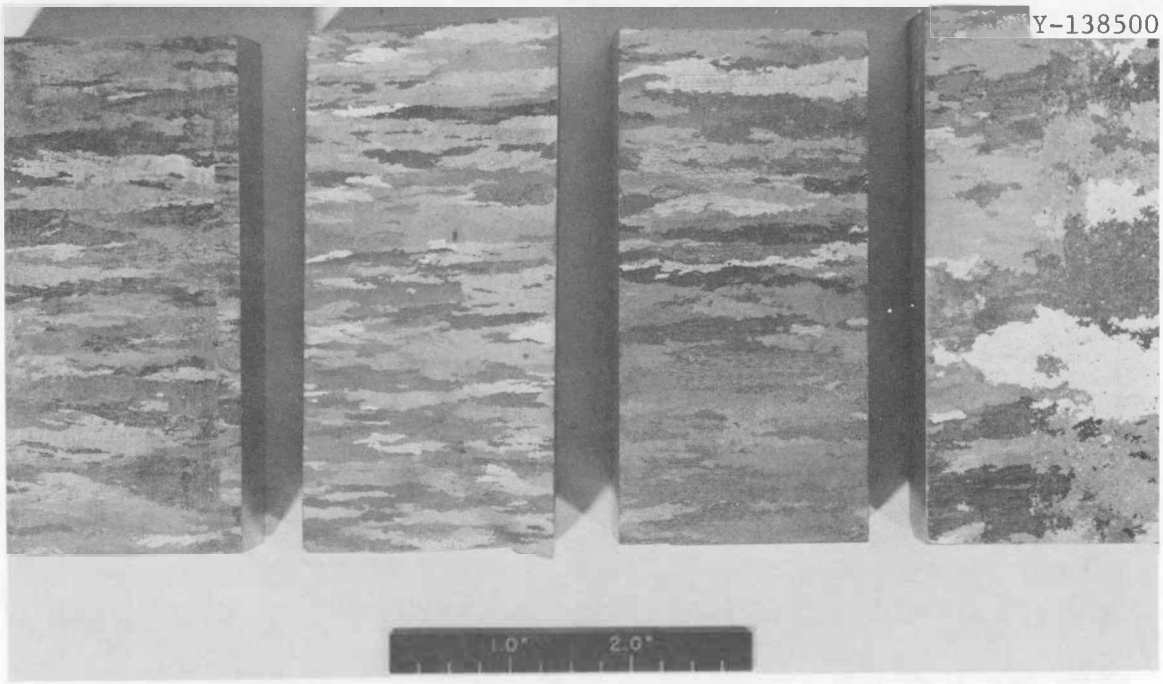

Fig. 4.13. Macrostructure of Centrifugally Cast Pipes — Radial Section. Left to right: CF8(L), CF8M(L), CF8(H), and CF8M(H). Scale is 6.4 mm (0.25 in.) per division.

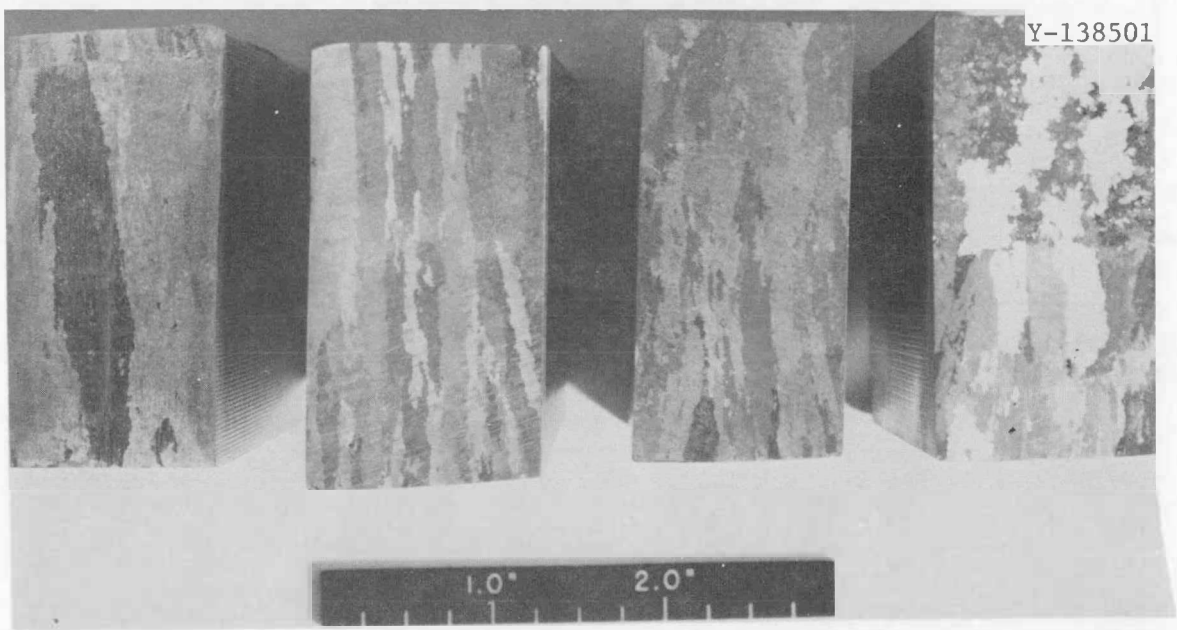

Fig. 4.14. Macrostructure of Centrifugally Cast Pipes — Section Normal to Pipe Axis. Left to right: CF8(L), CF8M(L), CF8(H), and CF8M(H). Scale is 6.4 mm (0.25 in.) per division.

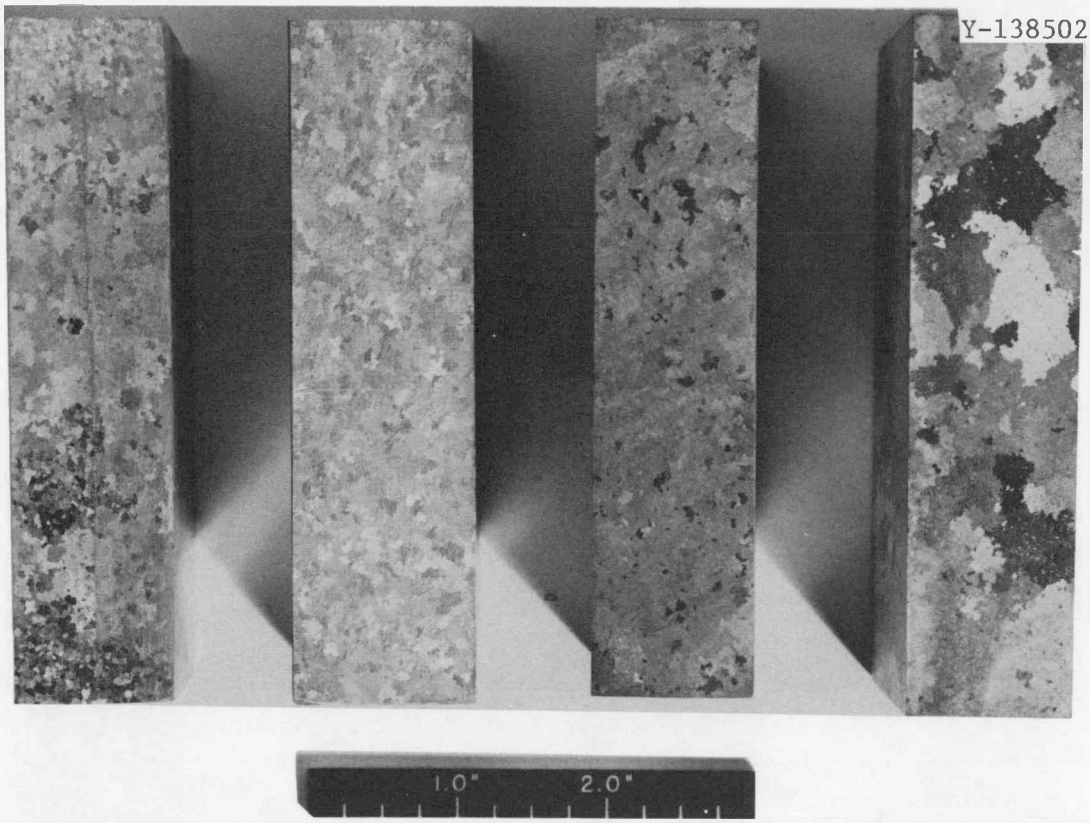

Fig. 4.15. Macrostructure of Centrifugally Cast Pipes — Outside Surface. Left to right: CF8(L), CF8M(L), CF8(H), and CF8M(H). Scale is 6.4 mm (0.25 in.) per division.

Table 4.4. Ferrite Numbers and Calculated Ferrite Contents of Centrifugally Cast Pipe

Designation	Calculated Ferrite Content (%)	Measured Ferrite Number (FN)			
		Outside Surface	Inside Surface	5 mm from Outside Surface	5 mm from Inside Surface
CF8(L)	12.8	1.3	0.5–1.0	0.3–3.3	0.5–1.0
CF8(H)	26.2	18–20	5–10	10–15	5–10
CF8M(L)	16.1	10–15	3–5	5–10	5–10
CF8M(H)	24.5	>30	10–15	20–25	10–15

5. ADVANCED ABSORBER MATERIALS*

V. J. Tennery and R. G. Donnelly

5.1 INTRODUCTION

The purpose of this program is to characterize and establish the physical and engineering properties and behavior of advanced neutron-absorber materials. These data will provide the basis for the selection, procurement, design, and engineering performance prediction of europium oxide and other potential candidate materials for fast reactor control and safety rod applications.

During this period the following report was issued:

M. M. Martin, *Performance of Eu_2O_3 in FTR Design-Oriented Irradiation Test in EBR-II*, ORNL-TM-5400 (June 1976).

5.2 CHARACTERIZATION OF EUROPIA

This subtask was completed in FY 1975.

5.3 CHARACTERIZATION OF ADVANCED MATERIALS

5.3.1 Eu_2O_3-W Cermet Development

No progress this report period.

5.3.2 EuB_6 Synthesis and Fabrication Development — A. E. Pasto

As reported previously,[1] this work is directed at powder synthesis and fabrication of pellets of EuB_6 as well as characterization of the stoichiometry, purity, and structure of the material. Results will allow selection of a synthesis powder mixture that will yield the desired characteristics of purity and phase composition in pellets suitable for irradiation testing.

Five batches of EuB_6 were produced during this period by vacuum reaction of mixtures of "Eu_2O_3" and "B_4C." The reduced material was crushed to −325 mesh and hot-pressed into dense pellets. Chemical

---

*Progress on work performed under 189a No. OH029.

analyses were obtained for the initial powder mixture, synthesized powder, and sintered pellets. X-ray diffraction, ceramographic, and immersion density analyses were performed on the pellets.

Chemical analyses identified the compositions of the raw materials as $Eu_{2.000}O_{3.144}$ and $B_{4.000}C_{0.871}O_{0.058}$. Thus, the europia was hyperstoichiometric with an excess of oxygen while the boron carbide was deficient in carbon and contained some oxygen as an impurity. From these results, it appeared that there would be difficulty in synthesizing pure EuB_6 from these starting materials since there was insufficient carbon available to remove all the oxygen as carbon monoxide during reduction of the Eu_2O_3. Consequently, the starting B/Eu ratio in the synthesis batches was varied from just below 6.000 to well above it.

Five batches (designated EB-8 through EB-12) were prepared by initially blending the europia and boron carbide powders in proportion to yield B/Eu molar ratios of 5.90 to 6.31. Each batch composition was then pressed into slugs, crushed, pressed, crushed again, and then repressed into three pellets and heated for 2 hr at 1650°C (3000°F) in a pumped vacuum of less than 1.3 mPa (10^{-5} torr).

From the composition of the mixed powders shown in Table 5.1, one would expect to lose about 16.4% by weight (total weight percentage of oxygen and carbon) during the reaction

$$Eu_2O_3 + 3B_4C \rightarrow 2EuB_6 + 3CO \uparrow .$$

Since the europium boride powders produced actually contained between 0.21 and 0.42 wt % O + C, the weight loss was expected to be less than 16.4%. However, as Table 5.1 shows, in all cases the theoretically expected weight loss was exceeded, indicating that substantial amounts of europium and/or boron were also being lost from the material during the synthesis. This may have occurred in several ways, including volatilization of europium as EuO or EuC_x and boron as boron oxides. The effluent gas from the furnace was not analyzed during these process steps, but such analysis in the future could be a means of identifying vaporizing species. Such data could provide help in identifying the

Table 5.1. Characterization of EuB_6 Powders and Pellets

Material Designation	Process State	Chemical Analysis,[a] wt %					B/Eu Mole Ratio	Lattice Parameter (Å)	Density (g/cm^3)	Average Weight Loss on Firing, %
		Eu	B	C	O	Total				
Theoretically Pure EuB_6	Hot Pressed	70.08	29.92			100.00	6.00	4.178–4.184[b]	4.94	
EB-8	Mixed Powders[c]	58.96	24.76	5.99	10.29	100.00	5.90			26.3
	As Fired[d]	70.24	29.58	0.055	0.16	100.04	5.92			
	Hot Pressed[e]	70.11	29.23	0.445	0.0146	99.80	5.86	4.1968	4.8514	
EB-9	Mixed Powders[c]	58.64	25.05	6.06	10.24	99.99	6.00			25.1
	As Fired[d]	69.58	29.67	0.092	0.142	99.48	5.99			
	Hot Pressed[e]	70.10	29.17	0.504	0.0091	99.78	5.85	4.1752	4.8526	
EB-10	Mixed Powders[c]	58.33	25.34	6.13	10.20	100.00	6.11			23.2
	As Fired[d]	70.69	29.82	0.141	0.139	100.79	5.93			
	Hot Pressed[e]	69.76	28.94	0.532	0.0105	99.24	5.83	4.1746	4.8691	
EB-11	Mixed Powders[c]	58.02	25.63	6.20	10.15	100.00	6.21			22.4
	As Fired[d]	69.24	29.92	0.220	0.142	99.52	6.07			
	Hot Pressed[e]	69.29	29.20	0.60	0.0112	99.10	5.92	4.1756	4.8689	
EB-12	Mixed Powders[c]	57.71	25.91	6.27	10.11	100.00	6.31			23.2
	As Fired[d]	69.09	30.31	0.262	0.160	99.82	6.12			
	Hot Pressed[e]	69.01	29.40	0.68	0.0157	99.11	5.99	4.1754	4.8729	

[a]Analytical results based on one sample of each material.

[b]Data from Schwetz and Lipp, "Die Verbindung EuB_6 als Absorberwerkstoff für Schnelle Reaktoren," *Atomwirtshaft* 18: 531–34 (1973).

[c]Analyses are for appropriate mixtures of "Eu_2O_3" and "B_4C." See text.

[d]Heated 2 hr at 1650°C (3000°F) in vacuum of $<10^{-5}$ torr (1.33 MPa).

[e]Hot-pressed in graphite dies at 41.4 MPa (6000 psi) under 0.10 MPa (1 atm) He, 1950°C (3540°F) for 120 min. Surfaces ground to remove graphite.

mechanism of boron and europium loss. Figure 5.1 shows that as the initial B/Eu mole ratio (and hence the C/O ratio) increases the observed weight loss decreases. This could indicate that either higher europium, higher oxygen content or both are associated with the increased loss as the B/Eu (C/O) ratio decreases. The boron and europium contents following heat treatment of the powders given in Table 5.1 are plotted in Fig. 5.2. One specimen of each batch was analyzed, so the accuracy and precision of the analytical results were not established, but a general trend is for higher boron and lower europium contents (i.e. higher B/Eu ratios) as the B/Eu ratio of the starting batch is increased. The europium content indicated for batch EB-10 is probably high, perhaps because of analytical problems, and evidenced by the total mass balance being greater than 100%. If this value were actually about 69.3 rather than the reported 70.69 value, the total mass balance would be 99.4 wt %, which is comparable to the other results. If the europium content were near 69.3 wt %, the maximum in Eu content and the minimum in B/Eu ratio shown in Fig. 5.2 would be eliminated and the plots would have a more normal behavior. Further support for this possibility is the orderly dependence of the carbon and oxygen contents (Fig. 5.3) as functions of initial B/Eu ratio. The europium content of the hot-pressed pellet of EB-10 (Fig. 5.4) lies on a smooth curve with the europium contents of other pellets in the series, and this leads us to suspect an analytical problem with the europium analysis of "as fired" powder EB-10.

To summarize the synthesis data, increasing the B/Eu ratio in the synthesis batch results in less weight loss on firing, a lower europium content, increased boron and residual carbon, and increased B/Eu ratio. The oxygen content of the powders appears to pass through a minimum as a function of the starting B/Eu ratio. Better estimates of the precision and accuracy of the analytical results will be obtained with further work and provide better confidence for the behavior of these variables. Oxygen contents were all between about 0.14 and 0.16 wt %.

The boride powders were crushed so as to pass a 325 mesh screen. The powders were fabricated into ceramics by hot-pressing in graphite dies at 1850 or 1950°C (3360 or 3540°F) under 0.1 MPa (1 atm) He.

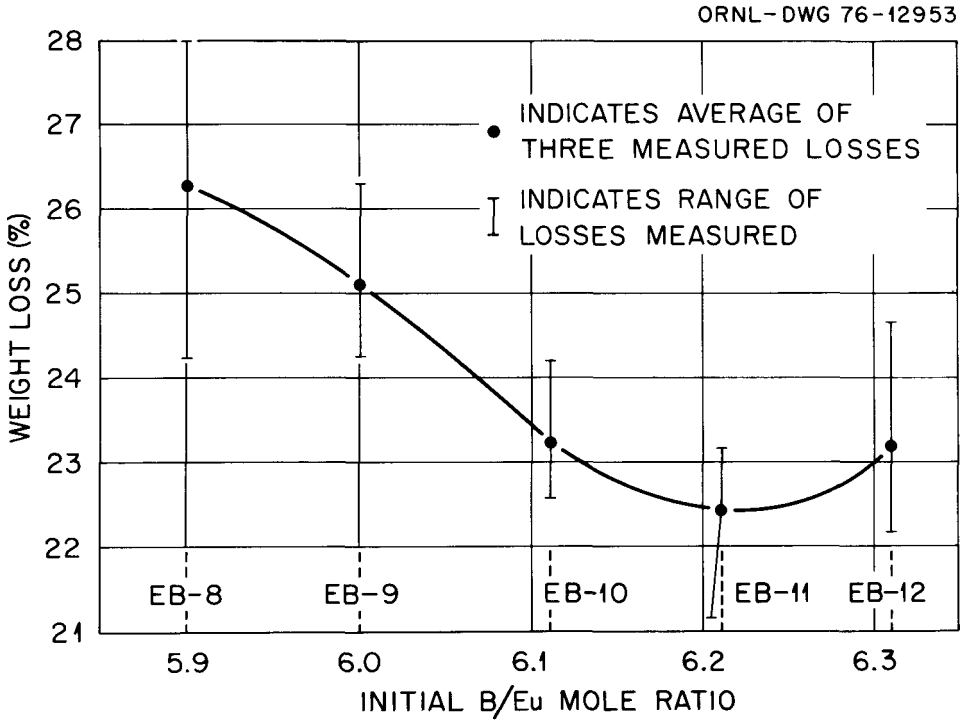

Fig. 5.1. Weight Losses During Synthesis of EuB_6.

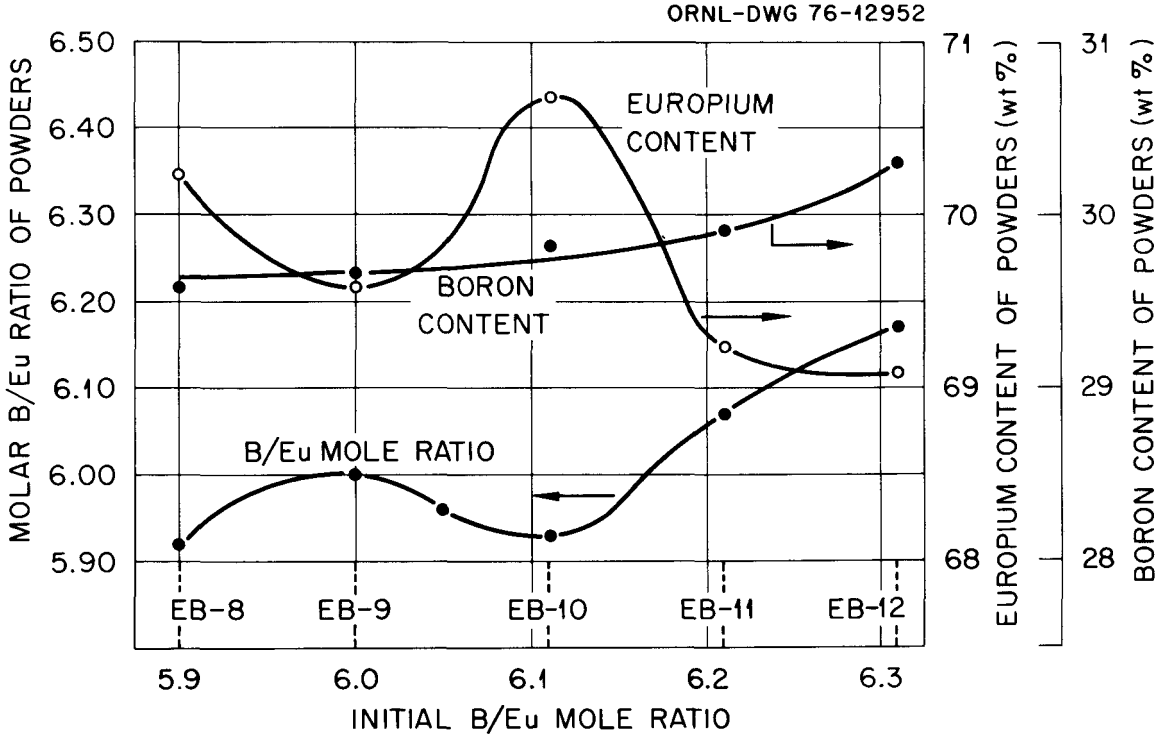

Fig. 5.2. Boron and Europium Content of EuB_6 Powders.

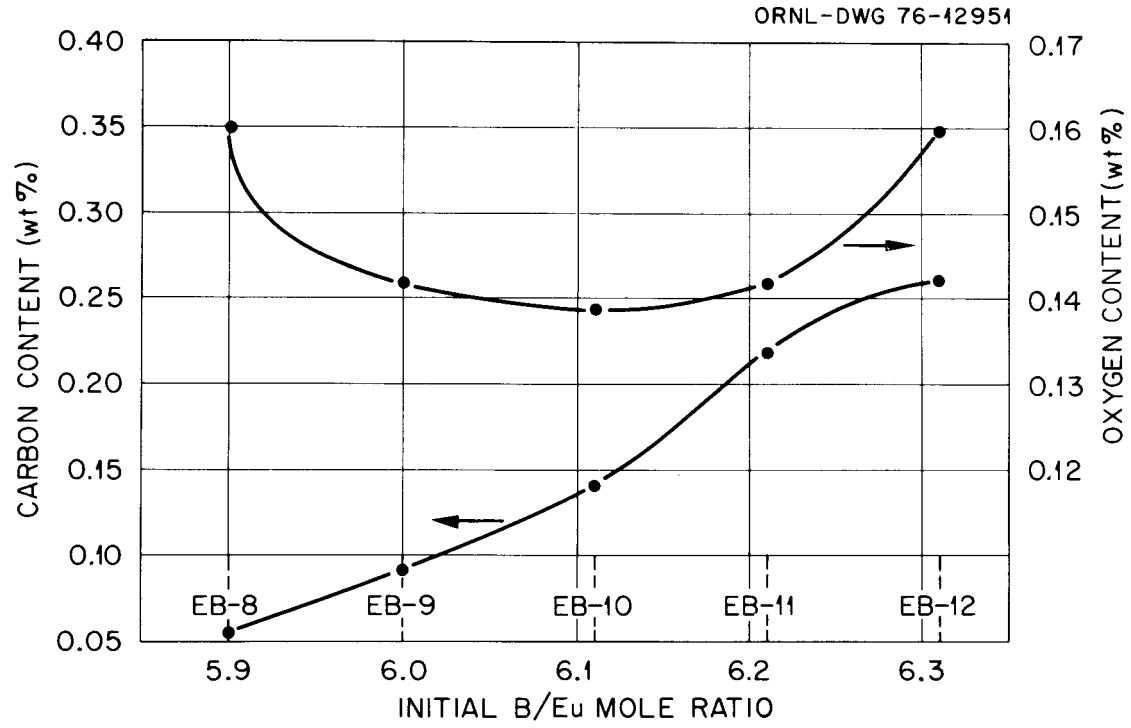

Fig. 5.3. Carbon and Oxygen Impurities in EuB_6 Powders.

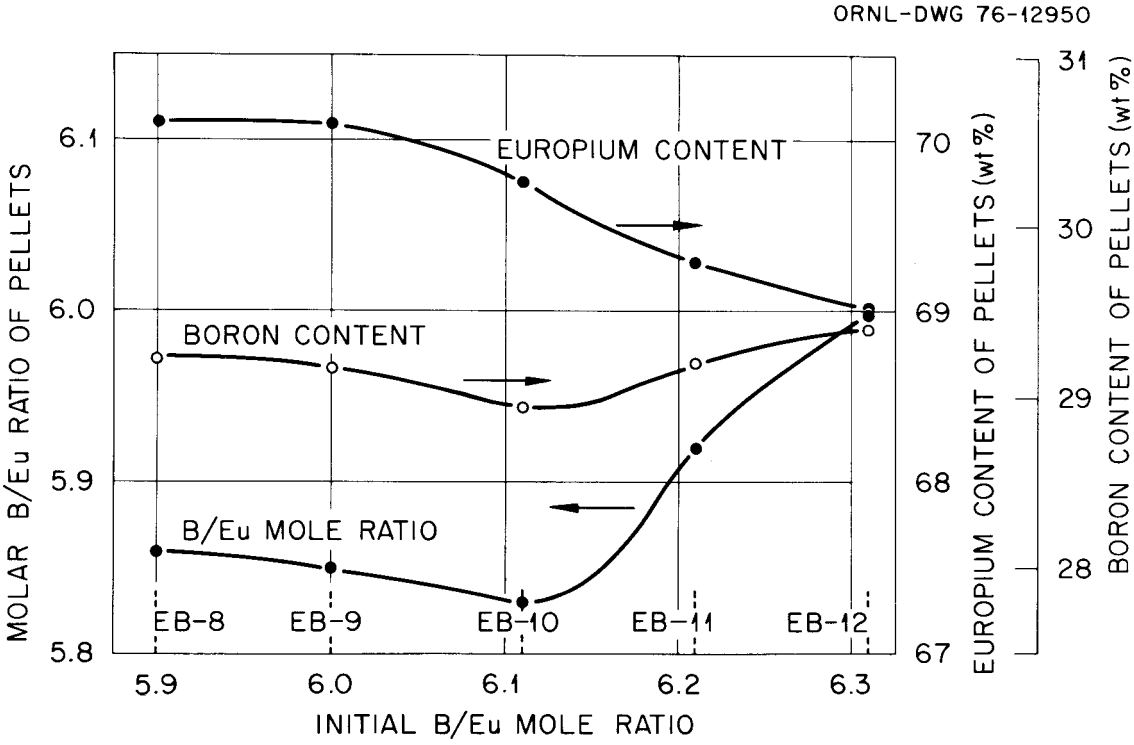

Fig. 5.4. Boron and Europium Content of Hot Pressed EuB_6.

Densities of pellets pressed at the lower temperature were about 85% of theoretical and were judged to be of insufficient density for control rod application. Data for the pellets pressed at the higher temperature are presented in Table 5.1 and plotted as a function of initial B/Eu ratio in Figs. 5.4 through 5.6. In Fig. 5.4, the final europium content is observed to decrease, while the final boron content and B/Eu ratio increase as a function of increasing initial B/Eu ratio. Ceramics having analyzed compositions nearest the theoretical value of 6.0 of EuB_6 were obtained for samples of EB-12, which had an experimental value of 5.99. For these ceramics, the final carbon content increases with the starting B/Eu ratio as shown in Fig. 5.5. This behavior is similar to that observed in the powders. For the hot-pressed ceramics, the carbon values are higher than those for the powders, in spite of the fact that any graphite from the die that adhered to the samples after hot-pressing had been removed before analysis. Before chemical characterization we ground the surfaces to reduce the diameters 0.15 mm (0.006 in.) and remove 0.25 mm (0.01 in.) from the ends of all the hot-pressed pellets. The oxygen content of the pellets exhibited a minimum as a function of the initial or starting B/Eu ratio. The oxygen contents of the pellets were about one-tenth those of corresponding powders. This is most probably due to carbon from the hot-pressing die reacting with oxygen in the sample to form CO, which subsequently left the pellet.

Evidence for a reaction occurring between the die and the samples was obtained when pellets were chemically analyzed before machining. These all yielded B/Eu ratios greater than 6.00, with values as high as 6.5. After machining, pellets from the same group yielded B/Eu ratios consistently less than 6.00. It is postulated that carbon (graphite) in contact with EuB_6 forms a carbide of europium, which volatizes at the hot-pressing temperature. This results in localized loss of Eu, and hence a product with a high B/Eu ratio. After this (reacted) surface layer is removed, the remaining material is of more homogeneous composition and a more representative bulk value is observed. It will therefore be quite important to identify the thickness of this inhomogeneity zone on hot pressed EuB_6 pellets and assure its removal before characterization or irradiation testing.

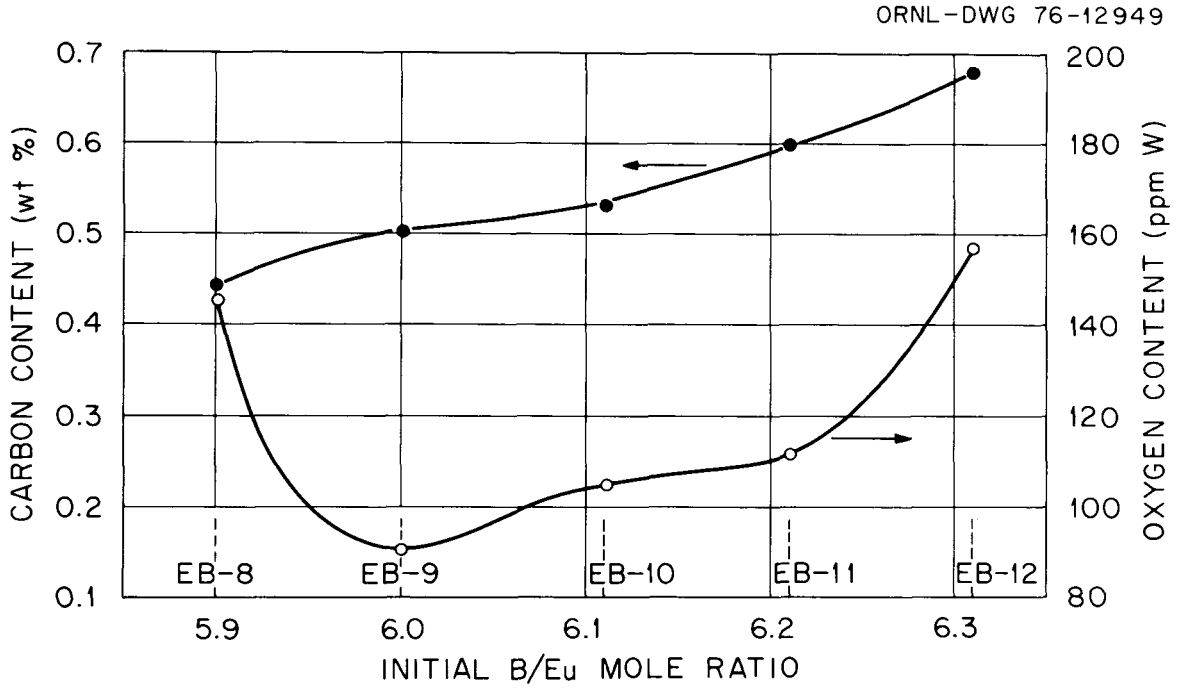

Fig. 5.5. Carbon and Oxygen Impurities in Hot-Pressed EuB_6.

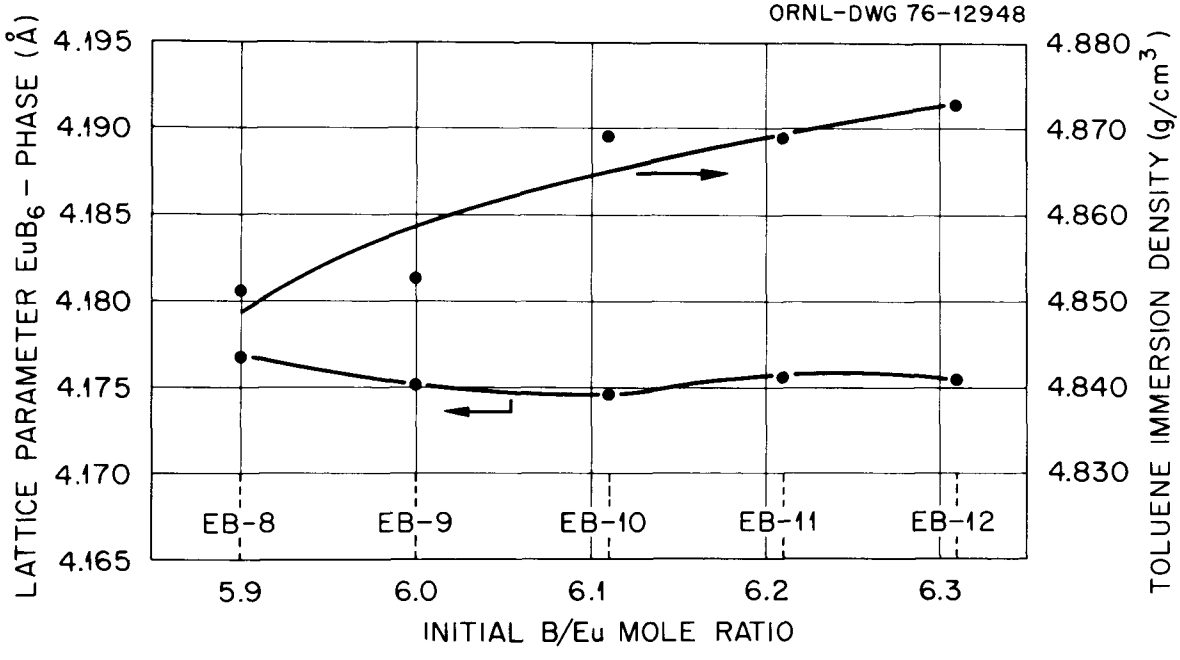

Fig. 5.6. Lattice Parameters and Densities of Hot-Pressed EuB_6.

The lattice parameter of the cubic EuB_6 phase was essentially constant at a_0 = 4.175 Å for all pellets (see Fig. 5.6 and Table 5.1). The density as measured by immersion in toluene in general increased with initial B/Eu ratio as shown in Fig. 5.6, but remained in all cases above 4.850 g/cm^3. For a lattice parameter of a_0 = 4.175 Å, calculation assuming the samples were pure EuB_6 shows that all pellets were denser than 98% of theoretical. No second-phase diffraction lines were observed in any of the x-ray diffraction patterns.

Ceramographic analysis of the pellets supported the high density figures as being realistic, and gave no evidence of any phase other than EuB_6. The microstructures in Fig. 5.7 also show that a bimodal grain size distribution is present in the microstructure. A matrix of grains less than 10 μm in diameter on the average surrounds larger grains with diameters of up to about 200 μm. A significant amount of the 2% residual porosity of the pellets is found within these large grains, indicating that discontinuous grain growth had occurred during the densification process. Figure 5.8, of a pellet of EB-9, show another effect associated with hot-pressing. Large grains tend to develop near the pellet circumference where it contacted the graphite die during fabrication.

Large grains in EuB_6 may prove to be detrimental to irradiation behavior of the material. Since helium will be produced in this material upon neutron capture by ^{10}B, this gas may collect within bubbles inside large grains and lead to an enhancement of swelling. Smaller grains would result in shorter helium diffusion path lengths to the grain boundaries and thus reduce swelling by allowing the gas to be released to these boundaries, where diffusion to the surface would occur more rapidly. Control of the grain size then may be an important consideration for this potential advanced absorber material. Discontinuous grain growth can be prevented by hot-pressing so as to produce a lower density, such as 92 to 95% of theoretical, such that the larger amount of porosity inhibits so called "breakaway" movement of certain grain boundaries with the resultant rapid increase in the size of some grains.

A significant result of the present work is that it demonstrated a relatively simple process that will produce single-phase europium

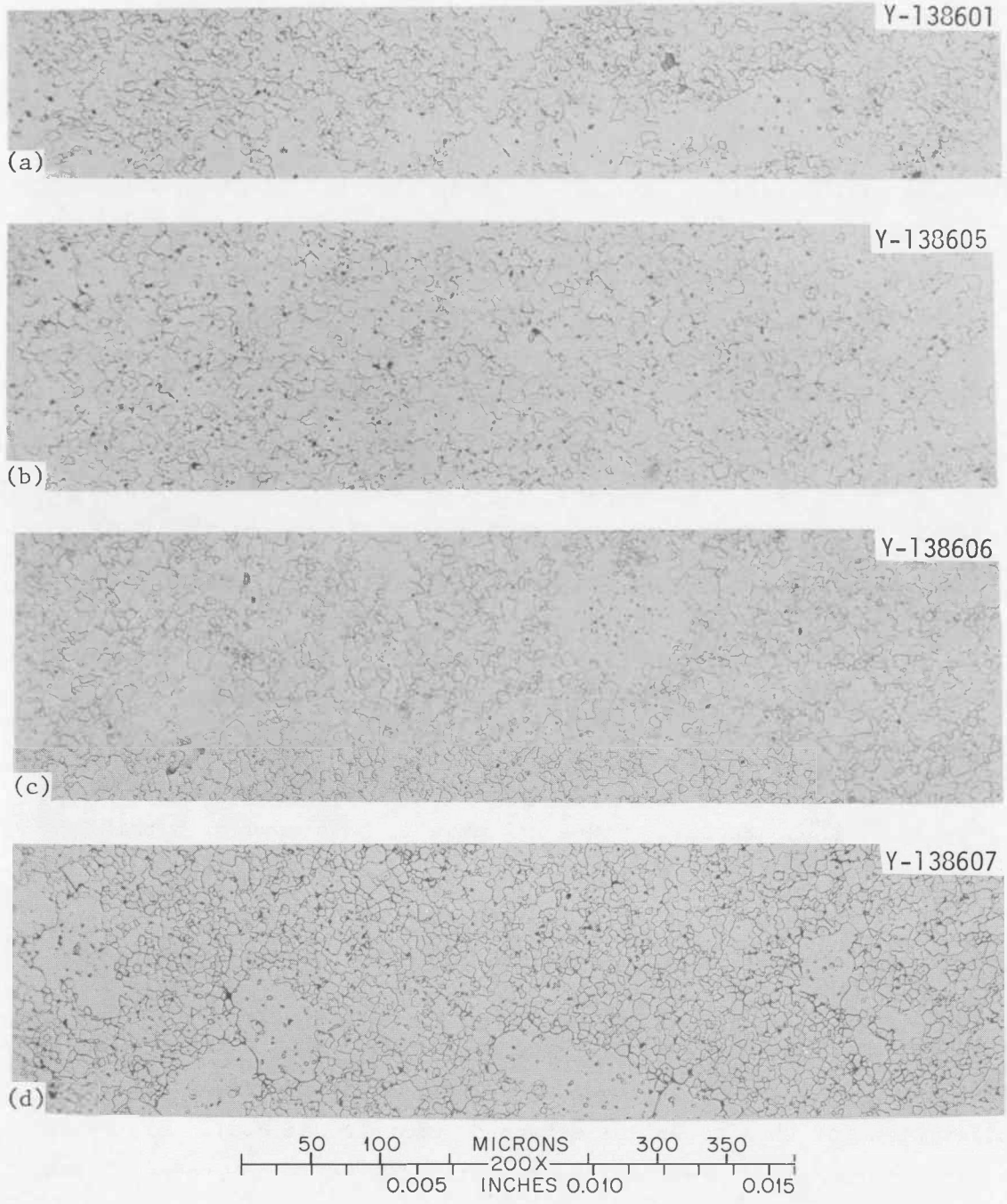

Fig. 5.7. Microstructures of Representative Areas of Hot-Pressed EuB_6 Pellets. 200×. (a) EB-8. (b) EB-10. (c) EB-11. (d) EB-12.

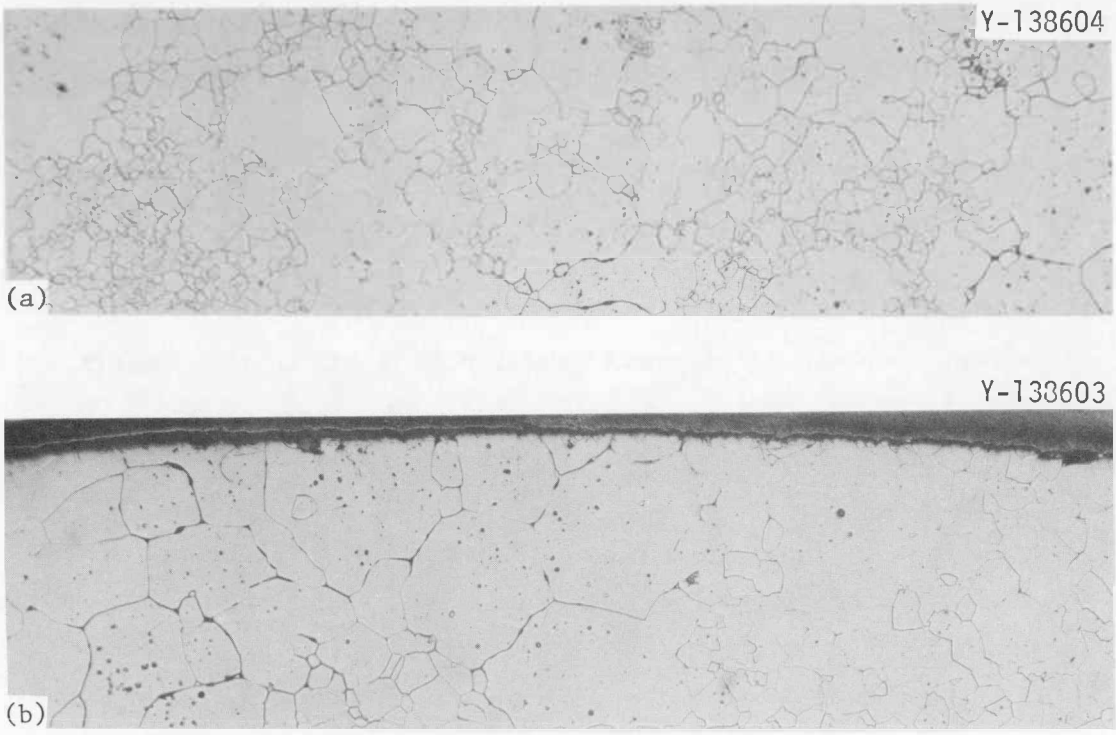

Fig. 5.8. Microstructure of Hot-Pressed EuB_6 Pellet EB-9. 200 . (a) Representative area. (b) Near edge.

hexaboride pellets of high density and low oxygen content. Stoichiometry can be varied over a reasonable range without evidence of the presence of second phases. Theoretical ratios B/Eu = 6.00 can be attained if desired. Further development work on this material will be directed to identification of the values of the processing parameters critical to controlling density and grain size in fabricated pellets. Later, the thermal conductivity of the material will be determined to higher temperatures than presently available data.[2]

5.4 IRRADIATION TESTING

5.4.1 Status of EBR-II Experiments

Upon completion of the postirradiation examination of the short- and mid-term subassemblies of the Eu_2O_3-bearing FDOT test, it was decided to leave the long-term subassembly in reactor longer than initially requested. Consequently an extension of the irradiation time

for this subassembly (X205A) was requested and approved. Goal exposure is now 37,000 MWd. Accumulated exposure through run 82, which ended on June 5, was 18,000 MWd.

The HEDL-ORNL instrumented irradiation test of Eu_2O_3, designated BICM-2 (YY06), has been extended to run until the end of EBR-II run 85.

5.5 PERFORMANCE ANALYSIS

A report on the irradiation behavior of Eu_2O_3 in the 6-month and 9-month pins of the FDOT was issued. See Sect. 5.1.

5.6 REFERENCES

1. A. E. Pasto, "EuB_6 Synthesis and Fabrication Development," *LMFBR Materials Development Program Quart. Prog. Rep. March 31, 1976*, ORNL-5157, p. 139.
2. A. E. Pasto and C. S. Morgan, *Status and Potential of Europium-Based Fast Neutron Absorber Materials*, ORNL/TM-5244 (February 1976).

ORNL-5218
Distribution Category
UC-79b, -h, -k

INTERNAL DISTRIBUTION

1–3. Central Research Library
4. ORNL — Y-12 Technical Library
Document Reference Section
5–11. Laboratory Records Department
12. Laboratory Records, ORNL RC
13. ORNL Patent Office
14. M. Bender
15. J. J. Blass
16. M. K. Booker
17. E. E. Bloom
18. C. R. Brinkman
19. D. A. Canonico
20. K. V. Cook
21. J. M. Corum
22. W. R. Corwin
23. F. L. Culler
24. J. H. DeVan
25. J. R. DiStefano
26. C. V. Dodd
27. R. G. Donnelly
28. W. P. Eatherly
29. D. P. Edmonds
30. M. H. Fontana
31. B. E. Foster
32. G. M. Goodwin
33. R. J. Gray
34. W. L. Greenstreet
35. J. C. Griess, Jr.
36. W. O. Harms
37. R. F. Hibbs
38–40. M. R. Hill
41. R. L. Heestand
42. P. R. Kasten
43. J. F. King
44. R. T. King
45. R. L. Klueh
46. K. C. Liu
47. A. L. Lotts
48. M. M. Martin
49–51. W. R. Martin
52. W. J. McAfee
53. R. W. McClung
54. H. E. McCoy
55. D. L. McElroy
56. C. J. McHargue
57. A. J. Moorhead
58. A. E. Pasto
59–66. P. Patriarca
67. S. Peterson
68. H. Postma
69. C. E. Pugh
70. P. L. Rittenhouse
71. T. K. Roche
72. J. L. Scott
73. V. K. Sikka
74. W. A. Simpson
75. G. M. Slaughter
76. J. H. Smith
77. S. D. Snyder
78. J. O. Stiegler
79. J. P. Strizak
80. R. W. Swindeman
81. D. B. Trauger
82. J. R. Weir, Jr.
83. G. D. Whitman
84. G. T. Yahr
85. P. M. Brister (consultant)
86. J. M. Duke (consultant)
87. S. D. Harkness (consultant)
88. W. A. Maxwell (consultant)
89. John Moteff (consultant)
90. Hayne Palmour III (consultant)
91. J. W. Prados (consultant)
92. N. E. Promisel (consultant)
93. E. W. Shuster (consultant)
94. D. F. Stein (consultant)

EXTERNAL DISTRIBUTION

95–96. ERDA DIVISION OF NUCLEAR FUEL CYCLE AND PRODUCTION, Washington, DC 20545

Director

97–98. ERDA DIVISION OF NUCLEAR RESEARCH AND APPLICATIONS, Washington, DC 20545

Director

99–100. ERDA DIVISION OF REACTOR RESEARCH AND DEVELOPMENT, Washington, DC 20545

Director

101–102. ERDA OAK RIDGE OPERATIONS OFFICE, P.O. Box E, Oak Ridge, TN 37830

Research and Technical Support Division
Director, Reactor Division

103–388. ERDA TECHNICAL INFORMATION CENTER, Office of Information Services, P.O. Box 62, Oak Ridge, TN 37830

For distribution as shown in TID-4500 Distribution Category, UC-79b (Fuels and Materials Engineering Development); UC-79h (Structural Materials Design Engineering); UC-79k (Components)

☆ U.S. GOVERNMENT PRINTING OFFICE: 1976-748-189/43